INFLUENCE OF GRAPHITIZATION ON PHASE TRANSFORMATION KINETICS AND MECHANICAL PROPERTIES OF LOW ALLOY STEELS

Jinhong Yang

Master of Engineering, Chengdu University of Science and Technology, 1990

Bachelor of Engineering, Chengdu University of Science and Technology, 1987

A thesis presented to the faculty of the

Oregon Graduate Institute of Science and Technology

in partial fulfillment of the requirements for the degree

Doctor of Philosophy

in

Materials Science and Engineering

June, 1999

The dissertation "Influence of Graphitization on Phase Transformation Kinetics and Mechanical Properties of Low Alloy Steels" by Jinhong Yang has been examined and approved by the following Examination Committee:

William E. Wood, Thesis Advisor
Professor
Department of Materials Science and Engineering
Oregon Graduate Institute of Science and Technology

Jack H. Devletian
Professor
Department of Materials Science and Engineering
Oregon Graduate Institute of Science and Technology

Lemmy L. Meekisho
Associate Professor
Department of Materials Science and Engineering
Oregon Graduate Institute of Science and Technology

Jack McCarthy
Assistant Professor
Department of Materials Science and Engineering
Oregon Graduate Institute of Science and Technology

ACKNOWLEDGMENTS

First of all, I would like to thank my thesis adviser, Dr. William E. Wood, for his academic guidance, encouragement, and financial aid through the course of this work.

Special thanks go to Dr. Jack H. Devletian, Dr. Lemmy L. Meekisho, Dr. Jack McCarthy for their guidance at various stages of the research and for their time and effort in reviewing the manuscript. Also, I greatly appreciate the help I received from Dr. David G. Atteridge, Dr. Margaret Ziomek-Moroz, Dr. Milton R. Scholl, and Dr. James T. Stanley.

I owe a lot to Mr. Robert Turpin and Mr. Kenneth Burns who have been patiently helping me in electrical and mechanical equipment adjusting and data acquisition. I would also like to extend my thanks to OGI staff, namely, Mrs. Roxanne Metzker, Mr. Douglas Davis and Mr. Andrew Huffstutter and Ms. Kristen Terry. I am grateful to the former OGI postdoctoral research associates, Dr. Lu Fang, Dr. Nong Jin, Dr. Jun Ding, Dr. Yuoping Gao, Dr. Xiaoyan Su and Dr. Qiong Qiu for their invaluable suggestions. I also would like to express my deep appreciation to my fellow students and friends: Dr. Xiao (Leo) Chen, Dr. Wei Su, Dr. Leilei Zhang, Hamid Faridi, Heidi Davis, Fabian Radulescu, Wenwei Yang, Jinshan Huo, Graham Tewksbury, William Bartley, Kevin Searles, and Rob Davis, without them, my study at OGI would not have been such a pleasant experience.

This research was funded by Oregon Cutting Systems Division, Blount Inc. My thanks also go to Mr. John DeHaven for his technical support.

Last, I heartily thank my husband, Jiaqing and my parents for all their understanding, and encouragement.

To my parents, Zhengde Yang and Xiaoling Ma

my husband, Jiaqing Pang

and my son, Chunlin Pang

TABLE OF CONTENTS

LIST OF FIGURES

LIST OF TABLES

ABSTRACT

Influence of Graphitization on Phase Transformation Kinetics
and Mechanical Properties of Low Alloy Steels

Jinhong Yang
Oregon Graduate Institute of Science and Technology, 1998

Supervising Professor: William E. Wood

Graphite is the equilibrium state of carbon in iron and steel. Cast irons usually contain graphite, while for steels carbon exists in solid solution and metastable carbides. However, graphite can be induced by the combination of steel cleaning technology, cold working and annealing process. This research studied (1) the characteristics of graphite and carbide phases in cold worked and annealed low alloy steels, (2) the graphite dissolution kinetics, and (3) the influence of graphite on martensite and Bainite transformation kinetics and mechanical properties of low alloy steels.

Focused Ion Beam cross-section and fractography study indicated that graphite/matrix interfaces in cold worked and annealed low alloy steels are well bonded. A previous proposed carbon diffusion model during cementite spheroidizing was confirmed by transmission electron microscopy. Transmission electron microscopy analysis also indicated that cold work can cause cementite dissolution.

Graphite dissolution kinetics were demonstrated as a function of austenitizing temperature and time. The effects of graphitization on martensite transformation were studied by Gleeble thermal-mechanical testing system. Graphite dissolution resulted in decreasing the martensite transformation start temperature and increasing martensite strength. Two Bainite TTT curves for steels with two graphite levels were developed.

The Bainite transformation kinetics were studied by curve fitting the experimental

transformation curves using Johnson-Mehl-Avrami (JMA) model, Austin-Rickett (AR) model.

The stress and strain distribution around a graphite particle in steel matrix was studied by finite element analysis. Results suggested that failure m ode depended on particle and matrix properties. Graphite breaking or debonding occurs only after matrix yielding. The particle/crack interaction was characterized using J integral. The J integral for an edge cracked matrix with graphite is greater than with Al_2O_3, but less than with a void.

CHAPTER 1
PREFACE

Graphitization can be defined as the formation of free carbon (graphite) in iron or steel. Graphite formed during the solidification process is called primary graphitization, resulting in the stable iron graphite structure. Gray (flake graphite) iron, ductile (spheroidal graphite) iron, and compacted graphite iron are cast irons representing examples of a primary graphitization. Graphite formation through the transformation of metastable metallic carbides following solidification is termed secondary graphitization. The most common process of secondary graphitization involves the decomposition of pearlite by transforming cementite, at elevated temperature, to iron and graphite. The age-related graphitization of carbon and low alloy steel is secondary graphitization.

1.1 PROBLEM DEFINITION

Graphitization in industrial alloys with a high carbon content (graphitised steel, cast iron) has been extensively studied. In low carbon steels (0.1%) graphitization is also possible. Recently, in the microstructure of cold rolled and annealed steels, finely dispersed, graphite nodules measuring 1-5 μm were observed in Japan, Russia and the United States. The graphite, located on the grain boundaries of primary austenite and at the joints of ferrite grains, caused numerous defects during deep drawing of 18YA steel[1]. Sueyoshi[2] found that graphite nodules promote the formation of micro-cracks in the neighborhood of a tool edge. It has been reported that graphite precipitation could occur over the surface of cold rolled

steel sheets during annealing, leading to a dark continuous staining of the coil[3,4,5], which has been a serious problem for sheet steel suppliers, because it impaired paintability and coating adherence of steels. Okamoto[6] observed that graphitization greatly reduced the tensile strength of steels. The main reason for the reduction in tensile strength was spheroidization, the dissolution of the fine carbides that give the material strength. C. J. Moss[7] noted that graphite nodules can act as cavity nuclei during creep testing because the interface between the graphite and matrix may separate at low levels of strain. Due to the reduced matrix strength (because speroidization) the cavity growth process is accelerated and the graphitized material exhibits both a reduced rupture strength and rupture ductility. It is unclear why graphitization has become a problem in the last two decades. To prevent failures caused by graphitization, the characteristics and kinetics of graphitization in carbon and low alloy steel must be studied.

Graphite formation in carbon and low alloy steel is achieved by three stages: carbides decompose, graphite nucleation, graphite growth. Graphitization is a process that irons or steels transform to their equilibrium state. Thermodynamically, graphite can be formed from ferrite and austenite with supersaturated carbon. Cementite will decompose into ferrite and graphite and cementite can be formed from austenite and graphite.

Graphite nucleation is heterogeneous. Graphite nucleation is primarily driven by availability of nucleation sites, while graphite growth kinetics are generally controlled by the diffusion/transport of the slowest moving species resulting in free carbon at the nucleated graphite phase. For graphite nucleated in microvoids, carbon diffusion may control the rate of graphitization; while Fe, Si diffusion may be more important for the case of graphite nucleated at grain boundaries. The kinetics of graphitization has been be described in the form of the Johnson-Mehl-Avrami equation or in Arrhenius terms. However, different n values and thermal activation energies were obtained. A better model is needed.

It has been found that graphite particles coexists with Al-Si inclusions in some steels. The function of inclusions in the graphitization of iron and steel has been disputed[8]. The effect of inclusions on graphitization was attributed to providing nucleation sites by promoting the formation of cavities and defects due to their physical properties differing

from the matrix. Also, their crystal structure may cause a more coherent fit for graphite formation.

The reasons why prior deformation or cold work could accelerate the graphitization process is not very clear. Some researchers suggested that cold work contributes to graphitization by creating more defects as nucleation sites and by decreasing the cementite stability[9].

The effects of alloy elements are complicated, because alloy elements may change carbon solubility, carbon mobility, carbide stability and inclusion formation. S and P content may be the controlling factors for graphite formed on free surfaces.

The effect of graphitization on the mechanical properties of carbon and low alloy steel is also rarely reported. The fracture mode of carbon and low alloy steels containing graphite is likely to be ductile fracture. To develop a satisfactory model of crack initiation and growth during ductile fracture, physical understanding, numerical simulation and experimental confirmation is essential.

1.2 RESEARCH OBJECTIVES

This study will investigate the nucleation mechanisms of graphite, and the influence of graphite on the properties of low alloy steel during processing and heat treatment. The following objectives are expected to be achieved:

(1) Determine whether the graphite nodules can be dissolved in cold working and annealing sheet steels; if possible, what is the optimum heat treatment; no efforts to dissolve graphite have been reported.

(2) Study the effects of carbide characteristics on graphitization.

(3) Study the effects of cold-work or plastic strain on cementite dissociation and graphite nucleation.

(4) Study the effect of graphite content on martensite transformation and Bainite Transformation kinetics.

(5) Study the effects of graphitization on mechanical properties of low alloy steels.

(6) Calculate the stress and strain concentration caused by graphite, Al_2O_3 and microvoids during using finite element analysis for studying the micro-mechanic mechanisms of ductile fracture.

(7) Study the interactions between a microcrack and graphite, or Al_2O_3 , or microvoids using finite element analysis.

1.3 THESIS OUTLINE

Chapter 1 is dedicated to the problems caused by graphitization, the research objective, the experimental and numerical approaches used in this work.

In chapter 2, a comprehensive literature review will be presented regarding the previous thermodynamic and kinetic study on graphitization, the influence of graphite on steel properties.

In chapter 3, optical, scanning electron, transmission electron microscopy were applied to characterize the graphite and carbides in cold rolled and annealed steels in order to explore the mechanisms of graphitizition and spheroidization.

In chapter 4, the graphite dissolution kinetics were investigated using a Gleeble thermal mechanical system. The influence of graphite content on martensite and Bainite transformation kinetics and mechanical properties were studied experimentally.

The fracture toughness of normally homogeneous materials has been the subject of countless experimental investigation and theoretical studies based on continuum mechanics. In reality, materials are heterogeneous. For a deeper understanding and qualification underlying process, microscopic heterogeneity has to be taken into account.

In chapter 5, the stress and strain concentration caused by a graphite particle in a steel matrix was studied by finite element analysis. To further study the effect of second phase particles on failure mode, stress concentration factors for Al_2O_3 and void in a steel matrix were also calculated.

Most researchers only considered the effect of a crack on the stress and stain distribution and neglected the interaction between crack and second phase particles. The

stress concentration at a crack tip would be influenced by the localized stresses around second phase particles.

In chapter 6, the interactions between second phase particles and sharp/blunt crack were investigated in chapter 6. J integral was used for characterizing the singularities caused by cracks and second phase particles.

Chapter 7 concludes the thesis work by identifying and suggesting the areas of future research work.

CHAPTER 2
LITERATURE SURVEY

2.1 THE IRON AND CARBON SYSTEM

2.1.1 Phase Diagram

The conventional phase diagram for iron and carbon system is shown in Figure 2-1, which includes both the metastable Fe-Fe_3C diagram and stable or equilibrium Fe-graphite diagram. The former is indicated by full lines, and the latter is indicated by dashed line. The construction of phase boundaries required many thermodynamic and metallurgical investigations. Currently, the evaluation of data and the resulting summary in form of thermodynamic relationships is still an interesting area.

Recently, the scientific community in Russia[10] has returned to the idea of a unified iron-cementite phase diagram ("monistic" theory which precede the modern universally accepted "dualistic" theory based on a diagram with two systems of lines: stable iron-graphite equilibrium and metastable Fe-Fe_3C equilibrium). It is suggested that cementite is also a equilibrium phase, not a metastable phase.

The graphite crystal structure is composed of a layer of hexagonally arranged carbon atoms; within the layers, each carbon atom is bonded to three coplanar neighbor atoms by strong covalent bonds. Interlayer bonds are weaker and of the van der Waals type.

The cementite phase has an orthorhombic crystal structure and is considered to have no deviation from stoichiometry as the activities and temperature vary. Experimental

evidence indicates that deviations from stoichiometry exist, but all the phase diagram calculations are based on perfect stoichiometry. The melting point of Fe_3C is therefore assumed to be congruent.

To understand the phenomenon of graphitization, it is necessary to study the thermodynamic possibilities for graphite formation from carbon in solution and the phase stability of cementite.

2.1.2 Graphite Formation from Ferrite

Below 1184 K, α-Fe dissolves very small amounts of carbon in equilibrium with graphite.

$$C \text{ (in solution)} \leftrightharpoons C \text{ (graphite)} \tag{2-1}$$

The partial molar Gibbs energy $\check{G}^{\alpha}_{C}$ of dissolved C in α-Fe in terms of the Henrian standard Gibbs energy $\dot{G}_{\alpha}$ as follows:

$$\check{G}^{\alpha}_{C} = \dot{G}_{\alpha} + RT \ln y^{\alpha} \tag{2-2}$$

where $y^{\alpha} \approx x^{\alpha}/3$, is the fraction of interstitial sites of bcc Fe occupied by carbon atom, x^{α} is the atomic fraction of carbon in α-Fe. According to the results of Kaufman-Redcliffe-Cohan (KRC), the Gibbs free energy change $(G^{\circ}_{gr} - \check{G}_{\alpha})$ for the reaction that graphite precipitates from α-Fe can be calculated by:

$$G^{\circ}_{gr} - \check{G}_{\alpha} = RT \ln (x^{\alpha}/3) + 26160 - 9.75T \tag{2-3}$$

This equation can be used for calculating the graphitization potential at different temperature and carbon content. When $(G^{\circ}_{gr} - \check{G}^{\alpha}_{C}) < 0$, graphite is spontaneous formed.

The recent results of Hasebe[11] for the Gibbs free energy change $(G^{\circ}_{gr} - \check{G}_{\alpha})$ are:

$$G^{\circ}_{gr} - \check{G}^{\alpha}_{C} = G^{\circ}_{gr} - \dot{G}_{\alpha} + RT \ln y^{\alpha} \quad (2\text{-}4)$$

At graphite saturation,

$$\begin{aligned} & G^{\circ}_{gr} - \dot{G}_{\alpha} \\ \approx\ & RT \ln {}^{s}y^{\alpha} \\ =\ & RT \ln ({}^{s}x^{\alpha}/3) \\ =\ & -99{,}750 + 33.6\,T + (8170 - 1.52\times10^{10} / T^{2} + 4.80\times10^{15} / T^{4}) \text{ [J/g-atom of C} \\ & (800 < T < 1200 \text{ K})] \end{aligned} \quad (2\text{-}5)$$

where $\Delta H^{\cdot} = 99{,}750$, $\Delta S^{\cdot} = 33.6$, R is Gas Constant, the "s" in ${}^{s}y^{\alpha}$ and ${}^{s}x^{\alpha}/3$ represents saturation state . The last set of three terms in the above equation is a purely empirical correction representing the effect of paramagnetism - ferromagnetism on the solubility of graphite in the range of 800 to 1200 K. Hasebe's equation is based on the experimental results from 823 K (0.0010 wt%C) to near the eutectoid temperature of 1013 K (0.0026 wt%C), which is the temperature range during which most secondary graphitization happens. The α-Fe and graphite boundary is satisfactorily represented by this equation from about 800 to 1013 K. At the eutectoid temperature of 1013 K, this equation yield $y^{\alpha} = 0.000319$ (0.0206 wt% C).

2.1.3 Graphite Formation from Austenite

The Gibbs energy change for graphite precipitate from γ-Fe can be expressed as[12]:

$$\begin{aligned} G^{\circ}_{gr} - \check{G}^{\gamma}_{C} &= - RT \ln a^{\gamma} \\ &= -45{,}360 + 18.4\,T - (57{,}400 + 11.2\,T)\, y^{\gamma} + RT \ln [y^{\gamma}/(1-y^{\gamma})] \quad \text{(J/mole)} \end{aligned} \quad (2\text{-}6)$$

where $\check{G}^{\gamma}_{C}$ is the partial molar Gibbs energy of dissolved C in γ-Fe, a^{γ} the activity of carbon in γ-Fe. When the temperature and carbon content are substituted in this equation and make

$G^{\circ}_{gr} - \breve{G}^{\gamma}_{C} < 0$, graphite keeps precipitating from γ-Fe until saturation.

At the graphite saturation, $G^{\circ}_{gr} - \breve{G}^{\gamma}_{C}$, and the left side of equation (6) is zero; then the solution of this equation for all the assigned temperatures yields the austenite/graphite boundary in Fe-C phase diagram. For example, at 1424 K, the eutectic temperature, $y^{\gamma} = x^{\gamma}/(1-x^{\gamma}) = 0.0977$ (2.06 wt% C); x^{γ} is the atomic fraction of carbon in γ-Fe; and at 1013 K, the eutectoid temperature, this equation yields $y^{\gamma} = 0.0314$ (0.671 wt%C).

2.1.4 Cementite Stability

During the process of solidification as well as during heat processing of an alloy the reaction

$$n\ \text{Fe-C} + m\ C_{gr} \rightarrow Fe_3C \qquad (2\text{-}7)$$

where Fe-C indicates the solution of carbon in iron. The course of the reaction can be determined by the evaluation of its free enthalpy as a function of temperature and the carbon content.

The change of free enthalpy ΔG^0 can be expressed as:

$$\Delta G^0 = G^0_{Fe3C} - G^0_{Fe\text{-}C} - G^0_{gr} \qquad (2\text{-}8)$$

where G^0_{Fe3C} is the free enthalpy of cementite, J/mol; G^0_{gr} is the free enthalpy of graphite, J/mol; $G^0_{Fe\text{-}C}$ is the free enthalpy of the solution of carbon in iron, J/mol.

The values of G^0_{Fe3C} and G^0_{gr} were evaluated using the formula[13]:

$$G^0 = \Delta H^0_{298} + \int_{298}^{T} C_p\,dT - T \cdot S^0_{298} - T \int_{298}^{T} \frac{C_p}{T}\,dT \qquad (2\text{-}9)$$

where ΔH^0_{298} is the change of molar standard enthalpy, J/mol; S^0_{298} is the molar standard

entropy, J/mol-K; c_p is the molar heat capacity.

The molar heat capacity of cementite and graphite were evaluated using the following formula:

for temperatures greater than 740°C[13],

$$C_{pgr} = 11.173 + 0.0109T - 488642T^{-2}\ , \text{J/mol-K} \quad (2\text{-}10)$$

$$C_{pFe3C} = 107.09 + 0.0012T, \text{J/mol-K} \quad (2\text{-}11)$$

for the temperature range of 298-2300 K[14],

$$C_{pgr} = 17.16 + 0.00427T - 87900T^{-2}\ , \text{J/mol-K} \quad (2\text{-}12)$$

for the temperature range of 273-463 K,

$$C_{pFe3C} = 82.17 + 0.08368T, \text{J/mol-K}) \quad (2\text{-}13)$$

the other data needed for evaluating the free enthalpy change ΔG^0,

$$\Delta H^0_{298,Fe3C} = 25{,}080 \text{ J/mol(Ref. 14), or } 22{,}590 \text{ J/mol(Ref.12)}$$

$$S^0_{298,\,Fe3C} = 101.15 \text{ J/mol (Ref. 14), or } 101.3 \text{ J/mol (Ref.12)}$$

$$S^0_{298,\,Cgr} = 5.68 \text{ J/mol-K (Ref. 14), or } 5.74 \text{ J/mol-K (Ref. 12)}$$

The free enthalpy of the carbon solution has been evaluated by the following formula:

$$G^0_{Fe\text{-}C} = RT\,(N_{Fe}\ln a_{Fe} + N_C \ln a_C) \quad (2\text{-}14)$$

where $N_{Fe,}\ N_C$ is the mole fraction of carbon and iron in the solution, a_{Fe}, a_c is the activities of carbon and iron in the solution, R is Gas Constant.

2.1.4.1 Cementite Formation from Austenite and Graphite

The activities of iron and carbon in austenite solution, corresponding with the temperatures of 1423, 1273, 1173, 1073, 1013 K had been evaluated for various carbon contents using the formulae given by Darken and Gurry[15]

$$\ln a_C = \ln N_C/N_{Fe} + 6.6\, N_C/N_{Fe} \quad (2\text{-}15)$$

$$\ln a_{Fe} = -N_C/N_{Fe} + 3.3(N_C/N_{Fe})^2 \quad (2\text{-}16)$$

The change of free enthalpy of the reaction (2-1) had been evaluated by Kosowski[13] for austenite temperature range. Values of free enthalpy are all negative and the carbon content in austenite, which changes in relatively wide range of 0.1-1.9%, affects the free enthalpy changes very slightly. These changes increase with the increase of temperature. The higher the temperature the more negative the changes of free enthalpy. His results suggested that cementite is thermodynamically stable and can be formed from Fe and Graphite.

2.1.4.2 Cementite Formation from Ferrite and Graphite

For α-Fe, sufficient activity data does not exist and the free energy $G^{\alpha}_{Fe\text{-}C}$ can not be calculated by the same way for $G^{\gamma}_{Fe\text{-}C}$. In α-Fe, the carbon solubility is so low, reaction (2-1) may be simplified as

$$3\alpha\text{-}Fe + C_{gr} = Fe_3C \quad (2\text{-}17)$$

The standard free enthalpy change for cementite formation $\Delta G_{Fe3C}{}^0$ can be calculated by the formula[16]:

$$\Delta G^0_{Fe3C} = 26690 - 24.8T \text{ (for the temperature range 463-1115 K)} \quad (2\text{-}18)$$

Therefore, below 1076K (803°C, 1477°F), cementite is unstable while α-Fe and graphite is stable. This result are in good agreement with the ΔG^0_{Fe3C} estimated by Darken and Gurry[17] for some temperatures (Table 2-1).

2.2 SOURCES OF FREE CARBON FOR GRAPHITIZATION

Graphite formation in carbon and low alloy steel is achieved by carbon supersaturation, graphite nucleation, and graphite growth. Excess free carbon atoms required for graphite formation come from carbide decomposition.

It is believed that free carbon mainly comes from the transformation of the metastable cementite:

$$Fe_3C \Rightarrow 3Fe + C \qquad (2\text{-}19)$$

Also, on the transformation of the metastable higher-carbon carbide including χ-carbide to cementite, the excess carbon is thought to promote the graphitization of steel[18, 19]:

$$3Fe_5C_2 \Rightarrow 5Fe_3C + C \qquad (2\text{-}20)$$

A magnetic analysis of phase transformations in the tempering of quenched C steels alloyed with Co showed that the initial stage of graphitization coincided with the onset of the breakdown of the χ-carbide and was not connected with breakdown of cementite[20].

It has been suggested that the nucleant or catalyst is the hexagonal-latticed ε-carbide, owing to its structural compatibility and the following reaction can provide excess carbon[21]:

$$\varepsilon\text{-carbide} \Rightarrow Fe_3C + C \qquad (2\text{-}21)$$

2.3 GRAPHITE NUCLEATION

Besides the generation/availability of free carbon to produce the critical nucleus size, another factor that influences the susceptibility to graphite nucleation is the existence of an appropriate nucleation site. It is generally accepted that graphite nucleation in iron and steel occurs in a heterogeneous fashion at sites where free carbon can be produced or to which free carbon can be effectively transported, and where the volume and graphite - matrix interface changes in sub-critical nucleus growth can be accommodated. Baranov and Bunin demonstrated this nearly 30 years ago, by theory and experiment [1]. However, the applicable mechanism of nucleation continues to be debated, more than one nucleation mechanism may be operative.

2.3.1 Homogeneous Nucleation of Graphite

During the homogenous nucleation of graphite in cementite or solid solution, the effect of increasing surface area on system free energy is equivalent to the effect of putting a pressure on the surface. The pressure level depends on the assumptions made regarding the nucleation mechanism, i.e. on whether the nuclei are formed on the basis of concentration fluctuations in the cementite or solid solution or as a result of breakdown of cementite into graphite and solid solution. Tkachenko[8] attempted to assess the hydrostatic pressure p in the formation of graphite nuclei by using the system of calculation suggested for martensitic transformation and therefore producing low results. In martensitic transformation there is only a change in the atomic lattice arrangement, whereas in graphitization one or two new phases are produced, with compositions which differ greatly from that of matrix. Assume the graphite embryos are spherical. The pressure in the graphite can be assessed from the surface tension σ at graphite-matrix interface and critical size r_c of the graphite nucleus.

$$p = \frac{2\sigma}{r_c} \tag{2-22}$$

At $\sigma = 500$ erg/cm^2 and

$$r_c = \sqrt[3]{\frac{3V}{4\pi}} \tag{2-23}$$

Where V is the volume of graphite nucleus which, according to the data quoted by Tkachenko is 288 A^3; $r_c \approx 4.1$ A and $p \approx 252$ kg/mm^2 considerably exceed the values obtained by Tkachenko. However, even if the Tkachenko data are used it can be shown that graphite cannot grow against this pressure. Carbon diffusion from cementite to graphite is determined by the difference of carbon activity in ferrite. The relative carbon activity for cementite and ferrite is found from $a_C^{Fe3C+\alpha Fe} = 0.0353 \exp(6900/RT)$ and at 700°C, $a_C^{Fe3C+\alpha Fe} = 1.25$. At a pressure level p in the graphite, the relative carbon activity for graphite and ferrite is

$$\ln a_C^{gr+\alpha Fe} = pV_{gr}/RT \tag{2-24}$$

Taking $p = 65.6$ kg/mm^2 and the molar volume of the graphite $V_{gr} = 5.3$ cm^3/mol, one obtains $a_C^{gr+\alpha Fe} = 1.54$, i.e. $a_C^{gr+\alpha Fe} > a_C^{Fe3C+\alpha Fe}$. This result implies that a graphite nucleus should disappear rather than grow. Thus it follows that the hydrostatic pressure in the graphite when ferrous alloys are graphitizing should not exceed the value:

$$p = RT/V_c \ln a_C^{Fe3C+\alpha Fe} \approx 35 \text{kg/mm}^2 \tag{2-25}$$

It can thus be assumed that the homogenous nucleation of graphite is scarce in ferrous alloy.

2.3.2 Heterogeneous Nucleation

One requirement for any location to qualify as a potential nucleating site is the presence of transformation volume change-accommodating defects in the form of vacancies and dislocations, high densities of which are associated with grain boundaries[22], inclusions,

strain-induced defect clusters, or all of the above at a single location. Bidash[1] found that the development of graphitization and graphite during spheroidizing annealing resulted from the defect presence in the atomic--crystalline structure of ferrite and cementite and the chemical inhomogeneity of ferrite around the plate-like cementite. Sueyoshi[23] founded that graphite crystallized on the preferential interfaces of non-metallic inclusions composed mainly of Al_2O_3 and SiO_2 or silicates. Effects of inclusions on graphite nucleation are summarized in 2.3.3.

2.3.3 Effect of Inclusions on Graphite nucleation

Nonmetallic inclusions promote the formation of cavities and defects in the crystal structure due to the difference between inclusions and matrixes in their melting point, thermal expansion coefficient, elastic modulus and plastic deformation ability, the difference between the diffusion coefficient of iron and the soluble component of inclusions.

If the freezing point of these inclusions is lower than the solidification range of the iron, shrinkage occurs when molten inclusions crystallize and the size of pores will be approximately equal to the difference between the volumes of these inclusions in liquid and solid state.

In the formation of cavities by diffusion, promoted by differences in partial hetero-diffusion coefficients, the inclusions present in an iron or steel may dissolve or grow, depending on their solubility compared with that in pure iron. In cases where the partial diffusion coefficients of the iron and the soluble component of the inclusion differ greatly, pores can be formed near the inclusion. Diffusion pores are found during the homogenization of a disordered solid solution[8]. Cavities formed by deformation and effect accumulation (holes , dislocations) occurs when there is a major difference between the thermal expansion coefficients of the inclusion and the iron matrix. A contact pressure $p = 4G(\alpha_1 - \alpha_2)dt$, in which G is the shear modulus and α_1 , α_2 are the thermal expansion coefficients of the dissolved impurity and inclusions, arises at the interface when iron which has a structure containing impurities is heated. The stress can be relieved either by

deformation of the matrix and inclusions or by the formation of discontinuities between them. The pores forming by means or another are effective during graphitization provided they are not covered with oxide or copper films and do not contain gases which prevent graphite formation.

Calcium, silicide, ferrosilicon, titanium, ferroaluminum silicon carbide are frequently used as modifiers in the production of graphitized ferrous alloy. Attention is draw to the fact that the chemical compounds introduced or forming during modification have low thermal expansion coefficients compared with pure iron[8].

Graphite particles are frequently found near non-metallic inclusions[24]. The catalytic role of inclusions in graphite nucleation is usually attributed to the alignment effect, but this is greatly over-rated. If the structures of graphite and the chemical compounds formed on introducing modifiers into Fe-C-Si melts are compared, it is obvious that there is less similarity than between the graphite, austenite, ferrite and cementite structures. The matrix can normally exert a greater alignment action on the formation of graphite lattice than can the non-metallic inclusions, because in many of the austenite, ferrite and cementite planes the lattice constants are close to those in the basal planes of graphite lattice. Quarrell and Hickley[21] showed that γ-alumina (which forms around 650°C) has, in the a_0 direction of its (110) plane, a 13% coherent fit with the (1100) plane of graphite, while the same planes for cristobalite and graphite show a 3% coherent fit. Pogreboni and Taran[21] found that the octahedral plane of austenite or ferrite fitted the basal plane of graphite with a coherent distortion of 2.1% and 4% respectively. Pomey's ε-carbides model[21] shows a 5% coherent distortion.

Therefore, any evaluation of the mechanism underlying the influence of inclusions on graphite nucleation in irons and steels during heat treatment should allow for the possibility of cavities and crystal lattice defects forming as the alloys are heated and cooled in addition to the aligning action of non-metallic inclusions.

2.4 GRAPHITE GROWTH AND MORPHOLOGY

When a graphite embryo reaches the critical size, the probability that the carbon atoms escape from the embryo by thermal vibration decreases, and graphite precipitate growth begins. Given the relatively small critical nucleus size and numerous nucleating sites available during the solidification of typical iron and steel, it is likely that graphitization is controlled by factors influencing graphite growth, rather than graphite nucleation. This is supported to some extent by more recent observations that Al and Si do not appear to have a significant effect on graphitization in the longer term (>30 years)[25]. But the growth mode of graphite in low alloy and carbon is not fully understood.

Growth of graphite nodules in cast iron is a case of faceted growth[26]. Graphite nodules are such that segments of their surface are parallel to the basal plane of hexagonal graphite and c-direction is parallel to the radial direction of nodule, so that the low basal planes minimize the surface energy of the nodule. Layer growth of basal planes leads to growth along the c-direction of graphite. Therefore, the nodules tend to grow radially. On the other hand, flake graphite tends to grow along the a-direction.

The graphite morphology is dependent on the pre-treatment[23]. In the normalized specimen the growth in c-axis direction specifically occurred along ferrite grain boundaries, whereas the crystal structure of most graphite in cold-rolled specimen with ease of graphitization was similar to spheroidal graphite in nodular iron, growing radially. The spheroidal graphite in cold-rolled steel was identified as polycrystalline graphite by the electron diffraction ring pattern[6].

Sueyoshi[23] found that the graphite particles nucleated in the inclusion surface grow along c axis with (0001) plane of graphite parallel to inclusion surfaces. The spheroid grows by tilting the surface of concentric shells with hexagonal (0001) basal planes. According to Patterson's surface energy calculation[6], the surface energy of the planes parallel to (0001) plane is 0.562 J/cm^2 , which is much smaller than 4.33 J/cm^2 the surface energy of prism plane. But according to L'nyanoy's calculation[27] from the ferrite decomposition data, the graphite surface energy was 180-290 erg/cm^2.

Inokuti[28] found the <002>- oriented graphite is formed preferentially on surface ferrite grains oriented to <110> sheet normal direction, and not on <100> nor <111> ferrite grains.

2.5 EFFECTS OF COLD WORK ON GRAPHITIZATION

Severe graphitization in carbon and low alloy steel in elevated -temperature service has only recently been observed[29, 30]. The phenomenon, which has been suggested as being related to plastic strain[6], Has not been studied in detail. Nevertheless, the potential effect of accumulated plastic strain on enhancing the susceptibility of iron and steel to graphite nucleation and growth, published nearly 30 years ago[9], suggested that the Cottrell atmosphere associated with dislocations may be instrumental in graphite nucleation.

2.5.1. Strain Nucleation

When a metal is plastically deformed by cold working, most of the mechanical energy is released as heat, but a small fraction of this energy is retained as stored energy inside the metal, thereby raising its internal energy. Thus the stored energy is the change in internal energy produced by plastic deformation. The stored energy exists in the crystals as point defects, dislocations, and stacking faults. These defects are heterogeneous nucleation sites for graphitization.

The graphitization promoted by cold working is associated with slip planes along Luders lines (elongated surface markings caused by localized plastic deformation that results from discontinuous yielding) in the metal where local yielding or plastic deformation occurred. The common mode of plastic deformation in metals is slip. Nucleation is strongly favored by presence of microvoids along slip planes of plastically deformed metal. Hence, the term "slip plane graphitization" has been applied to this phenomenon[31]. Inclusions, grain boundaries, metal lattice defects can also cause small holes to be developed during plastic deformation. At a minimum, the high density of dislocations at slip obstacles generated as

a result of plastic strain can provide the accommodation for volume changes associated with graphite formation. Strain aging may produce C supersaturating at locations of high defect concentrations such as a grain boundary, inclusion-matrix interface(inclusion behave as slip obstacles).

Cold working creates crystal structure defects in pearlite. These defects affect graphite formation during subsequent annealing. It would be natural to assume that the coarse cementite structure produced as a result of hot rolling and cooling treatment, ensures more defects in the metal base as a result of subsequent cold work and stimulates the nucleation and growth of graphitization during annealing.

Drawing, rolling, tensioning, hydraulic pressing and torsion, vary the cementite composition through an increase in the crystal lattice defectiveness[32]. A study has been made of a number of steels containing 0.8% C and a series of alloying elements (Mn, Si, Ni, Co, V, and Mo), using the nuclear gamma-resonance method[9]. Plastic deformation caused partial decomposition of the cementite, the extent of which was governed by the bonding energies the C atoms in the cementite lattice as an influence of alloy addition and by dislocation density in the ferrite. The extent of the decomposition increased as a degree of carbide particle dispersion increased. An effective means of suppressing the decomposition of cementite utilized alloying with elements that weaken the pinning of the dislocations by interstitial atoms. The alloying elements proved to be nonuniformly distributed among the G- and S-nodes of the cementite lattice, Mo, and Mn predominating at the G-nodes and Si at the S-nodes.

Cementite dissolution in plastically worked steel 70 was studied by thermomagnetic analysis[33]. Cementite dissolution during wire drawing torsion and extension at -196 to +20 °C correlates dislocation density and distribution. Cementite breakdown is accelerated at the temperatures used for dynamic strain ageing (e.g. 300 °C) and decreases, if the working temperature exceeds that at which the dislocation atmosphere can condense. The graphitization effect and the relationship between the degree of graphitization and the amount of cementite restored on heating the worked steel can be explained by that carbon is localized in crystal structure defects of various types, viz., dislocation groups and

micro-cracks.

2.5.2 Carbide Breakdown

Okamoto[6] found that voids were formed at cementite-ferrite interfaces in pearlite or between the fractured segments of cementite particles during cold-rolling process of sheet steels (Figure 2-2). These voids were not filled by iron atoms by annealing at 500°C for 1 hour. An example of a fractured cementite particle containing a void of 0.4 μm long, which is about 20% of the original cementite particle, is shown in Figure 2-3. This void seems large enough to accommodate the volume expansion, about 14%, as show below, accompanied by the graphitization of cementite.

$$Fe_3C \rightarrow 3\ Fe + C\ (Graphite)$$
$$V \rightarrow 0.911\ V + 0.227\ V = 1.138\ V \qquad (2\text{-}26)$$

where V = volume of cementite.

Kuo's experimental work[34] showed that deformation can fracture the continuous carbides in cast iron and enhance the nucleation of graphite so that the time for graphitization is reduced. Increased surface area of fine carbide produced by rapid solidification results in enhanced carbide dissolution rate and subsequent graphite nucleation rate. As a result the graphitization process should be controlled by the dissolution of carbide.

In summary, there are several mechanisms for the effect of plastic deformation on accelerating graphitization: (1) cold working creates more defects which serve as nucleation sites, such as the voids formed between the fractured cementite segments; (2) the chemistry of cementite is varied due to the defects in cementite lattice; (3) during cold working, cementite is broken and become unstable because of the increased surface energy.

2.6 EFFECTS OF ALLOYING CONTENT ON GRAPHITIZATION

Adding alloy elements to the iron-carbon system can change carbon solubility and mobility, carbide stability, and inclusion type. The effect of alloy elements on graphitization may vary with steel composition, heat treatment temperature and time.

2.6.1 Classification

ASM Metal Handbook classified the main elements that influence graphitization in terms of their graphitization potential[35]:

High positive graphitization potential (decreasing positive potential from top to bottom)
Carbon
Tin
Phosphorus
Silicon
Aluminum
Copper
Nickel

Neutral
Iron

High negative graphitization potential (increasing negative potential from top to bottom)
Manganese
Chromium
Molybdenum
Vanadium

This classification is based on the thermodynamic analysis of the influence of a third element on carbon solubility in the Fe-C-X system, where X is a third element. Although listed as a graphitizer (which may be true thermodynamically), phosphorus acts as a graphitization inhibitor in sheet steel[23]. The above classification should also include sulfur as a carbide former, although Mn and S can combine and neutralize each other. The resultant

Mn sulfide also acts nuclei for flake graphite. Fukui[36] found that with decreasing in manganese, phosphorus, and sulfur in high carbon sheet steel, cementite particles decompose to graphite during batch annealing after cold rolling.

Russia researchers[37] also divided elements to three group: C, Si, P, Al, Cu, Ni, Co increase C mobility and enhance graphitization. W, Mo, Mn, Cr, Mg, Nb, V, Ca, Ti, Zr, O reduce C mobility and inhibit graphitization. H, B, N, S increase activity and mobility of C, but inhibit graphitization.

2. 6.1.1 Silicon and Aluminum

Silicon and Aluminum increase the graphitization potential for both the eutectic and eutectoid transformations and increase the number of graphite particles. They form a solid solution in the matrix. Because they increase the ferrite/pearlite ratio, they lower strength and hardness. Borruto[38] demonstrated the very important role of Si as a graphitizing element in a modest increase from 2.10 to 2.60% sharply accelerated the kinetics of the process, regardless of the percentage of carbon in the steel. The Si/C ratio influenced the dispersion of the graphite and, as the ratio increased, the number of particles of graphite per unit of surface area also increased.

Several mechanisms are probably responsible for the reported increased graphitization susceptibility with increasing Al and Si. First, the supersaturating of C may occur at sites rich in Al and/or Si by the oxidation of these elements. Rosen and Taub[21] believed that carbon is liberated during the formation of Al or Si oxides and that the carbon concentration is highest around the newly formed oxides. They found that carbon solubility in α-Fe increases with the concentration of Al or Si present. Removal of these elements from the solid solution, through internal oxidation, immediately causes carbon supersaturating around the newly formed oxides, which are thus able to promote graphitization. However, this oxide formation mechanism for C supersaturating is likely to nucleate graphite only in the primary graphitization (solidification) phase. But secondary graphitization may occur due to the pre existing nuclei. Second, some researchers[21] found secondary graphite nucleated

near or at the interface of Al, Si inclusion/matrix. Third, A. K. Jena suggested that Al and Si segregate at the ferrite/cementite interface and retard cementite growth[39], and produce fine cementite has a more surface area than coarse cementite and less stable. Hence, Al and Si can accelerate cementite dissolution. Harry[21] suggested that the migration of Si towards the grain boundaries causes a high concentration of vacancy in immediate vicinity. Si also can decrease the interface energy between graphite and ferrite[26]. The interface energy at ferrite-graphite boundary in electrical steel Fe-3% Si and Armco Fe was 40-80 and 40-100 erg/cm^2, respectively.

Sobotka tried to verify the effect of an increased Al content on the tendency of steel graphitization by creep exploitation in the temperature region 500-550 °C[40]. His results proved that the kinetics of graphitization are influenced by both the working temperature and chemical composition of the steel, mainly the Al content. It appeared desirable to limit the maximum allowable Al content in the steel by 0.017%. The results further showed that the presence of non-metallic inclusions in the steel was not the necessary condition for graphite formation, this being in some contradictions to the hypothesis on the role of Al inclusions in heterogeneous nucleation of graphite particles during creep exploitation.

2.6.1.2 Other Elements

Small amounts of a number of other elements, for example N, Cl, and Br have a similar effect with carbide forming elements[41]. Nitrogen, always present in steels, is about the same atomic size as carbon and substitutes for carbon at interstitial atom sites in the ferrite matrix. Thus, a steel with free nitrogen will have fewer interstitial carbon atoms, and thus less chance to nucleate graphite.

2.6.2 Effect of Alloy Elements on Bonding Strength of Cementite

As for the nature of bonds in cementite, Fe-C bonds are very strong covalent bonds. On the other hand, Fe-Fe bonds are metallic. The big difference in electronegativity between

Fe-C plays an important role in strengthening its bonds. The formation of strong bonds in cementite is due to the following characteristics of Fe and C[42]: for Fe, (1) large metallic valence (6-valent), (2) strong bond with d-electrons, (3) electropositive against C atoms, (4) ability to form metalike carbide; for C, (1) large valence (4-valent), (2) strong covalent bond, (3) electronegative against Fe atoms.

The strength of Fe-C bonds can be changed by additional elements. The stronger the Fe-C bond, the more stable the cementite and the less likely is the formation of graphite. The properties of Fe and C atoms have the characters required for the bond in cementite when additional elements replace Fe or C atoms in cementite. Additionally, other elements must have similar atomic radius in order to enter into cementite.

In order to stabilize cementite, in another words, in order to strengthen its bonds, the following three conditions should be satisfied: (1) Large valence, (2) formation of strong covalent bonds, (3) large difference in electronegativity between metallic elements and non-metallic elements.

Thus, from these conditions, a group of elements centering about VIB family and VA family in the periodic table stabilize cementite and inhibit graphitization. To the contrary, the elements centering about IA family and VIII family promote graphitization.

The effect of alloy elements on carbon activity in cementite and stability of cementite has been studied[43]. From the standpoint of thermodynamics, multicomponent systems practically contains no completely insoluble elements even if their concentrations are so small that they cannot be detected[44]. Cementite, Fe_3C, at elevated temperatures has a region of homogeneity within which its composition may become nonstoichiometric[45]. Okamoto[46] demonstrated that silicon, without entering the composition of cementite, can nonetheless increase the content of carbon in this variable-composition phase. With increasing carbon concentration, the thermodynamic activity of Si element also increases[47].

2.6.3 Impurity Segregation

Graphite formation has been observed on clean iron surfaces while Fe_3C has not been

found[48, 49, 50]. The segregation properties of carbon on an iron (111) surface using AES, XPS and LEED methods have been studied[51]. In the segregation process, the following steps are observed with increasing C coverage: (1) adsorption of atomic C; (2) formation of chemisorbed molecules C_2*; and then (3) formation of a three-dimensional graphite structure. The calculation[52] of energy of different Fe and C clusters using the EHT (extended Huckel theory) method shows that the most favorable sites for adsorption of atomic carbon are on the reconstructed surface, where carbon atom is located under the iron atom. For the chemisorbed C molecule C_2*, the following model is proposed: one atom is located under the Fe surface and the second one on the Fe surface. The graphite domains on the Fe surface are oriented in the manner where the angle 13.5° between crystallographic orientations [-110]Fe and [10-10] graphite is formed.

If the Fe surface is covered by sulphur, the segregation process will result in the localization of adsorbed C atoms under Fe and S atoms. Further segregation process in this case leads to the formation of the three-dimensional cementite Fe_3C structure. In the case of surface coverage by sulphur the carbon molecule cannot be formed because there is no free site for adsorption on the surface, so graphite cannot be formed. In this case, the Fe_3C is formed under the sulphur monolayer, shown in Figure 2-4.

This experiment results may be used to explain effect of impurities such as S and P on graphitization. Inokuki[28] examined the effect of S, P on the graphite formation on the surface of sheet low carbon steel. He found that S had a stronger inhibition effect on the graphite formation than P. Okamoto[6] found reduction of both phosphorous and sulfur in 0.06% C or 0.5% C cold-rolled sheet steels graphitizes the surface cementite during annealing. The cold-rolling of carbon steel produces voids between cracked fragments of cementite particles, the inhibition of graphitization by P and S was attributed to the surface segregation tendency, as shown in Figure 2-4. The situation of graphite formed at inclusion/matrix interface, or cavities should be similar to that at free surface.

Yoshihara and Nii [53, 54] investigated the surface occupying elements of a commercial low-carbon steel during annealing in vacuum (10^{-7} Pa) by using Auger electron spectroscopy. Their experiment showed that the steel surface was entirely occupied by carbon (graphite)

when the steel was sputtered and kept at 620°C. However, when sputtered and then kept at a higher temperature of 770°C, initially carbon (speculated to be a form of carbide) and then P were enriched, and finally, sulfur became the predominant surface element. From these results, they concluded that surface segregation tendency was stronger in the following order: sulfur, phosphorus, and carbon. But from their segregation behavior curves (shown in Figure 2-5), it seems like that P segregated on steel surface at the same time with carbon. It is hard to say whose segregation tendency is stronger and carbide is formed before or after P segregation.

For the sheet surface graphite formation at subcritical temperatures, the following steps are speculated by Yano et al.[6]: (1) solution of carbide in the steel, (2) diffusion of carbon to the surface, (3) formation of cementite at the surface, and (4) decomposition of cementite. In this case, diffusion of phosphorus and sulfur to the sheet surface is far later than carbon. At the temperatures below 700°C, the diffusion coefficient of sulfur[55] is small compared to that of carbon. Therefore, these elements exert a small influence on graphite formation. Okamoto also found that extreme reduction of P and S caused graphitization even in the inside of cold-rolled low carbon sheet steels[6].

Therefore, the effects of S and P on graphitization depend on the segregation behavior. Iron and steel always contain traces of S and P, and after a sufficient long time sulfur, which is highly surface active, would displace all other segregated atoms. That may be one of the reasons why graphitization does not happen in most commercial steels. But during cold working, some fresh surfaces are created and due to slow segregation of S and P, graphite formation is easier than in the steels without cold working. The Mn content also need to be taken into account because S atoms can be combine with Mn to form MnS.

2.7 GRAPHITIZATION KINETICS

While there appear to be reasonable explanations for , and qualitative descriptions of the graphite nucleation phase, quantitatively useful time-temperature data on nucleation phase is relatively limited. Faulds[25] suggested graphitization could be predicted just from

the kinetics of graphite growth (progression), assuming the pre-existence of graphite nuclei. This assumption appears reasonable, given the numerous potential graphite nucleating sites and apparent submicroscopic critical nucleus size in carbon and low alloy steels.

The progression of graphitization is essentially controlled by the growth of individual graphite particles or nodules. The specific rate at which such growth occurs is controlled largely by the rate at which free C can be produced at, or transported to, the graphite particle, and the rate at which the Fe, Si or other atoms diffuse away from graphite nucleation site. For the case of graphite nucleation at cavities, the effect of Fe, Si diffusion on growth rate can be ignored. For the case of graphite nucleation at ferrite grain boundaries, Fe diffusion may be the controlling factor. The fact that fine carbides shorten the graphitization time shows the graphite kinetics also can be controlled by carbide decomposition.

2.7.1 Kinetics Models

The kinetics of graphitization progression or growth have been described by a sigmoidal (S-Shape) growth function, Johnson-Mehl-Avrami equation[56]:

$$y = 1-\exp(-Kt^n) \tag{2-28}$$

where y is the completed transformation fraction,

t is the exposure time, and K, n are constants.

n depends on the nucleation rate, growth rate, and graphite form. For homogeneous nucleation and constant nucleation rate, n = 4. The value of n decreases if nucleation is heterogeneous and nucleation rate decreases as the transformation proceeds. When all the nucleation sites are saturated early in a transformation, n reduces to the lower limit value, 3. Therefore, for three dimensional transformations the value of n is usually between 3 and 4. Rarely but it is possible for n to be greater than 4, e.g., when number of nucleation sites increases with increasing volume fraction of new phase. For two dimensional and one dimensional transformation, n ranges from 2-3 and 1-2, respectively.

For diffusion-controlled graphite growth, n should be a small value. For the growth controlled by carbides decomposition, n should be large. Sueyoshi[23] found the graphitization reaction in hypo-eutectoid alloy steels obeyed Johnson-Mehl-Avrami's equation with the reaction exponent value close to 2.5. The kinetic analysis of the first stage graphitization in Fe-C-Si white cast irons showed that the value of n gradually decreases during graphitization and finally becomes about one[57]. Rosen and Taub[21] showed that in an oxidizing atmosphere n=2, but when the steel was held under vacuum at the graphitization temperature prior to being introduced into the oxidizing atmosphere, n increased to 2.5 and to 3 after 7 and 30 hr respectively. However, it is hard to relate the n values extracted from experimental data to the expected value according to Christian[60], because the nucleation and growth mechanisms of graphite are not fully understood. Also n values depend on the methods used for monitoring the transformation.

The form of equation (2-28) does not provide a means of quantifying the thermal activation involved in the growth process, nor does it enable easy comparison between the growth rates in different situations (materials and exposure temperature). Review of the published sigmoidal growth curve data (graphite % versus logarithmic time) for C and C-Mo steels shows that a major portion of the growth curve following the initial S-bend can be approximated by a power-dependence on exposure time, i.e.:

$$y = Ct_g^{\,m} \tag{2-29}$$

where m is a constant, C is a temperature-dependent constant,

t_g is the exposure time following 'incubation," = t - t_i, where t_i is the incubation time. The physical significance of t_i is not known, but it facilitates the fitting of equation (2-29) to the observations. The temperature-dependent constant, C, may be replaced by an Arrhenius term describing a rate-controlling thermally activated process, so that equation (2-29) in the most general form, becomes:

$$y = A \exp(-Q'/RT)\, t_g^{\,m} \tag{2-30}$$

where A is a constant,

T is the exposure time in absolute units,

R is the Universal Gas Constant, and

$Q' \approx Q$, where Q is the activation energy for the controlling process;

Q' is expected to be equal to 3Q/2 for radial diffusion-controlled growth.

Equation (2-30) will henceforth be used to describe the kinetics of graphite growth beyond incubation.

Numerous attempts have been made to determine what process controls the growth rate of graphite particles/nodules[58]. The approach been taken is consistent with the classic time-dependent thermally activated processes (creep, carbide coarsening, etc.), Wherein the rate-controlling process is established through measurement of activation energy, Q (see equation 2-30). Table 2-3 summarizes the published activation energies for selected diffusing species and activation energy values for graphitization as published or derived from published data.

Table 2-3 illustrates the variability in activation energy values associated with graphitization and compares these values with the activation energies for diffusion of pertinent species in α-Fe. It has been shown that Mo increases the activation energy and reduces the graphite growth rate in the case of ductile irons, which can be explained on the basis of the improved stability of Mo carbides over the metastable cementite. Also, for the quenched Ni steel, the graphite growth activation energy is reduced considerably from the as-normalized condition, and approaches the activation energy for diffusion of C in α-Fe. The graphite growth activation energy in as-normalized steel is closer to that for vacancy/self-diffusion along grain boundaries or dislocations cores than for the diffusion of C in α-Fe. It was believed that cold work can reduce the "as-normalized" activation energy towards that for "as-quenched" condition[63]. Currently, there exists insufficient data to quantitatively describe the effect of cold-work or plastic strain on graphite growth.

2.7.2 Time-Dependence of Graphitization

Sueyoshi[59] found the incubation time of graphitization depends on alloy content. The higher the content of elements such as Si, Co and Ni which have partition coefficients in cementite to ferrite<1, the shorter the graphitization incubation time. It was accordingly suggested that the elements in cementite affected the stability of cementite.

Fujihira[60] has demonstrated from laboratory tests that, at a given aging temperature, the radial growth of individual graphite particles or nodules is parabolic in time; i.e., the particle radius, $r \approx t_g^{1.5}$. This proportionality implies that the graphite volumetric growth (proportional to r^3)and therefore, the fraction transformation, y, is dependent on $t_g^{1.5}$ (m=1.5 in eq. (3)). An analysis of the published experimental growth curves of Tanaka and Fujihira[61] on as quenched nickel steel (2%Ni, 1.2%Si, 0.24%C) and Niedzwiedz[23] on as quenched carbon steel (0.3% Al, 0.8%C) shows good agreement with this prediction exponent. It is important to note that the dependence of m on the quenching temperature (the temperature from which quenching was carried out) was observed by Tanaka and Fujihira to be negligible over a large range of quenching temperature above Ac_1.

It was observed that as the volume fraction of graphite increases, the hardness decreases with increasing the annealing time. But after annealing time reach a certain hours, the volume fraction of graphite stabilized[62] . This may be a proof that its amount approaches the equilibrium.

It is appears that, for carbon and alloy steels, the incubation period and actual graphite growth rate may vary as a function of the material chemistry, microstructure and initial heat treat condition (primarily through variation in the growth rate does not depend on these variables).

2.7.3 Temperature - Dependence of Graphitization

The formation of graphite embryos requires a concentration of interstitial carbon atoms. Hence, it was suggested graphite nucleation is most likely to occur at 705 to 735 °C,

since the highest concentration of interstitial carbon occurs at these temperatures[63]. However, the TTT relationship for subcritical graphitization in a number of hypo-eutectoid alloy steels showed that the nose of the "C" curve which was located at about 60°C lower than Ac_1 of each steel[59], not at above 700 °C. For uniform distribution of graphite in the matrix (precipitation of graphite in austenite and martensite), it is recommended that graphitizing annealing of steel 10Ni15 be conducted in the temperature range 600-650°C[64]. This is attributed to the denser distribution of cementite particles.

Port[30] suggested graphite growth is controlled by C diffusion process wherein carbon atoms migrate to graphite nodules from the supersaturated ferrite grains. As the grains become impoverished in carbon, the iron carbides dissolve, resupplying carbon atoms to the ferrite grains. At temperature below 400°C (750 °F), the diffusion rate of carbon is very low (Table 2-4). In addition, the carbide phase is nearly as soluble as the graphite phase (Fe-graphite, Fe-cementite phase diagram). Thus, the carbides will not readily provide carbon for graphite growth. Therefore, observable graphitization can only proceed at temperatures above 400°C.

It is generally known that carbide spheroidization competes with graphitization in carbon and low alloy steels subject to elevated temperature service. Which one of the two processes (graphitization or spheroidization) occurs, depends on the steel composition, microstructure, and exposure temperature. Increasing temperatures favor spheroidization. The Metals Handbook[65] shows, as an example, the temperature regimes within which either spheroidization (above 1025°F or 552°C) or graphitization (below 1025°F or 552°C) can be expected to be the dominant transformation process. In reality, the graphitization -to-spheroidization transition temperature varies in a manner not entirely predictable, and may differ significantly from 1025°F or 552°C[66]. Gofman[67] found that for steel 20, the pearlite spheroidization and carbide phase coagulation took place at temperatures > 500 °C, and the graphitization process occurred at temperature > 440 °C. Due to its potential embrittling effect, graphitization is of greater concern than is spheroidization.

Since graphitization and speroidization are diffusion controlled processes the transformation rate increases with temperature, graphitization occurring preferentially to

spheroidization at lower temperatures[7]. Graphitization and spheroidization are driven by different factors, spheroidization by reduction of surface energy and graphitization by approaching thermodynamic equilibrium.

2.7.4 Austenitizing Condition

The influence of austenitizing treatment followed by slow cooling on the graphitization in hypo-eutectoid alloy steels has been studied by Sueyosh[59]. It was found that the number of graphite nodules and the rate of graphitization remarkably depend on the austenitizing conditions. The difference in the numbers of graphite nodules can be 30 times due to different austenitizing temperatures. There is a optimum austenitizing temperature at which the annealing time for 50% graphitization is shortest, although the size of graphite is smaller, the number of graphite nodules is larger. The rate of graphitization increases with an increase in graphite nodule number. From both the result and the fact that the growth rate is independent of austenitizing conditions, it is suggested that the austenitizing conditions exert a major influence on nucleation of graphite.

For the pre-treatment that hold a steel at the austenitizing temperatures until traces of cementite disappear completely, and then slow cool down, the graphitization is most greatly stimulated. Cementite in pearlite formed was found to be fine lamellar. It is concluded that fine cementite is unstable because of larger surface energy and thereby may cause an easy nucleation of graphite.

Sueyosh[59] used a constant K represent the effect of austenitizing temperature and time on carbon diffusion:

$$K = D.\ t_A = D_0 \exp(-Q/RT) \qquad (2\text{-}31)$$

where D is diffusion coefficient, D_0 is vibration constant, t_A is austenitizing time, T is austenitizing temperature, Q is diffusion activation energy, R is gas constant. It is suggested that the diffusion process is the same for short time holding at high temperature or long time

holding at low temperature. If consider the diffusion occurs during heating process before reaching austenitizing temperature, a time t_0 is needed to add to t_A, where t_0 can be expressed by the below equation:

$$t_0 = (T\text{-}Ac_1)^2/(Q/R)v \tag{2-32}$$

where v is the heating rate. When a rapid heating rate is used, it is not necessary to consider t_0.

Combining equation (2-31) and (2-32), obtains:

$$\exp(-Q/RT)[t_A + (T\text{-}Ac_1)^2/(Q/R)v] = K_A \tag{2-33}$$

When considering the t_0 effect, a new constant K_A is used instead of K.

After substituting the carbon diffusion activation energy, 157 kJ/mol, and heating rate into above equation, it was found at different austenitizing temperature, the minimum time for 50% graphitization corresponds different austenitizing time, while it corresponds the same K_A. That means the effect of austenitizing time and temperature on graphitization is equivalent to the effect of carbon diffusion.

2.8 PREVENTING GRAPHITIZATION

Port[30] suggested that graphitization can be essentially eliminated by reducing operating metal temperature below 850°F and/or by specifying a low alloy steel containing at least 0.4% Cr. Minimizing graphitization can be achieved by

(1) Use Si killed carbon steel. Specify a maximum Al content such as 0.010% or lower.

(2) Use as-normalized carbon steel.

(3) Do not subcritical anneal carbon/Mo steel especially if the steel has been cold worked.

(4) Weld with no pre-heat or post-heat treatment if possible. Use low heat input to minimize the heat affected zone.

(5) Use normalization heat treatments where possible rather than soft anneal, temper, or high temperature stress relief anneal.

It is rarely reported whether the graphite can be removed by heat treatment. It was found[68] that under polythermal conditions (anisobaric, in particular) iron--carbon alloys carburizing treatment is possible at the expense of a transfer of some graphite into a solution and successive separation of C dissolved at high temperatures in a form of carbides and carbonitride. It occurs within the formation of surface 'white layers' in the zone of intensive sliding friction of iron graphite bearings, parts made of graphitized iron and other materials.

Thermodynamically, graphite is perfectly soluble in austenite in the case of carbon steels. This study evaluated whether the graphite nodules in the sheet steel after cold working and annealing can be removed by heat treatment.

2.9 FRACTURE MECHANISM

The effects of graphite on the fracture mode of steels have not been very well studied. Our current work indicated that a low alloy steel with graphite nodules fracture in a ductile mode. A large number of experimental investigations have shown that ductile fracture in metals is initiated from cavity nucleation in inclusions or at the interfaces between inclusions and the matrix, followed by cavity growth and coalescence through plastic deformation. In materials, where the second phase particles and inclusions are well bonded to the matrix, void nucleation is often the critical step; fracture occurs soon after the voids form. When void nucleation occurs with little difficulty, the fracture toughness properties are controlled by the growth and coalescence of voids; the growing voids reach a critical size, relative to their spacing, and a local plastic instability develops between voids, resulting in a failure.

2.9.1 Microvoid Nucleation

2.9.1.1 Void Nucleation Criteria

The critical condition of cavity nucleation has attracted much attention of researchers engaged in ductile fracture studies. At present three cavity nucleation criteria have been proposed and are being extensively used. They are the energy criterion, local stress criterion, and strain criterion[69, 70]. Tannaka showed that when the second phase particle size is larger than 250 Å ,the local stress criterion has the same effect as the energy criterion; the strain criterion has the same effect as energy criterion and is more appropriate for particles with small size[71]. However, strain criterion has been also used for large particles.

2.9.1.2 Stress Concentration

The stress concentration at second phase particles is due to the following factors:

(1) The difference between the elastic modulus of graphite/inclusion and matrix;

(2) The difference between the thermal expansion of graphite/inclusion and matrix;

Two cases are considered. The first one corresponds to particle that shrinks more rapidly than the matrix during cooling after thermal processing (heat treatment, casting, hot rolling, forging). These particles are assumed to debond from the matrix during cooling and subsequently behave as pores. Manganese sulfide inclusions are of this type. The second case involves inclusions that shrink less rapidly than the matrix after thermal processing and thus generate a compressive state of stress in the inclusion and tensile tangential stress in the matrix outside the inclusion, so-called tessellated stresses. Graphite and alumina particle are of this type.

(3) The difference between the plastic deformation of graphite/inclusion and matrix.

2.9.1.3 Void Nucleation Stress Models

Models have been established for predicting void nucleation at the interfaces between

second phase particles and matrix, but no model has been developed for void nucleation inside the particles. Nucleation has been studied at two distinct size scales. For particles whose size is comparable to the dislocation or slip band spacing, the local conditions are most appropriately discussed in terms of dislocation mechanisms, such as those reviewed by Goods and Brown[72]. Alternatively if the particles are large compared to slip band spacing, the stresses and strains near the particle matrix interface are most conveniently described in terms of continuum plasticity. The Goods and Brown dislocation model indicates that the local stress concentration increases with decreasing particle size; void nucleation is more difficult with larger particles. The continuum models apply to particles greater than 1μm in radius. Experimental observations usually differ from both continuum and dislocation models, in that void nucleation tends to occur more readily at large particles. However, these models only considered nucleation by particle-matrix debonding. Voids can also be nucleated when particles crack. Larger particles are more likely to contain small defects which can act like Griffith cracks. In addition, large nonmetallic inclusions, such as oxides and sulfides, are often damaged during fabrication; some of these particles may be cracked or debonded prior to plastic deformation, making void nucleation relatively easy. Further research is required to develop void nucleation models that are more in line with experimental data. However, a continuum model can still be used for comparing the stress concentration caused by particles with different material properties. Existed continuum models for estimating void nucleation stress are summarized below.

The general problem of stress and strain fields for ellipsoidal elastic inclusions has been presented by Eshelby[73]. The solutions for spherical elastic or cylindrical inclusions may be derived as special cases because the inclusion's orientation dependency is not a issue. In the particular case of rigid spherical inclusion the maximum interfacial stress occurs on the interface in the loading direction, and for a cylindrical inclusion has a magnitude:

$$\sigma_{rrmax} = 1.5\sigma \tag{2-34}$$

while for a spherical inclusion:

$$\sigma_{rrmax} = 2\sigma \tag{2-35}$$

The solution for general multi-axial loadings can be obtained as by superimposing uniaxial solutions. For example, the solution for shear is obtained by adding the stress field for uniaxial tension of magnitude + a to that of a uniaxial compression of magnitude -a rotated by $\pi/2$. The maximum interfacial shear stress for a rigid cylindrical inclusion then becomes:

$$\sigma_{rrmax} = 2\tau \tag{2-36}$$

In terms of the equivalent stress this may be written as

$$\sigma_{rrmax} = 2\sigma_e/\sqrt{3} \tag{2-37}$$

where σ_e is the effective stress, given by

$$\sigma_e = 1/\sqrt{2}\,[(\sigma_1 - \sigma_2)^2 + (\sigma_1 - \sigma_3)^2 + (\sigma_3 - \sigma_2)^2]^{1/2} \tag{2-38}$$

Since the Superposition principal is valid for linear materials a mean (hydrostatic) stress σ_m can be superimposed to give the general result

$$\sigma_{rrmax} = 2\sigma_e/\sqrt{3} + \sigma_m \tag{2-39}$$

where σ_m is defined as

$$\sigma_m = (\sigma_1 + \sigma_2 + \sigma_3)/3 \tag{2-40}$$

On this basis numerical solutions for cylindrical inclusion have been given by Argon and Safoglu[74], and for spherical particles by Thomson and Hancock[74]. According to the Argon model, the nucleation strain decreases as hydrostatic stress increases. That is, void

nucleation occurs more readily in a triaxial tensile stress field, a result that is consistent with experimental observation.

Bermin[75] et al applied Argon model to experimental data for a carbon manganese steel, but found that the following semi-emperical relationship gave better predictions of void nucleation at MnS inclusions that were elongated in the rolling direction. The critical decohesion stress was represented by:

$$\sigma_c = \sigma_m + C\,(\sigma_e - \sigma_{ys}) \tag{2-41}$$

where σ_{ys} is the yield strength and C is a fitting parameter that is approximately 1.6 for longitudinal loading and 0.6 for loading transverse.

2.9.2 Effect of Second Phase Particle Spacing on Fracture Toughness

The crack propagation process occurs through microcrack coalescence, and growth.

Krafft first related fracture toughness (K_{IC}) to second phase particle spacing (d_T) by the strain criterion. When the true strain at the first particle in front of a crack reaches strain hardening exponent, the crack grows.

$$K_{IC} = En\sqrt{(2\pi d_T)} \tag{2-42}$$

where E is elastic modulus, n is strain hardening exponent. This model is in good agreement with the experiment results for steel 4345 with MnS inclusions[75].

Osborne-Embury[76] estimated the critical condition for ductile fracture is when the true strain at an aggregative region reaches 2/3 of the true fracture strain, ε_f, under uniaxial tension. Based on this criterion, the fracture toughness is

$$K_{IC} = \frac{\sigma_s}{1-2\nu}\sqrt{\pi(1+n)d_T\left(\frac{E\varepsilon_f}{\sigma_s}\right)^{1+n}} \tag{2-43}$$

where ε_s is yield strain, σ_b is tensile strength.

Schwalbe[77] modified the Kraff model in 1974:

$$K_{IC} = \left[\frac{2}{3(1-\nu^2)} \sigma_b E \varepsilon_f d_T \ln\left(\frac{2}{3} \frac{\varepsilon_f}{\varepsilon_s} \right) \right]^{1/2} \tag{2-44}$$

His model fits the experimental results for Al alloy better than the other models.

Rice[78] replaced critical CTOD, δc, with the spacing d_T of second phase particles to estimate K_{IC},

$$K_{IC} = (2E\sigma_s d_T)^{1/2} \tag{2-45}$$

which is consistent with Kraft model.

J. Li's experimental results[79] for ultra-high strength steel with TiN showed the relationship of K_{IC} to d_T is

$$K_{IC} = (E\sigma_s d_T)^{1/2} \tag{2-46}$$

Table 2-1 ΔG^0_{Fe3C} **at different temperatures (J/mol).**

Temperature (K)	ΔG^0_{Fe3C} (J/mol)	Temperature (K)	ΔG^0_{Fe3C} (J/mol)
1200	-1799.1	700	+9137.9
1100	-966.5	600	+12200.3
1000	+1142.2	500	+15217.2
900	+3464.4	400	+17832.2
800	+6184.0		

Table 2-2 Thermal expansion coefficients of inclusions compared with pure iron and carbides[80, 81, 82, 83]

	Fe	SiO_2	Al_2O_3	Si_3N_4	SiC	CaO	TiO_2	TiC
$\alpha\times10\times^6$ /°C	15-23	2.0	8.0	2.5	5.2	9.0	7.4	4-8

	TiN	Fe_3C	$M_{23}C_6$	M_6C	Mo_2C	VC	Graphite	WC
$\alpha\times10\times^6$ /°C	9.4	12.6	10.4	9.2	6.1	7.3	3	4.5

Table 2-3 Activation Energy, Q as published or derived from published data[25, 59]

Materials	Process	Activation energy, Q kcal/mol(kl)
γ -Fe	Diffusion of C in γ-Fe	(157)
α-Fe	Diffusion of C in α-Fe	20 (84)
α-Fe	(Self/vacancy) Grain boundary or core diffusion	41(174)
α-Fe	(Self/vacancy) lattice diffusion	60 (251)
Ni steel -quenched from 1400°F(2%Ni, 1.2%Si, 0.24%C)	Graphite nodule growth	20.5 (86)
Ni steel-normalized(2%Ni, 1.2%Si, 0.24%C)	Graphite nodule growth	34.5(145)
Fe--C--Si white cast irons	Graphitization to 50%	(260)
hypo-eutectoid alloy steels)	Graphite nodule number increase	(166 to 193)
C-0.5Mo Steel	Graphitization to 50%	33.6(141)
Ductile iron(3.5%C)	Graphitization to 50%	30(126)
Ductile iron with Mo (3.5%C, 1%Mo)	Graphitization to 50%	59(248)

Table 2-4 Diffusion rates of carbon atoms in ferrite at different temperatures[40].

Temp. (°C)	Temp. (°F)	$D(cm^2/sec)\times10^{-8}$
400	750	1
435	815	2
490	910	5
540	1000	10
590	1095	20
675	1250	50

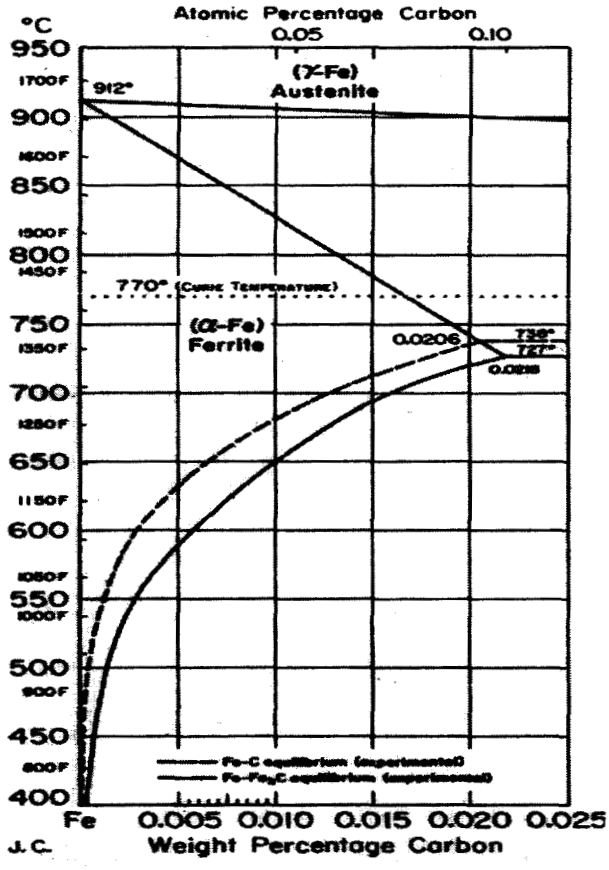

Figure 2-1 **Enlargement of lower, left-hand corner of carbon-iron diagram (ASM International Copyright).[84]**

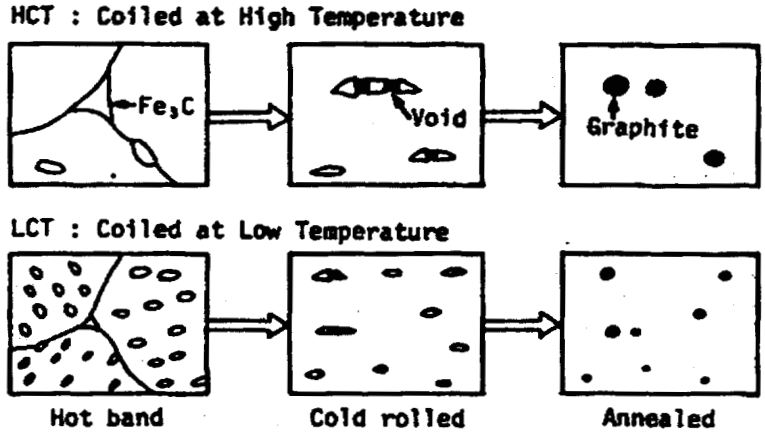

Figure 2-2 **Schematic illustration of graphitization process in high-purity low-carbon steel coiled at two different temperatures after hot roll (ASM International Copyright).[6]**

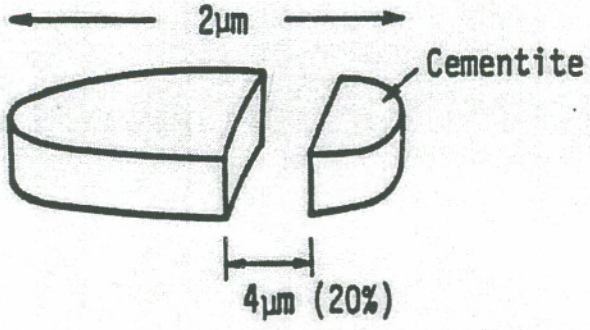

Figure 2-3 **Fractured cemented segments in 0.06 pct C steels, as-cold-rolled and as-annealed at 500 °C for 1 hour (ASM International Copyright).[6]**

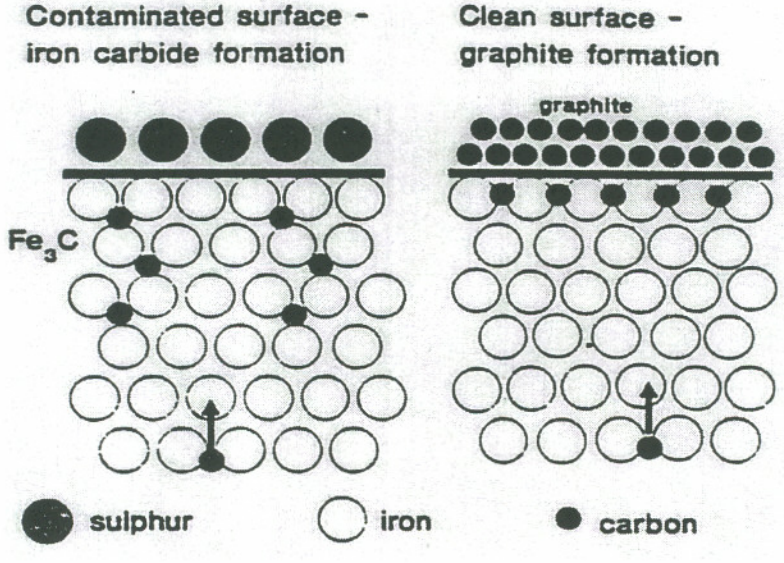

Figure 2-4 **Model of carbon segregation on clear and contaminated with sulfur iron surfaces (Elsevier Science Copyright).[51]**

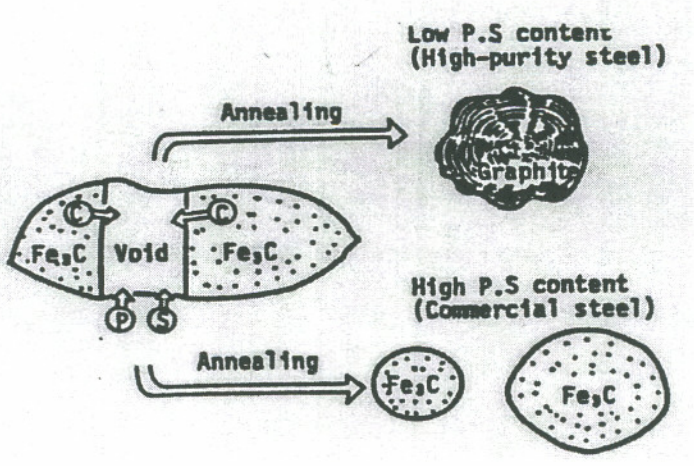

Figure 2-5 **Effect of phosphorus and sulfur on graphitization during annealing (ASM International Copyright).[6]**

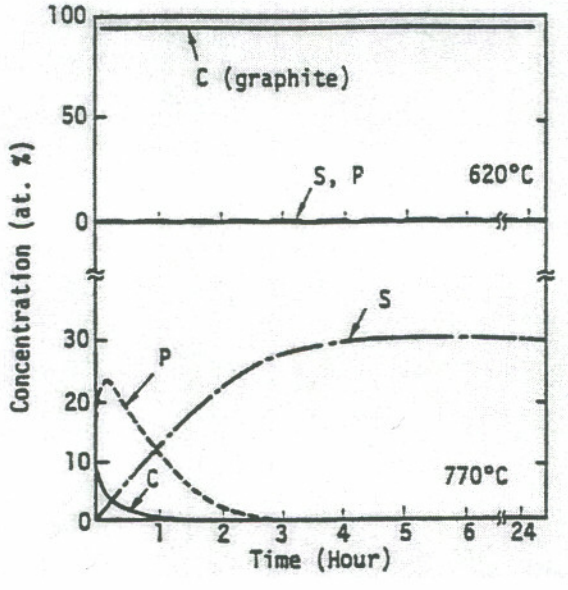

Figure 2-6 **Segregation behavior of carbon, phosphorus, and sulfur at sheet surface of commercial low-carbon AK steel after sputtering by Ar in vacuum at 620 °C or 770 °C (ASM International Copyright).[54]**

CHAPTER 3

CHARACTERIZATION OF GRAPHITE AND CARBIDE PRECIPITATES IN COLD WORKED AND ANNEALED STEELS

3.1 INTRODUCTION

Graphite particles have been reported in some thin sheets of cold work and annealed steels with high silicon content and no carbide formation elements[1,2]. Recently, graphite has been also observed in United States produced sheet steels for low Si content (0.24%) steel with carbide formation alloy elements, such as Cr or Nb. To study the graphite formation mechanism and the effects of graphite on steel properties, graphite and carbide precipitates need to be well characterized. In this work, two types of cold worked and annealed steels received from manufacturers were investigated: one contained Cr and the other Nb. The graphite nucleation sites were studied by optical microscopy. The size and quantity of graphite were measured by image analysis. The detail morphology and interface condition of the graphite were studied by scanning electron microscope examination of focused ion beam workstation produced site specific cross-sections. The graphite, carbide and matrix chemistry was identified by energy dispersive x-ray analysis. The crystal structures present in the steels were determined by transmission electron microscopy.

3.2 MATERIALS

The chemical compositions were listed in Table 3-1. The major difference between Steel 1 and Steel 2 is the Cr and Nb content. The 0.25% Chromium in Steel 1 was replaced

with about the same amount of Niobium in Steel 2. The production schedule for producing the hot band for both alloys was:

(1) Hot rolling finished at 1600 °F and coiled at 1200/1250 °F

(2) First Cold rolling: thickness reduction from 0.129 inches to 0.09 inches (25% reduction);

(3) Stress relieving annealing:

Temperature: 1310 °F, this temperature was measured at the coldest spot

Time: Two hours

Atmosphere: HNX- 5 to 6% H_2

Type of furnace: four coils high

(4) Cold rolling: thickness reduction from 0.09 to 0.06 inch (36% reduction)

(5) Final Annealing:

Temperature: 1330 °F, this temperature was measured at the coldest spot

Time: 24 hours

Atmosphere: HNX- 5 to 6% H_2

Type of furnace: four coils high

Cooling Rate: < 50 °F / hour

3.3 OPTICAL MICROSCOPY

3.3.1 Experimental Procedures

The soft and friable nature of graphite, in combination with the relatively hard matrix make metallographic sample preparation extremely difficult. Graphite particles were easily torn out wholly, or in part, leaving many micro cavities. To truly represent the size and shape of graphite and accurately assessment the microstructure, the following procedures were adopted:

The samples were cold mounted with Epoxfit. The resin and hardener were mixed at a ratio of 15:2. Wet grinding of the samples was conducted with 120, 240, 400, 600 grit SiC papers. Water was used as the lubricant and removed the abrasion debris from paper.

Abrasion on the final paper was the most important stage, because it was here that graphite might be damaged.

Rough polishing was done on a low-nap silk cloth using 6 micron diamond paste followed 1 micron diamond paste. Although high-nap cloths are extremely effective in removing scratches from previous operation, but they have an adverse effect on preserving graphite. Napless cloths are more suitable for retaining graphite but suffer from the limitation that they are less efficient in removing abrasion scratches, and sometimes cause further scratching of specimen surfaces. The use of velvet cloth or low-nap silk is a reasonable compromise. Fine polishing was conducted on a medium-nap Microcloth charged with a slurry of water containing 0.05-micron alumina. Automatic polishing gave better polishing results. The lapping wheel rotated at a speed of less than 300 rpm. High polishing pressure and short polishing times were used to avoid excessive polishing. After polishing, the lubricant was removed from the specimen surface by swabbing alcohol, then dried by rinsed with high-purity acetone and dried with hot air. Specimens were etched by swabbing with a 2% nital.

Optical microscopy examination was conducted on a Nikon Epiphot system at a magnification of 400 times. A quantitative study of the graphite content was done by Leco 2001 software. The contrast between graphite and matrix is large for as polished specimens. Therefore, only a few simple operations, such as sharpening, histogram modification, and thresholding, were involved for image processing to improve accuracy but not cause artificial effects on counting. Feature count and area percentage of graphite were measured. Fifteen fields were randomly selected on the plane parallel to rolling direction. The magnification of 400 times was used since it could clearly resolve graphite particles and also provided a relatively large field area for measurement. The two-dimensional area percentage was used to represent the volume fraction according to stereology.

The 95% confidence limit (95% CI) was estimated by

$95\%\ CI = 2.0\ s / (n-1)^{0.5}$

where s is the standard deviation, n is the number of fields.

The volume percentage estimate is given as

$V_V = A_A \pm 95\%$ CI

The relative accuracy associated with the estimate can be obtained as

$\%RA = 95\%$ CI / $A_A \times 100$

The graphite contents measured on polished and etched specimens were greater than on as polished specimens, because more graphite was observed after etching. Therefore, all the image analysis in this study was conducted on as-polished specimens.

3.3.2 Results

Figure 3-1 shows the graphite distribution in cold-rolled and spheroidizing annealed Steel 1. Graphite frequently formed at ferrite grain boundaries, especially triple points. The grain boundary diffusion rate for carbon is much higher than bulk diffusion. Also thermodynamically, grain boundaries are carbon trap sites and nucleation sites. Graphite particles formed in Steel 1 were usually in the range of one to three microns. There are fewer carbide particles in the grains containing graphite particles. However, the carbide particles nearest to the graphite did not completely dissolve. The rate of cementite dissolution was probably the slowest process, but no attempt was made to develop a quantitative relationship.

Figure 3-2, an optical micrograph on polished and etched Steel 2, shows that the graphite particles formed in Steel 2 had a larger size distribution, the largest graphite particle was 14 microns. Image analysis results for three polished planes of cold rolled and annealed Steel 2 are listed in Table 3-2. The area fractions of graphite from S-T, T-L, and L-S sections all were about 1.0%. The letter's L, T, and S denote the longitudinal, transverse and short transverse directions, related to the rolling direction. Analysis of variances indicated that the difference in area observed was of no statistical significance.

Graphite in Steel 1 was distributed more uniformly and had a nodule morphology. But in steel 2, some graphite preferentially formed along carbide bands. The light yellow and angular Nb(C, N) carbides were less than one half micron.

3.4 SCANNING ELECTRON MICROSCOPY

3.4.1 Experimental Procedures

Three kinds of specimens were used to study graphite morphology by SEM: as polished, 2% nital etched, and focused ion beam micromachined cross sections. Preparation procedures for as polished or polished and etched specimens are the same as those for optical specimens.

The graphite/matrix interfaces in mechanically polished specimen surfaces might be damaged during polishing. Hence, a focused ion beam (FIB) cross-section was made to study the bonding condition between graphite and matrix. The FIB collimated beam traveling parallel to the cross-section causes much less damage to the interface than mechanical polishing. A hole of 20 μm × 10 μm × 6 μm was milled across a large graphite particle in Steel 2, shown in Figure 3-3. Rough Cutting was done by the FIB beam with a 2800 Å spot size and 4000 pA current. The thin wall edges were cut by the beam using an1100 Å spot size and 250 pA current. Interface condition was studied in SEM by tilting 45°.

Graphite and inclusion particles are identified in the Zeiss Digital 960 Scanning Electron Microscope (SEM) configured with a Link energy dispersive spectrum (EDS). Secondary electron (SE) mode and windowless x-ray detector were used. Electron Flight Simulator software was used for determining the optimum accelerated voltage. It was found that under 10 kV accelerating voltage, the electron penetration depth in graphite is less than 2 μm. Most of the graphite particles observed were usually around 2 μm in size. Hence, x-ray spectrums should only indicate the chemical composition of graphite.

All the SEM work was conducted in a ZEISS SEM at 5 to 30 kV. Focused ion beam sample preparations were conducted using a FEI 610 workstation.

3.4.2 Results

Graphite particles formed in Steel 1 and Steel 2 were shown in Figure 3-4 and 3-5,

respectively. Graphite particles in Steel 2 were often observed forming at carbide interfaces especially broken Nb(C, N) particles (Figure 3-6). During cold rolling, the angular shape and high Young's modulus of Nb(C, N) caused the greatest stress concentration. It can be seen that the microcracks in Nb(C, N) are evident in Figure 3-6. Also, the graphite grew along grain boundaries where carbon atoms could diffuse along grain boundaries. In Figure 3-6a, two other small graphite particles were also observed in triple points. Clearly, there were not many spherical carbides around the graphite. That suggested that the carbon atoms forming graphite came from dissolved cementite and not from broken Nb(C, N). The chemical bond of Nb-C is much stronger than that of Fe-C.

In Steel 1, most of graphite had a spherical shape. However, In Steel 2, Nb promoted a nonhomogeneous distribution of graphite and carbide. Many graphite particles were coarse and irregular shaped in Steel 2. Graphite could agglomerate to decrease the particle/matrix interface energy. Figure 3-5d presents a graphite which may be agglomerated from four small graphite nodules.

SEM analysis on FIB cross-sections of Steel 2 showed that the interface between graphite and matrix is perfectly bonded, with no evidence of voids (Figure 3-3 a and b). However, the interface was irregular shaped on a submicron scale. The particle composition is given in Figure 3-3c. The major content was carbon with a trace amount of Ga, a byproduct of the focused ion beam milling process.

X-ray analysis was done at spots on the matrix, carbides, graphite and other inclusions in Steel 1 and Steel 2 samples. The X-ray spectra are presented in Figure 3-7 and 3-8 for the matrix, graphite, carbides and inclusions in Steel 1 and Steel 2, respectively. As these spectra show, in Steel 1, besides carbon, Al and Si were also detected in many graphite particles in Figure 3-7a. This suggested that graphite particles preferentially formed at regions with Al and Si segregation, or nucleated on Al and Si rich inclusions. The matrix materials of both Steel 1 and Steel 2 are relatively pure iron (Figure 3-7b and 3-8b) and the majority of the alloying elements were detected with the carbide phase (Figure 3-7c and 3-8c, d). It can be seen the spheroidized carbides are not pure Fe_3C but rich with Cr and Mn alloy element. It is well known that Cr and Mn, carbide forming elements, are easily soluble in

cementite (Mn can even completely substitute for iron in it). The other inclusions contain some elements among Al, Si, S, Mn, Mg, Ca, and O, as shown in Figure 3-7d.

In steel 2, pure carbon was detected in most of graphite (Figure 3-8a). Nb was detected in some graphite too. Graphite may be formed on a Nb(C, N). Spheroidized carbides contain C, Mn, and Fe (Figure 3-8c), while Fe, Nb, N and C were detected in angular particles (Figure 3-8d).

3.5 TRANSMISSION ELECTRON MICROSCOPY

To study the effect of cold work on cementite dissociation, a sub-sized plate tensile specimen (gage length = 1 inch) was broken under a slow loading rate (0.001 inch/second) using an Instron test system. A 3-mm disk was punched in the necked area. The material is steel 1 after hot rolling and first step cold rolling.

To study the carbide characteristics of cold worked and annealed steels, TEM specimens were prepared from the final spheroidizing samples that had received.

3.5.1 Experimental Procedures

TEM samples were prepared by electropolishing. The specimens were manually thinned to 150 μm thickness by grinding successively on 120, 240, 400, 600, 800 grit papers. Three millimeter diameter disks were punched from the thin foils. The disks were electro-polished at 50 volts in 5% perchloric acid in methanol maintained at - 40°C in a double jet unit. The polishing current was about 60 mA. After a hole was made by thinning the center of disks, the disks were immediately rinsed in methanol.

TEM studies were conducted in a Hitachi H-800 electron microscope operated at 200 kV. EDS was used to determine the composition of carbides. The advantage of electro-polished TEM samples is that x-ray spectra were collected from pure carbides without any substrate effect, because in the center hole area of the electro-polished samples, carbides protruded from the matrix along hole edges Figure 3-9.

3.5.2 Results for Carbide Characteristics

The TEM bright field images revealed many spheroidized carbides both along grain boundaries and at the grain interior in Figure 3-10. Spectra were collected from both the matrix and carbides, the results were the same as shown in Figure 3-7c, which confirmed that the Mn and Cr peaks are from carbides and not from the matrix.

Diffraction analysis was conducted to identify the carbide type in Steel 1, shown in Figure 3-11. The lattice constants of possible carbides with Mn, Cr and Fe in Steel 1 are listed in Table 3-3. By inputting the lattice constant of cementite (a = 4.5241 Å, b = 5.5088 Å, c = 6.7416 Å) into Desktop Microscopist, the simulated <111> cementite diffraction pattern (Figure 3-12) matched Figure 3-11 very well.

3.6 DISCUSSION

3.6.1. The Carbide Spheroidizing Mechanism

The spheroidized carbide microstructure is one of the most stable microstructures of the steel and is desirable when (1) maximum ductility and minimum hardness on low- and medium- carbon steels or (2) maximum machinability and formability as in high carbon steels is required. Also, It is generally known that carbide spheroidization competes with graphitization in carbon and low alloy steels subject to elevated temperature service. Graphitization and spheroidization are driven by different factors, spheroidization by reduction of surface energy and graphitization by approaching thermodynamic equilibrium.

The mechanism of pearlite spheroidization by heating the pearlite structure to a temperature just below A_1 and holding for a prolonged period involves (1) breaking up the cementite lamella into small particles, (2) formation and subsequent dissolution of smaller spherical shaped particles, and (3) growth of larger spherical particles due to the reduction in interfacial energy. The growth (or coarsening) rates of a spheroidized microstructure has been given by the following equation[85]:

$$\frac{dr}{dt} = \frac{2\gamma V_{cm}^2 C_c^{\alpha} D_c^{\alpha}}{V_{\alpha} RTr_1}\left(\frac{1}{r} - \frac{1}{r_1}\right) \qquad (3\text{-}1)$$

where γ is the interfacial energy, V_{cm} and V_{α} are the molar volumes of cementite and ferrite, respectively, C_c^{α} is the mole fraction of carbon in equilibrium with cementite in ferrite, D_c^{α} is the effective carbon diffusivity in ferrite, R is the gas constant, T is the absolute temperature, r is the average size of the already spheroidized particles, and r_1 is the radius of the newly formed particles. This equation indicates that the rate of speroidization is directly proportional to the diffusivity of carbon in ferrite and decreases with increasing mean size of particles in a spheroidized microstructure.

For the first stage of spheroidization, it has been suggested that cementite breakdown is due to defects in cementite, such as dislocation and sub-grain boundaries. The curvature of interfaces between ferrite and cementite close to the sub-grain boundaries is smaller than the other interfaces. Therefore, the ferrite close to cementite sub-grain boundaries has high carbon concentration, which cause carbon atoms diffuse to the interfaces with a larger radius. To keep the equilibrium of surface tension forces between cementite , ferrite and cementite sub-grains, carbon atoms keep diffusing away from sub-grain boundaries until the cementite sub-grains are separated. This model's schematically shown in Figure 3-14. The TEM bright field image partially proved this model, shown in Figure 3-15.

3.6.2 The Plastic Deformation Ability of Cementite

Figure 3-14 shows that the cementite lamellae in pearlite structure started dissolving in deeply deformed Steel 1 before spheroidizing annealing. Several possible slip systems in deformed cementite crystals have been proposed[86, 87, 88, 89]. It appears that a fine pearlitic structure and a high hydrostatic compressive state, as in wire drawing and cold rolling, favor the plastic deformation of the cementite lamellae.

Recently, it has been pointed out by several authors that cementite can undergo a

partial dissolution during heavy cold working for pearlitic or low carbon steel[90, 91]. According to these authors[92], the driving force for cementite dissolution could come from the fact that the interaction energy between a carbon atom and a dislocation exceeds the binding energy between carbon atoms and iron atoms in cementite, i.e., the heat of solution of cementite (~0.5 eV or 48 kJ/mol)[93] The interaction energies between C and N atoms and dislocations are 0.78 eV/atom and 0.47 eV/atom, respectively[94]. Therefore, carbon atoms may be attracted toward dislocations crossing the cementite lamellae during deformation or by dislocations located in ferrite near the ferrite-cementite interface and form "Cottrell atmosphere." This concept proposed by Cottrell and Bilby is generally accepted. The amount of C and N atom migration towards the dislocation were determined as a function of dislocation density (L), the diffusion coefficient of interstitial in matrix (D), time and temperature (in degrees Kelvin)[95]:

$$W = 1 - \exp\left[-3L\left(\frac{\pi}{2}\right)^{1/3}\left(\frac{ADt}{kT}\right)^{2/3}\right] \qquad (3\text{-}2)$$

where W is the amount of solute segregated to dislocation, k is the Boltzmann constant and A is a constant defining the intensity of solute-dislocation interaction. In this model, the driving force for C and N migration is elastic potential. The limitation of this model is that back diffusion and the saturation of elastic potential were not counted. Therefore, this model only can describe the initial stage of "Cottrell atmosphere" forming. However, it gives a good explanation for the cementite dissolution during cold work. According to this model, the graphite could precipitate along the dislocation lines and grow by incorporation of carbon atoms transported by rapid diffusion along the dislocation lines. No TEM attempt has been done to prove it. But preferential nucleation along the rolling direction were observed, shown in Figure 3-1 and 3-2.

Mossbauer spectroscopy on a pearlitic steel with 86% area reduction by cold drawing showed that the cementite decomposition took place during cold working and no additional decomposition during the followed aging process[96]. Cementite decomposition during cold work is different than dissolution due to heating to austenite temperature. The latter is a

classical problem of phase stability and does not need previous deformation. V. T. L. Buono et al[95] suggested the association of C atoms, coming from a cementite, with neighbor dislocations at the cell walls would lead to the formation of a layer with a high concentration of carbon atoms at the interfaces between ferrite and cementite. No report of a direct observation of such carbon enriched area was found in the literature, its formation is supported by observation of graphite layers in the vicinity of cementite lamella, after deformed pearlitic steels were submitted to subcritical annealing[97] .

Languillaume and Baudelet[92] found that the cementite lamellae are not uniformly resolved but are composed of crystallites of very small size (only few nanometers), which seems to indicate that this phase has undergone strong perturbations during wire drawing.

Two possible causes for the increase of the cementite free energy during cold work. First, considering that cementite lamellae sustains a high stress during deformation, one may consider the effect of stored elastic energy in this phase. However, even if assume that cementite deforms during cold work under a stress equal to its theoretical strength, typically E/50 with E being the cementite Young's modulus, this effect can be reasonably neglected when compared with the estimated size effect[98]. Second, there is a possible effect of chemical disordering during cold working. Due to the ordered structure of cementite, intense dislocation glide activity in this phase may introduce a large quantity of antiphase boundaries which, as cold work strain increases, leads to a progressive loss of the long-range order in the cementite structure.

The carbon super saturation in the as-deformed structure is similar to the amount that can be found in some quenched iron-carbon alloys. Aging of such quenched alloys involves successive carbon segregation around dislocations, pre-precipitation by carbon cluster formation, and finally iron carbide precipitation.

From Figure 3-4 and 3-5, it can be seen that the ferrite domains are no more of a lamellar type but are granular, even if the grains were elongated in the cold rolling direction. Cementite globules are located at ferrite grain boundaries or triple junctions and seem to have undergone coalescence.

3.6.3 Manufacturing Variables

In practice, a considerable overlap between the mechanisms takes place, and more than one or different combinations of mechanisms may dominate for graphite formation.

Bidash found that in cold rolled 18YuA steel, graphite formed along the boundaries of primary austenite grains and at the junctions of recrystallized ferrite grains[1]. It is well known that the properties of cold-rolled steel depend to a significant degree on hot rolling schedules, and above all on the temperature at the end of rolling, cooling rates from the temperature at the end of rolling to that at winding into a coil, and also on the coil cooling schedule. The schedule for cooling strip form the temperature at the end of rolling to that at winding into a coil in modern rolling mills is specified by spraying water on the outlet roller, supplied under pressure through upper and lower nozzles of sprayers, the length of the sprayer operating zone, the amount of water supplied, and also the rate of strip movement over the roller.

With high cooling rates for hot-rolled strips to the winding temperature, eutectoid decomposition of austenite proceeds with formation of fine pearlitic grains and finely and medium differentiated lamellar cementite. With low cooling rates, for example with insufficient spraying, with considerable thickness or high movement rates over the roller, the austenite decomposes with formation of coarsely differentiated lamellar pearlitic cementite, or ferrite and cementite in form of coarse precipitates along ferrite grain boundaries.

Disruption occurs in the eutectoid structure after high levels of deformation, particularly in unfavorably orientated pearlite grains where the cementite plates located perpendicular to the deformation direction. Cementite plates break down into mutilple parts which move relative to each other forming folds, and the continuity of ferrite and cementite is also disrupted (Figure 3-15). The possibility of dissociation of a considerable part of the cementite and transfer of carbon to dislocation was noted by Gavrilyuk[9].

Defects of the atomic-crystalline structure in ferrite and cementite formed during cold plastic deformation will affect the formation of the structure during post-deformation annealing, and above all with spheroidization and coalescence.

Cold plastic deformation causes non-uniform dislocation density and affects carbon diffusion and iron self-diffusion. Cold plastic deformation will strongly affect the annealing structure of coarsely differentiated eutectoid, since in this way the atomic-crystalline structure of pearlitic grains is disrupted. Microdiscontinuities form ferrite and cementite, part of the cementite dissociates, and carbon is transferred to dislocations. An increase, as a result of cold deformation, chemical inhomogeneity of the ferrite matrix for carbon around lamellar cementite is a good thermodynamic stimulus, not only for accelerating spheroidization and coalescence of cementite, but also for precipitation of carbon in micro discontinuities and the development of cementite graphitization.

Carbon at the surface of micro pores and fine cracks precipitates easily since stresses are not needed for matrix deformation during graphite nucleation and growth, and also evacuations of iron atoms form the interphase surface into matrix.

3.6.4 Carbon Diffusion And Transport

A summary of free carbon source, carbon transport, the possible sites for graphite nucleation is shown in Figure 3-16 which was modified by the author based on Bernstein's hydrogen embrittlement model[99].

Free carbon atoms stay in the interstitial iron matrix and cause lattice distortion. Therefore, an elastic strain field is formed around carbon atoms. This strain field will interact with the strain fields around the other defects, such as inclusions, microvoids, dislocations, dislocation arrays, precipitates, grain boundaries, solute atoms. Then these defects attract carbon atoms to their surroundings and become carbon "traps" or "sinks."

Carbon atoms transport in dislocation cores or as associated Cottrell atmospheres may be several orders faster than lattice bulk diffusion. When dislocations pass microvoids or inclusions, the collision of dislocations with opposite signs will cause carbon atoms in Cottrell atmosphere to be dumped in voids or inclusion interfaces, shown in Figure 3-17.

Flemings introduced a model to simulate a graphitization process in austenitizing temperature range[100]. In this study, a similar model was built for the graphitization process

controlled by carbon diffusion in ferrite, as shown in Figure 3-18.

The solubility of carbon in ferrite at α/cementite interface $C_{\alpha/c}$ is higher than that at graphite/α interface $C_{\alpha/gr}$. If the spacing between a cementite and adjacent graphite particle is d, carbon diffuses from cementite to graphite down the gradient $(C_{\alpha/c} - C_{\alpha/gr})/L$. Assuming the steady condition of one-dimensional diffusion exists at particle/matrix interface, and neglect curvature effects. From Fick's first law, the rate of carbon diffusion is

$$J = - D (C_{\alpha/c} - C_{\alpha/gr})/L \quad (\text{mole/cm}^2.\ S) \tag{3-3}$$

where J is the flux of carbon atoms.

The carbon fluxes come entirely from the dissolution of a volume fraction f_c of cementite with composition C_c. Thus, the total transport of carbon atoms across a cross-sectional area A of a small volume AL is

$$AJ = AL \frac{d(C_c f_c)}{dt} \tag{3-4}$$

Combining above two equations and integrating from $f_c = f_c^o$ at t = 0 yields

$$f_c = f_c^o - \frac{D}{L} \cdot \frac{C_{\alpha/c} - C_{\alpha/gr}}{C_c} \tag{3-5}$$

For complete elimination of the cementite, at $t = t_e$, $f_c = 0$, then

$$t_e = f_c^o \frac{C_c}{C_{\alpha/c} - C_{\alpha/gr}} \cdot \frac{L}{D} \tag{3-6}$$

Although these equations are simplifications, they illustrate the important variables involved in graphitization. Fine cementite structures and high diffusion coefficients, large driving force $(C_{\alpha/c} - C_{\alpha/gr})$ will accelerate cementite dissolution and graphite formation. Experimental work has proved that a rapid cooling rate will cause a finer cementite lamellar structure and increase the graphitization rate[59]. Some alloy element such as Si, will separates

the metastable limit of ferrite solubility further from the stable limit, thus increasing the driving force ($C_{\alpha/c}$ - $C_{\alpha/gr}$). Recently, Neri et al found that the fastest graphitization rate occurs from approximately 650 to 660 °C which agrees with results from previous researchers[101]. As shown in Figure 2-1, the highest driving force is at about 650 °C. This simple model perfectly supports the experimental results about the Si effect on graphitization and the temperature range for the fastest graphitization rate.

However, the solution of cementite cannot be controlling in the initial stage of growth because at the start the ferrite, in equilibrium with cementite, is super saturation relative to graphite and thus, for a short time at least, the nodule will obtain carbon by depletion of ferrite. As the available carbon is used up, the solution of cementite will start and, if it is the slowest process, will assume control.

3.7 SUMMARY AND CONCLUSIONS

Graphite and carbides in cold rolled and annealed low alloy steels were characterized using optical, scanning electron and transmission electron microscopy. The following conclusions can be drawn:

1. Focused ion beam cross section showed that graphite in cold worked and annealed steels has a perfect interface with iron matrix.
2. Carbides in graphitized steel 1 were identified as cementite rich with Mn and Cr. There were two kinds of carbides in steel 2, one was spheroidized cementite, another was angular Nb (C, N).
3. Graphite preferentially formed at the regions segregated with Al, Si in steel 1. In steel 2, graphite preferentially formed at broken Nb(C, N).
4. Transmission electron microscopy study supported the cementite spheroidizing mechanism that carbon atoms diffuse from sub-grain boundary to the cementite lamellar surface with smaller curvature.
5. TEM study on deeply cold worked steels showed that cold work could accelerate cementite dissolution but no Nb(C, N) dissolution.

6. A carbon diffusion driving force model was proposed which gave good explanations for the nose location in published graphitization "C" curves, for the observation that fine pearlite favors graphitization, for Si effect on graphitization.
7. A dislocation transport model was proposed to illustrate the function of inclusions on graphitization during cold work.

Table 3-1 Chemical compositions of steels.

	C	Mn	P	S	Si	Cr	Ni	Mo	Al	Nb
Steel 1	0.68	0.33	0.005	0.014	0.24	0.25	0.20	0.099	0.053	0
Steel 2	0.67	0.40	0.01	0.005	0.27	0	0.25	0.12	0.053	0.25

Table 3-2 Image analysis results for as cold-rolled and annealed Steel 2.

Positions	Graphite, %	No. of Graphite	X length	Y Length
T-S (AR)	1.2			
L-S (R)	0.9246	80.8	204.1	234.5
	1.0582	75.1	209.0	241.2
	0.9016	83.9	205.3	251.4
L-T	1.1182	58.5	177.7	175.0
	1.0124	53.4	178.3	193.7
	0.9422	49.7	163.6	172,4

Table 3-3 Lattice constants of carbides.

	Crystal system	Fe, M/C	a, Å	b, Å	c, Å
Fe_3C	Orthorhombic	3	4.524	5.509	6.742
ε	Hexagonal	2.4 to 3	2.735	2.735	4.339
χ	Monoclinic	2.2 or 2.5	11.563	4.573	5.058

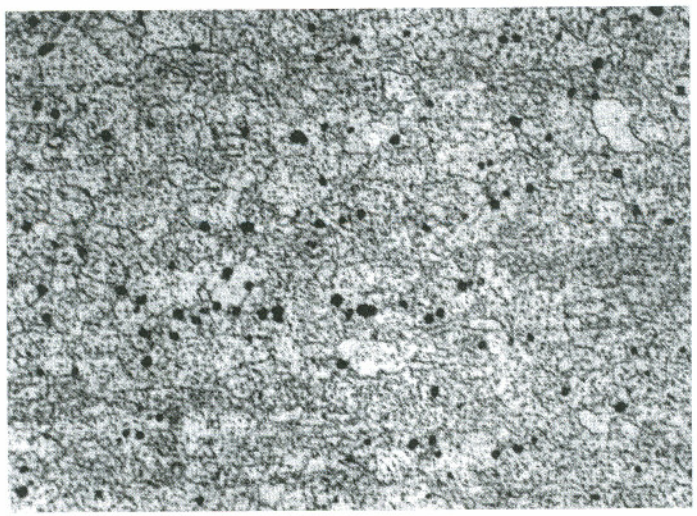

Figure 3-1 Optical microscopic observation of cold-rolled and annealed Steel 1. (400 X)

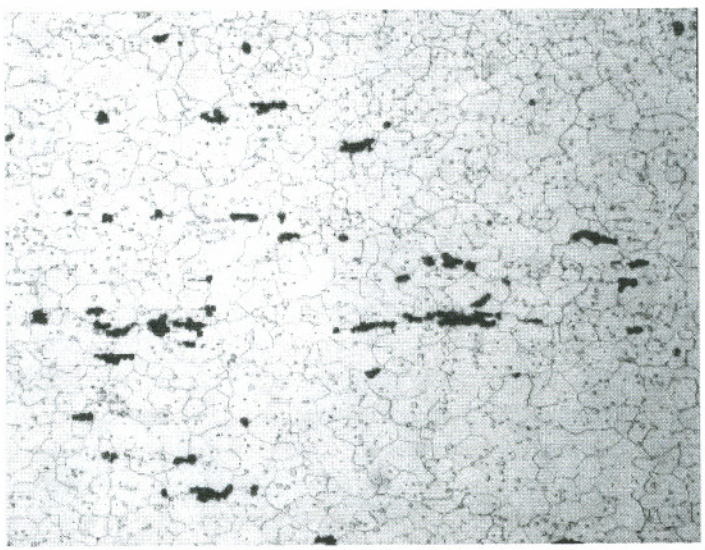

Figure 3-2 Optical microscopic observation of cold-rolled and annealed Steel. (500X)

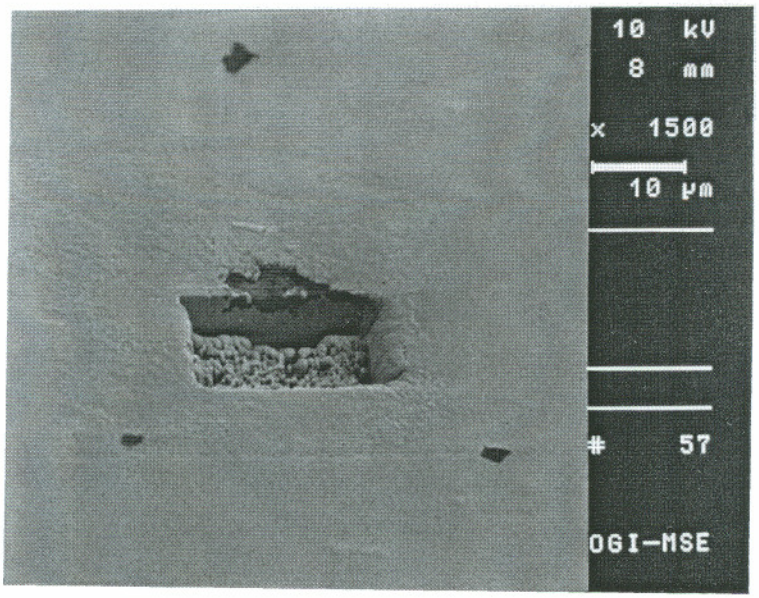

(a)

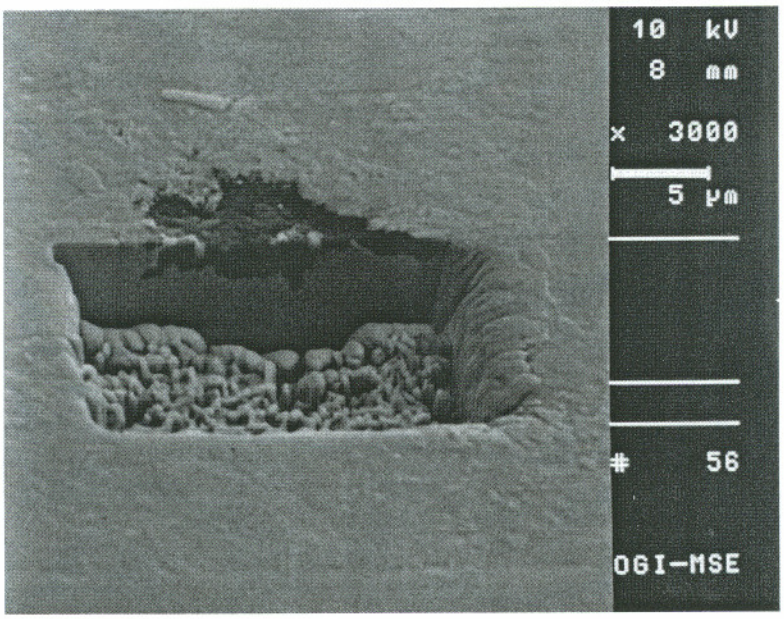

(b)

Figure 3-3 SEM sample preparation by focused ion beam and the observation on the graphite/matrix interface condition in Steel 2.

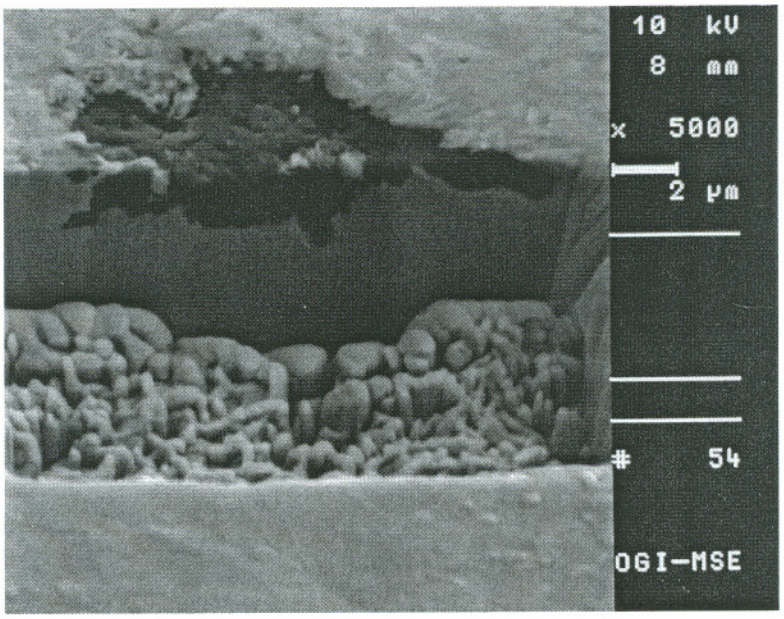

(c) Closer view of the graphite/matrix interface

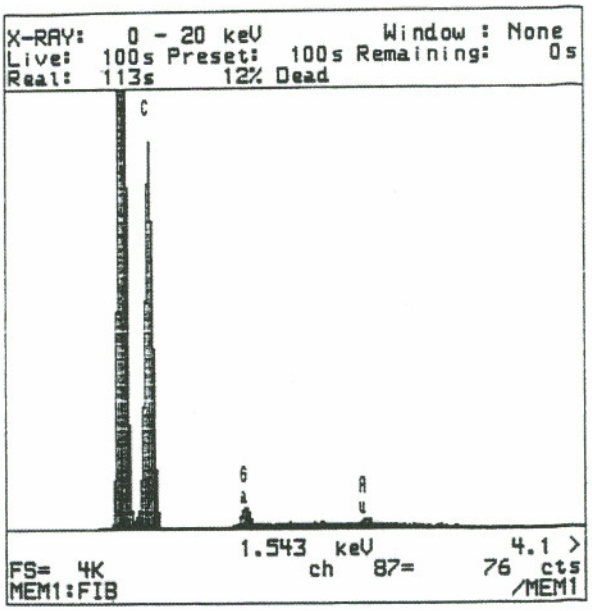

(d) X-ray spectrum from the cut particle

Figure 3-3 SEM sample preparation by focused ion beam, the observation on the graphite/matrix interface condition in Steel 2, and the particle composition determined by energy dispersive spectrum.

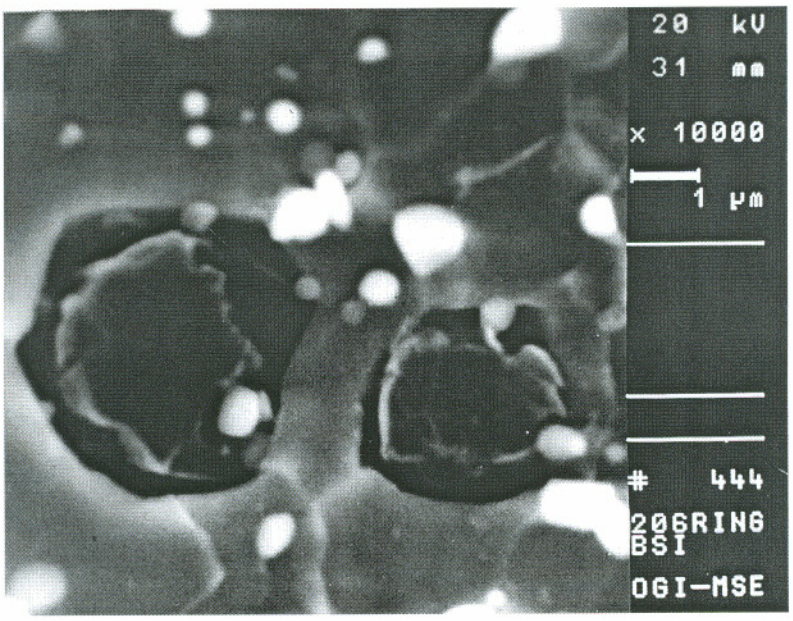

(a)

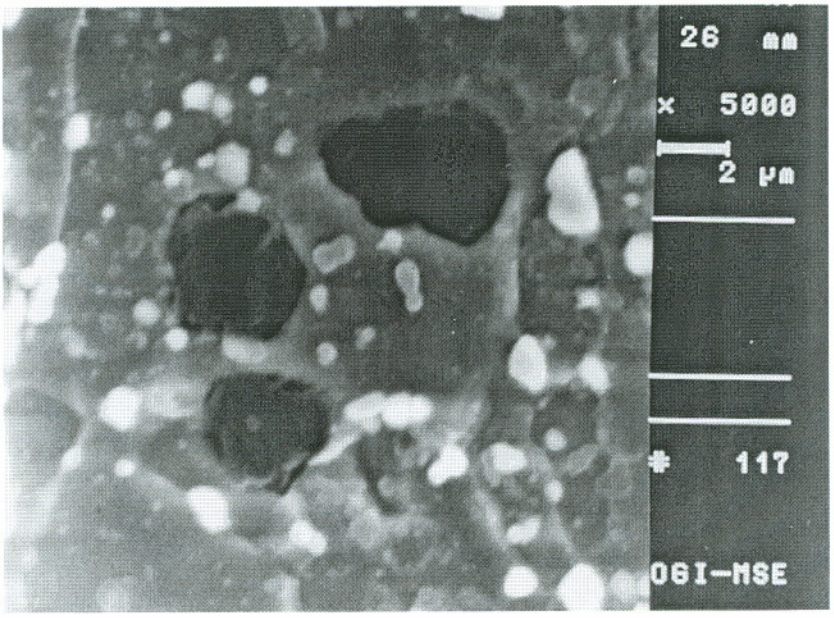

(b)

Figure 3-4 SEM observation on cold-rolled and annealed Steel 1.

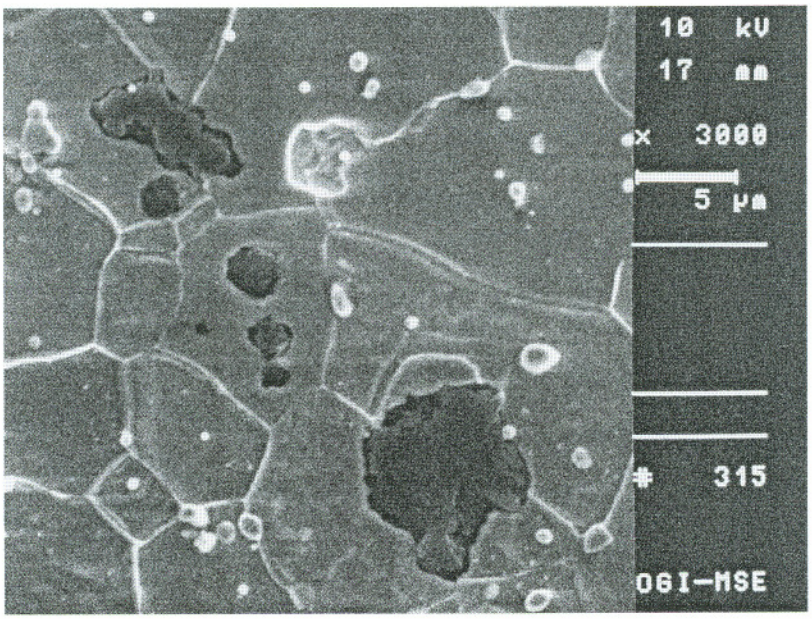

(a)

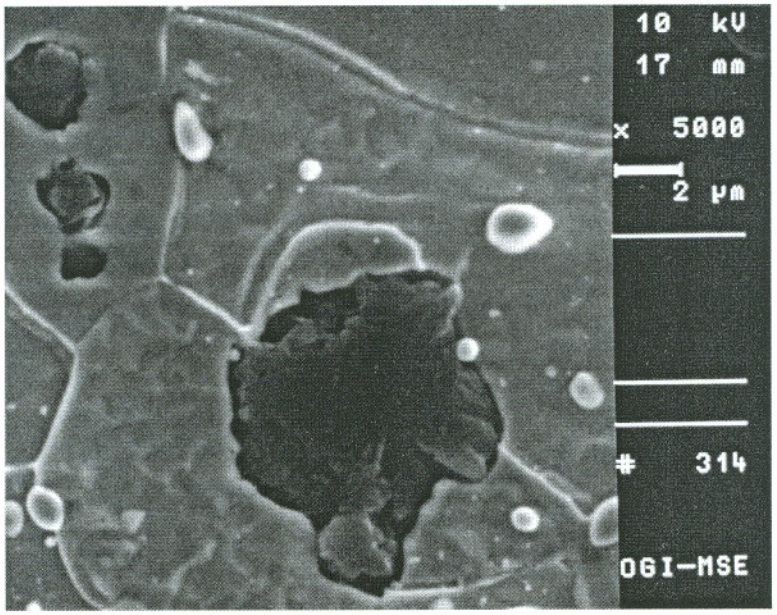

(b)

Figure 3-5 SEM observation on cold-rolled and annealed Steel 2.

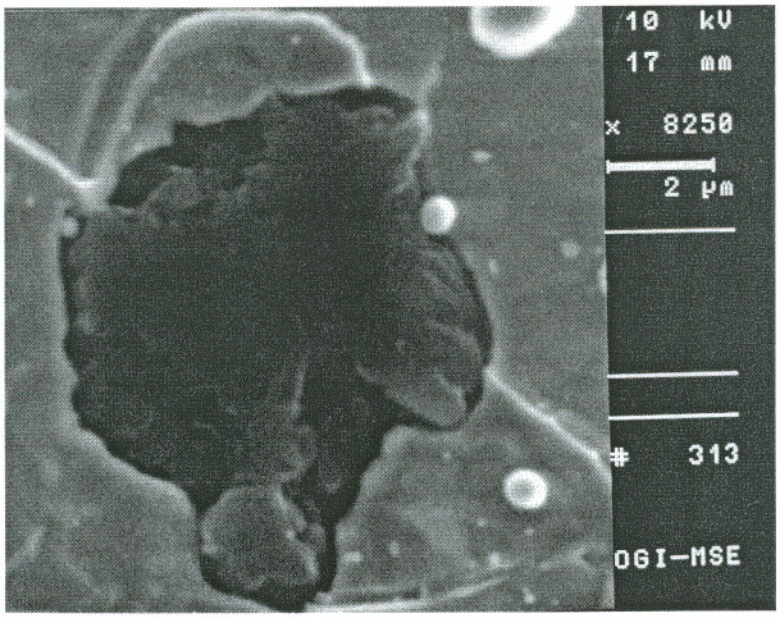

(c)

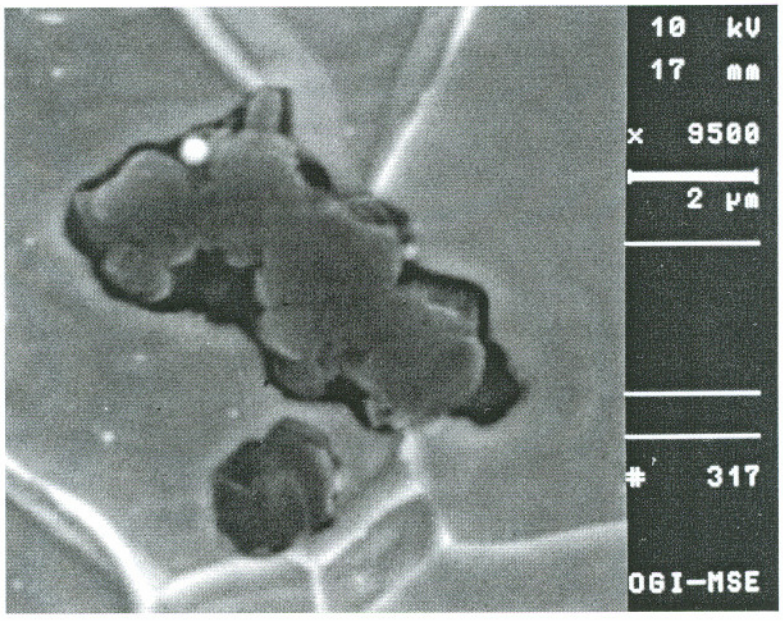

(d)

Figure 3-5 SEM observation on cold-rolled and annealed Steel 2.

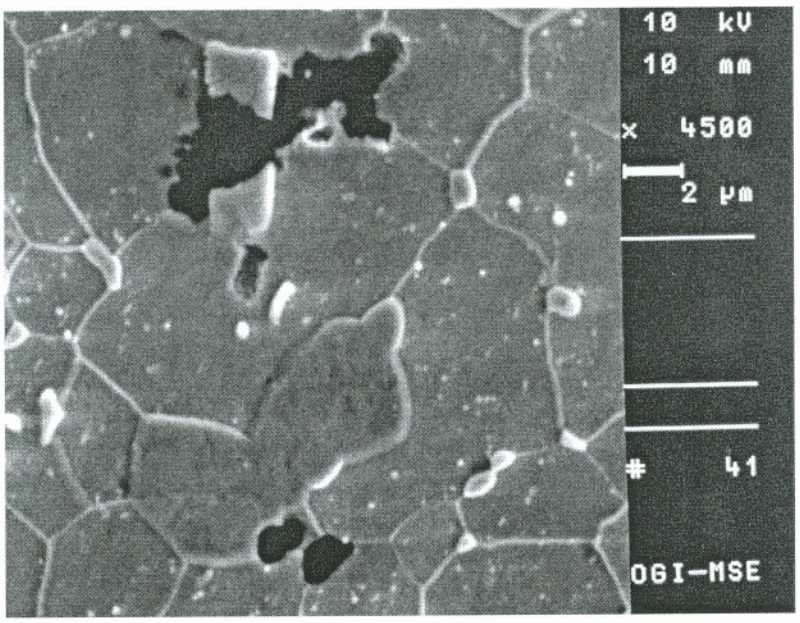

(a)

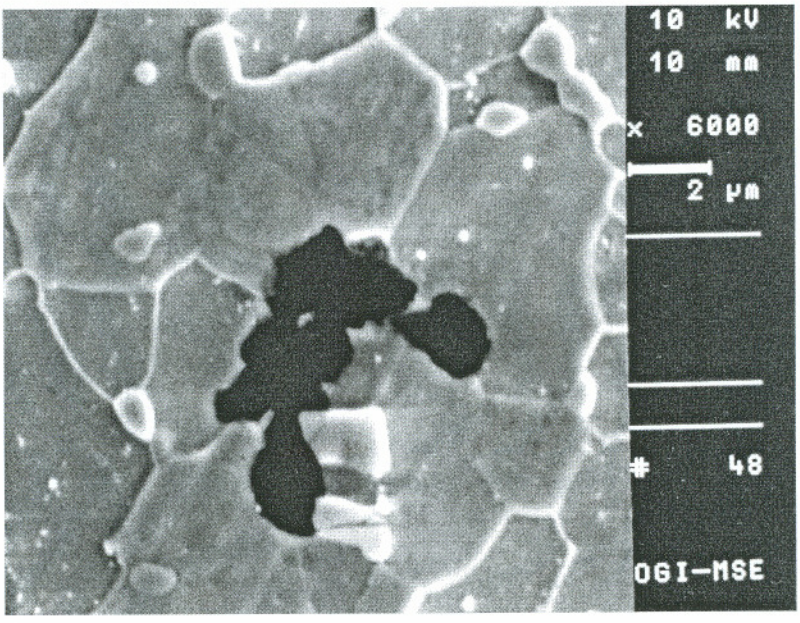

(b)

Figure 3-6 Graphite nucleated at a broken Nb(C, N).

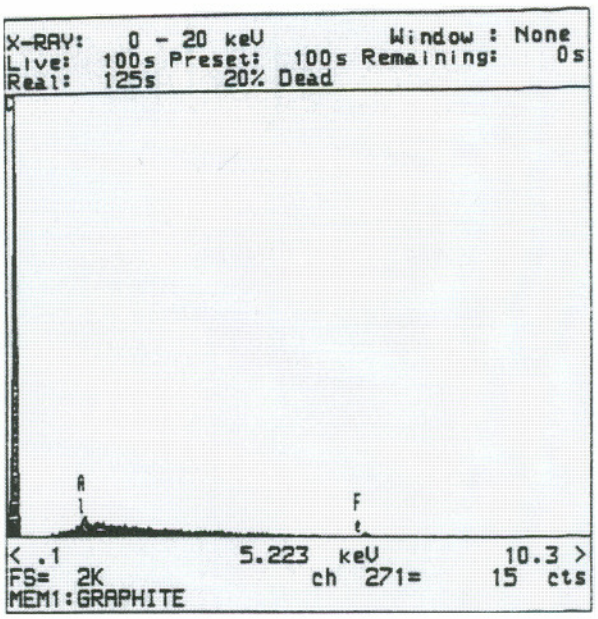

(a) Graphite

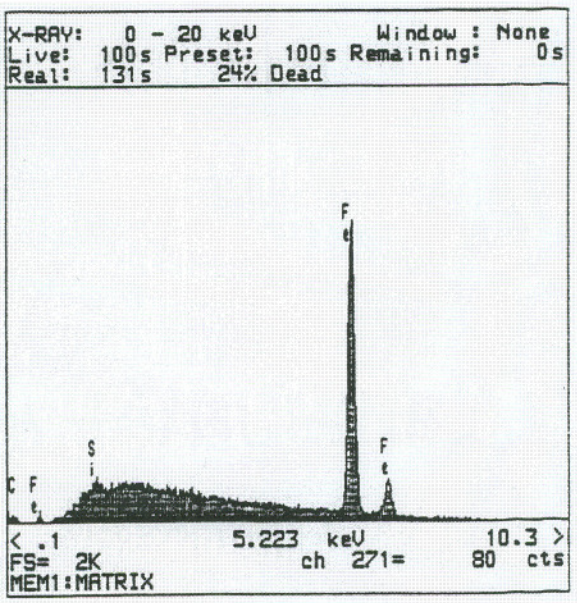

(b) Matrix

Figure 3-7 X-ray spectra from the graphite, matrix, carbides and inclusions in Steel 1.

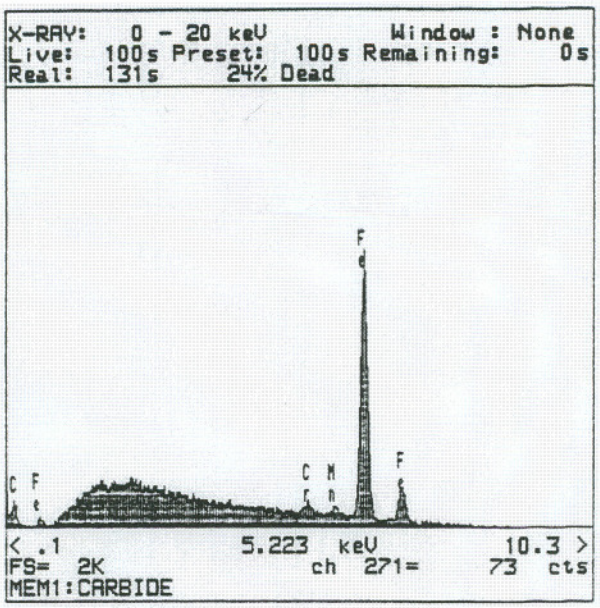

(c) Carbide

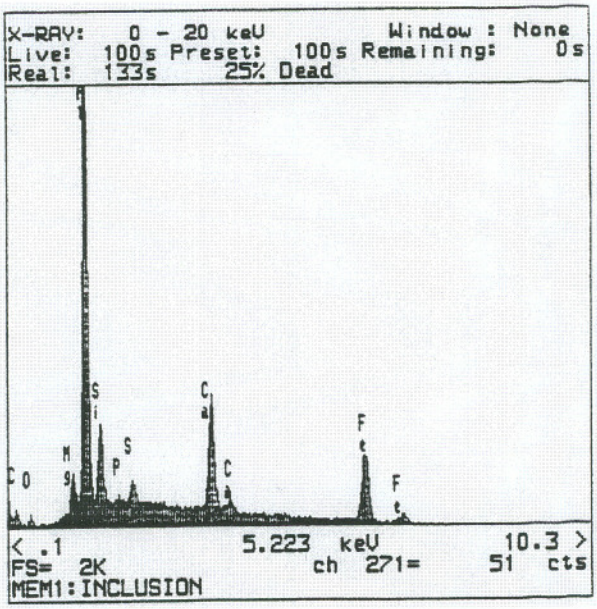

(d) Inclusion

Figure 3-7 X-ray spectra from the graphite, matrix, carbides and inclusions in Steel 1.

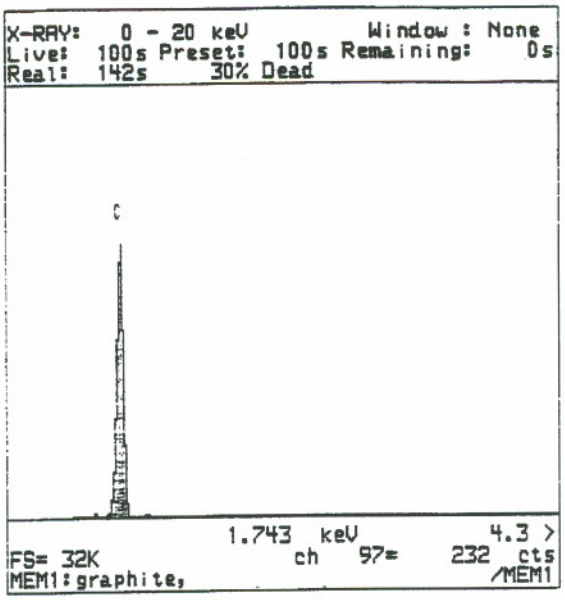

(a) Graphite

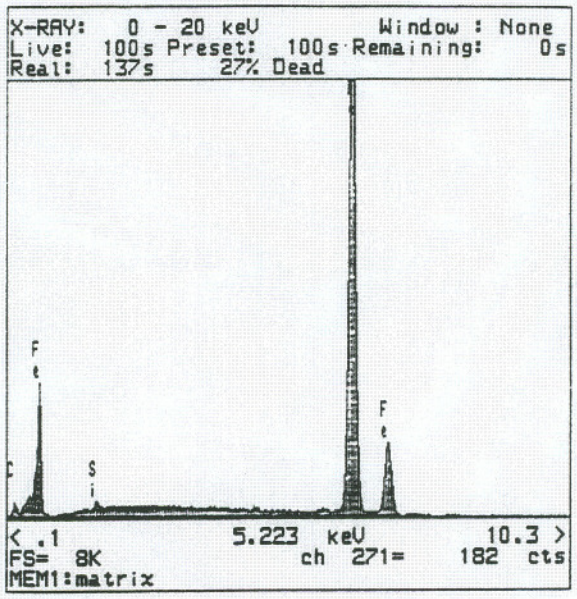

(b) Matrix

Figure 3-8 X-ray spectra from (a) graphite, (b) matrix, (c) cementite, and (d) Nb(C, N) in Steel 2.

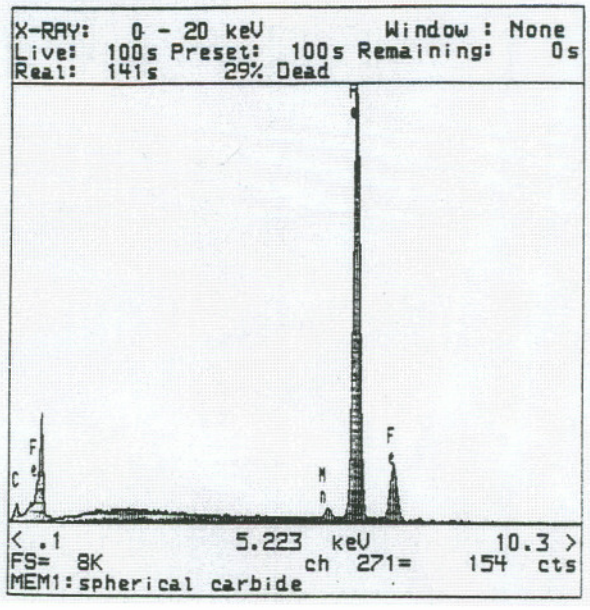

(c) Cementite

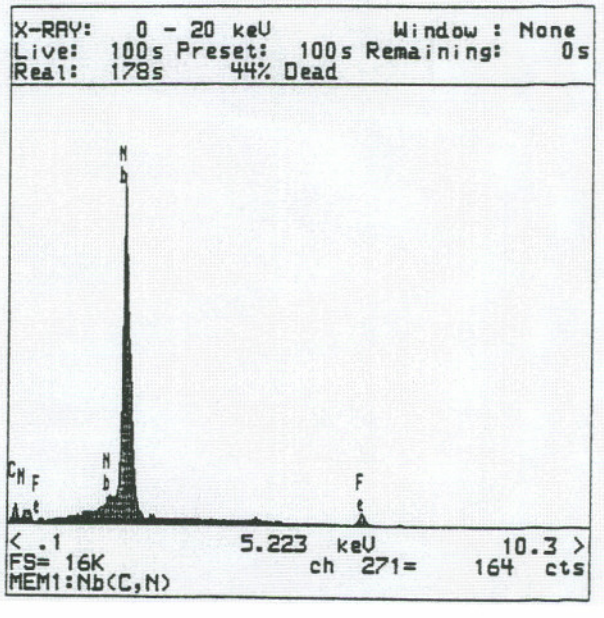

(d) Nb(C, N)

Figure 3-8 X-ray spectra from (a) graphite, (b) matrix, (c) cementite, and (d) Nb(C, N) in Steel 2.

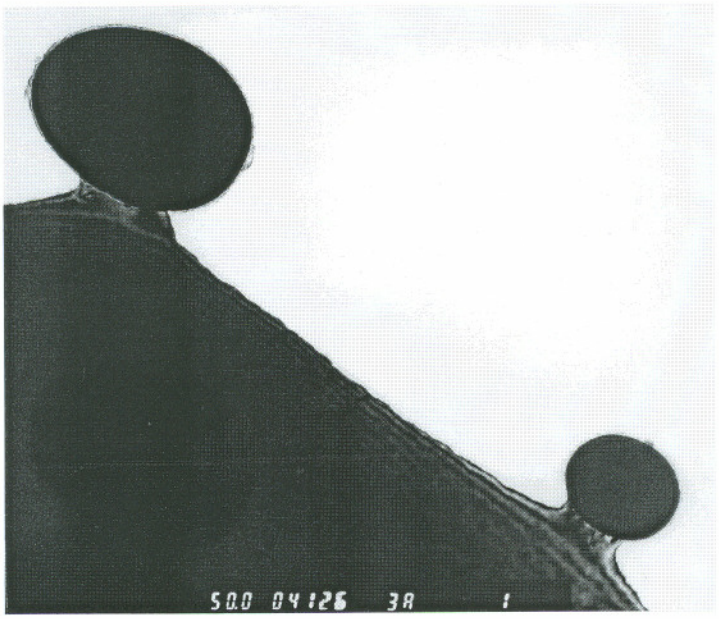

(a)

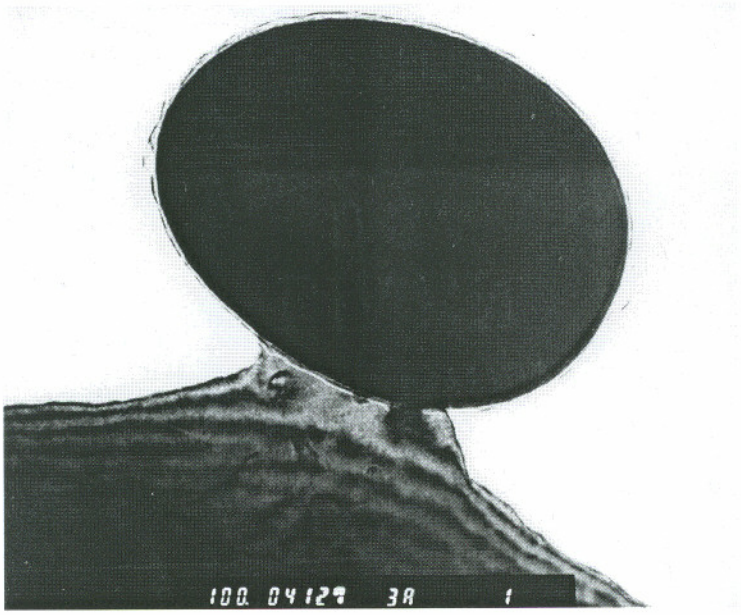

(b)

Figure 3-9 Spheroidizing carbides protruding from the center hole edge of an electro-polished specimen.

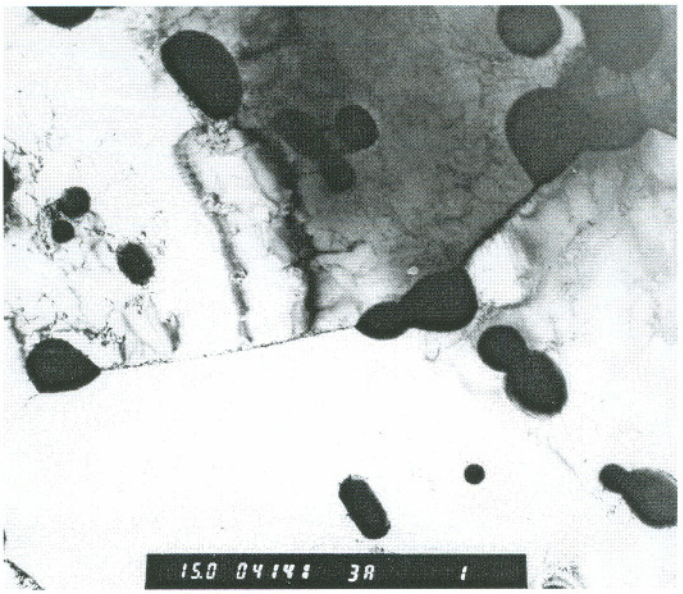

(a) Carbide distribution in Steel 1

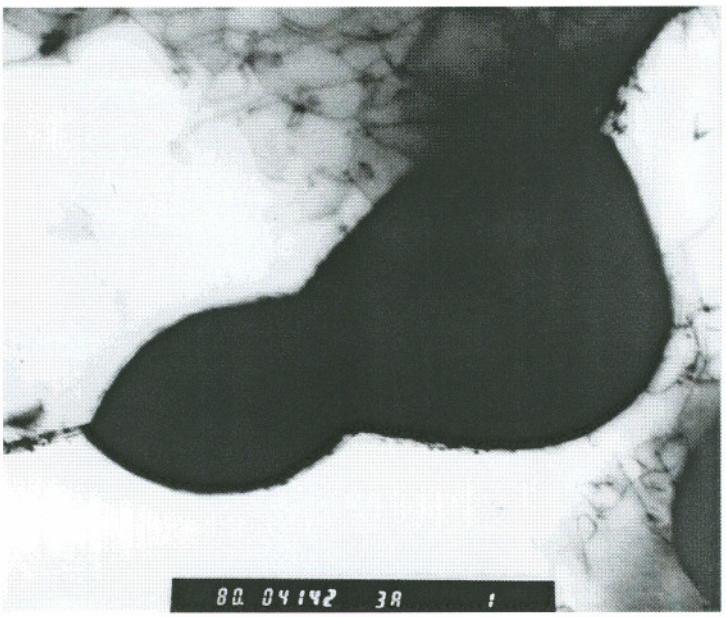

(b) Cementite precipitate along a grain boundary

Figure 3-10 TEM bright images of the carbide precipitates in Steel 1.

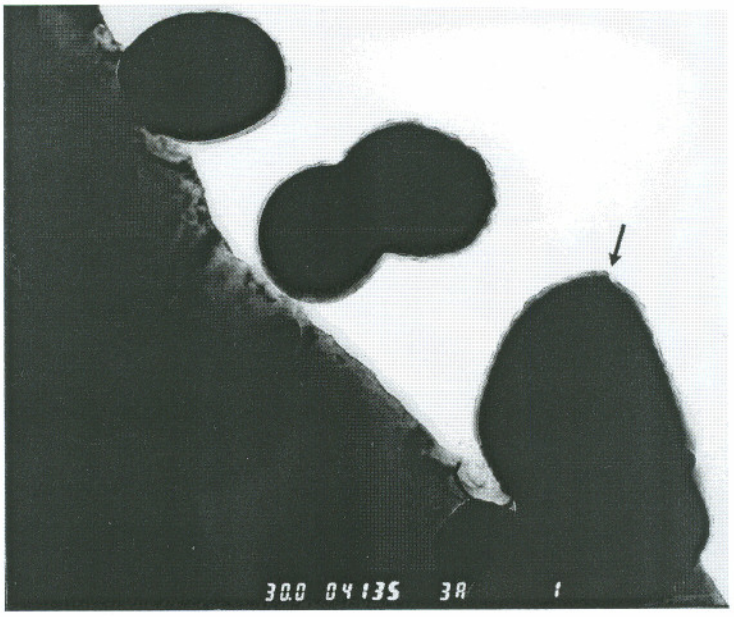

(a) TEM bright image

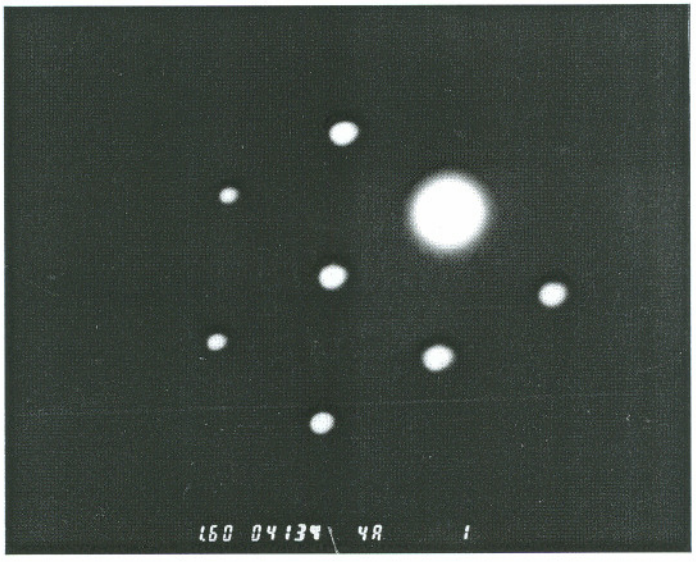

(b) Diffraction pattern

Figure 3-11 X-ray diffraction pattern of a carbide in Steel 1.

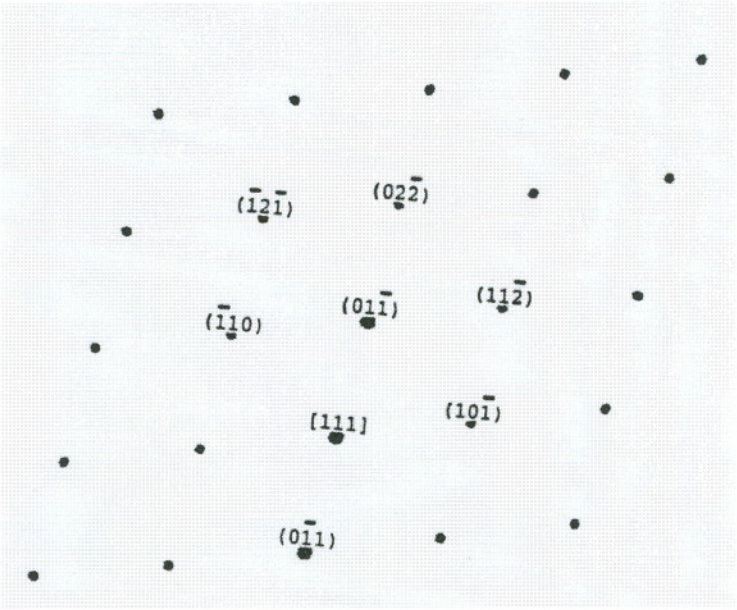

Figure 3-12 X-ray diffraction pattern of cementite simulated by Desktop Microscopist.

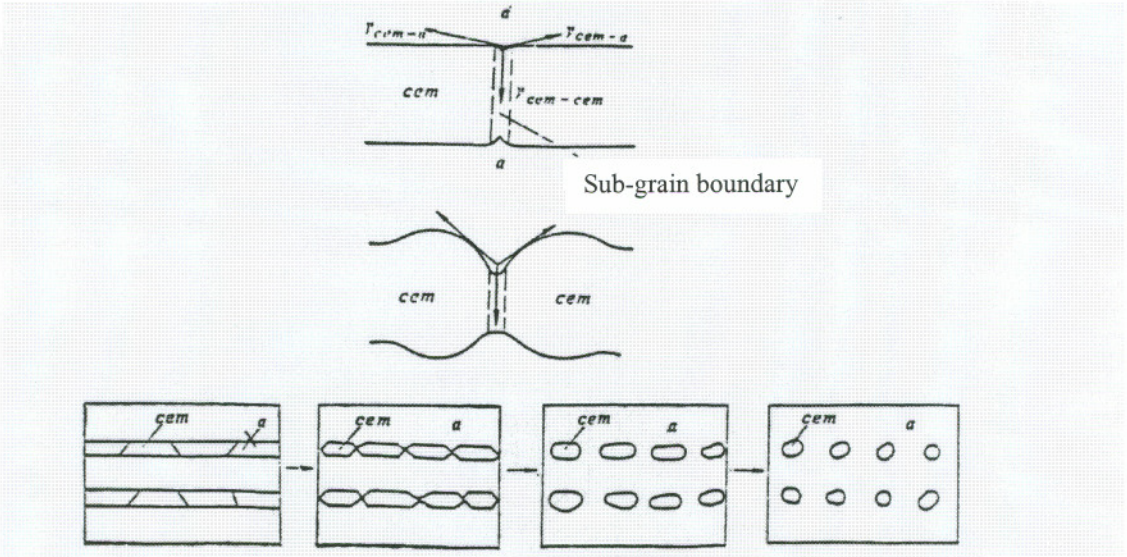

Figure 3-13 Schematic cementite spheroidizing model.

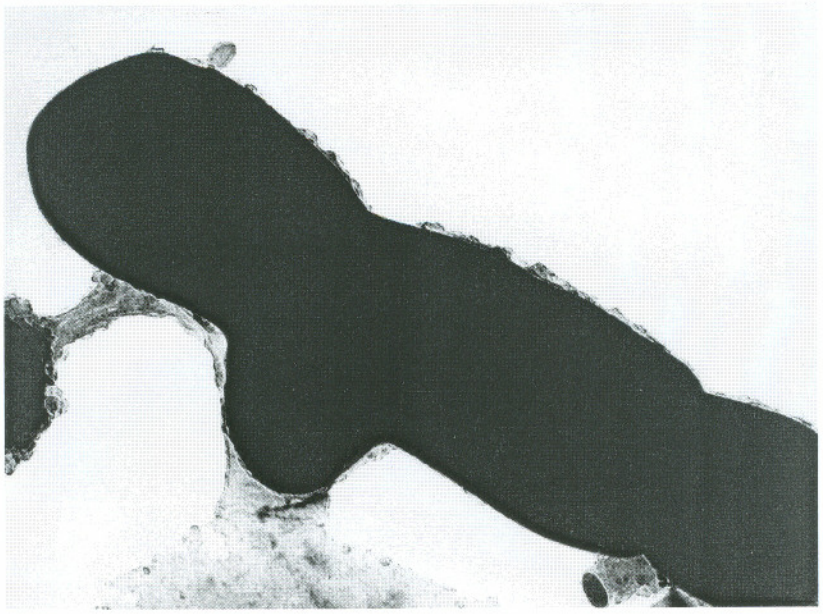

Figure 3-14 TEM bright image of a carbide precipitate during the spheroidizing transformation (40,000 X).

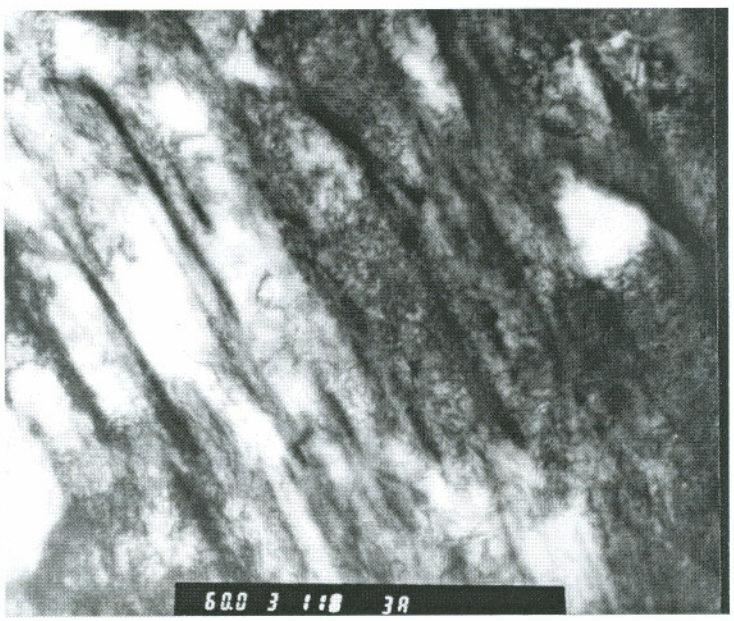

Figure 3-15 Dissolving cementite in Steel 1 after deep cold deformation but before spheroidizing annealing.

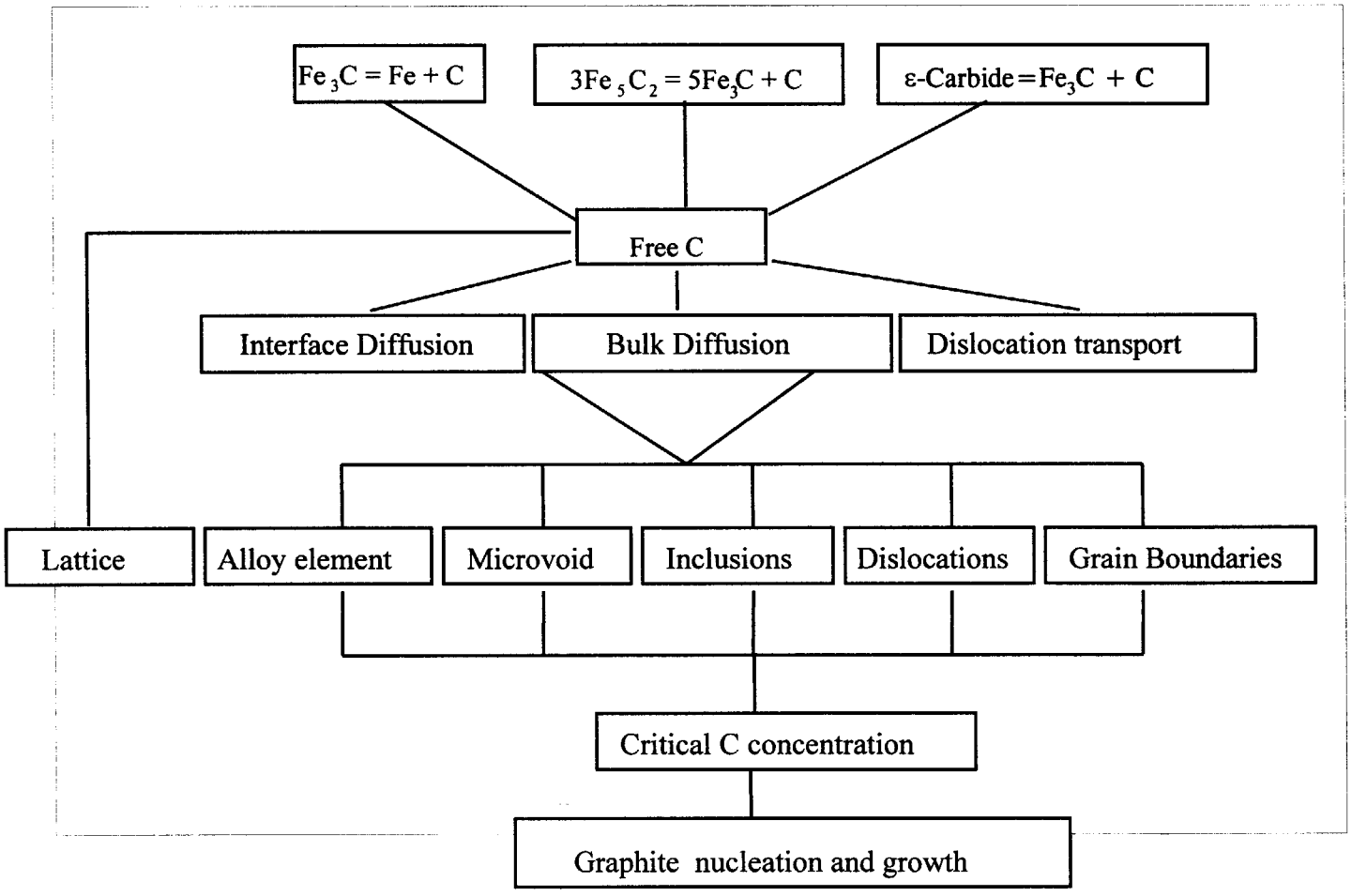

Figure 3-16 Summary of free carbon sources, carbon transport, and possible sites for graphite nucleation.

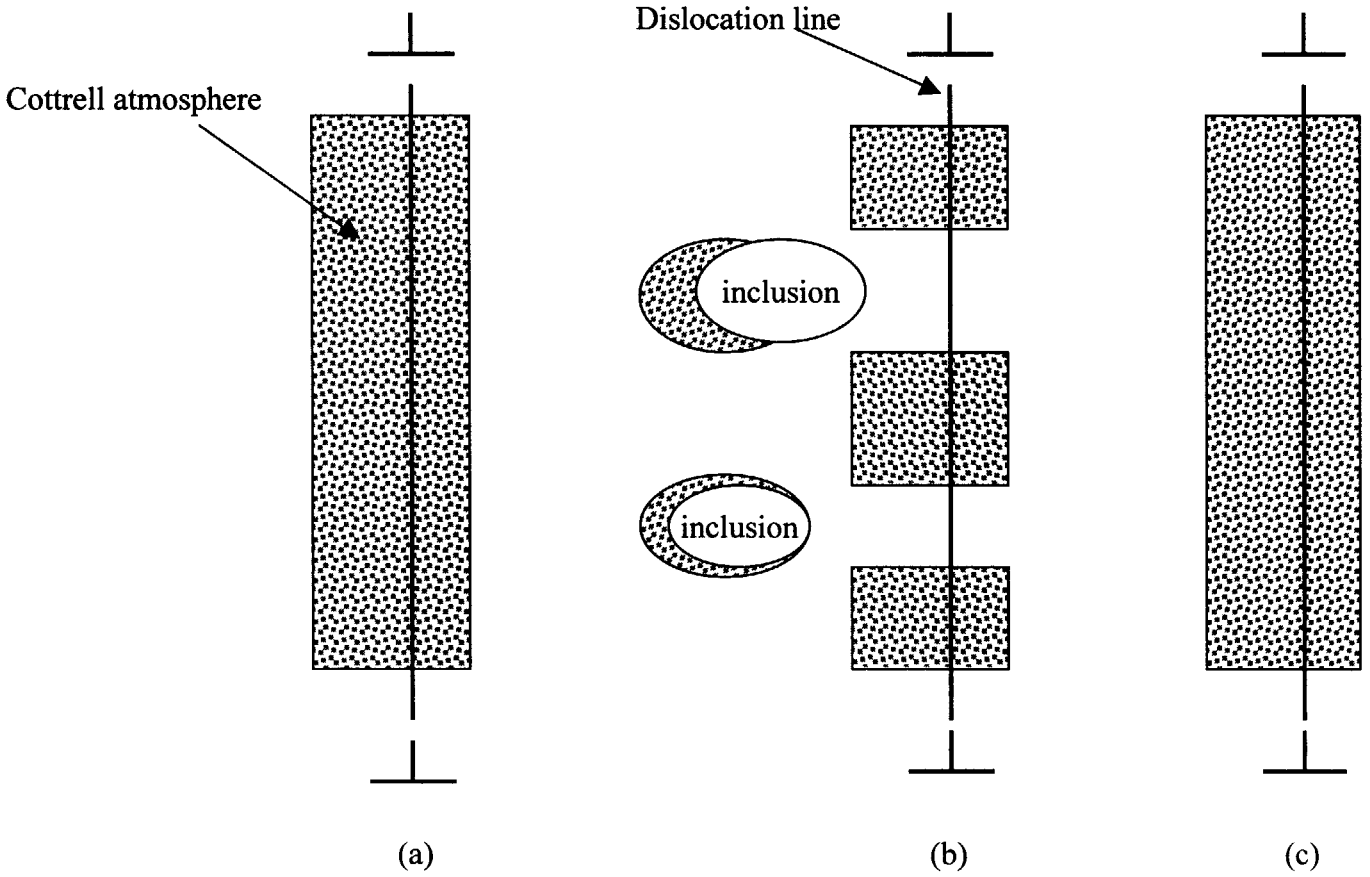

Figure 3-17 Carbon transport by dislocations. (a) carbon atoms form "Cottrell atmosphere" along dislocation lines; (b) carbon atoms are dumped into inclusion interfaces when dislocations pass inclusions by the collision of dislocation with opposite signs; c) more carbon atoms segregate at dislocation lines.

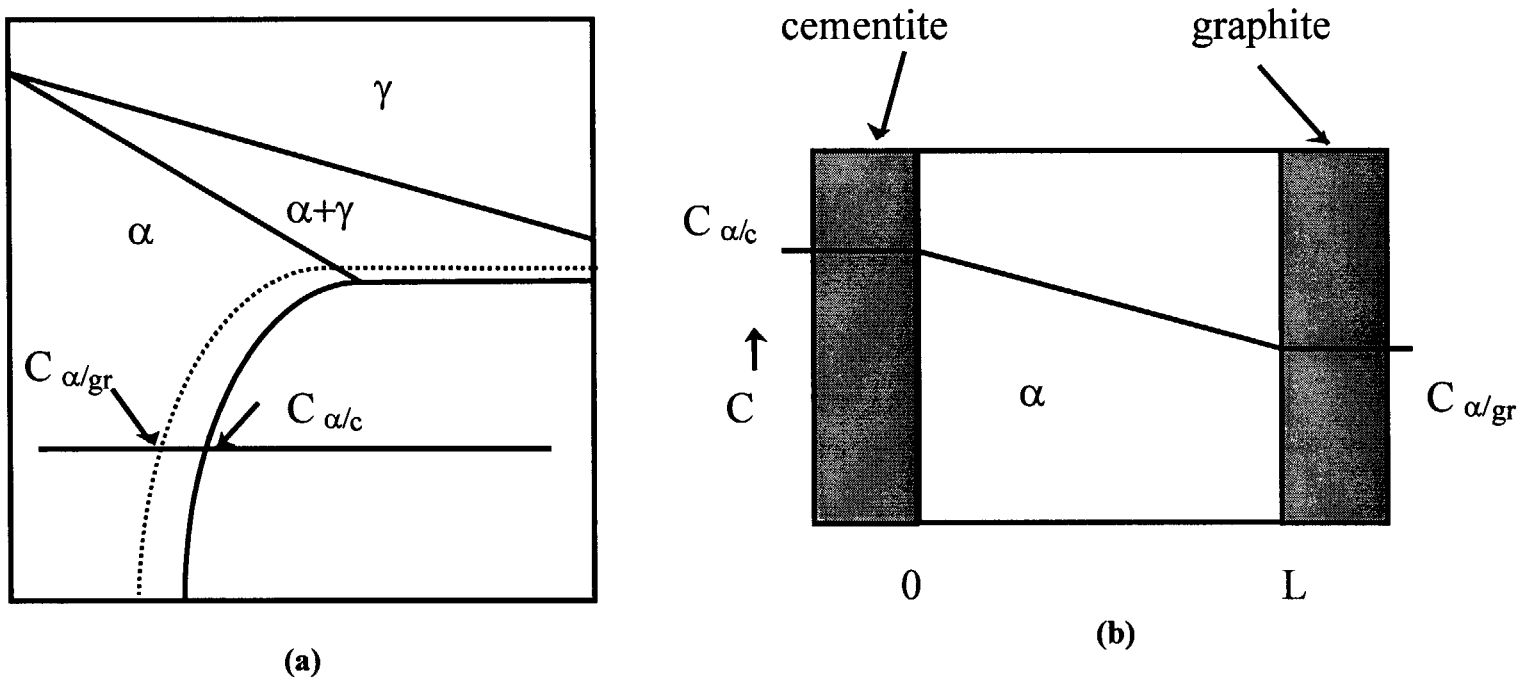

Figure 3-18 **Driving force for carbon atom diffusion in ferrite.**
(a) the lower, left-hand corner of carbon - iron diagram;
(b) carbon concentration at the interfaces of cementite/ferrite and graphite/ferrite.

CHAPTER 4
INFLUENCE OF GRAPHITE ON BAINITE AND MARTENSITE TRANSFORMATION

4.1 INTRODUCTION

Sometimes graphite formation cannot be avoided due to manufacturing processes or service conditions. The effects of graphite formation on other phase transformations and the final mechanical properties of steels are not clear. According to phase diagrams (thermodynamics), graphite can be dissolved in the austenite region. The question is whether the dissolution process is practical. This work first studied the graphite dissolution kinetics. Results demonstrated graphite in cold worked and annealed steels could be dissolved in a short time, unlike its formation process, and also the graphite content could be controlled by adjusting dissolution time and temperature. The effects of graphite content on Bainite and martensite transformation kinetics were investigated using a Gleeble thermal-mechanical system. The mechanical properties of steels with different graphite contents were studied by fracture toughness testing, and hardness testing.

4.2 GRAPHITE DISSOLUTION

4.2.1 Experimental Procedures

Cold worked and annealed Steel 2 was used to study the graphite dissolution kinetics. The chemical composition and graphite contents are listed in Table 3-1 and 3-2,

respectively. The sample configuration is shown in Figure 4-1. The specimen was 12 mm wide and 1.6 mm thick, a little wider than the bar diameter, 10 mm, recommended by Dynamic System, Inc., for phase transformation studies using Gleeble 1500 thermal-mechanical system. The working zone was 40 mm long.

The specimens were clamped by water-cooled copper jaws. A pair of Chromel-Alumel K type thermal couple, with temperature range from -133 °C to 1400 °C and 0.1 °C resolution, was welded at the center of the specimen. Each sample was subjected to controlled heating and cooling. The dilation change in the crosswise direction of each sample was measured with a dilatometer gage during the process. The measured temperature and dilation changes were then used for the determination of phase transformations.

First, Steel 2 with 1.0% graphite was austenitized in 1000 °C for 2 hours to determine if graphite could be dissolved. It was found that a volume shrinkage occurred during austenitizing isothermal holding. Then a series of graphite dissolution tests was conducted at different austenitizing temperatures and times. Austenitization parameters are presented Table 4-1.

After a sample was placed in the specimen chamber, the chamber was evacuated and then back filled with argon. A certain level of negative pressure was deliberately maintained in the chamber during the austenitization process. In this study, each sample was heated to the austenitization temperature in two minutes. After holding at austenitizing temperature for a planned time, specimens were cooled to room temperature by helium gas quenching.

The metallographic samples were sectioned along two planes. The specimen sectioning was conducted by abrasive-wheel cutting under water cooling, at a low speed to prevent overheating. Optical microscopy and image analysis were used to determine the graphite contents using the same procedures described in chapter 3. The first section was along width direction at the position where the thermal couples located. This exposed the plane the heat treatment temperature was exact the same as the controlled. The second section was parallel to the length direction. This plane showed the graphite content and microhardness as a function of the austenitizing temperature gradient.

4.2.2 Results and Discussion

The dilation versus time curve for Steel 2 isothermal held at 1000 °C for two hours is presented in Figure 4-2. The dilation decreased as the holding time increased. That indicated there was a volume shrinkage occurred at these temperatures. The volume of graphite is 3.5 times the volume of iron due to their relative densities.

Table 4-2 presents the image analysis results including the graphite area fraction, graphite number, X length and Y length in a field. Figure 4-3 shows the graphite area fraction and number as a function of austenitizing time at 830 °C. Clearly, graphite couldn't be dissolved considerably at 830 °C held for less than five minutes. Interestingly, the graphite number increased when austenitizing at 1000 and 830 °C for five minutes. It is probably due to some large particles were first broken down to several small particles. When the austenitizing time was greater than 10 minutes, the number and dimensions of graphite particles were markedly decreased. When the dissolution temperature rose to 1000 °C, most of the graphite disappeared after 30 minutes. The dissolution temperature effect on the graphite content is shown in Figure 4-4.

X length and Y length were designated as the total horizontal length and vertical length of all detected pixels in image analysis. In this study, the horizontal direction was parallel to the rolling direction, while the vertical direction was perpendicular to rolling direction. For all the samples, the Y lengths are slight greater than X length, similar to the as received conditions (Table 3-2). During the dissolution process, although the size and number of graphite particles were reduced, the morphology of graphite did not change too much.

The standard deviation, 95% confidence limit, and relative accuracy for area fraction measurements are presented in Table 4-3. Note that the relative inaccuracies for most measurements are less than 15%. Graphite has the highest grey level comparing to MnS and carbides. It was very easy to use thresholding to separate graphite with MnS and carbides. Therefore, 30 fields' measurement could give a relatively small standard deviation. Only the relative inaccuracy of the specimen austenitized at 1000 °C for 30 minutes was 22% because

the graphite content was so low. More fields are needed to improve the accuracy of the measurement on this sample. No attempts were made to measure the graphite contents of the samples held at 1000 °C for longer than 30 minutes.

Therefore, Graphite may provide good machinability of a ferrite material and then be redissolved by heat treating to produce high strength and wear resistance. However, the heat treatment temperature and time for graphite dissolving may vary with steel composition.

4.3 MARTENSITE TRANSFORMATION

During the graphite dissolution study, the effects of graphite content on martensite transformation start points and hardness was also studied.

4.3.1 Experimental Procedures

M_S Measurement

To measure the Ms temperature, data acquisition started at the same time as the quenching started. Figure 4-5 shows typical profiles of the temperature and dilation changes at the center of the sample work zone during the quenching. The cooling rate shown in Figure 4-5 was the maximum which could be achieved with such a quenching process. The changes of dilation and temperatures were saved into both ASCII and graphical files for postprocessing.

Two methods were used and compared in the determination of Ms temperature. The Gleeble 1500 thermal-mechanical system has software which has the capability of determining Ms temperature from the measured temperature and dilation data. It uses graphical interfaces to interactively determine the temperature point where the dilation-time curve deviate from nominally a straight line when cooling from high temperatures. The accuracy of such a determination is then subject to individual judgement.

The Ms also can be determined by curve fitting the linear portion of the dilation

curve. First, the temperature and dilation data were save in ASCII files. The dilation - time and temperature - time curves were plotted by *Kaleidagraph*, a data analysis and graphic presentation program developed by Synergy Software. Then plot a straight line by curve fitting the linear portion of dilation - time curve. The Ms was determined as the temperature as which the dilation - time curve deviates from curve fitting straight line.

Hardness Measurement

Microhardness testing can be regarded as a simple method of micromechanical testing. In this study, to consider the effects of the graphite dissolution on martensite hardness, Knoop micro hardness tests were conducted using a LECO M-400 instrument with a 500 gram loads. Samples were prepared by regular metallurgical polishing. Final polishing was done using 0.05 micron alumina. Six measurements were taken along the center line of each specimen. The average was used to represent the hardness of the specimen under the corresponding heat treatment.

Also, a longitudinal cross-section of a Gleeble sample austenitized at 1000 °C for 30 minutes was made to verify the hardness change as a function of graphite dissolving temperature. The temperature fields were measured using four pairs of Chromel-Alumel K type thermal couple, with temperature range from -133 °C to 1400 °C and 0.1 °C resolution, along longitudinal direction every 5 mm apart. Six mircohardness measurements were conducted along the longitudinal direction every 2 mm.

4.3.2 Results and Discussion

Martensite Transformation Start Points

The Ms values for different austenite conditions are listed in Table 4-3. The temperature versus cross-strain curve is shown in Figure 4-5. As the austenitizing temperature and time increased, the martensite transformation start point decreased. The

cross-strain change during transformation for the specimen austenitized at 1000°C for 30 min was greater than that for the specimen austenized at 830°C.

It is expected that the Ms will be decreased by increasing the carbon content in the austenite solid solution. Without a chemical effect, the Ms should rise as the austenitizing temperature rises and holding time increases, because the grain size increases and some defects can be eliminated, the martensite transformation resistence decreases. The Ms for the sample austenitized at 1000 °C for 60 minutes was not the lowest due to the transformation resistence. As the solid solution carbon content increases, some twinned martensite may be generated during quenching instead of forming all dislocation martensite.

There are many empirical equations for the calculation of Ms temperatures of steels. The accuracies of such equations have been thoroughly assessed. In this research, the modified Ms equation by Kung and Raymond[102] based on the linear equation originally proposed by Andrews[103] was used:

$$Ms\ (°C) = 539 - 423\ C - 30.4\ Mn - 17.7\ Ni - 12.1\ Cr - 7.5\ Mo + 10\ Co \qquad (4\text{-}1)$$

The calculated M_s for Steel 1 and Steel 2 are around 275 °C. Experimental results showed Ms for Steel 1 without graphite was 260 °C which is close to the calculated values. The Ms of Steel 2 was 280 °C when austenitized at 1000 °C for 30 minutes. Based on the equation (4-1), the carbon content in the matrix is about 0.42% for the Steel 2 austenitizing at 830 °C for five minutes. This suggested that there is about 0.15% carbon was in graphite.

Hardness measurement results

Hardness measurements from transverse cross sections are shown in Table 4-4 and Figure 4-6. The longer the austenitizing time at 830 °C, the higher the martensite hardness. However, the hardness did not increase further as the holding time at 1000 °C was greater than 30 minutes. Also, the hardness of martensite austenitized at 1000 °C was generally higher than at 830 °C for a given holding time. The image analysis results gave a good

explanation to the dependence of martensite hardness on austenitzing conditions. Generally, the hardness of quenched steel is due to three main factors:

(1) solid solution strengthening by carbon;

(2) work hardening due to transformation itself;

(3) hardening due to twin interfaces.

The strength of martensite is mainly due to solid solution strengthening by carbon, and the transformation twins in martensite plates contribute at most only a base strength. Image analysis results revealed that the longer the austenitizing time at 830 °C, the more graphite dissolved, and thus the more interstitial carbon atom in martensite lattices. Most of the graphitic carbon atoms went into solution when the holding time at 1000 °C was more than 30 minutes. At 1000 °C, more carbides will be dissolved, thus the hardness level is higher than at 830 °C. Figure 4-7 presents the hardness profile and austenitizing temperature profile along the longitudinal direction of a Gleeble sample for which the center of working zone was austenitized at 1000 °C for 30 minutes. This figure further confirmed the relationship between martensite hardness and austenitizing temperature, graphite content, carbon content in solution.

The effect of carbon on strength of martensite was first developed into a quantitative theory by Winchell and Cohen[104]. They proposed a model that the strength of martensite varied linearly with the cube root of the carbon content up to 0.4 % C. Later, Owen et al pointed out that the solution hardening of carbon in martensite was proportional to the square root of the carbon content and did not vary linearly with carbon content as in ferrite[105]. Kelly and Nutting showed that the Winchell-Cohan model predicted a lower value than experimental results and Owen's model agreed well with experimental results[106]. Quantitatively determination of the carbon content in solid solution for different austenitizing conditions could be the future work of this study.

It seems that steels can be softened to a level of low-carbon steels by converting cementite to graphite without adding any special element. On the other hand, since graphite is perfectly soluble in austenite in the case of carbon steels, hardening can be achieved by proper soaking the steel in the austenite range followed by quenching. Therefore,

graphitization seems to be applicable to provide a new high-carbon steel, which is very soft during forming but which can be hardened after heat treatment.

4.4 BAINITE TRANSFORMATION

High-strength bainitic steels have a number of desirable mechanical properties, such as a combination of good toughness and wear resistence. This research examined the role of graphite on Bainite transformation kinetics and the role of transformation temperature on hardness after isothermal transformation. Steel 2 samples with 0.47% and with 0.06% graphite area fraction were used. Two Bainite transformation TTT curves were developed for these two graphite levels using Gleeble thermal-mechanical test system. Micro hardness tests were conducted for Bainite structure of both Steel 1 and Steel 2 transformed at different temperatures. The measured hardness results were compared with those predicted by existing empirical equations.

4.4.1 Experimental Procedures

For analysis of transformation kinetics, a physical property (e.g., hardness, electrical resistivity, and enthalpy, dilation), P, of the material subject to investigation can be traced as a function of time and temperature. The fraction transformed, f, can be defined as

$$f = [P(t) - P_s]/[P_f - P_s] \tag{4-2}$$

where P_s and P_f are the physical properties of the solution-treated specimen and fully transformed specimen, respectively. The reference state P_s and P_f cannot be considered in general as constants because they normally depend on temperature. However, the difference $P_f - P_s$ may be considered almost constant at temperatures under experimental consideration.

In this study, the dilation was used as the physical property to determine the Bainite transformation kinetics, because there is a volume expansion during the transformation from

austenite to Bainite.

The sample configuration is shown in Figure 4-1, the same as for specimens used for studying graphite dissolution. First, specimens were austenitized and gas quenched to vary the graphite contents. Austenitizing temperature and time were determined according to the results of graphite dissolution study. The 1000 °C for 30 minutes heat treatment produced samples with low graphite content (0.06% area fraction). Heat treating at 830 °C for 10 minutes produced samples with much higher graphite content (0.47% area fraction). Steel 1 without graphite was also austenitized at 830 °C for 10 minutes. Next, to measure the incubation and completion time, the sample was austenitized at 830 °C for five minutes and gas quenched to the isothermal transformation test temperature within the Bainite reaction range, and then held for a time long enough for the Bainite reaction to reach completion.

It is imperative to estimate the temperature range of Bainite reactions in order to design the experiments effectively. Usually, Bainite reaction range is designated by its upper limit, Bs, and lower limit, Ms temperatures. Therefore, it is necessary to estimate the Bs and Ms temperatures. In this research, the research used the modified equation based on the original formula by Kirkaldy and the formula originally proposed by Steven and Hayne[107]:

$$Bs = 830 - 270\,C - 90\,Mn - 37\,Ni - 70\,Cr - 88\,Mo \quad (4\text{-}3)$$

$$Bs = 637 - 58\,C - 35\,Mn - 15\,Ni - 34\,Cr - 41\,Mo \quad (4\text{-}4)$$

The higher value generated from Equation 4-3 and 4-4 was used in this research for the experimental design. The temperatures for conducting isothermal phase transformation measurements and the quantity of samples used at each temperature were then decided based on the calculated Ms and Bs temperatures.

The recorded temperature and dilation changes were then used for the determination of Bainite transformation incubation and completion times, using the commercial Kaleidagraph computer software program. A typical dilation versus time curve and a temperature versus time curve is shown in Figure 4-8. The isothermal holding was assumed to start when there is a sudden change in the slope of the measured temperature around the

programmed isothermal holding temperature. Ideally, the dilation curve should remain constant until a phase transformation occurs. However, there wa always certain degree of drifting in the dilation data because it takes time for the temperature distribution in the assumed isothermal cross section to become uniform. The minimum, D_{min}, and maximum, D_{max}, of dilation values after the start of isothermal holding were measured. The volume fraction is calculated according to the following equation:

$$f = (D - D_{min}) / (D_{max} - D_{min}) \quad (4\text{-}5)$$

where f_v is the volume fraction of transformed Bainite normalized by its equilibrium volume, D is the dilation at a given transformation temperature and time. In this study, the incubation time was designated as the holding time when f_v reaches 1%. The completion time was designated as the holding time when f_v reaches the value 99%.

4.4.2 Results And Discussion

4.4.2.1 TTT Curves

The Bainite TTT curves for steel 2 with 0.06% and 0.47% graphite are presented in Figure 4-9. The graphite content did not significantly influence the overall transformation kinetics. It is obvious that the curve shape did not vary with the volume fraction of graphite. The fastest Bainite transformation start points were at around 440 °C for both graphite levels. There were two noses in the transformation start curves, which were at around 350 °C and 400 °C for Steel 2 with 0.47% graphite, at around 320 °C and 380 °C for Steel 2 with 0.06% graphite. The corresponding nose locations were 20 °C apart for these two graphite levels, while there was a difference of 40 °C for the martensite transformation start points. The slowest finish temperature was at around 380 °C for Steel 2 with 0.47% graphite and at 320 °C for Steel 2 with 0.06% graphite. Also, the TTT curve for Steel 2 with 0.06% graphite in lower temperature was slightly moved to the right. After dissolving some graphite, the

carbon content in solid solution is increased. And thus, the number of carbon atoms involved in diffusion process of transformation is increased. For increasing temperature, carbon diffusion rates increase. Number of carbon atoms involved in diffusion process cannot significantly influence the overall transformation rates. Therefore, only the lower Bainite transformation rate is appreciably affected.

All the specimens were machined to the same width. Therefore, the effects of transformation temperatures and graphite contents on the volume of transformed austenite to Bainite could be studied by dilation versus transformation temperature curves, shown in Figure 4-10. For both graphite levels, the degree of Bainite transformation decreased with increasing isothermal transformation temperature. Above 450°C, no dilation was observed, indicating that the amount of Bainite transformation was negligible. The influence of transformation temperature was significant for the steel with low graphite content. At the lower transformation temperatures, more Bainite was transformed for steels with lower graphite content. However, at the higher transformation temperatures the steel with 0.47% graphite had a higher Bainite transformation fraction than did the steels with 0.06% graphite. Therefore, the curves of total expansion versus temperature showed a decreasing slope as a function of graphite levels, or say, showed an increasing slope as a function of carbon content in solid solution.

4.4.2.2 Bainite Transformation Kinetics

Various models have been proposed for describing isothermal transformation kinetics, such as Johnson-Mehl-Avrami (JMA)[56], Austin-Rickett (AR)[108], the time law for normal grain growth, and the kinetic function for homogeneous reactions. All these kinetic functions are usually composed of two factors: (i) the rate-time factor and (ii) the impingement factor related to the fraction untransformed. The transformation rate is small in the beginning, increases to the maximum, and then decreases to zero due to impingement effects. The above mentioned kinetic functions can be generated by introducing different impingement factors, which may allow for retardation in reaction rate due to the

impingement.

The JMA equation and AR equation which are commonly used for describing isothermal solid state transformation, are expressed as

$$df/dt = kn\,(1- f)(kt)^{n-1} \quad \text{(JMA)} \tag{4-6}$$

$$df/dt = kn\,(1- f)^2(kt)^{n-1} \quad \text{(AR)} \tag{4-7}$$

where $k = C \exp(-Q/RT)$, c is the pre-exponential factor, Q = the activation energy, t = time, R = the gas constant, T = the absolute temperature. The time exponent, n, is a parameter depending on the nucleation mechanism and the growth process. The term related to the fraction untransformed, $(1 - f)$ or $(1 - f)^2$, includes an impingement factor of 1 to 2 which is commonly used to correct some effects such as a depletion of solute content in untransformed matrix due to competitive growth of the reaction products, a direct collision of two advancing reaction products, or an exhaustion of nucleation sites.

Lee and Kim[109] introduced an impingement factor of modified form $(1-y)^{c+1}$ is introduced to obtain an isothermal transformation kinetic function which may replace these existing kinetic equations. This approach makes a mathematical expression integrable, and permits the clarification of the correlation between the transformation behaviors of these kinetic functions. The modified JMA / AR type transformation kinetic equation is written in the form

$$df/dt = kn\,(1- f)^{c+1}(kt)^{n-1} \tag{4-8}$$

where c is the impingement exponent. By a suitable choice of the impingement exponent, it is possible to account for a large portion of transformation with a constant n value.

AR Model

Recently, Lee and Kim[115] obtained several kinetic equations by introducing, in

addition to the parameters k(T) and n, an adjustable fitting parameter termed the "impingement factor," c. They showed that c=0 corresponds to JMA kinetics, while for c=1 the following equation was obtained

$$\alpha = 1 - \{[k(T)t]^n + 1\}^{-1} \tag{4-9}$$

To study the validity of AR equation and to compare it with the JMA theory, the ability of JMA and AR equation to fit experimentally obtained transformation curves of a large number of precipitation reactions, has been compared by Starink[110].

JMA model

A well-known procedure is plotting of ln [ln $(1 - f)^{-1}$] versus ln t; from the slope of straight line obtained, a value of n can be derived, while a value for k follows from the part cut from the ordinate. Today many numerical analysis software programs can calculate n and k by directly curve fitting transformation curves into the JMA equation. Simply guessing a set of n, k values as an initial condition, and the iterating will give the best fit.

The ability of JMA and AR equation to fit experimentally obtained curves have been compared, shown in Figure 4-11. Normally, to compare kinetics equations with experimental data, the main requirements for experimental data are

(1) Transformation data should be available over the entire transformation range.

(2) Scatter should be low.

(3) Transformation curves should be sigmoidal.

In this study, all the tests were held long enough to reaction completion. The sensitivity and high sampling rates of Gleeble assured that the record transformation curves were smooth and reflected the real characteristics of Bainite transformations. The curve fitting results suggested that JMA equation is more appropriate for the study of Bainite transformation reactions. It can be seen that the predicted transformation curve based on JMA model exactly followed the experimental curve and the regression coefficient R for

JMA model were slight higher than that for AR.

Time exponent n

The time exponents, n, in JMA and AR model were given in Table 4-7 and Figure 4-12 for two graphite levels. It has been observed that the time exponent n was not sensitive to the graphite content. For the sample with only 0.06% graphite, the incubation time of Bainite transformation was still very short. Generally as the carbon content in solid solution increases, the reaction rate drops, because more carbon atoms are involved in the diffusion process. However, for Steel 2, it seems that the Nb(C, N) has a significant effect on the overall Bainite transformation kinetics by comparing the TTT curves of Steel with 0.06% Graphite and Steel 1 with no graphite. In Steel 2, Nb (C, N) served as both graphite nucleation sites as shown in chapter 2. Nb(C, N) may also serve as Bainite nucleation sites. The Bainite nucleation sites and their number was not influenced by the graphite dissolution process variations because Nb(C, N) only can be dissolved at the temperature above 1250 °C.

From the study of upper Bainite transformation of a cast steel with B+G+A microstructure[111], it was found that all the carbon enriched in a retained austenite diffuses from ferrite supersaturated with carbon but not from graphite. The matrix is expected to contain no carbide until the carbon-enriched retained austenite decomposes. When the carbon-enriched retained austenite begins to decompose, the lattice constant of bainitic ferrite increases. The decomposition seems to form carbide and ferrite supersaturated with carbon. At lower Bainite transformation temperatures, the carbon enrichment in retained austenite occurs in the same ways as at upper Bainite transformation temperature. However, the enrichment requires a longer transformation time because of a lower carbon diffusion rate. Therefore, carbides precipitate from the carbon enriched retained austenite in upper Bainite transformation and from the ferrite supersaturated with carbon in lower Bainite transformation. Graphite doesn't participate in Bainite transformation.

4.4.2.3 Bainite Hardness

Figure 4-13 shows the hardness as a function of graphite content, alloy elements, and transformation temperature. The hardness decreases as the increasing of transformation temperature, graphite content. Steel 1 without any graphite had a significantly higher hardness than steel 2. For steel 2, the sample with more graphite had lower hardness. For either lower Bainite or upper Bainite, the effect of graphite amounts on hardness was almost the same.

The hardness of Bainite was primarily dependent on the chemical composition and the mean transformation temperature. The hardness of Bainite was examined for a range of transformation temperatures and several steels with varying chemical composition. The hardness of the bainitic steel was a function of the isothermal transformation temperature and its variation has been correlated with the transformation behavior.

The hardness of Bainite was independent of prior austenite grain size, even the latter influences the Bainite sheaf thickness[100]. This was not expected since the Bainite subunit size is hardly influenced by the austenite grain size. Since the subunits are much smaller, they exert an overriding influence on strength. This conclusion is consistent with Irvine's observation that the hardness of fully Bainite microstructure is not sensitive to the austenitizing temperature[112]. Therefore, the hardness difference between the steels austenitized at 1000 °C for 30 minutes and 830 °C for 10 minutes should be only due to the graphite content.

A Bainite hardness prediction model has not been well established. Terasaki[113] developed a simple empirical model for predicting the hardness in the neighborhood of the weld heated affected zones:

$$Hv = 150 + 188\, C_{EQ} \tag{4-10}$$

$$C_{EQ} = C + \frac{Si}{3} + \frac{Ni}{26} + \frac{Cr}{9} + \frac{Mo}{3} + V \tag{4-11}$$

where Hv is the Vicker's Hardness, C_{EQ} is the carbon equivalent.

Yurioka et al [114] proposed two predictive equations:

$$Hv = 117 + 197\, C_{EII} \qquad (4\text{-}12)$$

$$(C_{EII} \leq 0.075\%)$$

$$Hv_B = 145 + 130 \tanh (2.65 C_{EII} - 0.69) \qquad (4\text{-}13)$$

$$(C_{EII} \geq 0.075\%)$$

$$C_{EII} = C + \frac{Si}{24} + \frac{Mn}{5} + \frac{Cu}{10} + \frac{Ni}{18} + \frac{Cr}{5} + \frac{Mo}{2.5} + \frac{V}{5} + \frac{Nb}{3} \qquad (4\text{-}14)$$

As the relationship between transformation temperatures and Bainite hardness cannot be shown as function formulae, regression equations are derived:

Steel 1(0.65% C) with no graphite:

$$\text{Knoop} = 1373 - 3.52\, T + 2.8 \times 10^{-3}\, T^2, \quad R=0.993 \qquad (4\text{-}15)$$

Steel 1 (0.66% C) with no graphite:

$$\text{Knoop} = 1484 - 3.92\, T + 3.2 \times 10^{-3}\, T^2, \quad R=0.997 \qquad (4\text{-}16)$$

Steel 2 (0.67% C) with 0.47% graphite:

$$\text{Knoop} = 1424 - 4.36\, T + 4.2 \times 10^{-3}\, T^2, \quad R=0.994 \qquad (4\text{-}17)$$

Steel 2 (0.67% C) with 0.06% graphite:

$$\text{Knoop} = 1256 - 3.28\, T + 3.2 \times 10^{-3}\, T^2, \quad R=0.975 \qquad (4\text{-}18)$$

where T is the transformation temperature. It can be seen that Eq. (4-15) - Eq.(4-18) have a correlation coefficient more than 0.97. Future work might study how these equations are related to carbon equivalent.

The hardness is generally greater than the value than Yurioka's model and Terasaki's model predicted, especially at low transformation temperatures. The hardness of steels agrees with these two models only at high transformation temperatures. The relationship between transformation temperature and Bainite hardness of high strength steels can be perfectly described by a second order polynomial equation.

4.5 FRACTURE TOUGHNESS EVALUATION

4.5.1 Experimental Procedures

The single edge cracked plate tension specimen (SECT) shown in Figure 4-14 was used for fracture toughness tests[115]. This specimen is more efficient than the symmetrically cracked specimen with respect both to the material and required loading capacity. The single edge notch with 0.075 mm root radius was machined by electric discharge machining. The specimen thickness is 0.06 inch. The total crack length over specimen width, a/W, was controlled between 0.45 and 0.55 as the ASTM suggested[117].

Gross[116] obtained an analytical solution for the stress distribution in the SECT specimen by means of a boundary value collocation method, and provided a suitable expression for the stress intensity factor K_I. The toughness K_Q can be calculated by the following equation:

$$K_Q = \frac{P_f}{BW}\sqrt{\pi a}\,Y\left(\frac{a}{W}\right) \qquad (4\text{-}19)$$

where P_f is the load at failure, W and B are specimen width and thickness, respectively, a is crack length, and

$$Y\left(\frac{a}{W}\right) = 1.12 - 0.231\frac{a}{W} + 10.55\left(\frac{a}{W}\right)^2 - 21.72\left(\frac{a}{W}\right)^3 + 30.29\left(\frac{a}{W}\right)^4 \quad (4\text{-}20)$$

In order to make a precise comparison of the fracture toughness obtained on each steel, it is necessary to take into account the strength variation. To do this it is satisfactory to express the results in terms of the parameter $(K_Q/\sigma_{ys})^2$. This parameter is measured in inches and is a function of the critical defect size which the material will withstand when the gross stress approaches the yield strength. In this work, materials are heat treated to the same hardness and thus the same yield strength. Therefore, the K_Q values can be directly used to compare the fracture toughness. The relationship between hardness and yield strength of steel can be expressed by the empirical equation[117]:

$$\sigma_{ys}(ksi) = 0.145*[3.25*HV(10kg) - 349] \quad (4\text{-}21)$$

where HV(10 kg) is Vickers hardness number using a 10 kg load. The calculated yield strength agreed with measured value very well. In this work, the calculated yield strength values were used for thickness validity examination.

One as-received specimen was used to study the graphite failure mode when tested in the cold worked and annealed condition. To study the effect of graphite content on Bainite fracture toughness, eight specimens were austenitized at 830 °C for different times, and helium quenched to 330 °C, then held at 330 °C for 10 minutes. To study the effect of graphite content on fracture toughenss of quenched and tempered steels, eight specimens were austenitized at 830 °C for different time, then helium quenched to room temperature. To lower the martensite strength level, and avoid temper martensite brittleness (200 - 350 °C) and tempering brittleness (450 - 650 °C), the tempering treatment was chosen as 425 °C for 30 minutes. The heat treatment schedule is presented in Table 4-8.

Fatigue precracking was carried out in an Instron machine of a capacity of 20,000 pounds under tension-tension conditions using a sine wave. The load ratio R was kept below 0.1. Fracture toughness tests were carried out using the same Instron machine at 0.01 inch/sec displacement speed under room temperature. The load output was recorded by a

computer via a Keighley Asyst Viewdac 2.0 software system. Viewdac is an integrated software system for data acquisition, process control, and data processing. The sampling rate is 500 hertz. Crack size, a, at the onset of fracture was measured by a traveling microscope with a resolution of 0.0001 inch.

Fractographic examinations were conducted by a ZEISS Secondary Electron Microscope at 25 KV. For each specimen of Steel 2 the region adjacent to the fatigue precrack was examined, since this is the region of crack initiation during fracture toughness tests.

The fracture surfaces of steel 1 were examined. Due to limited material availability, the fracture surfaces was prepared by the following method:

(1) A 0.5 mm notch was made by saw-cutting at the center of a piece of Steel 1 (10 mm × 5 mm× 1.5 mm)

(2) Wedged the notch open with a split pin inserted into the specimen mouth.

This method generated the same failure mode as fracture toughness tests used for Steel 2.

4.5.2 Results

The load-time curve for the as-received specimen of Steel 2, shown in Figure 4-15, indicated that the specimen had good ductility. This curve represents the load- displacement behavior because the test was operated under displacement control and constant crosshead displacement was used.

The fracture surfaces of Steel 1 and Steel 2 in the cold worked and annealed condition were shown in Figure 4-16 and 4-17, respectively. It can be seen that for both steels the graphite broke into pieces but no interface debonding was observed, which is different with the failure mode in cast iron. In cast iron, the failure is initiated at the graphite/iron interfaces[118, 119]. The fatigue fracture surface in the precrack region of steel 2 is shown in Figure 4-18. It is obvious that the graphite particles on the fatigue fracture surfaces were not as many as in the final break region and few graphite particles were broken. Therefore, in the

final break region, the crack propagation depends on the coalescence of void formed by graphite breaking; in the fatigue region, the graphite content is not the only variable for controlling the crack growth path and rate.

The fracture toughness testing results for tempered martensite and Bainitic samples are listed in Table 4-8 and 4-9, respectively. Graphite content did not significantly affect the fracture toughness. Graphite is a weak phase and could be a crack nucleation site. On the other hand, after the graphite dissolution, the carbon content in the matrix was increased and the matrix became more brittle. Therefore, the fracture toughness did not improve too much by graphite dissolution.

4.6 CONCLUSIONS

1. This work confirmed that graphite can be dissolved by controlling the austenitizing conditions. As the austenitizing temperature and time increased, the volume fraction of graphite decreased. Graphite can be completely dissolved by austenitizing at 1000 °C for more than 30 minutes.
2. Martensite transformation start temperature decreases with decreasing graphite volume fractions.
3. Martensite hardness increased as graphite content decreased.
4. Bainite TTT curves for steels with and without graphite were established in this work. Analysis in terms of the AR and JMA yields values of the time exponent n in the range of 2 to 3 and 1 to 2, respectively.
5. Graphite content did not significantly influence Bainite transformation kinetics, but affected the fraction of transformed Bainite. It has been observed that transformation fraction decreased as the transformation temperature increasing. In the lower Bainite regime, more Bainite was formed in the low graphite steel. However, in the upper Bainite regime, more Bainite was formed in the high graphite content steel.
6. Bainite hardness depends on both transformation temperatures, graphite content,

alloy composition. The less graphite, the higher the Bainite hardness. The relationship between transformation temperature and Bainite hardness of high strength steels can be perfectly described by a second order polynomial equation.

7. The failure mode of graphite in fracture toughness testing showed that the graphite had very good bonding condition with matrix. No interface debonding was observed.
8. The fracture toughness of Bainite and martensite did not significantly affected by graphite dissolution process. Although graphite is a weak phase in steels, the matrix brittleness increased by graphitic carbon dissolving into solid solution.

Table 4-1 **Effect of austenitizing conditions on graphite area fraction, number, total length in Y direction (parallel to rolling direction) and X direction (against rolling direction).**

Austenitizing condition		Graphite, %		No. of Graphite		X length		Y Length	
Temp., C	Time, min								
As Received		0.9246 1.0582	**0.9914**	80.8 75.1	**78**	204.1 209.0	**206.6**	234.4 241.2	**237.8**
830	5	0.8788 1.0128	**0.9458**	93.2 103.6	**98**	193.4 219.1	**206.3**	233.1 267.0	**250.1**
	10	0.4295 0.5081	**0.4688**	84.9 84.9	**85**	128.5 147.1	**137.8**	155.7 174.8	**165.3**
	30	0.4576 0.4098	**0.4337**	48.9 44.7	**47**	104.9 91.70	**98.3**	124.2 112.9	**118.5**
	60	0.3321 0.2694	**0.3008**	46.1 44.7	**45**	91.53 78.53	**85.0**	104.5 85.15	**94.83**
1000	5	0.8464	**0.8464**	99	**99**	197.7	**197.7**	226.9	**226.9**
	30	0.0425 0.0713	**0.0556**	19.1 25.4	**22**	18.60 36.61	**27.61**	18.12 41.94	**30.03**

Table 4-2 Standard deviation, 95% confidence limit and relative accuracy for graphite area fraction measurements.

Austenitizing condition		Graphite, %				
Temp., C	Time, min	Two sets of 15 fields	Avg.	STD	95%CI	RA, %
As Received		0.9246 1.0582	**0.9914**	**0.2249**	**0.08353**	**8.43%**
830	5	0.8788 1.0128	**0.9458**	**0.2736**	**0.1016**	**10.0%**
	10	0.4295 0.5081	**0.4688**	**0.1099**	**0.04082**	**8.71%**
	30	0.4576 0.4098	**0.4337**	**0.1566**	**0.05816**	**13.4%**
	60	0.3321 0.2694	**0.3008**	**0.1216**	**0.04516**	**15.0%**
1000	5	0.8464 (30 fields)	**0.8464**	**0.2524**	**0.09374**	**11.1%**
	30	0.0425 0.0713	**0.0556**	**0.0329**	**0.01223**	**22.0%**

STD: Standard deviation
Avg: Average

Figure 4-3 Martensite transformation start points and martensite hardness dependence on austenitizing conditions.

Temperature	Time, min	Graphite %	Ms, °C	Hardness, HRC	Knoop
830 °C	5	0.95	320	50.5	550
	30	0.43	323	53.5	603
	60	0.30	309	55.5	641
	120	-	296	55.5	641
1000 °C	5	0.85	300	55	628
	30	0.06	280	58	696
	60	-	292	58	687
	120	-	301	58	694

Table 4-4 Predicted and measured Ms and calculated Bs temperatures.

Steel	Ms,°C		Bs, °C	
	Eq.(4-4)	Experiment	Eq. (4-5)	Eq. (4-6)
Steel 2 (0.06% Graphite)	275*	305	579*	567
Steel 2 (0.047% Graphite)	275*	280	579*	567
Steel 1 (without Graphite)	275	260	586	573

* Assume the Nb has the same effect as Cr

Table 4-5 Incubation and completion time of Bainite transformation of Steel 2.

Steel 2 with 0.47 % graphite			Steel 2 with 0.06 % graphite		
Temperature	Incubation	Completion	Temperature	Incubation	Completion
324	1.030	84.77	294	2.100	110.0
354	0.594	90.20	324	1.760	195.0
384	0.990	95.20	354	2.100	113.0
397	0.7818	53.67	384	0.6083	67.10
414	1.080	44.50	417	0.9675	29.03
443	0.4977	17.50	440	0.2211	24.61

Table 4-6 Effect of transformation temperature and graphite volume fraction on shape constant n in JMA and AR models.

Graphite area fraction	Transformation Temperature					
	300 °C		325 °C		354 °C	
	JMA	AR	JMA	AR	JMA	AR
0.95 %	-	-	1.46	2.35	1.40	2.18
0.06%	1.29	2.06	1.46	2.38	1.40	2.26
Graphite area fraction	384 °C		415 °C		445 °C	
	JMA	AR	JMA	AR	JMA	AR
0.95 %	1.61	2.75	1.69	2.74	2.07	3.28
0.06%	1.42	2.33	1.92	3.07	1.82	2.92

Table 4-7 Bainite Hardness as a function of Bainite Transformation temperature and graphite contents.

Austenitizing	Graphite %	Hardness (knoop) under different Transformation Temperatures					
		300 °C	330 °C	360 °C	390 °C	420 °C	450 °C
830 °C for 10 min	0.47	-	454	397	366	343	308
1000 °C for 30 min	0.06	527	477	462	390	347	352

Table 4-8 Heat treatment schedule and fracture toughness testing results for tempered martensite.

Step 1 Quench to vary graphite content			Step 2 Tempering		Fracture testing
Temp, °C	Time, min	Graphite, %	Temp, °C	Time, min	$K_{max,}$ ksi-in$^{1/2}$.
830	5	0.95	425 °C	30	82.4
	30	0.47	425 °C	30	79.8
	60	0.30	425 °C	30	81.0
	120	-	425 °C	30	84.1

Table 4-9 Heat treatment schedule and fracture toughness testing results for Bainite.

Step 1 Quench to vary graphite content			Step 2 Bainite transformation		Fracture testing
Temp, °C	Time, min	Graphite, %	Temp, °C	Time, min	K_{max}, ksi-in$^{1/2}$.
830	5	0.95	330 °C	10	68.0
	30	0.47	330 °C	10	72.4
	60	0.30	330 °C	10	69.8
	120	-	330 °C	10	76.3

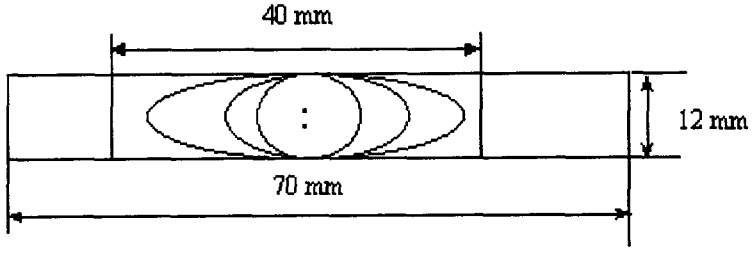

Figure 4-1 Gleeble specimen configuration for graphite dissolution, Bainite and martensite phase transformation studies.

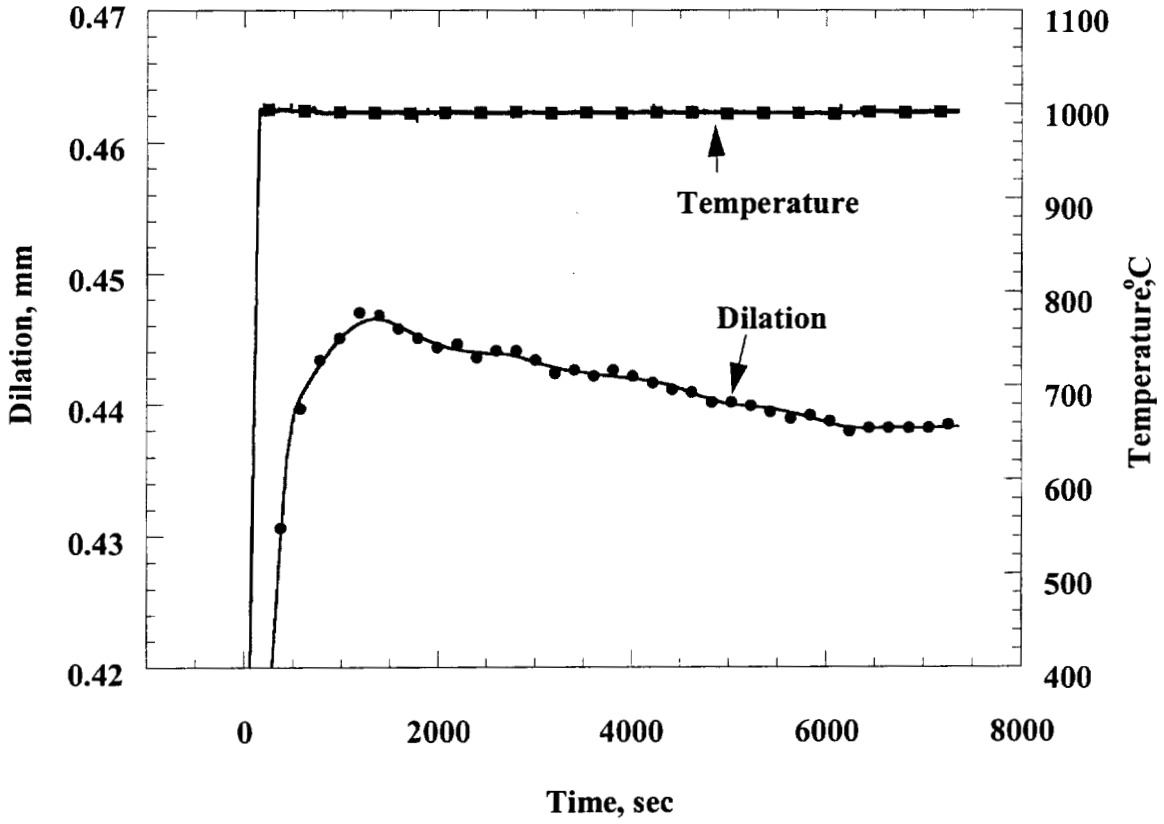

Figure 4-2 **Specimen shrinkage during graphite dissolution treatment at 1000°C for two hours.**

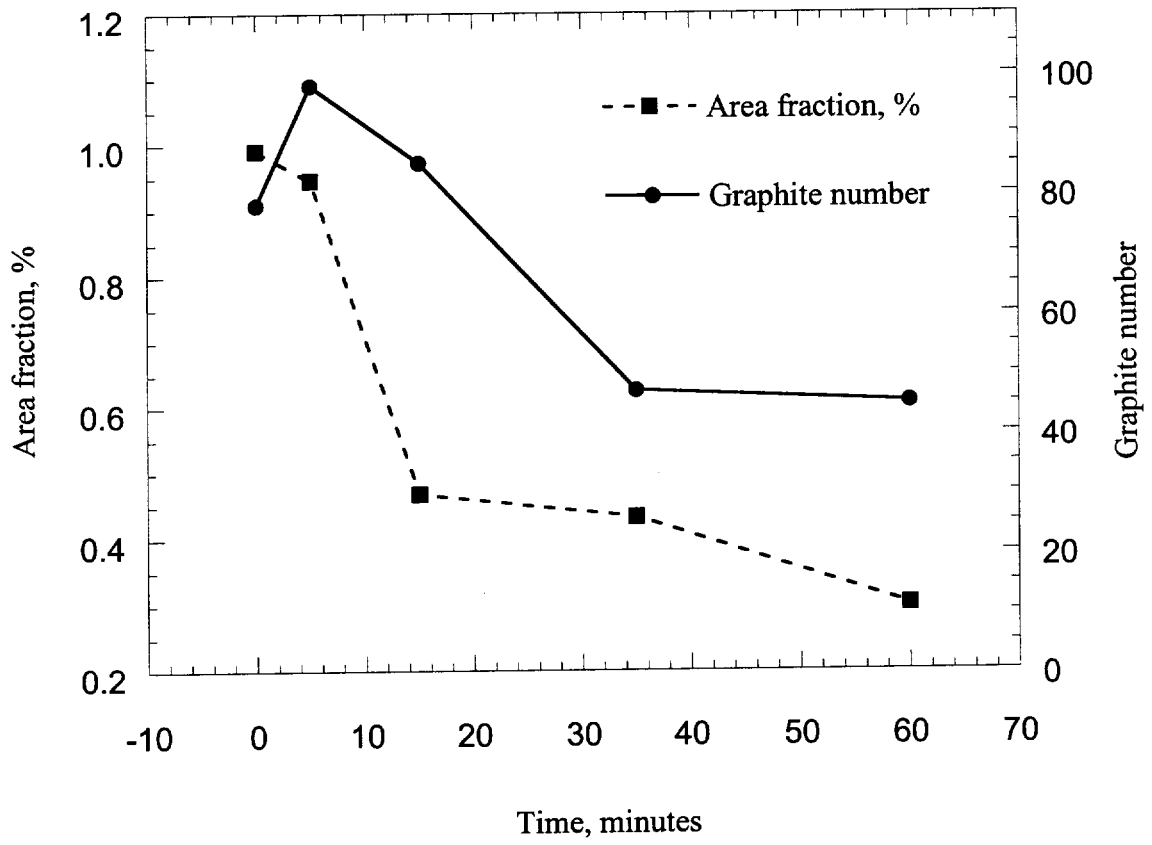

Figure 4-3 Graphite content as a function of austenitizing time at 830 °C.

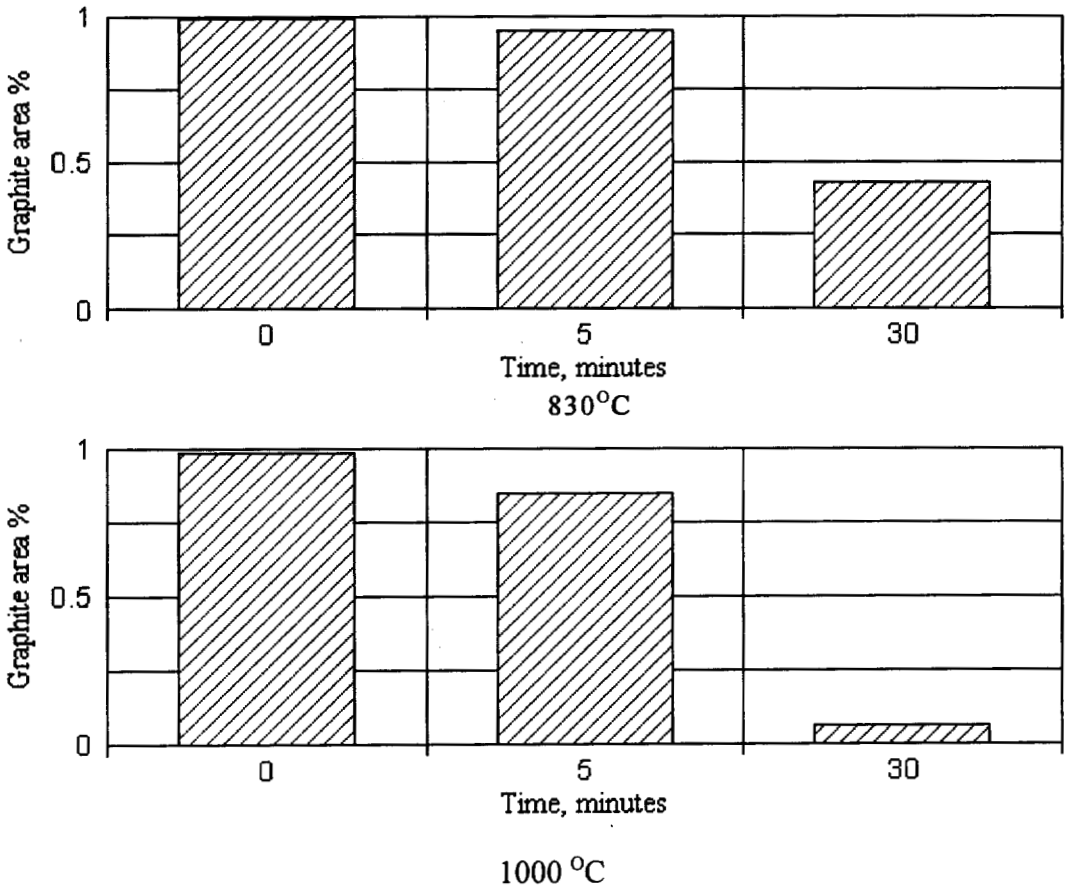

Figure 4-4 Graphite content as a function of dissolving temperature and time.

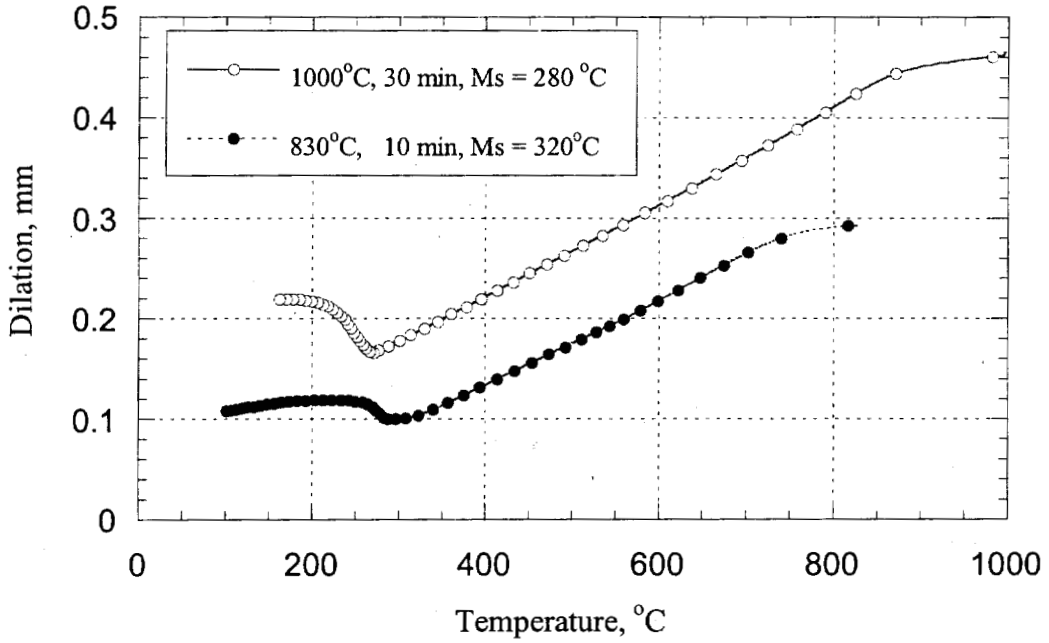

Figure 4-5 Dilation versus temperature curves for the quench processes of Steel 2 austenitizing at 1000 °C for 30 minutes and 830 °C for 10 minutes.

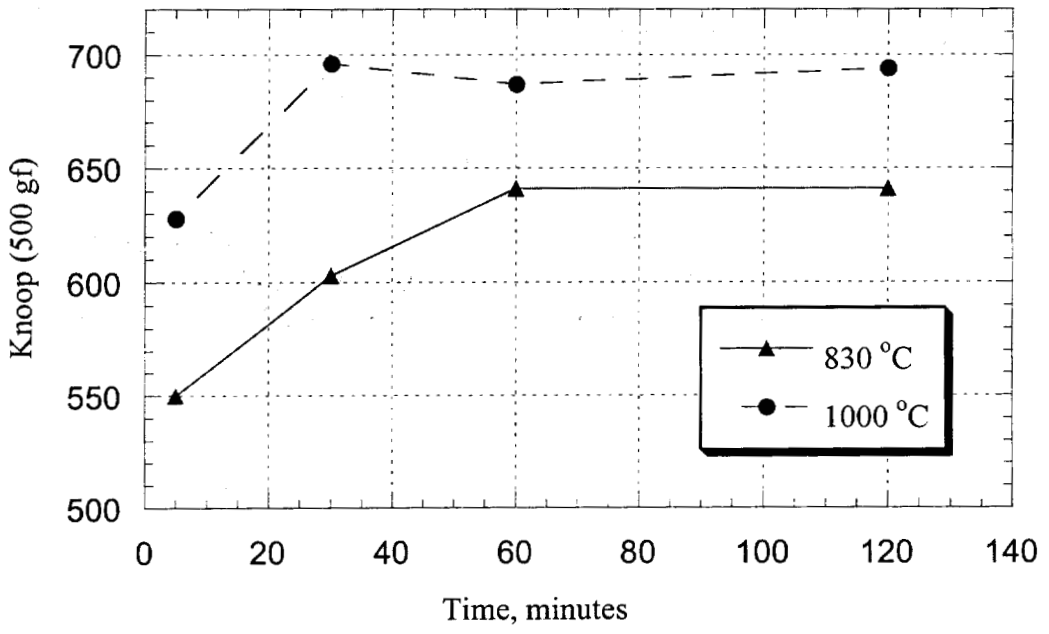

Figure 4-6 Martensite hardness as a function of austenitizing time and temperatures

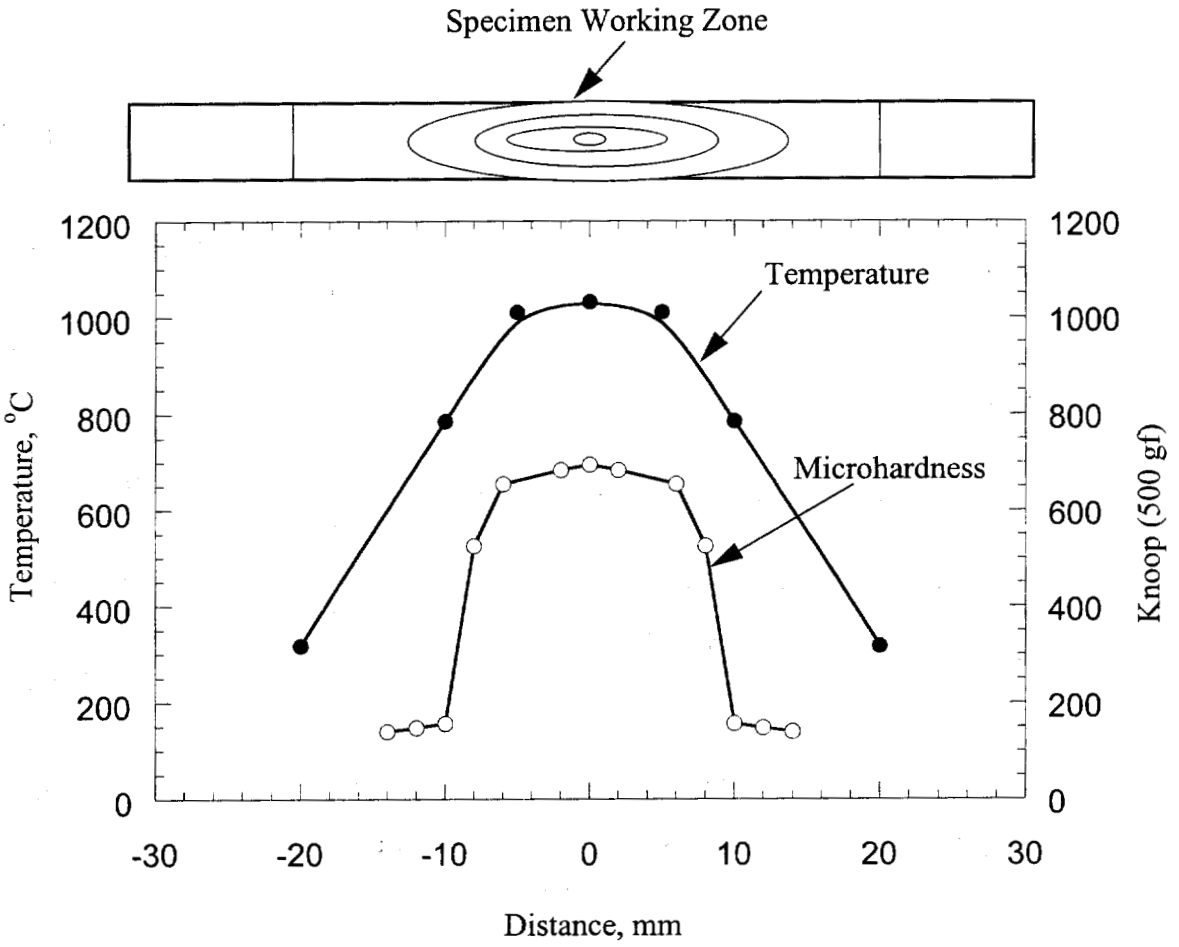

Figure 4-7 Austenitizing temperature profile and martensite hardness profile along the longitudinal cross section of a Steel 2 Gleeble sample austenitized for 30 minutes.

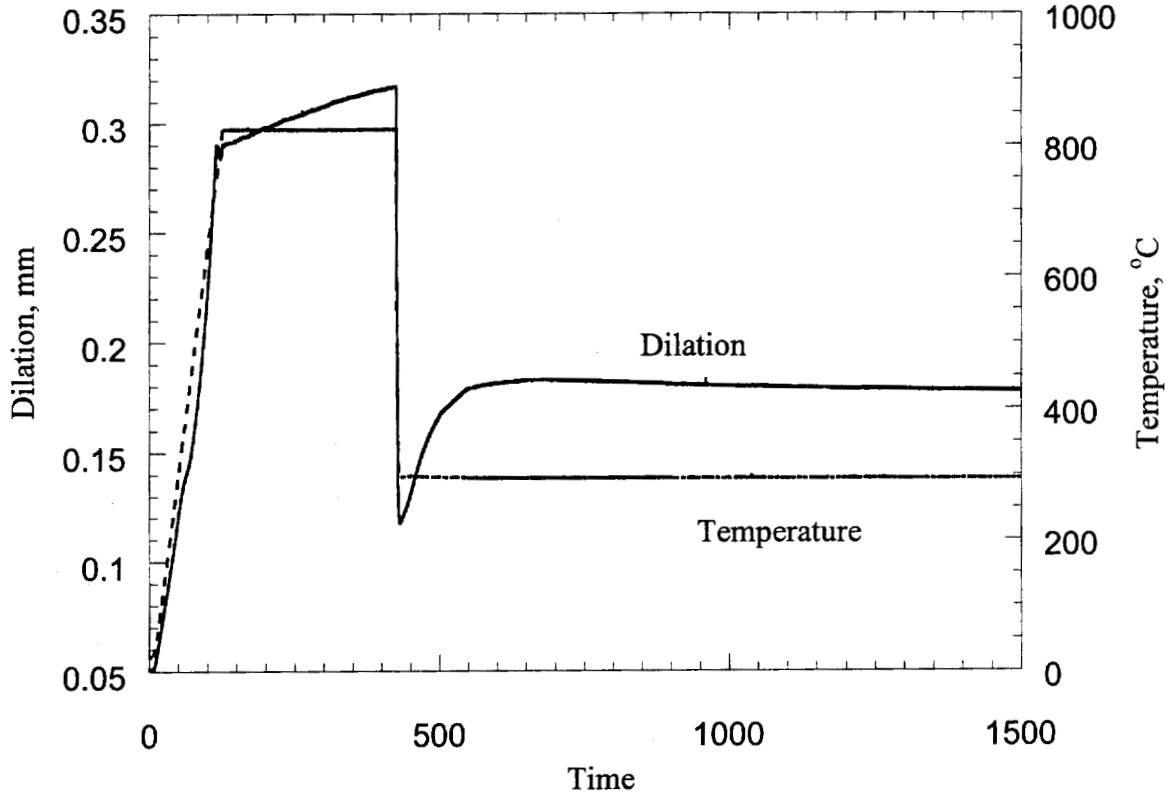

Figure 4-8 Typical dilation and temperature versus time curves.

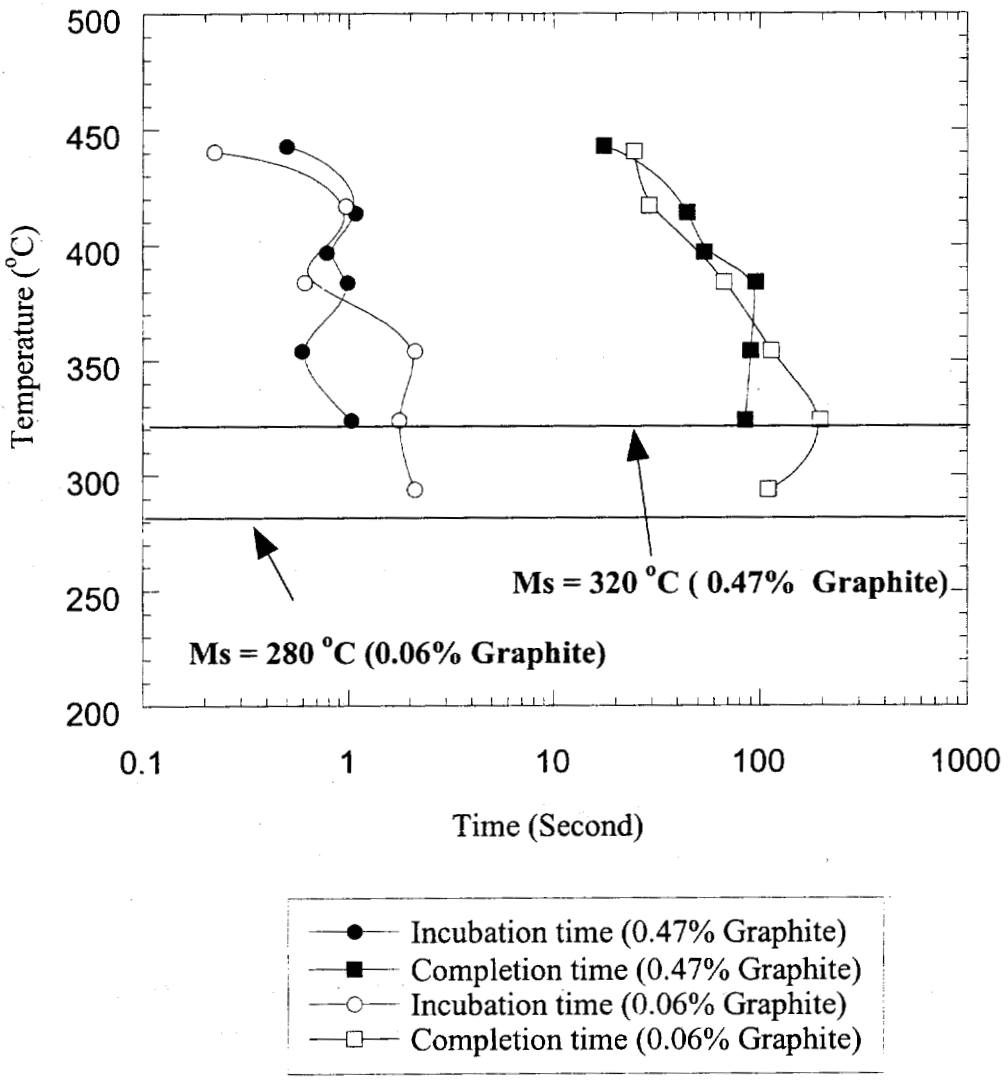

Figure 4-9 Bainite transformation TTT curves for Steel 2 with 0.06% and 0.47% graphite .

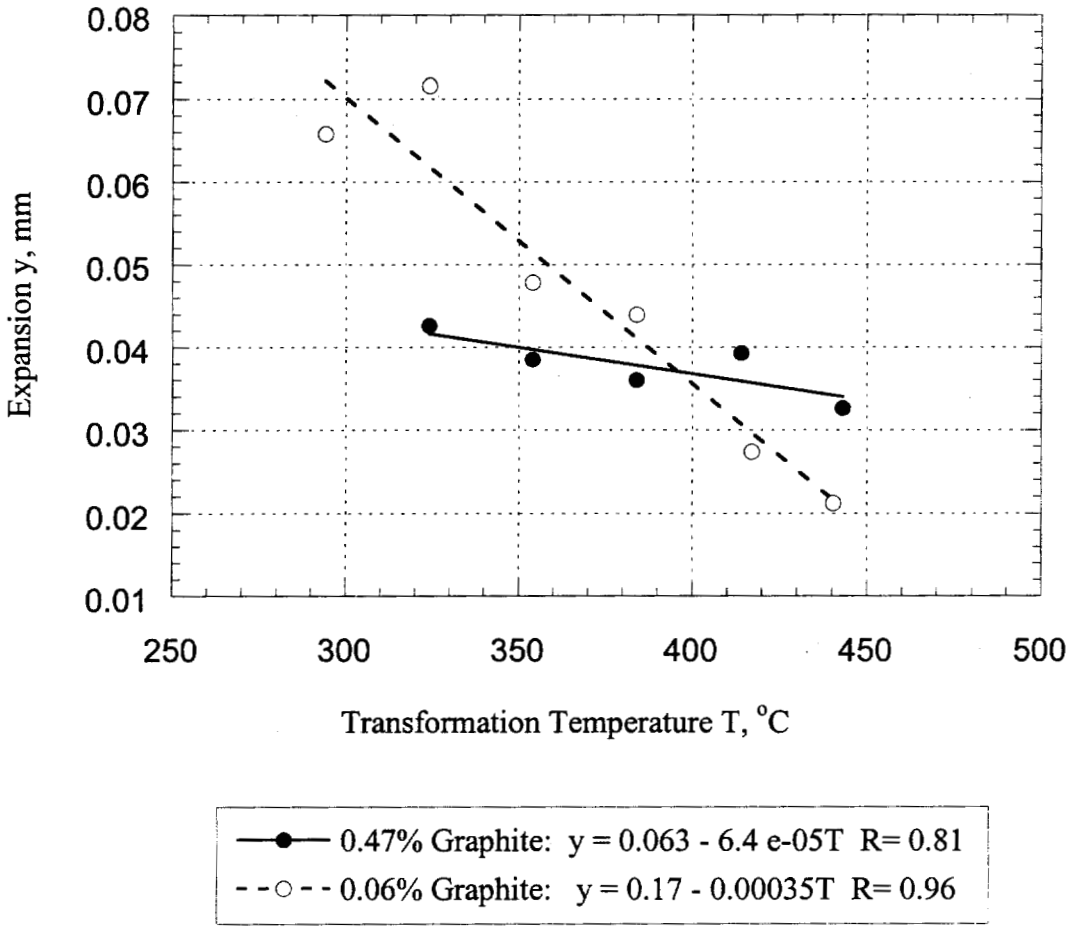

Figure 4-10 Expansion versus Bainite transformation temperature curves for Steel 2 with two graphite levels

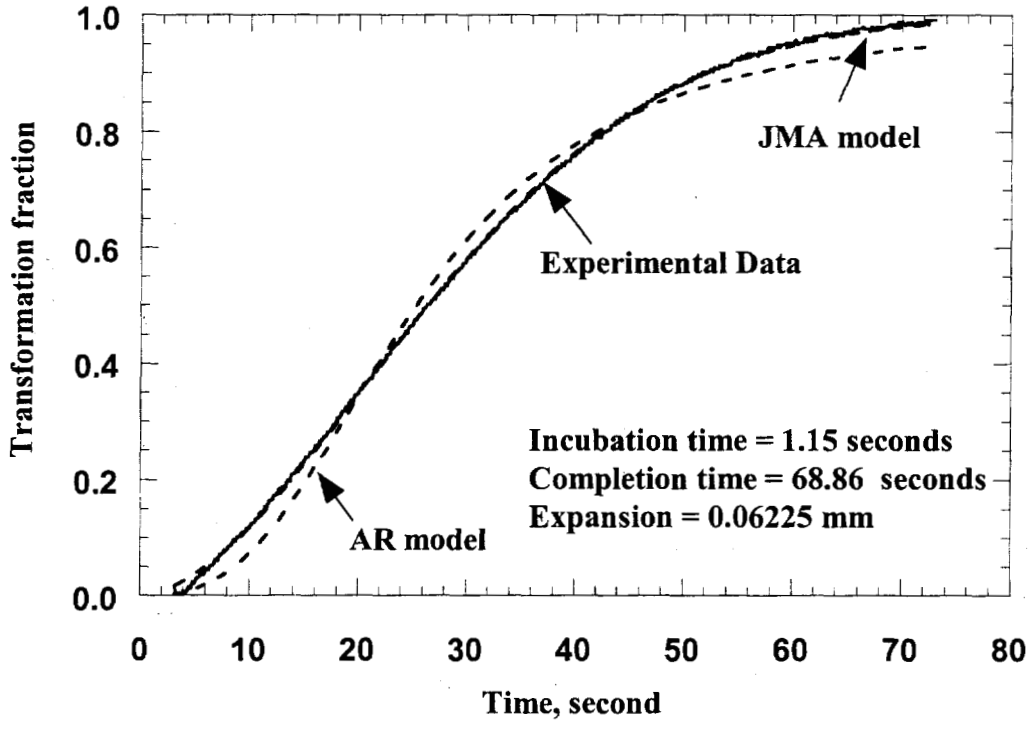

JMA: $f_v = 1-\exp(-m1*t^{m2})$		
	Value	Error
m1	0.0021071	2.0073e-05
m2	1.7704	0.0027071
Chisq	0.011602	NA
R	0.99986	NA

AR: $f_v = 1-((m1*m0)^{m2}+1)^{-1}$		
	Value	Error
m1	0.039452	0.00015388
m2	2.7463	0.025901
Chisq	0.41625	NA
R	0.99514	NA

Figure 4-11 Comparison of experimental Bainite transformation fraction versus time curve at 385 °C with model predictions.

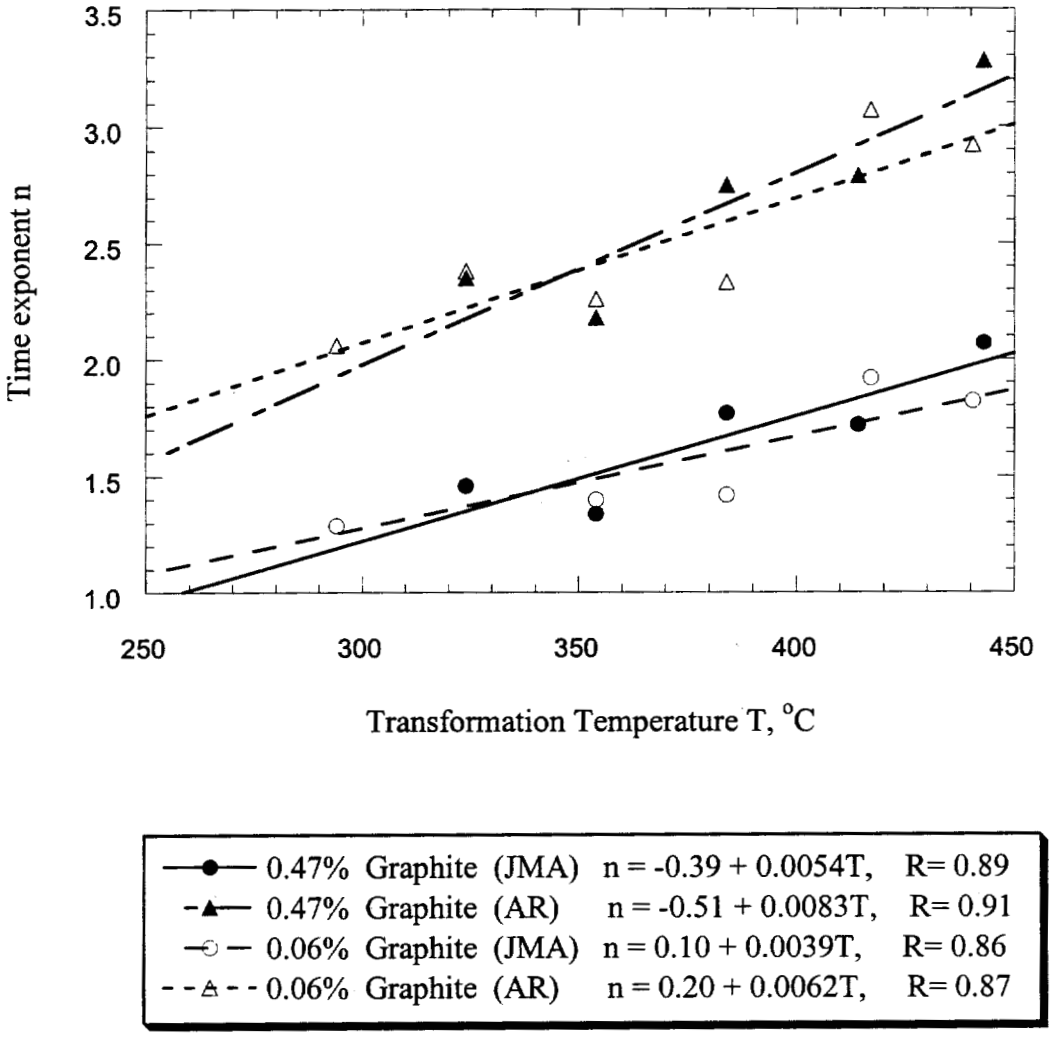

Figure 4-12 Time exponent n in JMA model and AR model for Steel 2 with two graphite levels

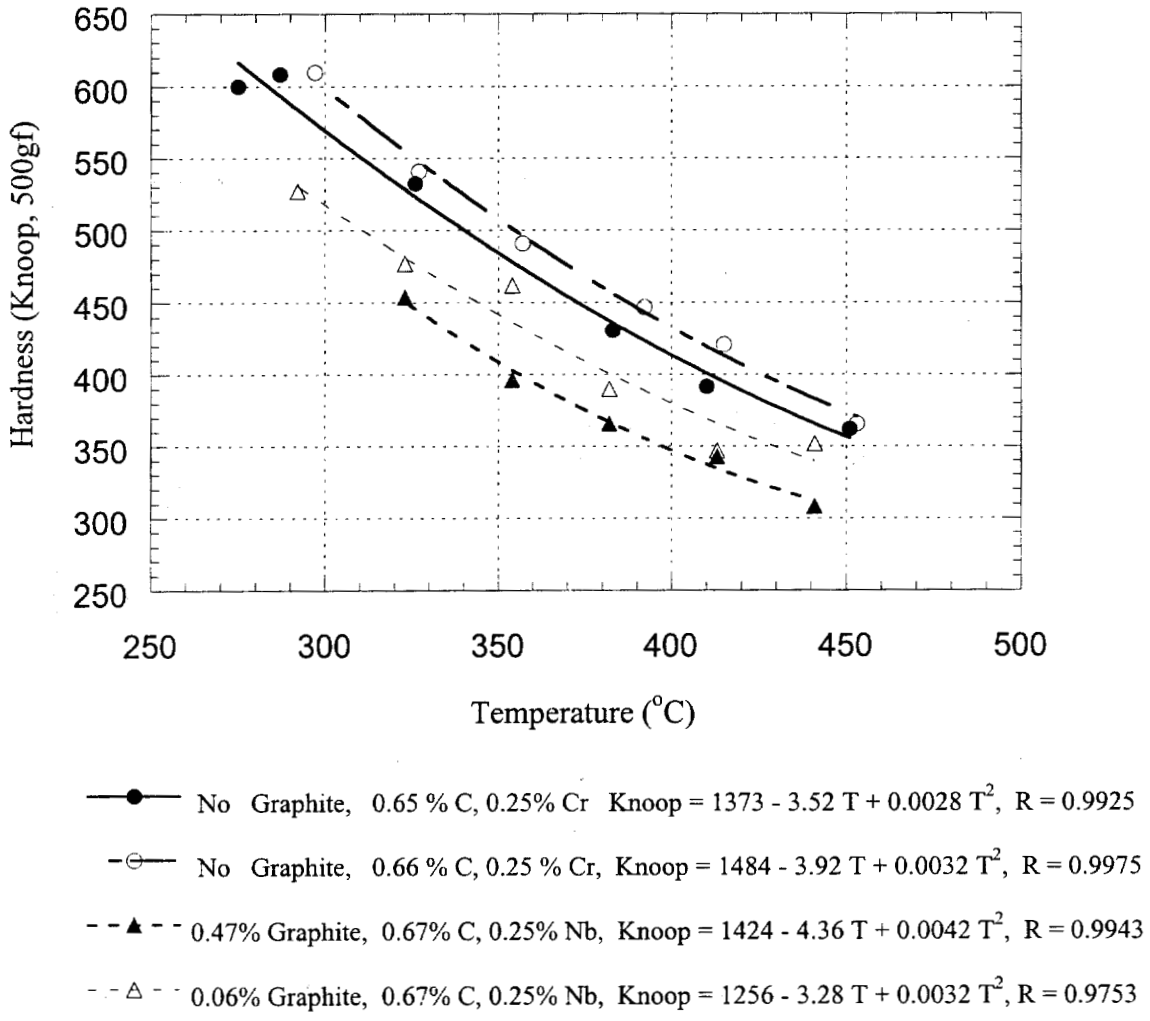

Figure 4-13 Bainite hardness as a function of graphite content, chemical composition and transformation temperature.

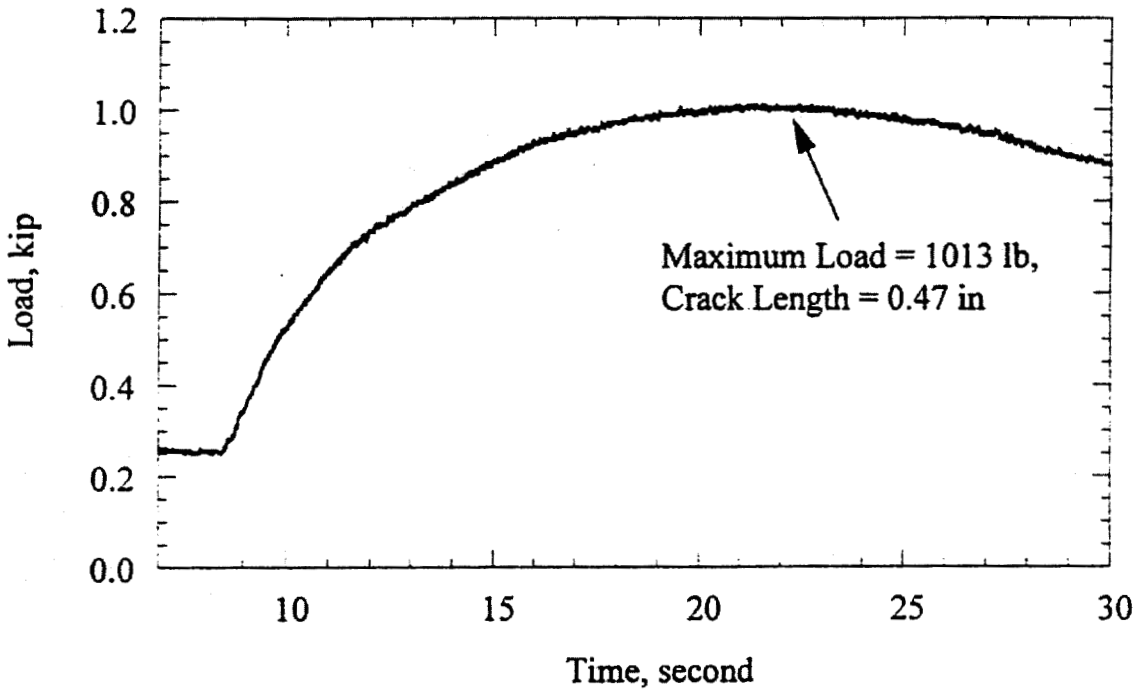

Figure 14 **Load-time curve for the fracture toughness testing using cold worked and annealed Steel 1.**

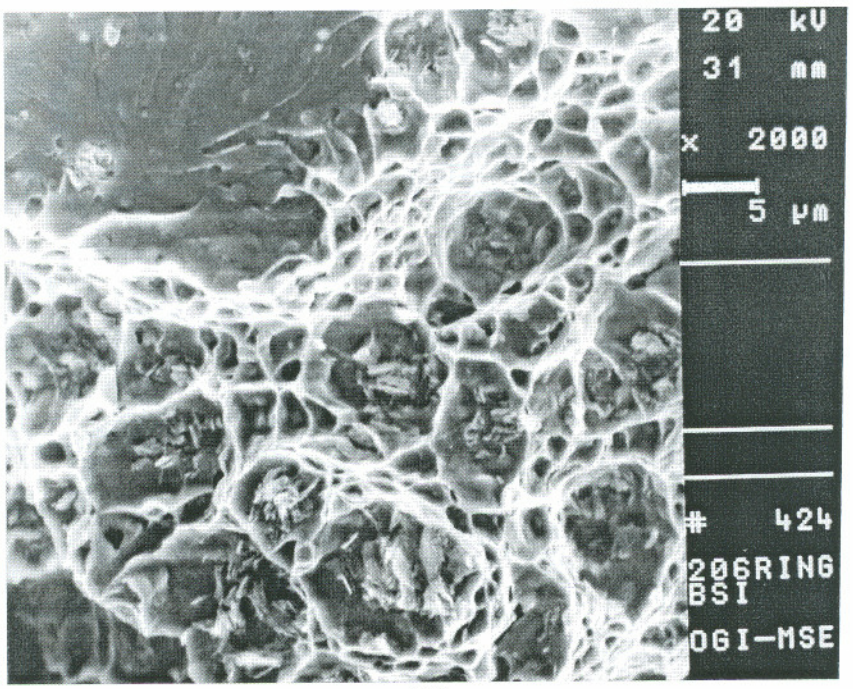

(a)

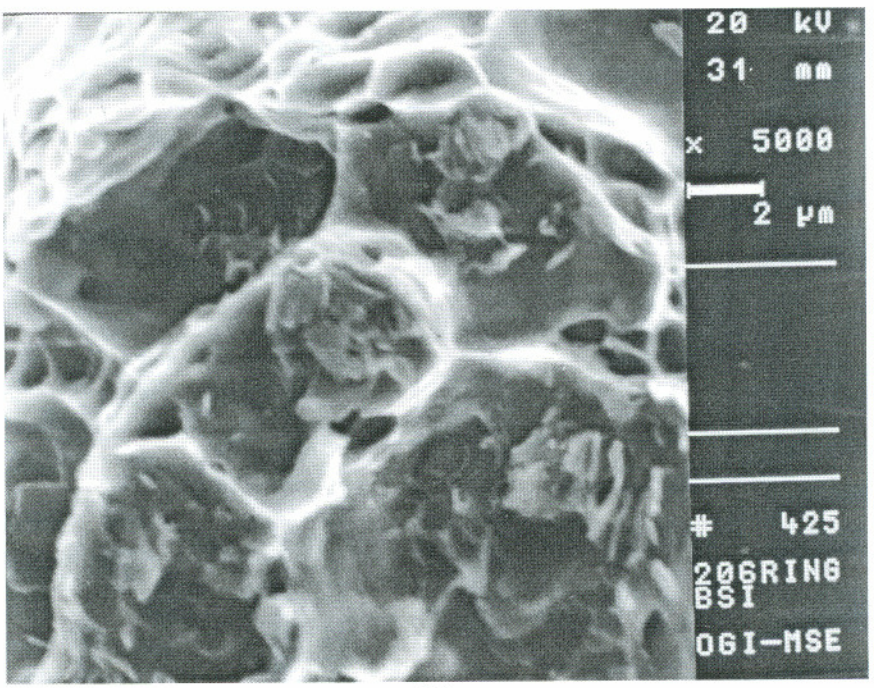

(b)

Figure 4-15 Fracture surfaces of Steel 1.

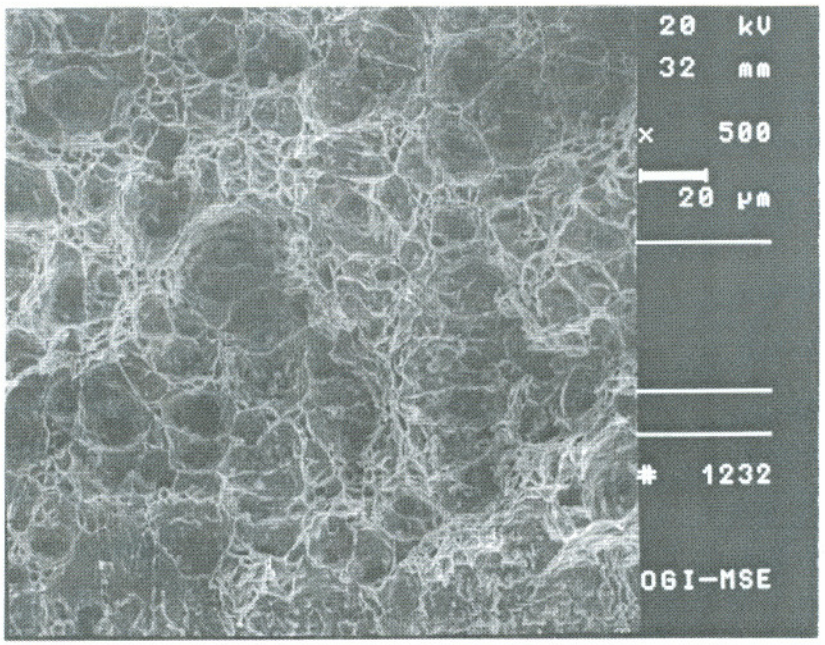

(a)

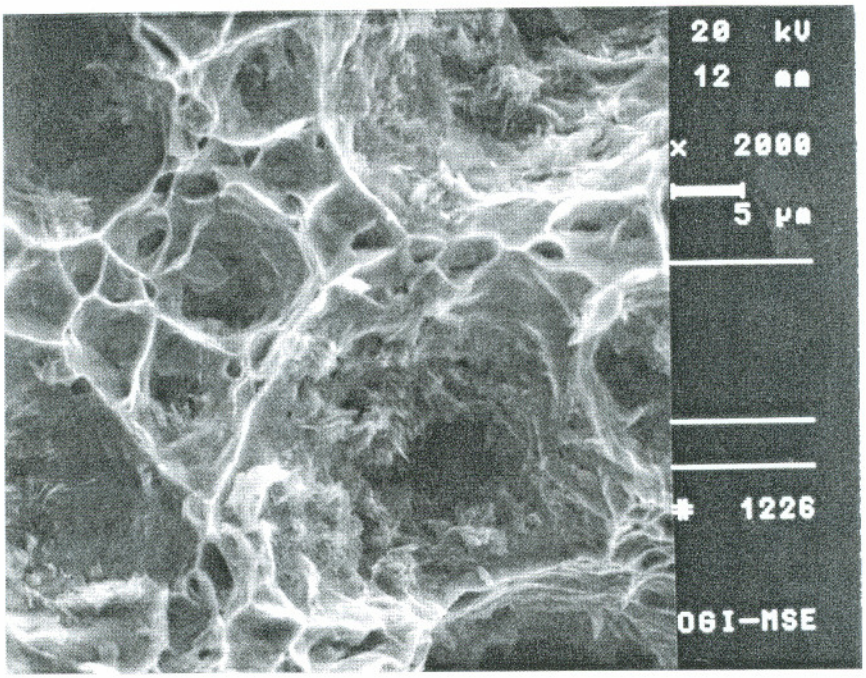

(b)

Figure 4-16 Fracture surfaces of Steel 2.

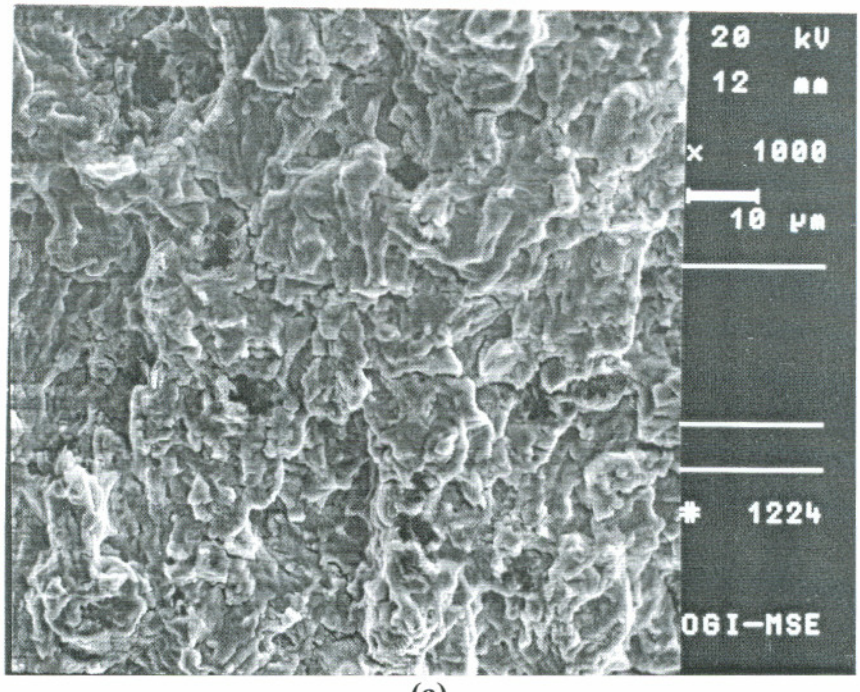

(a)

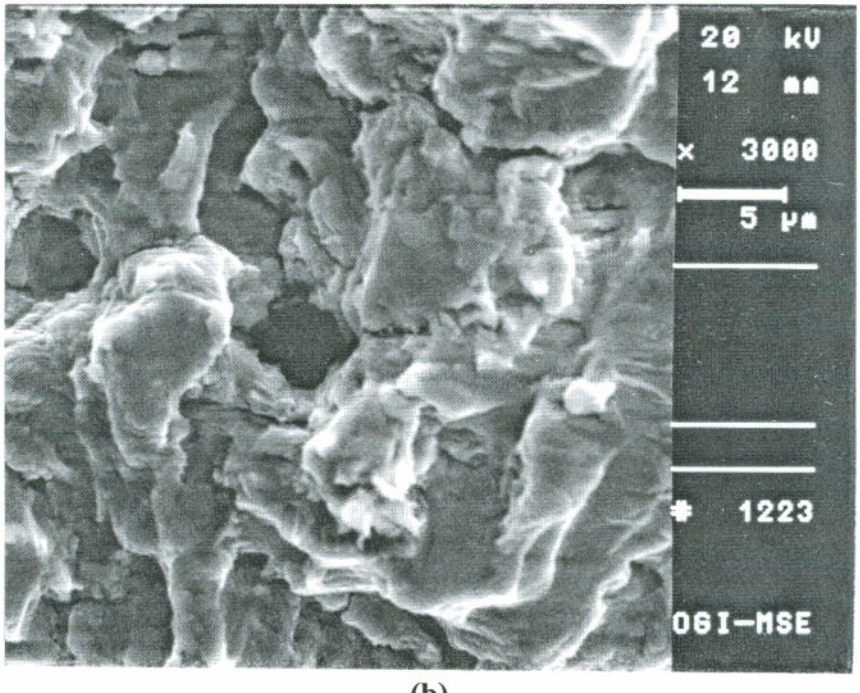

(b)

Figure 4-17 Fatigue fracture surface of Steel 2.

CHAPTER 5
NUMERICAL ANALYSIS ON PARTICLE/MATRIX MECHANICAL INTERACTIONS

5.1 INTRODUCTION

Much of the current research activity in the micromechanics of solids is centered on the initiations of fracture in iron and steels, the ultimate goal of these efforts being guidelines by which to design these materials for increased toughness. Fracture initiation represents the culmination of the three-stage process: voids nucleate at inclusions by particle breaking or interfacial debonding, grow by plastic deformation, and coalesce with each other (microcrack formation) or a dominant crack (crack extension). The exact mechanism by which this process occurs is complex and often involves the interaction of different kinds of defects such as small (submicron) and large voids and inclusions, cracks and dislocations[120]. An outstanding problem in mechanics and physics of solids is to predict and explain, form micro mechanisms for ductile and brittle failure related to second phase particles.

For alloys with relatively small (sub microns), closely spaced particles, dislocation theory provides a comprehensive model of mechanical behavior[121]. Studying the work hardening by larger particles in dispersion-hardened single crystal, Ashby pointed out that many two phase alloys work harden much faster than do those with a single phase because the two phases are not equally easy to deform. Such alloys are plastically nonhomogeneous. The gradients of deformation require that geometrical necessary dislocation be stored and also that glide dislocations supplying the bulk strain must cut through these secondary

dislocations, and overcome the remaining long-range back stress from the particles in order to move. He successfully predicted a parabolic type of hardening for stress-strain behavior within copper single crystals containing small Si_2O particles.

However, for those classes of alloys composed of large widely spaced particles, the dislocation theory is not as well as developed. For an applied uniaxial tension, the plane elasticity problem can be solved by using the Airy stress functions[122]. Eshelby presented a systematic method using classical mechanics which calculate the elastic displacement field to reveal the stress concentrations around an isolated ellipsoidal inclusion. The method uses a sequence of cutting, straining and welding operations. The approach operated by means of equivalent inclusion with an imaginary transformation strain (or eigenstrain) from the assumption of uniform strain in ellipsoidal inclusions.

Applying Eshelby's analysis, the basic role of a hard particle in a metal matrix subjected to tensile loading has been examined by X. Q. Xu et al[123]. The general interaction between the inhomogeneity and matrix is characterized by the following: a hard inclusion creates a high perturbation of triaxial stresses at the poles along the line of loading; a hard inhomogeneity carries higher stress than the matrix; the stress level in the particle is determined by the misfit of the two phases; all the perturbation fields are scaled by inclusion size.

This conventional mechanical analysis could not be extended to nonlinear behavior in the matrix, nor to irregular geometries in particles. The best method that is then left is probably a finite element calculation of stress and strain distribution in the matrix. Also an advantage of computer simulation is that it is possible to examine the effects of modifying the particle's properties and matrix properties, the geometry and distribution of second phase particles in an alloy in order to optimizing these parameters before attempting to actually prepare such alloys, or heat treat such alloys. As discussed in chapters 2 and 3, the size and volume fraction of graphite particles by be controlled by austenitizing temperature and time, the matrix can be a variety of microstructures with different yield strengths. The inclusion type and shape can also be controlled by varying the chemical composition, melting temperature of an alloy.

Most current FEA studies focus on the stress carrying ability of hard particles in composite. In this work, the effects of graphite particles, Al_2O_3 inclusions, and voids on stress and strain concentration were examined to predict the void initiation modes. A graphite particle represents the cases that an alloy contains "soft particles," while Al_2O_3 inclusion represents that the cases that an alloy contains "hard particles."

5.2 CONSTITUTIVE RELATIONS AND YIELD CRITERION

In the generalized form, Hooke's law can be expressed as

$$\sigma_i = \sum_{j=1}^{6} C_{ij}\varepsilon_j \qquad (5\text{-}1)$$

$$(i, j = 1, 2, 3, ...6)$$

where σ_i are the stress components, ε_j are the strain components, and C_{ij} is the stiffness matrix. It can be shown that $C_{ij} = C_{ji}$. In plane stress condition, above equation can be simplified to

$$\begin{vmatrix} \varepsilon \\ \varepsilon_2 \\ \gamma_{12} \end{vmatrix} = \begin{vmatrix} a_{11} & a_{12} & a_{16} \\ a_{21} & a_{22} & a_{26} \\ a_{16} & a_{26} & a_{66} \end{vmatrix} \begin{vmatrix} \sigma_1 \\ \sigma_2 \\ \tau_{12} \end{vmatrix} \qquad (5\text{-}2)$$

For isotropic materials, in plane stress condition:

$$a_{11} = a_{22} = 1/E; a_{12} = -\nu/E;$$
$$a_{66} = 2(a_{11} - a_{12}) = 1/G; a_{16} = a_{26}$$

For axisymmetric solids:

$$\begin{vmatrix} \sigma_r \\ \sigma_\theta \\ \sigma_z \\ \tau_{rz} \end{vmatrix} = \frac{E}{(1+\nu)(1-2\nu)} \begin{vmatrix} (1-\nu) & \nu & 0 & 0 \\ \nu & (1-\nu) & \nu & 0 \\ 0 & \nu & (1-\nu) & 0 \\ 0 & 0 & 0 & \frac{(1-2\nu)}{2} \end{vmatrix} \begin{vmatrix} \varepsilon_r \\ \varepsilon_\theta \\ \varepsilon_z \\ \gamma_{rz} \end{vmatrix} \qquad (5\text{-}3)$$

where σ_r , σ_θ and σ_z are the normal stresses in the r, θ and z directions respectively and τ_{rz} is the shear stress in the rz plane. ε_r , ε_θ , and ε_z are the normal strains in the r, θ and z directions respectively. γ_{rz} is the shear strain in rz plane.

The initiation of plasticity is determined by use an equivalent or effective stress, based on Huber-von Mises yield criterion, and defined as

$$\sigma_{eff} = \frac{1}{6}[(\sigma_1 - \sigma_2)^2 + (\sigma_2 - \sigma_3)^2 + (\sigma_3 - \sigma_1)^2] \qquad (5\text{-}4)$$

where σ_1 , σ_2 and σ_3 are the principal stresses.

5.3 SINGULAR ZONE AND PLASTIC ZONE

When a structure containing a crack or an interface is subjected to external traction or thermal loadings, a singular field will be observed. When the material has an elastic-plastic response, a plastic zone will be observed too when the effective stress reaches the yielding stress. The singular stress field and plastic zone size determine the failure process and failure mode.

A singular field can be defined by

$$\sigma_{ij} = Qr^{-\lambda} f_{ij}(\theta) \qquad (5\text{-}5)$$

where Q is the stress intensity factor and λ is defined as singular power (or singular strength) ($\lambda > 0$), $f_{ij}(\theta)$ is trigonometric function; r and θ represent a polar coordinate system.

Plastic Zone can be calculated analytically or by FEA.

(1) Analytical Approach:

$$\sigma_y = \sigma_e = Q_e r_p^{-\lambda} \tag{5-6}$$

$$r_p = \left(\frac{Q_e}{\sigma_y}\right)^{-\lambda} \tag{5-7}$$

(2) Finite Element Analysis

The plastic zone size can be calculated be the effective stress contours. In this study, the plastic zone size around a second phase particle was estimated by this method.

5.4 ELASTICITY OF GRAPHITE PARTICLES

M. J. Dong using Hashin-Schtrikman bounds calculated the elastic moduli of graphite nodules in cast iron[126]. For spherical inclusions, Hashin-Schtrikman bounds are given by the following equations. For upper bounds,

$$k^+ = k_M \frac{(1-f_0)[\alpha_M k_i + (1-\alpha_M)k_M] + f_0 k_I}{k_M + (k_I - k_M)\alpha_M (1-f_0)} \tag{5-8}$$

$$\mu^+ = \mu_M \frac{(1-f_0)[\beta_M \mu_i + (1-\beta_M)\mu_M] + f_0 \mu_I}{\mu_M + (\mu_I - \mu_M)\beta_M (1-f_0)} \tag{5-9}$$

$$\alpha_M = \frac{1}{3}\frac{1+\nu_M}{1-\nu_M} \tag{5-10}$$

$$\beta_M = \frac{2}{15}\frac{4-5\nu_M}{1-\nu_M} \tag{5-11}$$

where k and μ refer to the bulk moduli and shear moduli, respectively, and indexes M and *I* refer to the ferrite matrix and the graphite inclusions respectively. The term ν_M is the

Poisson's ratio of matrix. The term f_0 is the volume fraction of graphite nodules.

For lower bounds,

$$k^- = k_I \frac{(1-f_0)[\alpha_I k_M + (1-\alpha_I)k_I] + f_0 k_M}{k_I + (k_M - k_I)\alpha_I(1-f_0)} \quad (5\text{-}12)$$

$$\mu^- = \mu_I \frac{(1-f_0)[\beta_I \mu_M + (1-\beta_I)\mu_I] + f_0 \mu_M}{\mu_I + (\mu_M - \mu_I)\beta_I(1-f_0)} \quad (5\text{-}13)$$

Introducing the bulk and shear moduli of the ferritic steel (206 and 78.9 GPa, respectively) and of the cast iron (173 and 70.8 GPa, respectively), these equations yield for the graphite inclusions:

$17 \text{ GPa} < k_I < 45 \text{ GPa}$

$12 \text{ GPa} < \mu_I < 24 \text{ GPa}$

and

$28 \text{ GPa} < E_I < 61 \text{ GPa}$

$0.22 < \nu_I < 0.27$

The lower values for the inclusion correspond to the Hashin-Schtrikman upper bounds. In the calculation of the lower bound, the constituent having the lowest moduli, i.e., the graphite, is considered as the matrix, whereas it is the reverse in the calculation of the upper bound. The upper bound matches better the actual configuration of the material. Dong thought that the graphite moduli should be close to the values found using the upper bounds of Hashin-Schtrikman: $k_I = 17$ GPa, $\mu_I = 12$ GPa, $E_I = 28$ G_a, $\nu_I = 0.22$.

The elastic moduli of graphite are highly anisotropic. The Young's moduli are 27 and 686 GPa along the c and a axes of hexagonal crystal[124]. In the nodules, the c axes are along the radial direction. Era et al.[125], assuming perfect spherical symmetry, calculated an average Young's modulus equal to 303 GPa. This value is far above the one which Dong found close to the Young's modulus in the c direction, equal to 28 GPa, which has been confirmed by Diericke et al., using nanoindentations[126]. This could be due to the imperfect

actual crystallographic construction of graphite nodules, as described by various authors[127,128]. These authors showed that the microstructure of graphite spherulites consists of fanlike areas formed from monocrystaline platelets with sizes ranging from several to tens of nanometers radically and hundreds of nanometers circumferentially. These monocrystalline of platelets are weakly bonded together by intercalary layers containing dislocations and faults. Consequently, Dong's group believed that the transverse high stiffness of the hexagonal crystal can never be activated when deforming graphite nodules, except under hydrostatic pressure[126]. Therefore, only the weak bonding along radial c axises contributes to the elastic modulus of the spherical graphite nodules, thus explaining the low equivalent modulus.

5.5 MATERIAL PROPERTIES

The material properties are presented in Table 5-1. The matrix was treated as an elastic-plastic body and all second phase particles have a linear elastic response. The stress-strain curve of matrix is shown in Figure 5-1, which is plotted from the experimental tensile test results for cold worked and annealed Steel 1 without graphite. So far graphite particles in cast irons or steels are treated as voids or elastic bodies, because the plastic deformation ability is much lower than matrix. Many graphite products have high tensile strength but only have less than 1% elongation. The thermal coefficient of graphite is less than that of matrix. Thus, graphite particles shrink less than matrix during cooling process and do not debond due to thermal history. The graphite particles formed during cold work and 400-700 °C annealing processes will not develop a large thermal residual stress compared the graphite formed during solidification. In this work, the thermal residual stress is neglected. It has been discussed in literature reviews that graphite particles nucleate at preferential sites to minimize the coherency misfit. Experimental work showed graphite particles in cast iron didn't debond or break before the surrounding matrix yielded, and the matrix plastic deformation first started at the graphite/matrix interface. These results imply that assuming graphite has a perfect bonding with matrix may give a more realistic simulation than just taking as graphite as voids.

All the graphite simulations in an iron matrix were based on graphite acting as a void or a polycrystalline graphite with high Young's modulus[129]. Dong's calculation results in 1997 and Diericke's nanoindentations in 1994[133] showed the Young's modulus of graphite particles in an iron matrix is about 28 Gpa. All the calculations in this study are based on these new material properties.

5.6 ASSUMPTION AND BOUNDARY CONDITIONS FOR UNIT CELL MODEL

For the particles located on the surface, or the particles in a really thin sheet material, the stress and strain distribution can be modeled by plane stress assumption. For the particle embedded inside a thick material, axisymmetric assumption can be used. A unit cell model was found to be a very effective tool for second phase particle study.

It was assumed that the graphite or Al_2O_3 particles in steel can be represented by a periodic regular array of equal sized particles with an AAA stacking sequence, shown in Figure 5-2. The periodic array is subdivided into a regular array of individual hexagonal cells, which are furthermore approximated by circular cylinders, to allow simple axisymmetric calculations. Other cell structures like cubic primitive and cubic body centered require 3D analysis and it has been shown that hexagonal arrangement with axisymmetric unit cell calculation gave a lower bound solution[120].

The particle is located in the center of the cell. Assume the displacements are continuous at interfaces by nodal connectivity. Due to symmetry, 1/4 unit cell was used for calculation. During calculation, opposite edges remain parallel. Straight boundaries are kept by coupling all the nodes in these boundaries with the same displacement. The finite element mesh is illustrated in Figure 5-2. The mesh consists of 1520 eight-noded isoparametric quadrilateral elements. Since the maximum stresses are expected to occur close to the particle/matrix interface, the elements close to the interface are much smaller in size than the finite elements in other non-critical locations. All loads applied were static in nature. In this study, the tolerance of force convergence is less or equal to 0.1% by default.

Deformation of the microcell is achieved by imposing a displacement or load on line

DC with boundary condition as follows:

Line AB, displacement symmetry, y direction displacement = 0;

Line AD, the axis for axisymmetry;

Line DC, a straight boundary, all nodes have the same displacement in y direction;

Line BC, a straight boundary, all nodes have the same displacement in x direction.

This model fixes the y direction of Line AB, but allow it to contract in x direction, making AB a mirror symmetry line.

5.7 UNIT CELL MODEL RESULTS

The stress and strain distributions along Line AD and AB in Figure 5-2 were extracted to represent the mechanical response along the particle axes parallel to tensile direction and perpendicular to the tensile direction. In this study, two cases were investigated to explore the elastic behavior and elastic-plastic behavior of steels containing graphite nodules:

(1) 300 MPa applied stress (0.75 of matrix yield stress);

(2) applied stress was 450 MPa (1.125 of matrix yield stress).

5.7.1 Stress and Strain Distribution Around a Graphite Particle

Normal Stress σ_y along the Tensile Direction

In fracture mechanics, the normal stress σ_y is a key factor that determines whether a material fails or not, depending on the stress intensity. Figure 5-3 presents the normal stress contour around a graphite particle when the applied stress was 300 MPa. Figure 5-4 (a) and (b) illustrates the normal stress profile along the particle axis AD(parallel to the tensile direction) and along the axis AB(perpendicular to tensile direction), respectively. The highest normal stress was located at the matrix surrounding the particle equator. The graphite particle carries a much lower stress than the steel matrix. The stress was uniformly

distributed in the graphite particle which is consistent with the famous result dealing with a single inclusion by Eshelby[73]. He found that the stress field in an ellipsoidal and perfectly bonded inclusions, subjected to either a uniform remote transformation strain or a uniform remote traction, is constant. The solution of a single inclusion is applicable for the dilute case, in which inclusions are far away from each other and do not interact.

Along the tensile direction (Line AD), the lowest normal stress is located at the interface between graphite and matrix, then gradually increases to a value close to the applied stress as shown in Figure 5-4(b). There are two low stress zones at the north and south poles which are similar to the distribution for a hole in an elastic matrix. Using the lines of force concept is a convenient way to visualize the stress field patterns. Because the graphite carried lower stress, less lines of force go through the particle and resulting in a more dense stress line outside the equator.

Figure 5-5 presents the normal stress contour around a graphite particle when the applied stress was 450 MPa. Figure 5-6 (a) and (b) illustrates the normal stress profile along the particle axis AD and AB when the applied stress was 450 MPa . It is obvious that when the applied remote stress was greater than the matrix yield stress, the graphite particle carried a higher normal stress than the matrix. The highest stress in a graphite particle was located at the center of the particle, while the highest normal stress in the steel matrix was located along poles and away from the interface a small distance. The two lowest stress zones at poles for elastic loading became the highest stress zone in the matrix and the region surrounding the particle equator became the lowest stress zone.

Von Mises Stress (Equivalent Stress) σ_{eqv}

In metal elasticity and plasticity, the effective stress is a measure of distortion in materials. Figure 5-7 and 5-8 show the effective stress contour around a graphite particle under 300 and 450 MPa, respectively. The effective stress profile along the particle axes parallel to the tensile direction and perpendicular to tensile direction were illustrated in Figure 5-4 and 5-6. The effective stress has a similar distribution pattern with the normal

stress which reflects that the normal stress along tensile direction makes the dominated contribution to the effective stress value for the material under uniaxial tension. As the applied remote stress was equal to 75% yield stress of matrix (300 MPa), the graphite particle carried a much lower effective stress than the steel matrix. The highest effective stress was located at the equator and reached the yield stress of matrix, created a small plastic zone along the particle equator. That is consistent with Dong's experimental result that the iron matrix yielded first along the equator[119]. Along the tensile direction (Line AD), the effective stress had a sharp increase at the interface between graphite and matrix, then dropped to the lowest value in matrix, shown in Figure 5-4 (b), finally gradually increased to a value close to the applied stress. There were two low stress zones at the two poles which were similar to the normal stress distribution.

As the applied remote stress was greater than yield stress, the effective stress in the particle was higher than in matrix (shown in Figure 5-5 and 5-8). The highest effective stress in a graphite particle located at the center of the particle. But the lowest effective stress is located at the interface.

The Hydrostatic Pressure σ_m

The hydrostatic stress is a measure of a mean stress state. It is directly related to the specific volume change whereas the effective stress responds to distortion at local state. In metal plasticity, the hydrostatic pressure is usually not considered to play a significant role in metal yielding. But it may be very important for interface debonding. Figure 5-9 and 5-10 shows the hydrostatic stress contour around a graphite particle under 300 and 450 MPa, respectively.

Figure 5-4 shows that along Line AB, when loaded to 75% of matrix yield stress, the largest mean stress concentration in the matrix is close to the interface. Along Line AD, the lowest mean stress in the matrix is at the interface. If the hydrostatic pressure dominates the interface debonding process, it suggests that debonding may not be easily occur in the elastic regime.

Figure 5-6 presents that under 450 MPa, the highest hydrostatic stress is close to the pole interfaces and 2.53 times of far field hydrostatic stress.

The Normal Strain and the Equivalent Strain

Figure 5-11 and 5-12 illustrate the strain distribution under 300 MPa and 450 MPa applied stresses, respectively. Clearly, under 300 Mpa, the graphite particle deforms more than the steel matrix. The lowest strain is located at the matrix close to the pole of the graphite particle. The highest strain magnitude is located at the graphite/matrix interface along the equator. Under 450Mpa, the graphite particle deforms less than the steel matrix along Line AD. The lowest strain is located at the matrix close to the pole of the graphite particle. The highest strain magnitude is located at the graphite/matrix interface along the pole.

5.7.2 Stress and Strain Distribution Around an Al_2O_3 Particle

Figure 5-13 and 5-14 illustrate the stress distribution along an Al_2O_3 particle axis AD (parallel to the tensile direction) and the axis AB(perpendicular to tensile direction), under 300 MPa and 450 MPa, respectively.

The Normal Stress along the Tensile Direction

For the applied remote stress of 300 MPa, the Al_2O_3 inclusion carried a higher stress than the steel matrix. The stress is uniformly distributed in the particle. The stress particle carried is 1.3 times of the far field stress. The highest normal stress in matrix is located at the pole interfaces which is different with the situation of steel with particles. The lowest normal stress is located at the equator interface between Al_2O_3 and matrix, then gradually increases to a value close to the applied stress as shown in Figure 5-13(a).

Figure 5-14 shows that, as the applied remote stress is greater than yield stress, the

highest normal stress in the particle is located at the center of the particle and is 1.6 times of the far field stress. The highest normal stress in the steel matrix is located along poles and away from the interface a small distance. The lowest stress is located at the region surrounding the particle equator.

Von Mises Stress (Equivalent Stress).

Figure 5-13 and 5-14 illustrate that independent of whether the applied load was higher than yield stress or not, the Al_2O_3 carried higher effective stress than the steel matrix. The regions close to the two poles of the particle always carried higher stress than the regions close to the equator of the particle.

As the applied remote stress was equal to 300 MPa (75% yield stress of matrix), the local stress concentration was not high enough to cause local yielding, unlike the cases of steel with graphite.

The Hydrostatic Pressure

As shown in Figure 5-13 and 5-14, the highest hydrostatic stress was always located in the matrix close to particle pole regions and is 1.7 times and 3.2 times of the far field value when applying 300, 450 MPa remote stress, respectively.

The Normal Strain ε_y and the Equivalent Strain ε_{eqv}

Figure 5-15 and 5-16 illustrated the strain distribution along AB and AD line. The particle deforms less than the steel matrix. The highest strain is located at the matrix close to the pole of the particle. Under 300 MPa, strain concentration only occurs at pole interfaces. Under 450 MPa, strain concentration appears at both pole and equator interfaces, but the magnitude of strain at pole interfaces is much higher than equator interfaces.

5.7.3 Stress and Strain Distribution Around a Void

Figure 5-17 and 5-18 presents the stress distribution around a void instead of a second phase particle.

The Normal Stress along the Tensile Direction

As the applied remote stress is equal to 75% yield stress of matrix, 300 MPa, the highest normal stress in matrix is located equator edges of the hole and is 1.52 times of the far field normal stress. Unlike the linear elastic material, the highest stress at a hole edge is three times of the far field stress. The lowest normal stress is compressive and located at pole edges of the hole.

When the applied remote stress is greater than yield stress, the highest normal stress is still located at the equatorial plane and is 1.46 times of the far field stress. The lowest normal stress in the steel matrix is located along poles and away from the interface a small distance. There are two compressive zones close to the pole edge.

Von Mises Stress (Equivalent Stress).

Unlike the normal stress, the effective stress is always positive. Under 300 MPa, the local stress concentration could cause local yielding at equatorial edges. Comparing Figure 5-15 and 5-6, it can be found that a hole creates a larger plastic zone than a graphite particle of the same size. Under 450 MPa, the highest effective stress is at the pole edge and decreases at a rate of $1/r^{0.37}$.

The Hydrostatic Pressure

The highest hydrostatic stress is always located at the equatorial edge and is 1.8 times and 1.9 times of the far field value when applying 300, 450 MPa remote stress,

respectively.

The Normal Strain and the Equivalent Strain

Figure 5-19 and 5-20 illustrate the strain distribution along AB and AD line. When a graphite or Al_2O_3 particle was replaced by a hole, the strain distribution kept the same pattern no matter what the applied stress level was. The strain concentration at the void edge was much higher than that at a particle/matrix interface.

5.8 DISCUSSION

5.8.1 Effects of Particle Types on the Stress/strain Concentration Factors (SCF)

The stress/strain concentration factor (SCF) is defined as:

SCF = (Maximum Stress or Strain) / (Far Field Stress or Strain)

The maximum stress, strain and SCF is listed in Table 5-2 to 5-5. Figure 5-21 and 5-22 present the SCF under 300 MPa and 450 MPa, respectively. It is seen that a void caused a larger strain concentration than did graphite and Al_2O_3 . Simply treating a graphite particle as a void may overestimate the strain concentration.

It is well known that the SCF of a circular hole in an elastic body is three. Replacing our axisymmetry boundary condition to plane stress and material properties to elastic response and keeping the same mesh, SCF of normal stress in tensile direction is 3.08 which is in good agreement with analytical solution. Also the structural percentage error in an energy norm is 2.1%. For nonlinear problems, verification is sometimes impossible and the structural percentage error in an energy norm cannot be calculated by Ansys. Usually an elastic solution is used as the justification test for mesh design.

Another famous solution[69] for interfacial stresses around a rigid inclusion in an

incompressible (i.e., $\nu = 0.5$) linear material can be obtained directly form the theory of elasticity:

$$\sigma_{rr} = p\left[4\left(\frac{\varrho}{r}\right)^2 - 3\left(\frac{\varrho}{r}\right)^4 + 1\right]\cos 2\theta \tag{5-14}$$

$$\sigma_{\theta\theta} = p\left[3\left(\frac{\varrho}{r}\right)^4 - 1\right]\cos 2\theta \tag{5-15}$$

$$\sigma_{zz} = p\left[2\left(\frac{\varrho}{r}\right)^2\right]\cos 2\theta \tag{5-16}$$

$$\sigma_{r\theta} = p\left[2\left(\frac{\varrho}{r}\right)^2 - 3\left(\frac{\varrho}{r}\right)^4 - 1\right]\sin 2\theta \tag{5-17}$$

where p is the boundary shear traction and ρ the radius of the cylinder. The tensile stress is maximized at $\theta = 0^\circ$ and is equal to two times the boundary shear traction. The interfacial shear strain is maximized at $\theta = 45^\circ$ and is also equal to twice the distant boundary shear strain. However, these results are independent to the Young's modulus of the particle and matrix. Also, current FEA results showed the maximum stress is not necessary exactly at an interface which agrees with Watt's results[123].

5.8.2. Effect of Particle Size

The graphite particle size effect on stress concentration is listed on Table 5-6 (Applied stress = 300 MPa). The graphite size has a significant influence on normal stress and hydrostatic stress. The greater the graphite size, the higher the stress concentration.

Goods and Brown[72] have developed a dislocation model for void nucleation at submicron particles. The estimated that dislocations near the particle elevate the stress at the interface by the following amount:

$$\Delta\sigma_d = 5.4\,\alpha\mu\,(\varepsilon_1 b/r)^{1/2} \tag{5-18}$$

where α is a constant that range from 0.14 to 0.33, μ is the shear modulus, ε_1 is the maximum remote normal strain, b is the magnitude of the Burger's Vector, and r is the particle radius. The total maximum interface stress is equal to the maximum principle stress σ_1 plus $\Delta\sigma_d$. Void nucleation occurs when the sum of these stress reaches a critical value:

$$\sigma_c = \Delta\sigma_{d+} \sigma_1 \tag{5-19}$$

This model indicates that local stress concentration increases with decreasing particle size; void nucleation is more difficult with larger particles. However, Many investigators have reported that in a given sample, large inclusions appear to produce cavities sooner than small ones. Some of the previous explanations of this effect appear to be erroneous, such as for instance the energy explanation of Gurland and Plateau[69] which was discussed to be only a necessary condition for cavitation. For interface debonding, the explanation advanced by Palmer and Smith[69] that large inclusions may act as more efficient sinks for embrittling impurities could certainly be valid but not likely be responsible for this phenomenon in all cases. For particle breaking, it may also due to the defect density inside a large particle being higher than that of a small particle. Some single crystal whisker tensile testing results showed that the single crystal with a large diameter has lower tensile strength[130]. Argon[69] pointed out that it is reasonable to expect that the effect may have its origin in interaction between inclusions. From dimensional analysis it is clear that the stress concentration cannot be dependent on inclusion size for the case of an isolated large inclusion (surface energy restrictions being unimportant) in an infinite medium where there is only one length dimension. When inclusions are in very infinite media or when many inclusions are present in a body so that their spacing becomes of order of their diameter, a new length parameter appears in the analysis. It can be readily seen, however, that even in this case the stress concentration will be only dependent on the ratio of inclusion size to spacing. If all inclusions are of the same size, this would make the stress concentration dependent only on the volume fraction of second phase particles but not directly on the inclusion size. It is clear, therefore, that an inclusion size dependence of the stress concentration can occur, only if local variations of volume fractions exist, making it possible for some larger than average

inclusions to be neighbors at a spacing equal to or smaller than the average spacing. The nit cell model actually take account the effect of spacing and volume fractions. But the unit cell model cannot be used to study situations when particles are so close that their stress field is overlapping. A better model needs to be developed.

5.8.3 Relationship Between Material Properties and Particle Damage Mode

Three are distinct modes of particle associated damage in materials: particle shattering, particle/matrix interface decohesion, and particle fracture. Void formation in steels can also be due to the breakdown of matrix near particles. These are illustrated in Figure 5-23.

Material properties of matrix and particles can be modified to vary the stress and strain concentration. Three situations are common for a material with second phase particles:

(1) $E_m > E_p$, $E_m^T < E_p^T$;
(2)$E_m < E_p$, $E_m^T < E_p^T$;
(3)$E_m > E_p$, $E_m^T > E_p^T$.

where E_m and E_p represent the Young's modulus of matrix and particle, respectively; while E_m^T and E_p^T is the tangential modulus of the materials that exhibit linear strain hardening. The tangential modulus of a material represent the stiffness of material after the material starts to yield. These parameters ultimately determine the different failure mechanism by varying the orientation and position of maximum stress and strain. (Figure 5-23)

Materials Properties: $E_m > E_p$, $E_m^T < E_p^T$

Figure 5-23 (a) shows the stress-strain curve and the maximum stress positions for graphite in a steel with a low stain hardening rate. In an elastic regime, the stress and strain curve of matrix has a greater slope than graphite and the graphite is relative soft to the

matrix. Previous results show that the graphite particles only carry a very low stress and maximum stress is at the equatorial interface. But after the matrix starts yielding, the stress-strain curve of matrix has a smaller slope than graphite. The graphite starts carry higher stress than matrix. Also, the maximum normal stress at an interface is moved to the poles. Therefore, the possible failure mode could be the interface debonding at poles after the matrix starts yielding. At this point, graphite starts behaving like a void. Hence, the maximum stress moves to the matrix near the equatorial interface. Finally, the linking of voids begins with internal necking between adjacent voids. Figure 5-24 shows a transient analysis on the unit cell model of the steel matrix with a graphite particle. Node 913, 601 are the nodes at the pole and equator, respectively. It is very obvious that the stress at node 913 is much lower than the stress at node 601 at the elastic loading stage, and suddenly jump to the highest stress after the applied stress reach yield point.

Graphite nodules were normally treated as a hole which does not carry any load when applying a remote stress on matrix. Current results using the focused ion beam cross-section showed that graphite did not just stay in a hole but maintained conformance with the matrix. Dong's experimental results[119] for graphite nodules in cast iron showed that no damage of graphite nodule interfaces was observed in the "elastic" part of load-displacement curve and the first decohesions occurred at the pole cap of nodules when the applied stress was equivalent to the macroscopic yield stress. This current finite element analysis study shows that graphite particles are hardly debonded during elastic loading, because the minimum stress and strain is at the pole. Only after plastic deformation starts, does the maximum normal stress and hydrostatic stress locate at the pole.

The previous study[119] showed that the failure mode of cast irons is debonding the interfaces between graphite particles and iron matrix. However, current fractography results (Chapter 4) indicates that graphite shattered into small pieces in the low alloy steels. The explanation can be that the graphite nodules in cast iron formed during solidification process, and large graphite nodules in cast irons may act as more efficient sinks for embrittling impurities. Current focused ion beam cross section study (Chapter 3) revealed that graphite has perfect bonding condition with the steel matrix. And also graphite nucleation is related

to the low S and P contents in steels (see discussions on the effect of impurity on graphite formation in Chapter 2). Therefore, the graphite formed in cold worked and annealed steels should have a clean interfaces and high bond strengths. However, in cast irons, phosphorus and sulfur are the most common minor elements and always present. They can be as high as 0.15% for low quality iron. Therefore, in cast irons, fracture initiates the graphite/iron interfaces.

The stress needed to break a graphite particles can be estimated by energy analysis. Assume the crack formed in graphite is the same as the graphite diameter, the critical condition for forming the first crack through graphite is:

$$(q\sigma)^2 a^3/E = 2\gamma a^2 \tag{5-20}$$

where q is the stress concentration factor, σ is the remote average stress. Therefore,

$$\sigma = q^{-1} (2E\gamma/a)^{1/2} \tag{5-21}$$

Therefore, the larger the graphite, the easier to break. According to L'nyanoy's calculation[27], the graphite surface energy was 180-290 $\times 10^{-7}$ J/cm^2 which is the lowest surface energy reported. Applying $\gamma = 180 \times 10^{-7}$ J/cm^2, the stress for graphite breaking is 709 MPa. And when q = 1.42 (see Table 5-3), the remote stress needed applied to break a 2-micron graphite nodules is 499 MPa which is over the matrix yield stress (400 MPa). Therefore, independent of graphite interface debonding or graphite breaking, the matrix must undergo massive yielding.

Materials properties: $E_m < E_p$, $E_m^T < E_p^T$

Figure 5-23 (b) shows the stress-strain curves for the cases that the particle is always "harder" than the matrix and always carries more stress than the matrix, such as Al_2O_3 inclusions in steels. There is competition between particle breaking and interface debonding.

Which failure mode dominates depends on the particle strength and interface condition.

Materials Properties: $E_m > E_p$, $E_m^T > E_p^T$

Figure 5-23 (c) presents a void in any materials or a graphite in high work hardening ability steel. The degree and pattern of stress and strain concentration don't change before and after macro plastic deformation starts.

5.8.4. Effect of Stress Field Around an Al_2O_3 Particle on Graphite Formation

In chapter 1, the alignment effect was reviewed. The lattice constants of ferrite and cementite are closer to the lattice constants in basal planes of graphite lattices than alumina. A Therefore, the alignment effect is not the main reason for graphite nucleation at Al_2O_3 /matrix interfaces. One explanation would be the stress gradient induced diffusion. During annealing, the driving force could be the carbon concentration difference between graphite/ferrite interfaces and cementite/ferrite interfaces. During cold work, there is a stress concentration at Al_2O_3 interfaces providing the driving force for carbon diffusion.

$$J_o \propto \frac{D}{RT} V_C \frac{\partial \sigma_h}{\partial x} \tag{5-22}$$

$$C = C_0 \exp\left(\frac{V_C \sigma_h}{RT}\right) \tag{5-23}$$

where J_o is the diffusion flux caused by hydrostatic stress gradient. V_C is the molar volume of carbon in an iron matrix. C is the equilibrium carbon concentration in the stressed lattice. C_0 is the equilibrium carbon concentration in an unstressed lattice. D is the carbon diffusivity in iron[131].

Cold work causes stress concentration at defects, such as inclusions, and microvoids. For example, the hydrostatic stress is much higher at the interface of an inclusion. FEA results showed that the hydrostatic stress at the interface of Al_2O_3 is 3.73 times of far field

stress. At the Al_2O_3 interface, the carbon concentration could be exponentially increased according to above equations. Current FEA results also showed the hydrostatic stress concentration caused by a void or a soft particle is much smaller than Al_2O_3. All the defects may have the thermodynamic potential to act as heterogeneous nucleation sites. The magnitude of the potential depends on many factors, and one is hydrostatic stress concentration.

Graphitization is a process by which a steel transforms toward its equilibrium state. However, depending on service conditions, this process may take years. Deformation, in the context of both strain and strain state, has a significant influence on graphite precipitation kinetics and the rate. Deformation provides enhanced C diffusion through the creation of dislocation "pipes', as well as other defects such as intersecting micro-shear bands which also provide energetically favorable precipitation nucleation sites. The matrix around Al_2O_3 particles is highly deformed. The strain concentration factors for normal strain and effective strain both equal to 2 according current calculations. A lot of dislocation "pipes" may exist around Al_2O_3.

Dislocation pipe diffusion originally developed in the form[132]:

$$D_{c(b)} = D_{c(0)} + \rho A_p D_p \tag{5-24}$$

where $D_{c(0)}$ is the undeformed (bulk) lattice diffusivity, ρ is the dislocation density, D_p is the dislocation pipe diffusivity, and A_p is the dislocation pipe (cross-section) area. Since stress (σ), and strain (ε), and dislocation density (ρ) are related by

$$(\sigma - \sigma_0) = K_1 \varepsilon^n = K_2 \rho^{1/2} \tag{5-25}$$

where σ_0, K_1, K_2, are constants and n is the strain-hardening exponent.

$$D_{c(b)} = D_{c(0)} + K_3 \varepsilon A_p D_p \tag{5-26}$$

The diffusion rate in the matrix surrounding an Al_2O_3 particle could be greatly accelerated due to cold work process, because the final cold work reduction was 65% or more in the investigated steels.

5.9 CONCLUSIONS

1. The materials properties of particle and matrix determine the locations of maximum stress and strain concentration at the particle/matrix interface, also the stress and strain transferring and carrying ability.
2. Graphite particles are hard to break and debond from matrix without plastic deformation because of their load carrying ability and the maximum stress location.
3. Modeling a graphite particle as a void will overestimate the stress and strain concentration around this particle and cannot explain the graphite/matrix interface debonding phenomena.
4. Stress induced diffusion could be one of the reasons graphite nucleated in the interface or near an inclusion like Al_2O_3. The carbon concentration at the Al_2O_3/matrix interface could be $e^{3.7}$ times of far field carbon concentration.

5.10 FUTURE WORK

1. After particle/matrix debonding, the frictional forces between particle and matrix need to be considered. Contact elements could be used to model this situation.
2. There are also possibly some partially debonded particles. A void formed at interfaces could be modeled to represent this case.
3. Interfaces may be treated as a third material with material properties different with both particle and matrix.
4. Thermal residual stress should be considered: thermal residual stress is the same for all directions, independent on the applied tensile stress direction. It will affect the magnitude of stress level. But it won't affect the location of the maximum stress

concentration and so the initiation location of a microcrack.

5. In-situ SEM, TEM or quasi-dynamic tensile testing, using two features as reference points to measure the displacement and strain. Then verify the model.
6. Effect of particle shape and spacing on stress and strain distribution.

Table 5-1 Materials properties used in numerical modeling.

Material	Modulus of elasticity (GPa)	Poisson's ratio	Coefficient of thermal expansion, per °C
Graphite	28	0.22	3×10^{-6}
Pore	0	-	-
Alumina[133]	390	0.25	8×10^{-6}
Matrix	200	0.3	10×10^{-6}

Table 5-2 Maximum stress and strain in matrix (Applied stress=300 MPa).

	σ_y		σ_{eqv}		σ_m		ε_y		ε_{eqv}	
	Max MPa	SCF	Max MPa	SCF	Max MPa	SCF	Max %	SCF	Max %	SCF
GR	437	1.47	401	1.35	171	1.61	0.281	1.84	0.350	1.79
Al_2O_3	397	1.32	367	1.22	185	1.74	0.188	1.23	0.240	1.17
Void	457	1.52	402	1.34	191	1.75	0.343	2.26	0.471	2.41

Table 5-3 Maximum stress and strain in particle (Applied stress=300 MPa).

	σ_y		σ_{eqv}		σ_m		ε_y		ε_{eqv}	
	Max MPa	SCF	Max MPa	SCF	Max MPa	SCF	Max %	SCF	Max %	SCF
GR	74.7	0.25	74.7	0.25	-	-	0.264	1.73	0.330	1.69
Al_2O_3	388	1.29	411	1.37	-	-	0.132	0.86	0.133	0.65
void	0	0	0	0	0	0	0	0	0	0

Table 5-4 Maximum stress and strain in matrix (Applied stress=450 MPa).

	σ_y		σ_{eqv}		σ_m		ε_y		ε_{eqv}	
	Max MPa	SCF	Max MPa	SCF	Max MPa	SCF	Max %	SCF	Max %	SCF
GR	639	1.42	473	1.05	377	2.53	6.89	1.54	10.2	1.53
Al_2O_3	782	1.74	505	1.12	541	3.73	9.06	2.00	13.5	2.00
Void	656	1.46	574	1.28	309	1.93	14.4	2.88	22.6	3.03

Table 5-5 Maximum stress and strain in particle (Applied stress= 450 MPa).

	σ_y		σ_{eqv}		σ_m		ε_y		ε_{eqv}	
	Max MPa	SCF	Max MPa	SCF	Max MPa	SCF	Max %	SCF	Max %	SCF
GR	570	1.27	691	1.54	-	-	2.23	0.50	2.94	0.44
Al_2O_3	786	1.75	833	1.85	-	-	0.21	0.05	0.28	0.04
Void	0	0	0	0	0	0	0	0	0	0

Table 5-6 Effect of graphite size on stress concentration.

Graphite Size	r = 1 μm	r = 1.5 μm	r = 3 μm	r = 4 μm
Normal Stress (MPa)	443	437	461	555
Effective Stress (MPa)	401	401	401	405
Hydrostatic stress (MPa)	187	171	194	290

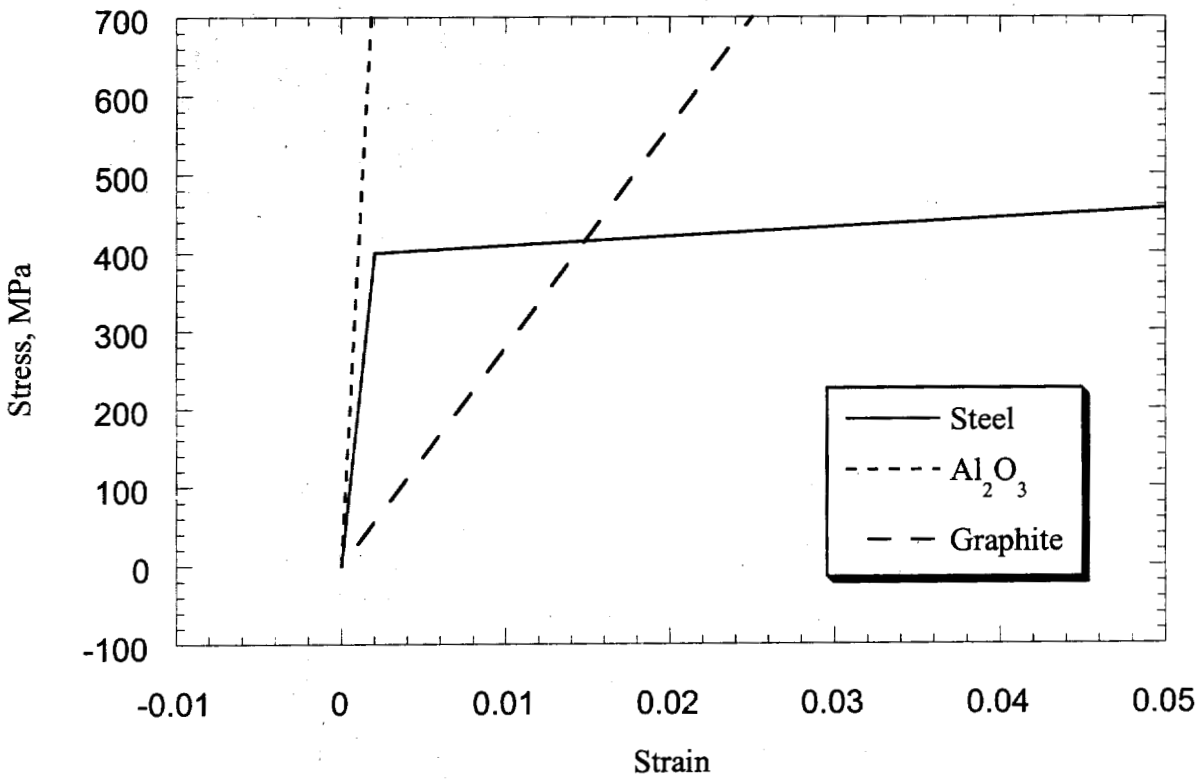

Figure 5-1 Materials properties of steel matrix, graphite, and Al_2O_3.

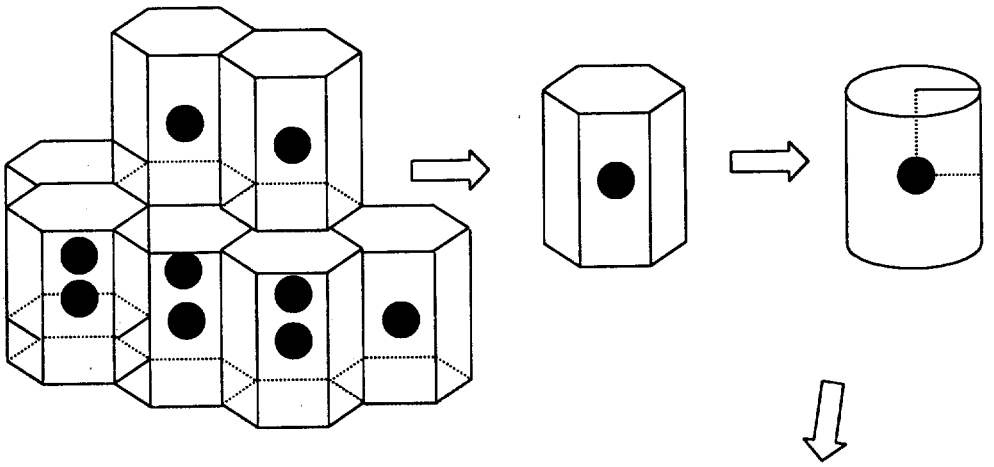

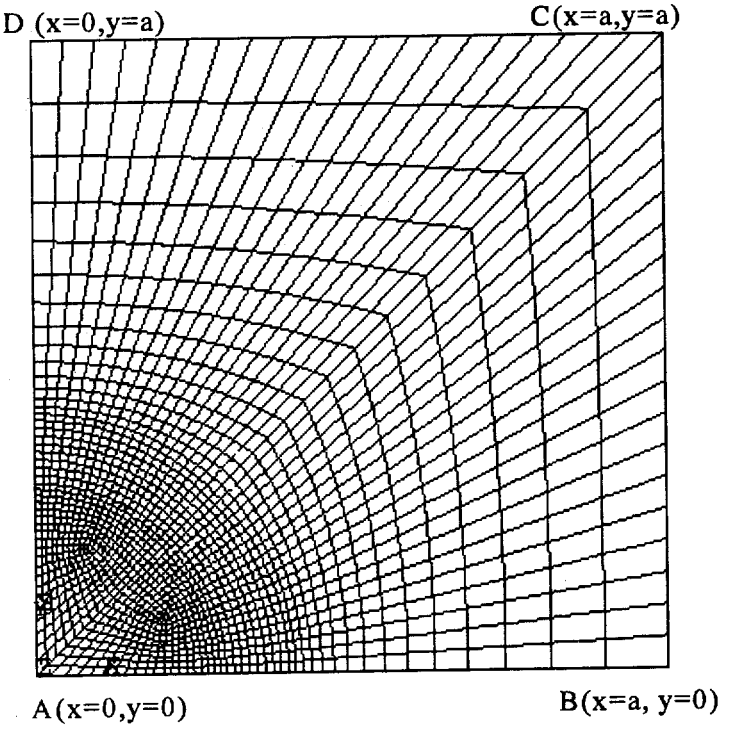

Figure 5-2 Unit cell model.

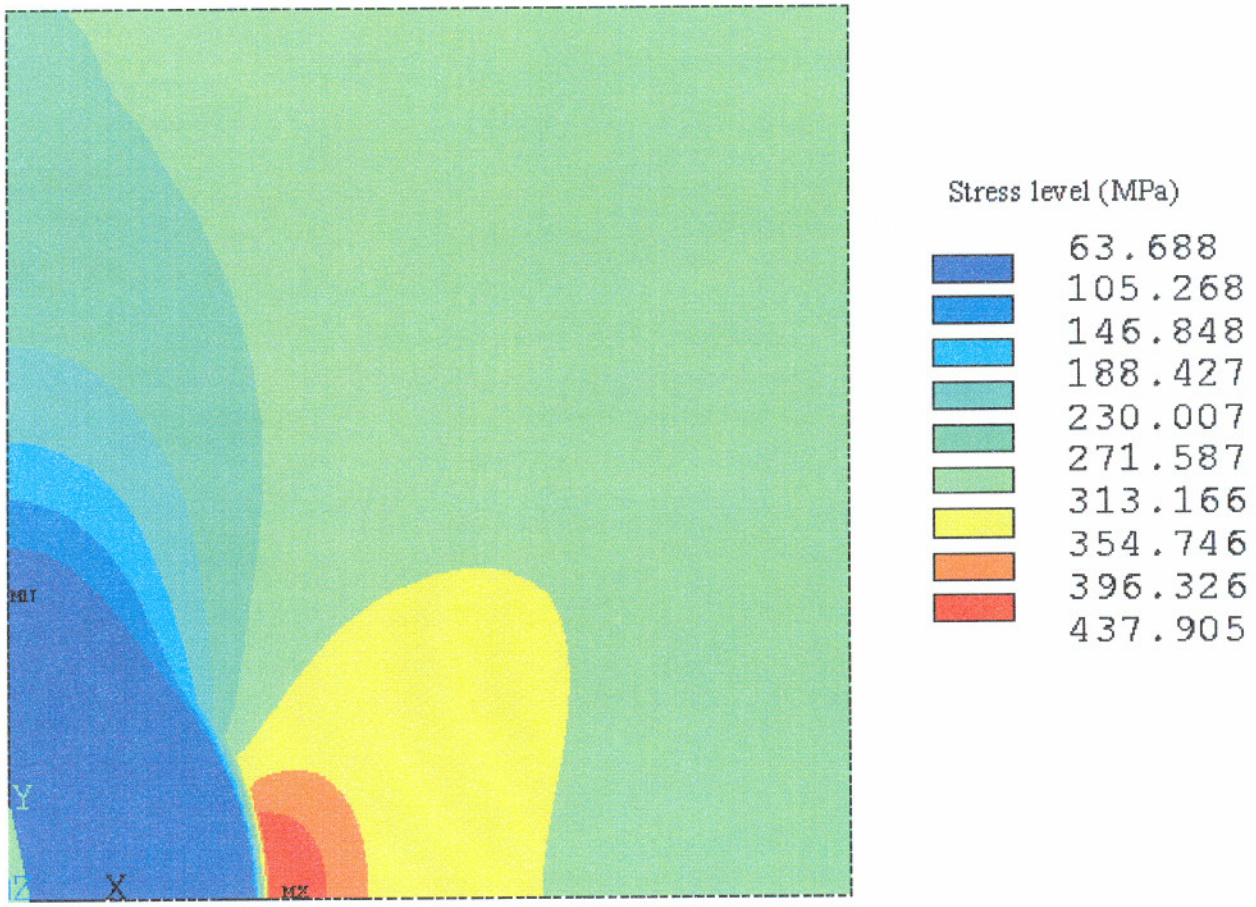

Figure 5-3 Normal stress contour around a graphite particle (Applied stress = 300 MPa).

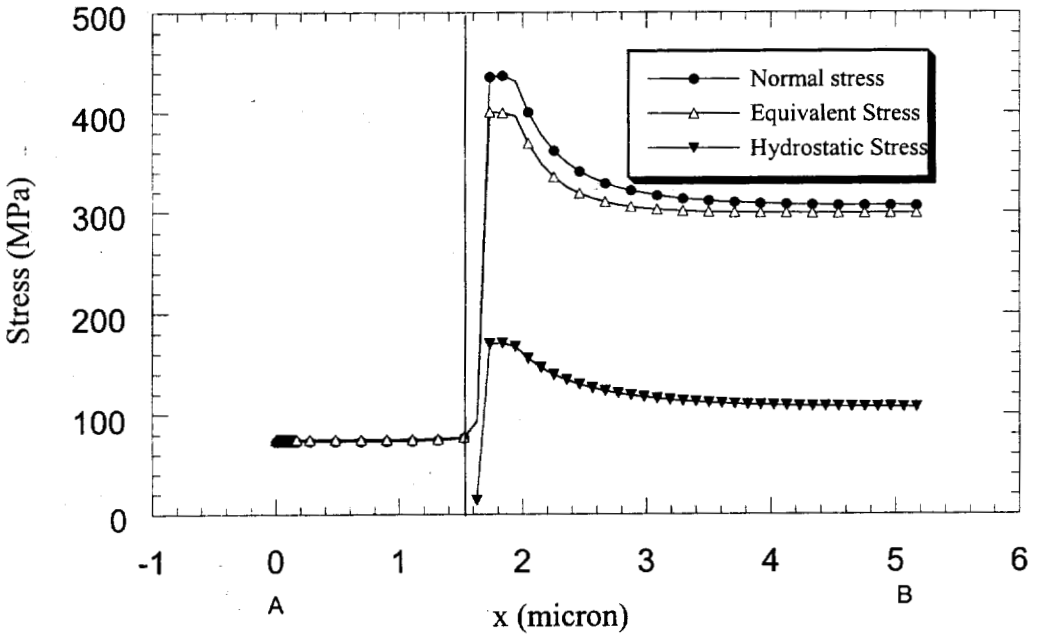

(a) Stress distribution along Axis AB

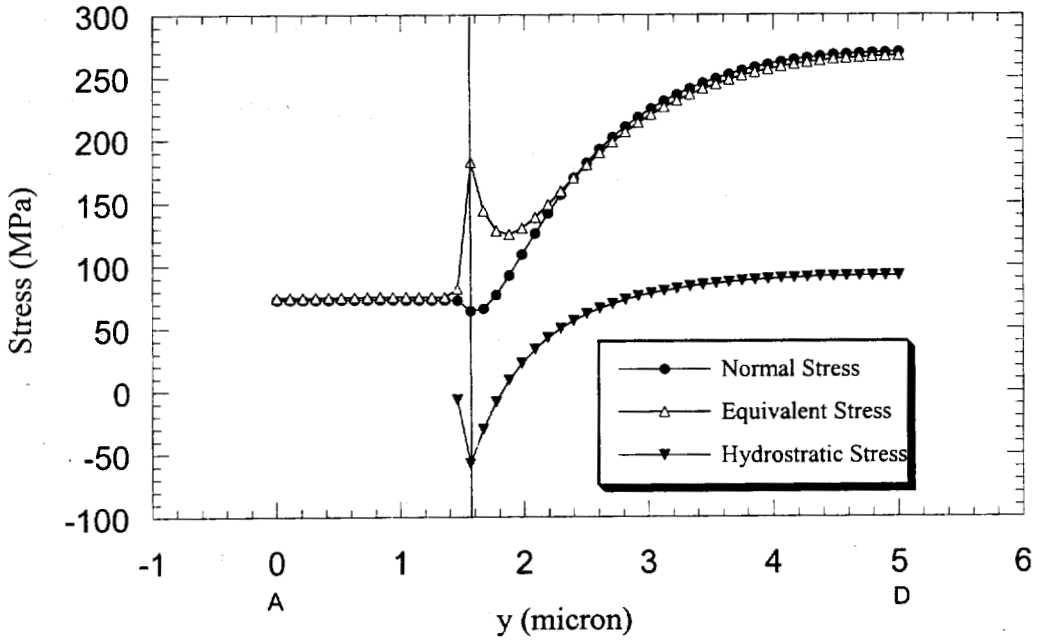

(b) Stress distribution along Axis AD

Figure 5-4 Stress distribution in the steel with a graphite particle (Applied Stess = 300 MPa).

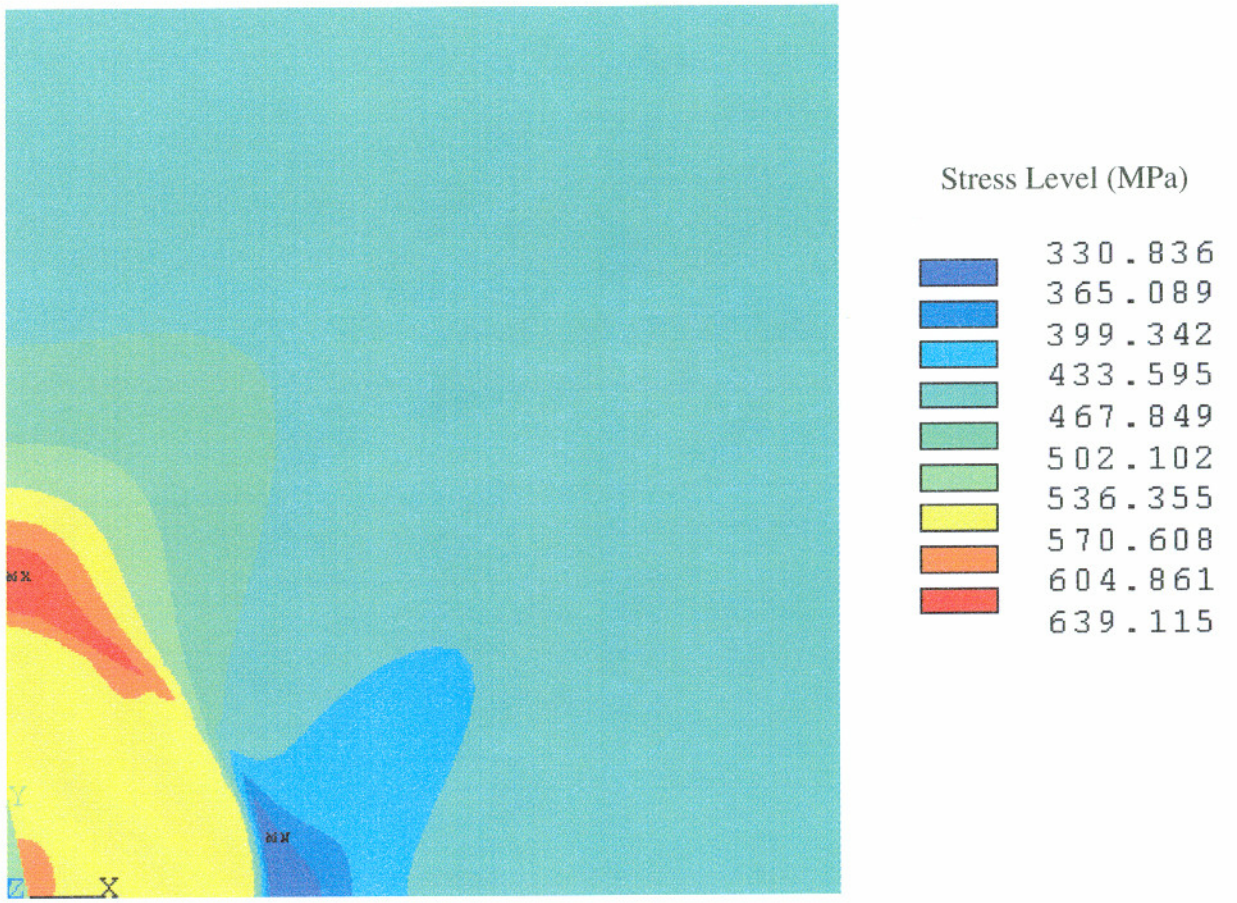

Figure 5-5 Normal stress contour around a graphite particle (Applied stress = 450 MPa).

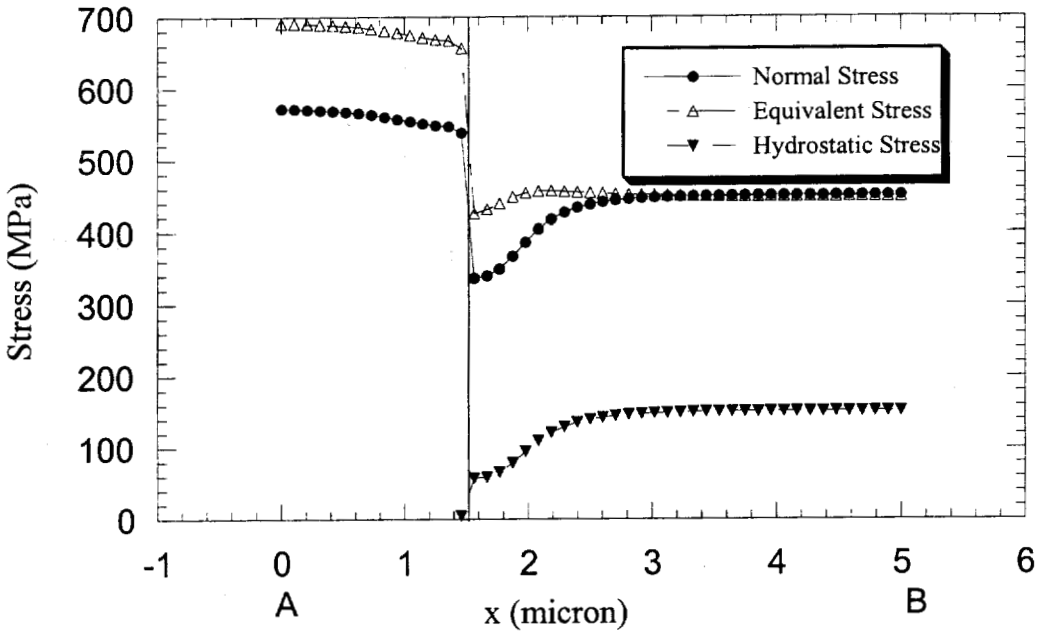

(a) Stress distribution along Axis AB

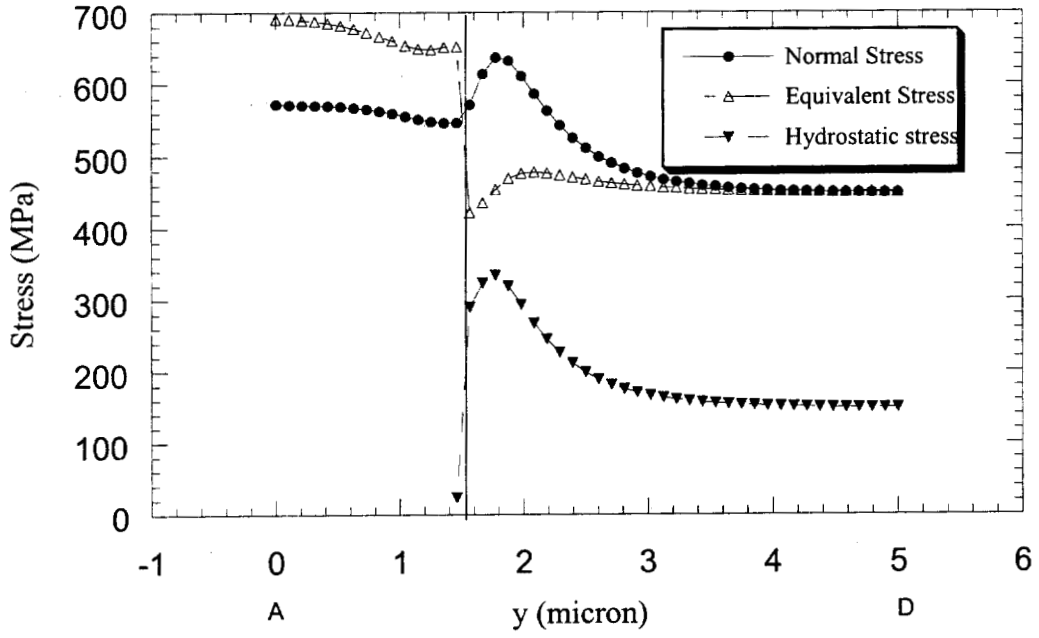

(b) Stress distribution along Axis AD

Figure 5-6 Stress distribution for a steel matrix with a graphite particle (Applied Stress = 450 MPa)

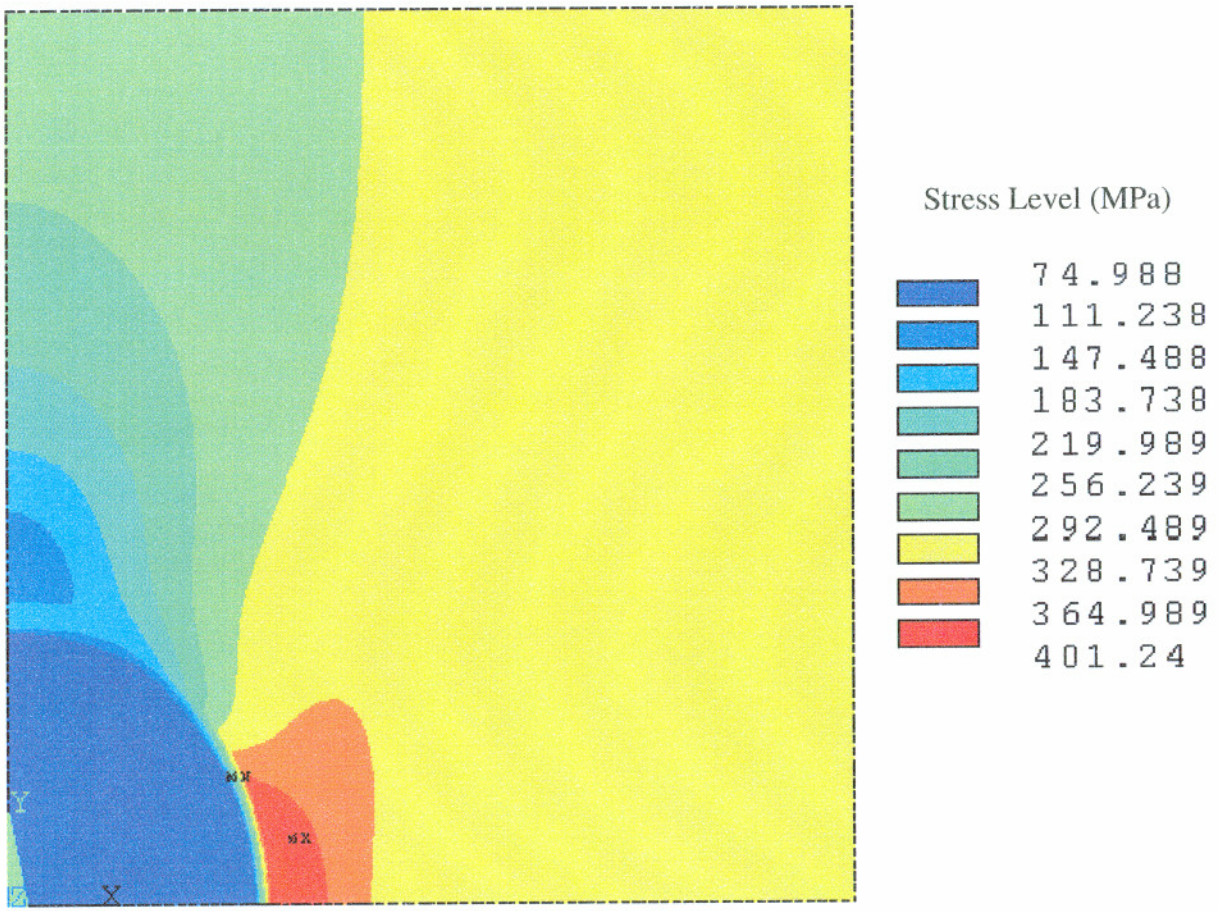

Figure 5-7 Equivalent stress contour around a graphite particle (Applied stress = 300 MPa).

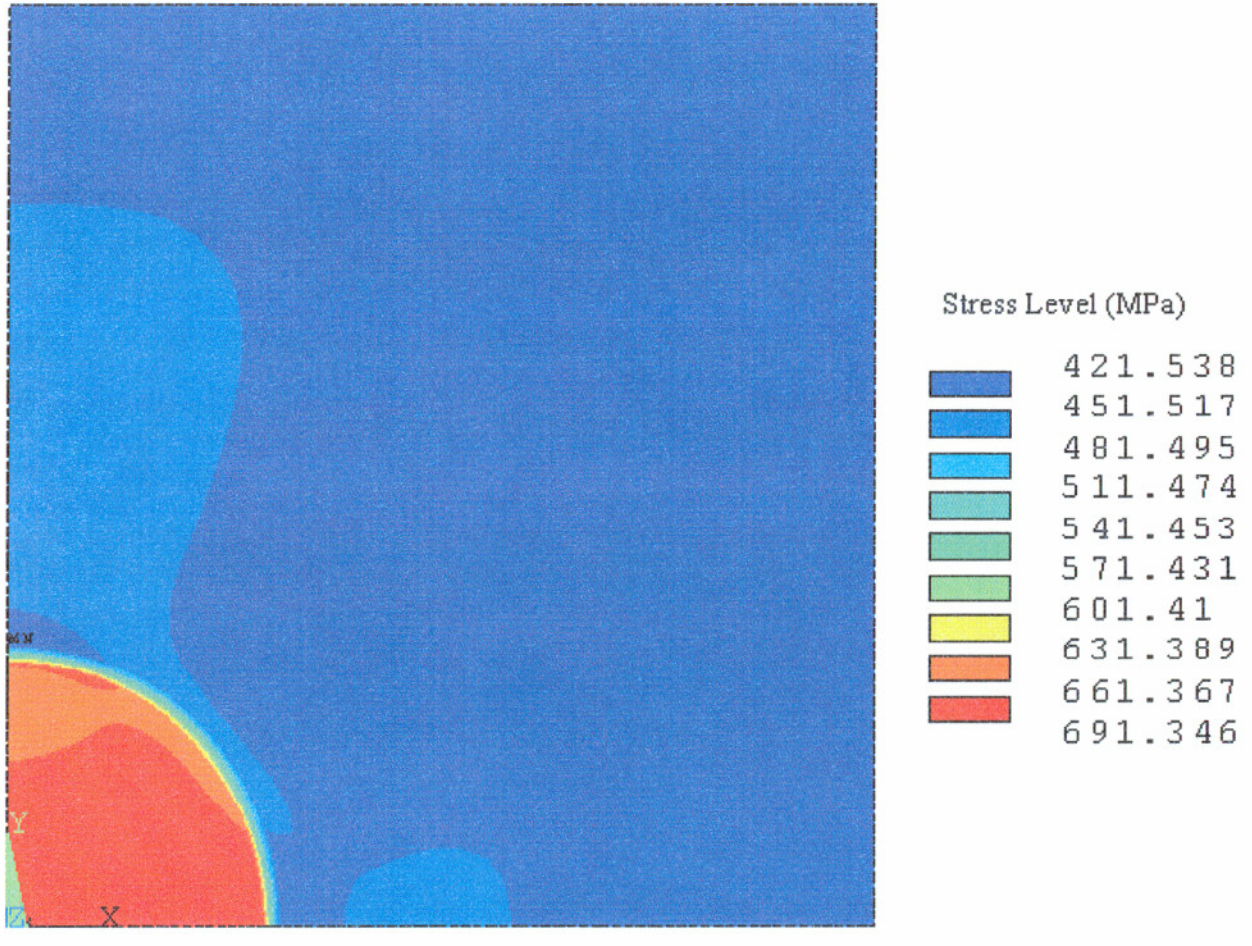

Figure 5-8 Equivalent stress contour around a graphite particle (Applied stress = 450 MPa).

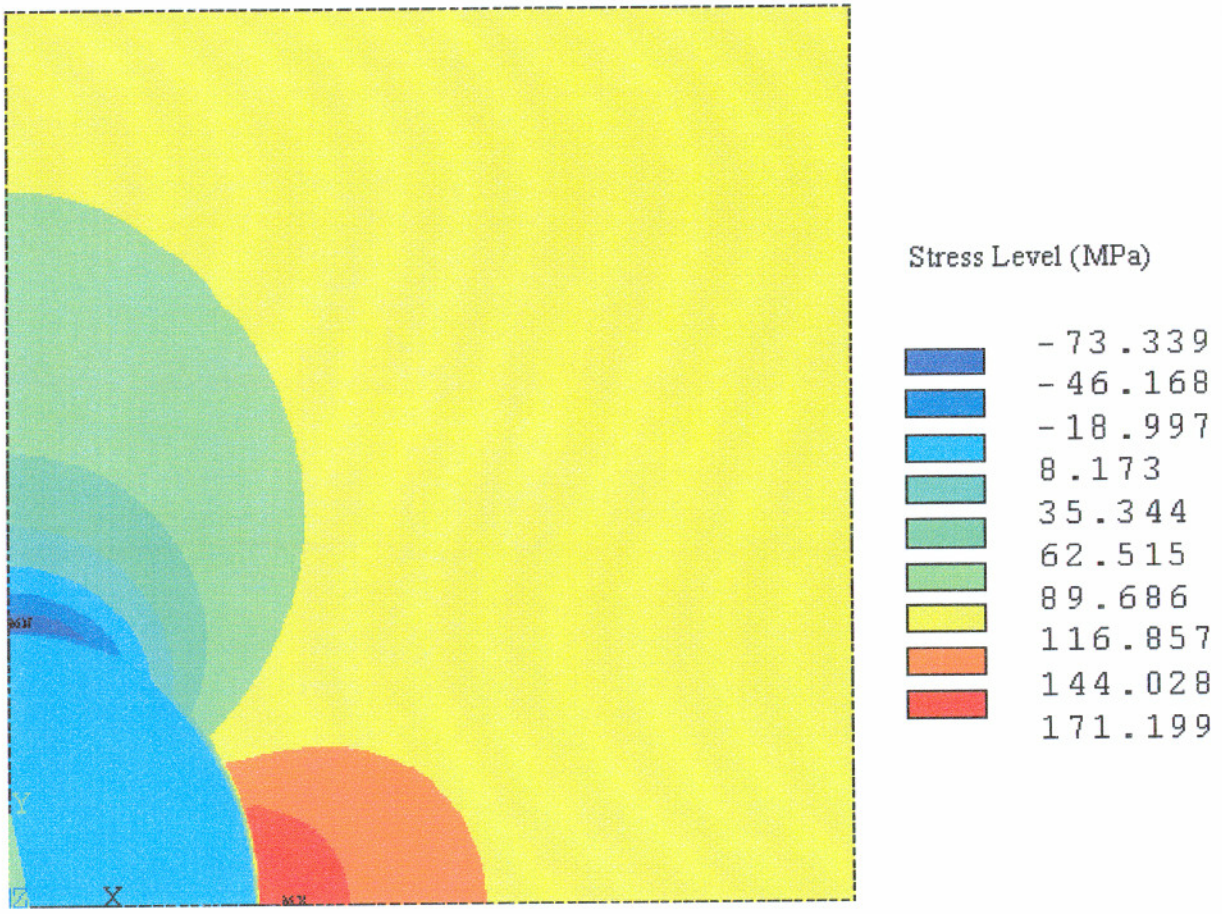

Figure 5-9 Hydrostatic stress contour around a graphite contour (Applied stress = 300 MPa).

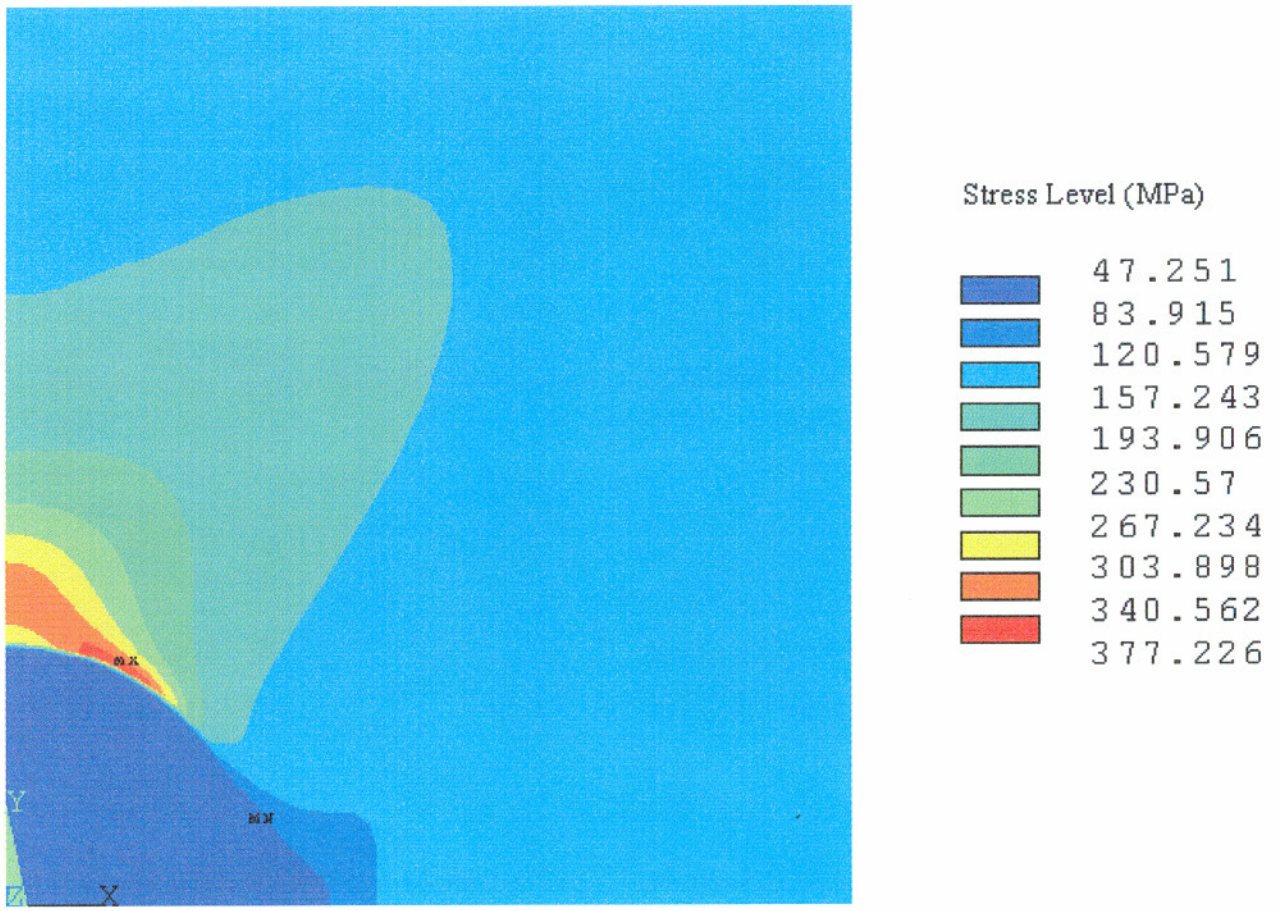

Figure 5-10 Hydrostatic stress contour around a graphite particle (Applied stress = 450 MPa).

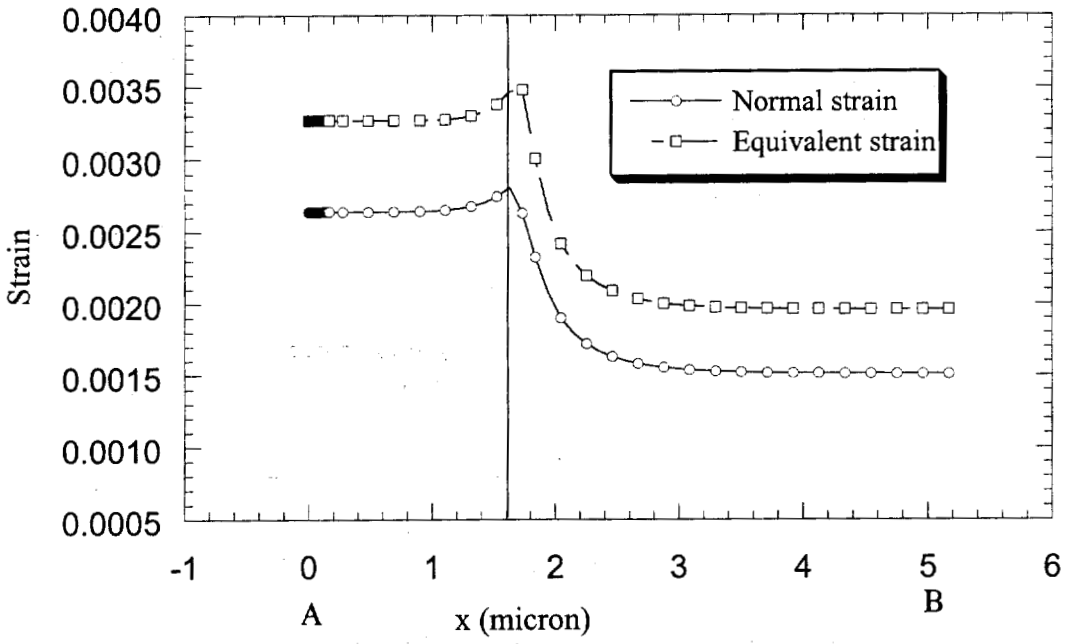

(a) Strain dstribution along Axis AB

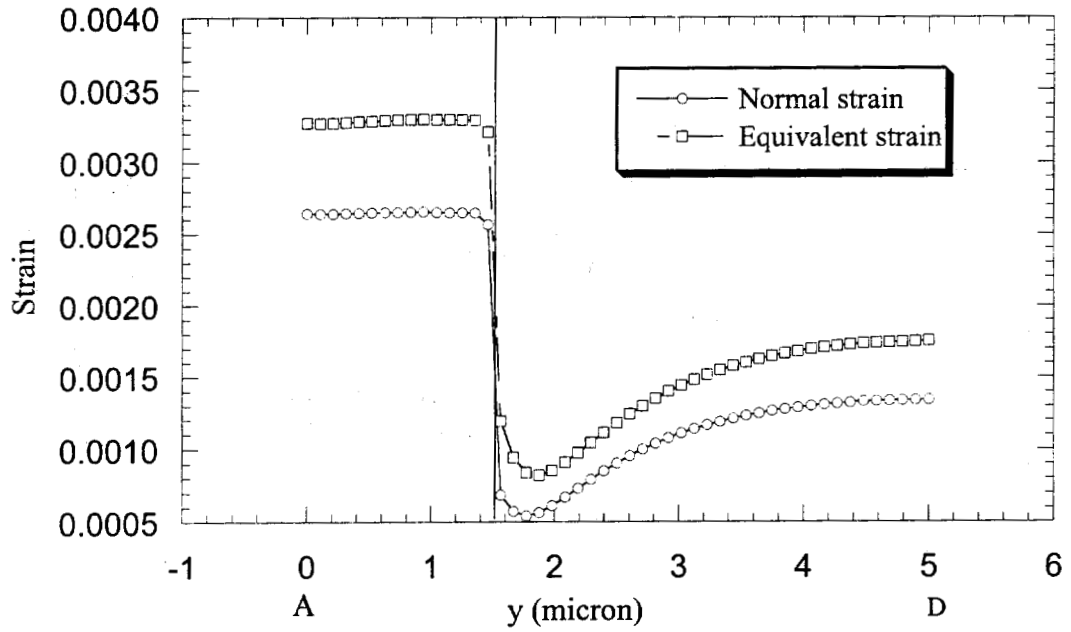

(b) Strain distribution along Axis AD

Figure 5-11 Strain distribution for a steel matrix with a graphite particle (Applied Stress = 300 MPa).

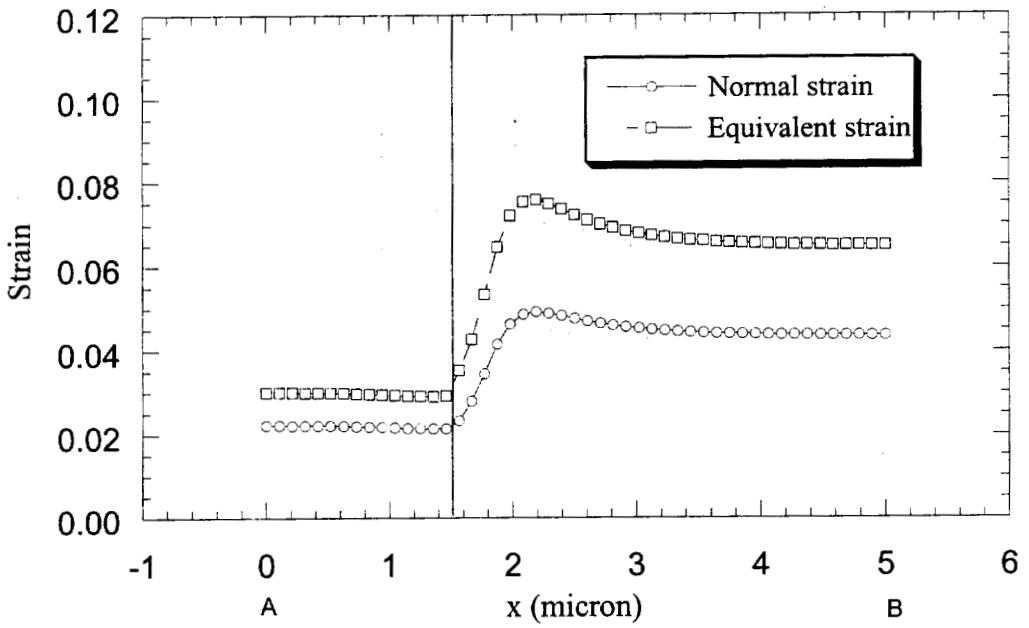

(a) Strain distribution along Axis AB

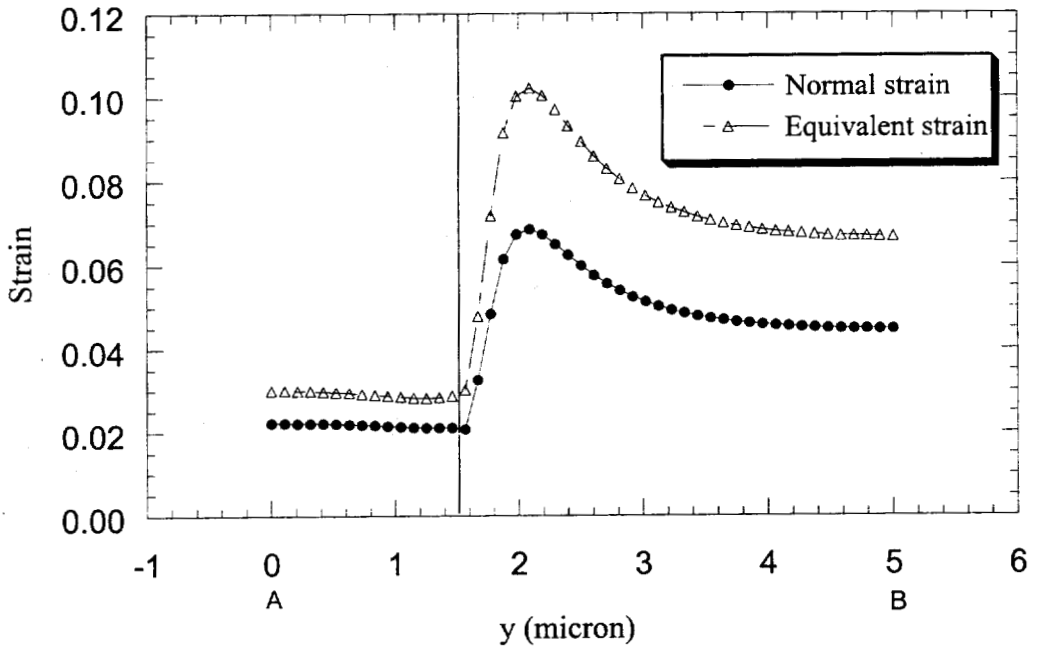

(b) Strain distribution along Axis AD

Figure 5-12 Strain distribution for a steel matrix with a graphite particle (Applied Stress = 450 MPa).

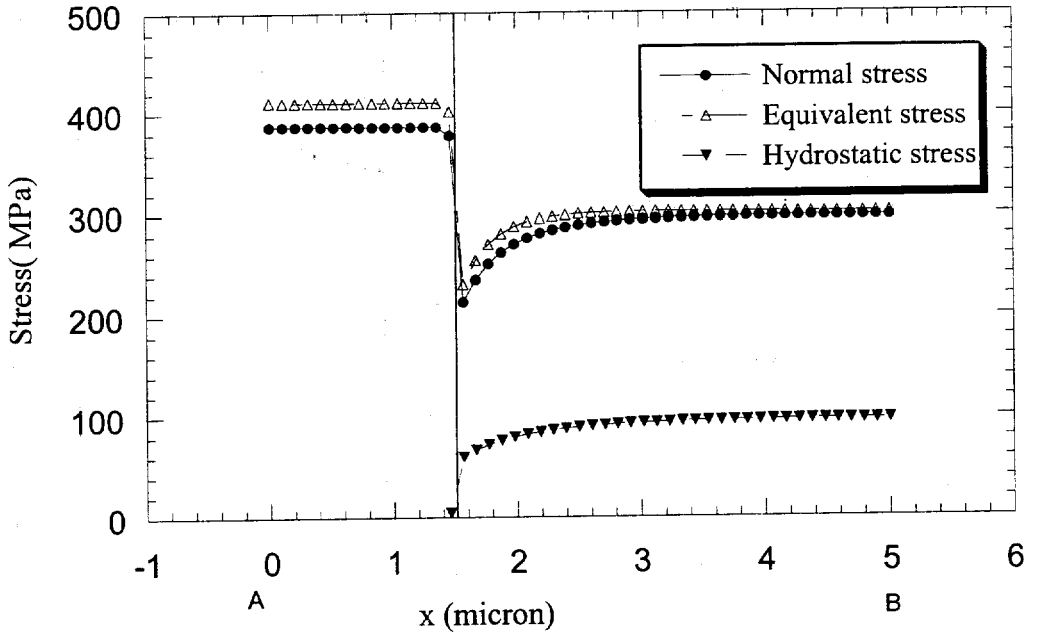

(a) Stress distribution along Axis AB

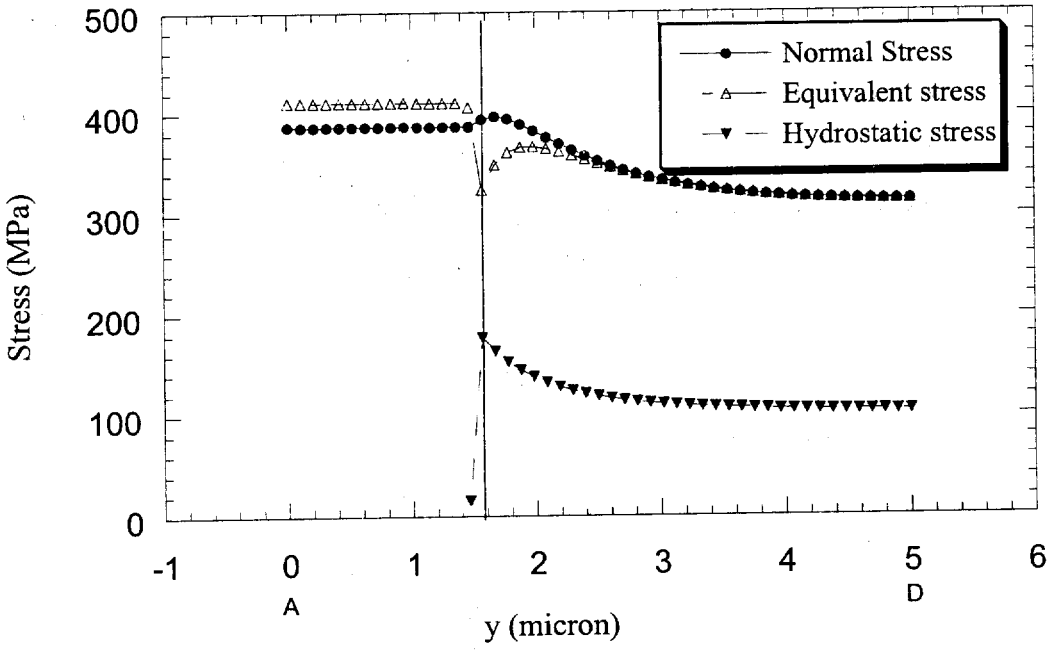

(b) Stress distribution along Axis AD

Figure 5-13 Stress distribution for a steel matrix with an Al_2O_3 particle. (Applied Stress = 300 MPa)

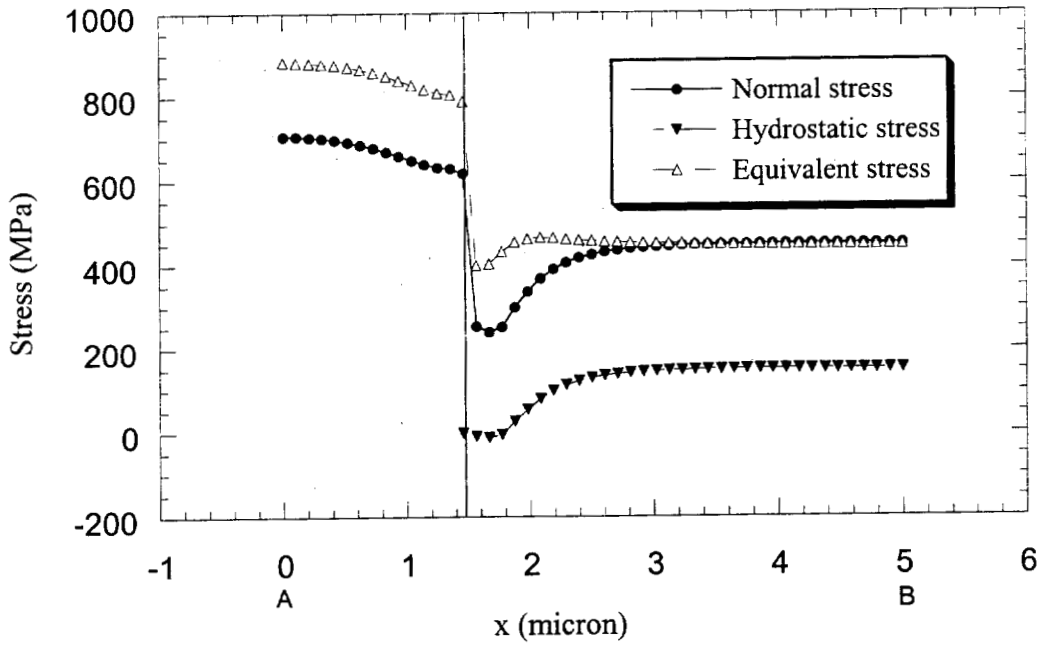

(a) Stress distribution along Axis AB

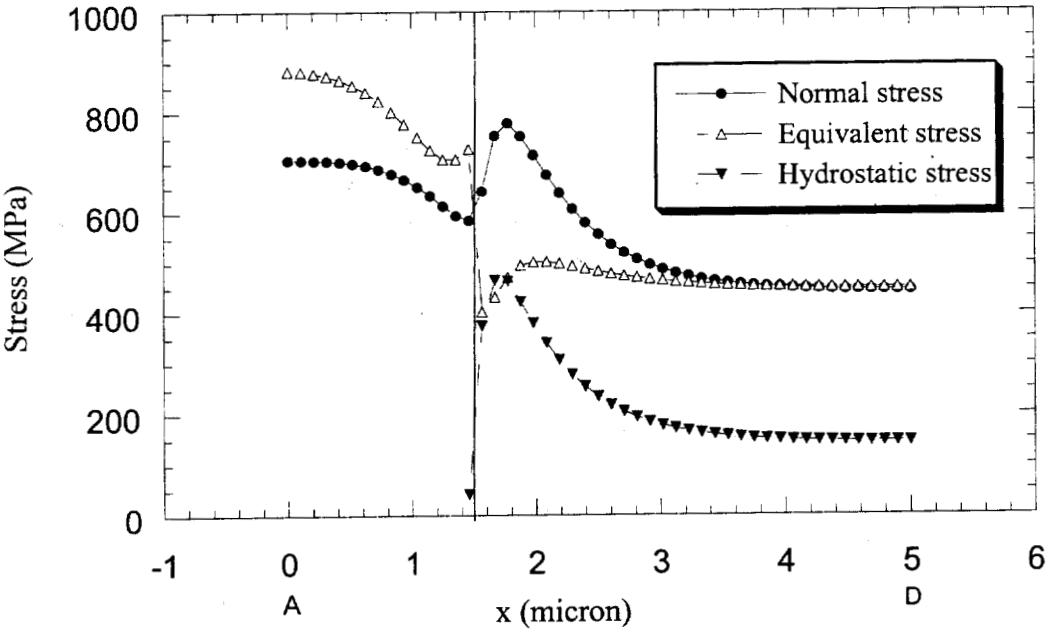

(b) Stress distribution along Axis AD

Figure 5-14 Stress distribution for a steel matrix with an Al_2O_3 particle (Applied Stress = 450 MPa)

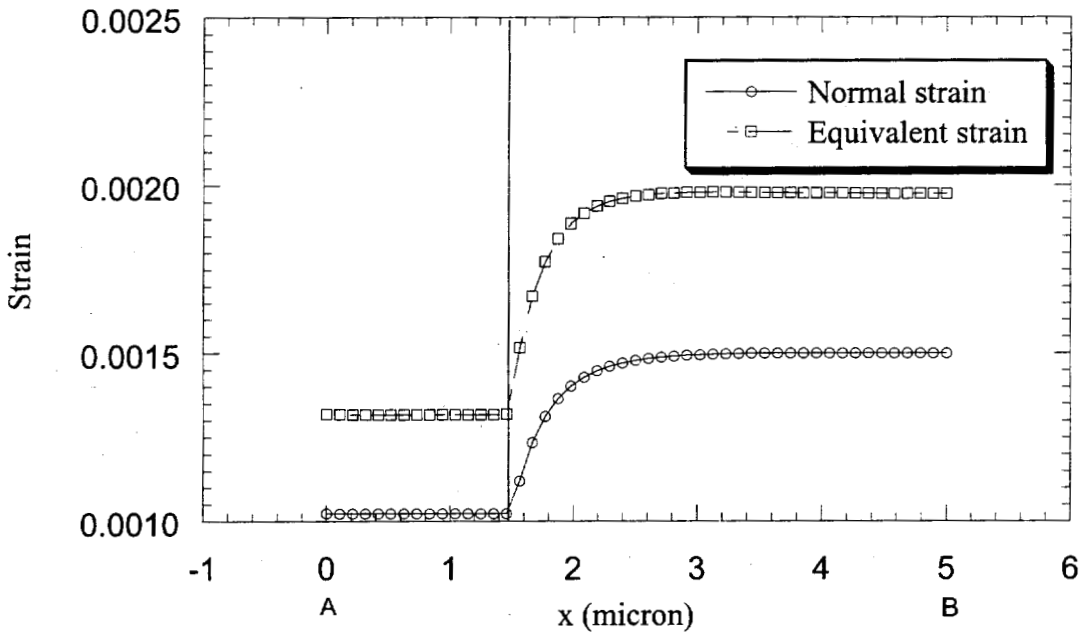

(a) Strain distribution along Axis AB

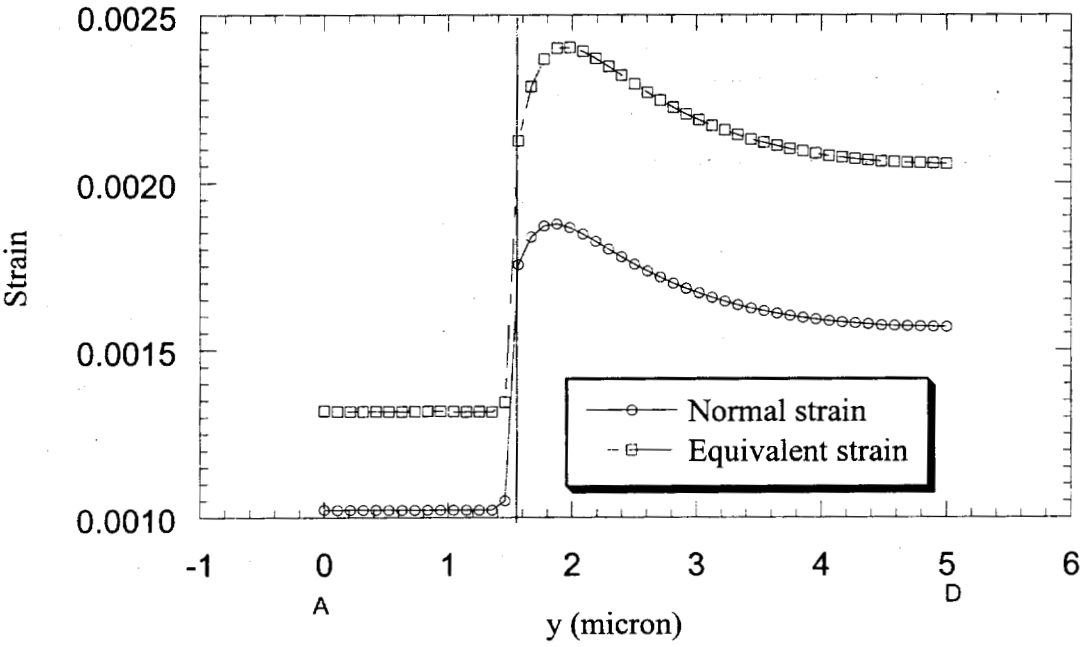

(b) Strain distribution along Axis AD

Figure 5-15 Strain distribution for a steel matrix with an Al_2O_3 particle (Applied Stress = 300 MPa)

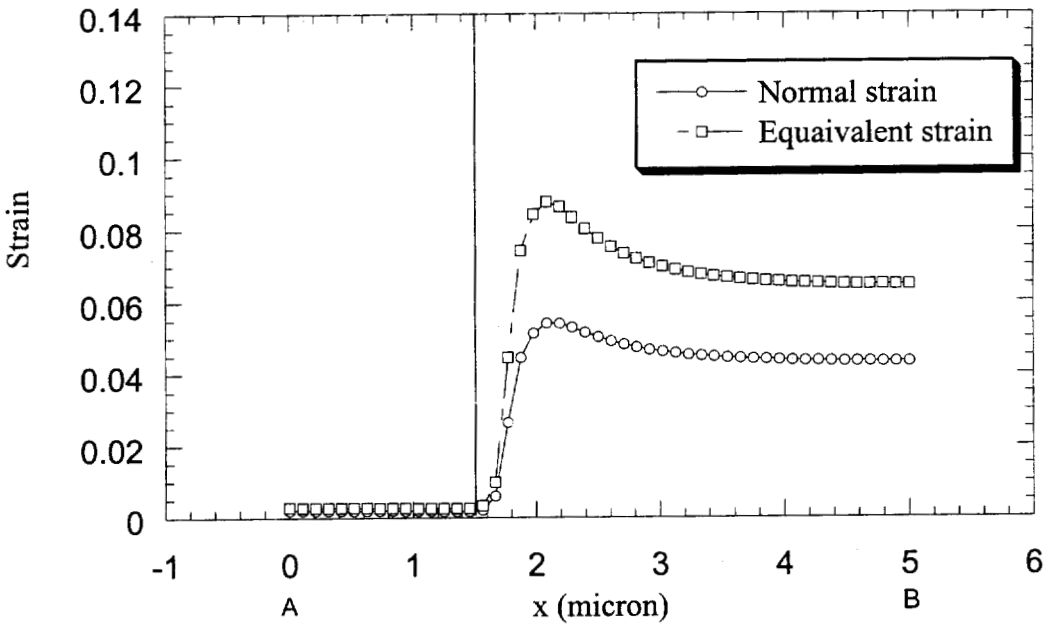

(a) Strain distribution along Axis AB

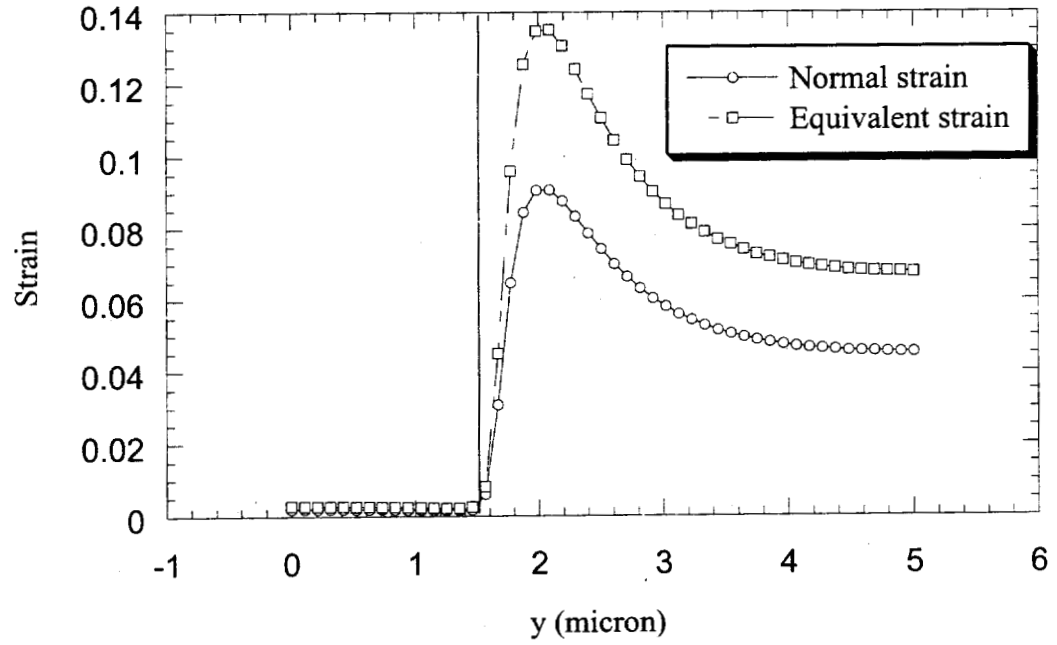

(b) Strain distribution along Axis AD

Figure 5-16 Strain distribution for a steel matrix with an Al_2O_3 particle (Applied Stress = 450 MPa)

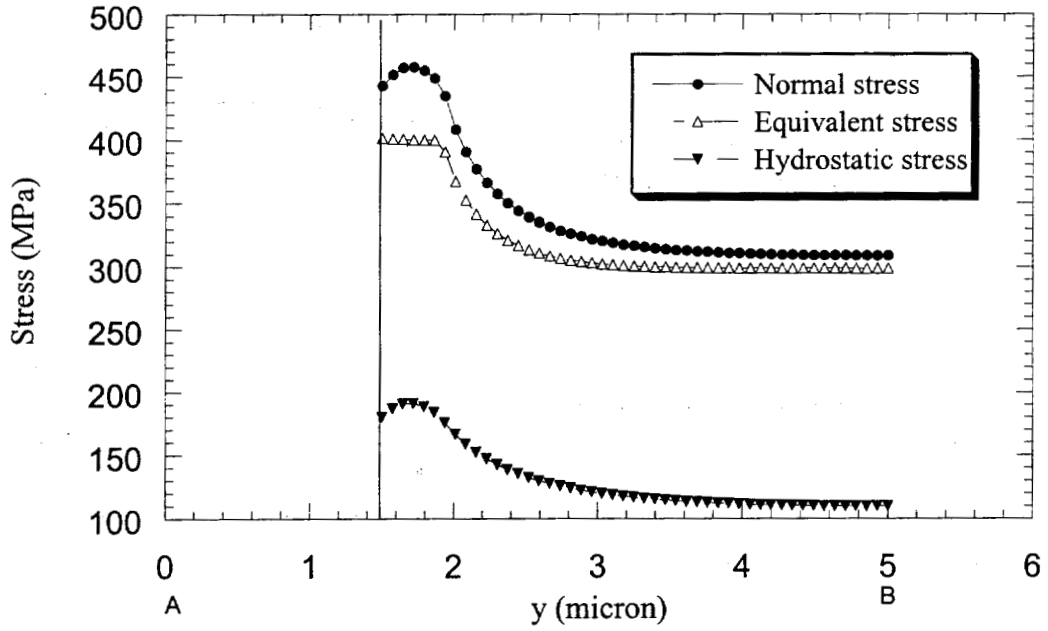

(a) Stress distribution along Axis AB

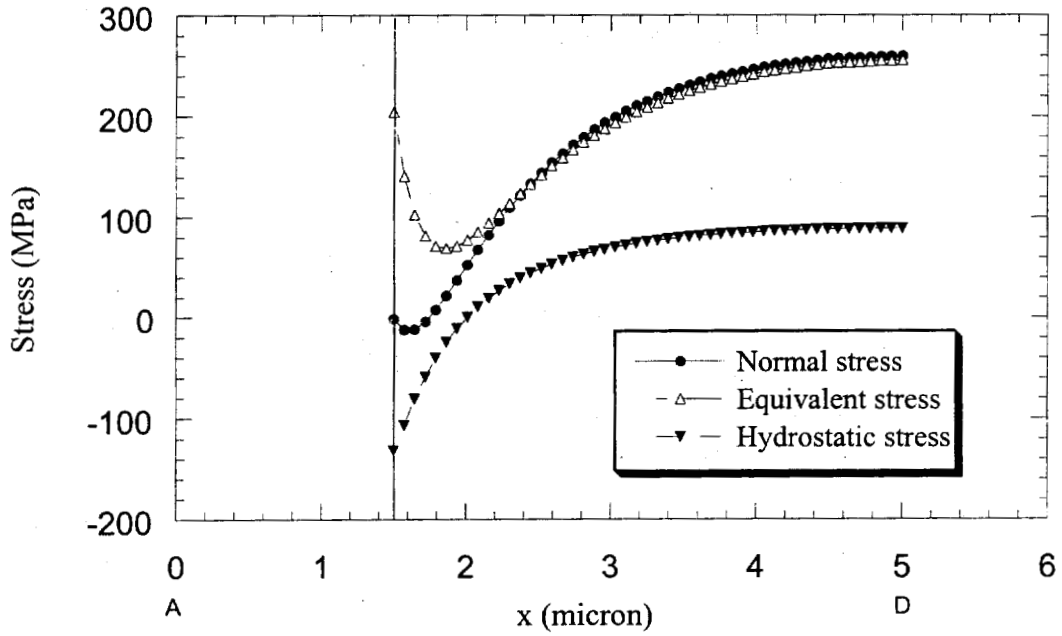

(b) Stress distribution along Axis AD

Figure 5-17 Stress distribution for a steel matrix with a void (Applied Stress = 300 MPa).

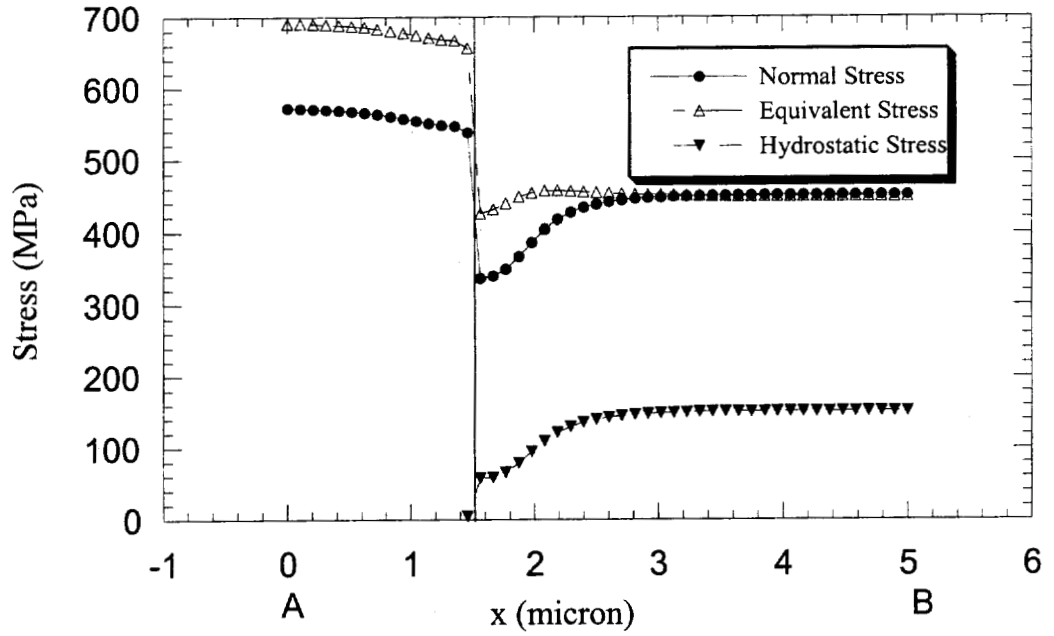

(a) Stress distribution along Axis AB

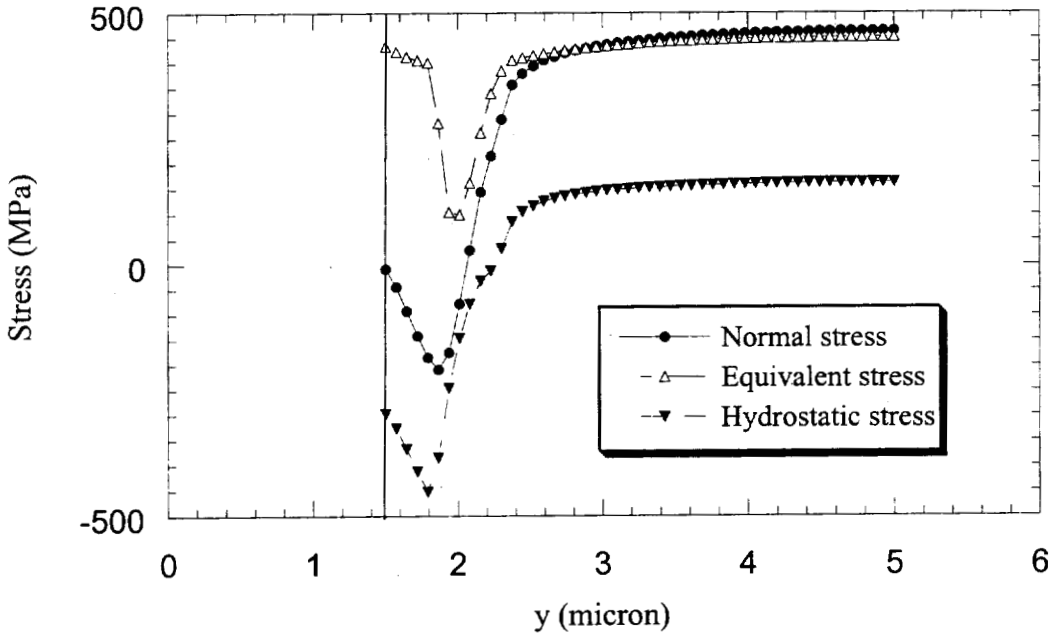

(b) Stress distribution along Axis AD

Figure 5-18 Stress distribution for a steel matrix with a void (Applied Stress = 450 MPa).

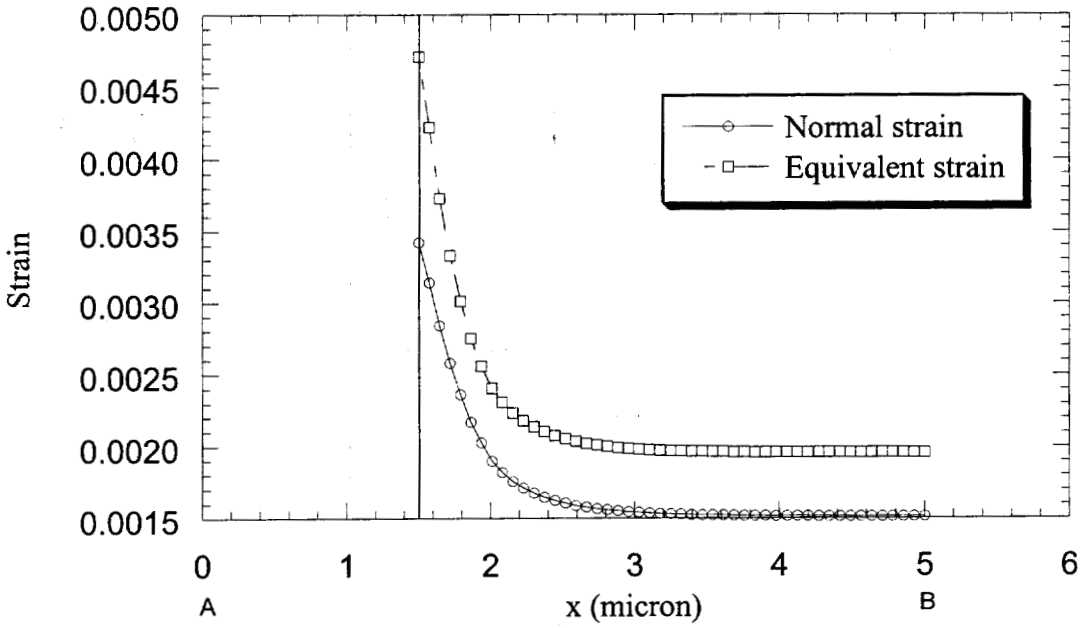

(a) Strain distribution along Axis AB

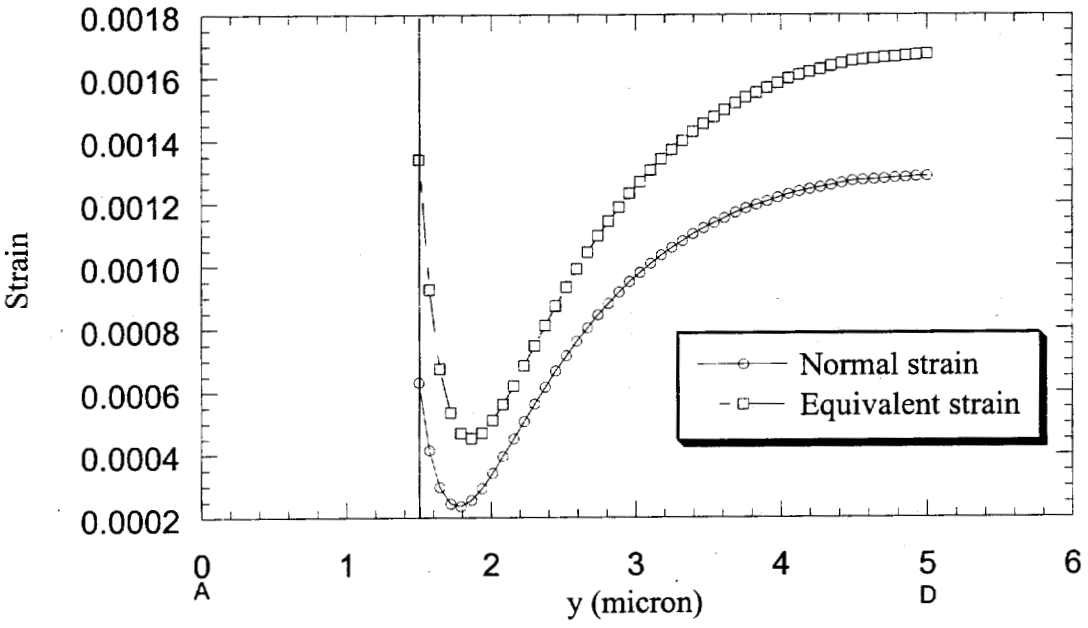

(b) Strain distribution along Axis AD

Figure 5-19 Strain distribution for a steel matrix with a void (Applied Stress = 300 MPa).

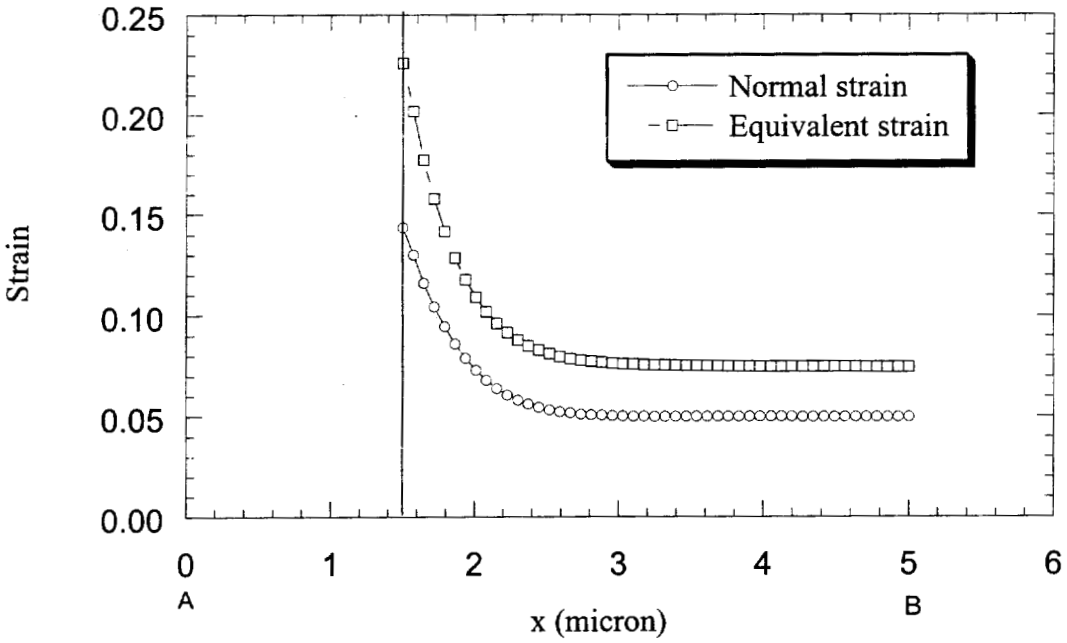

(a) Strain distribution along Axis AB

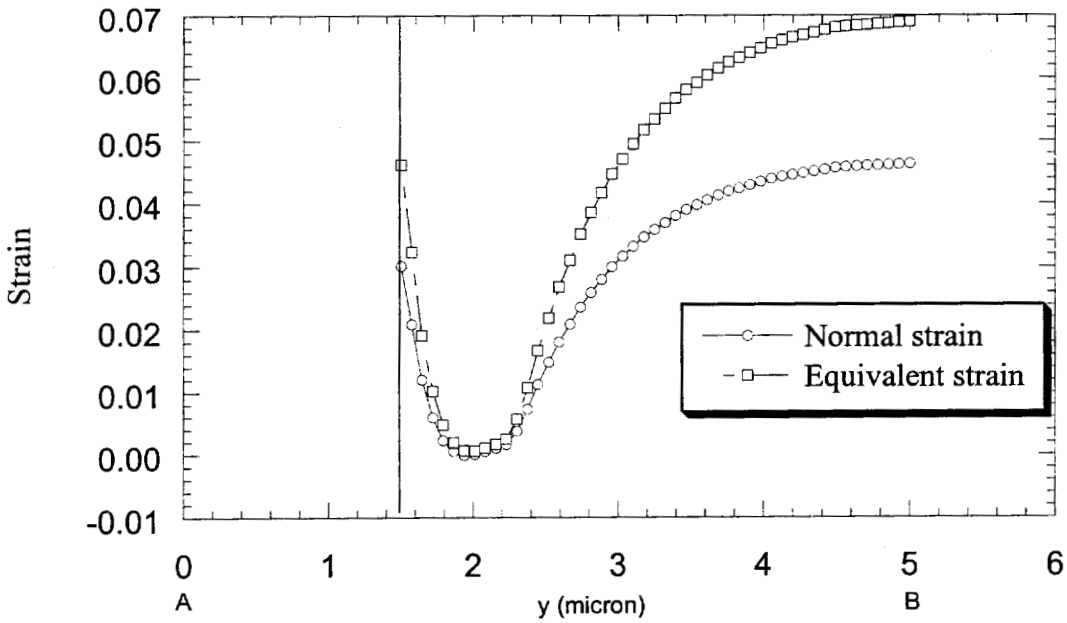

(b) Strain distribution along Axis AD

Figure 5-20 Strain distribution for a steel matrix with a void (Applied Stress = 450 MPa).

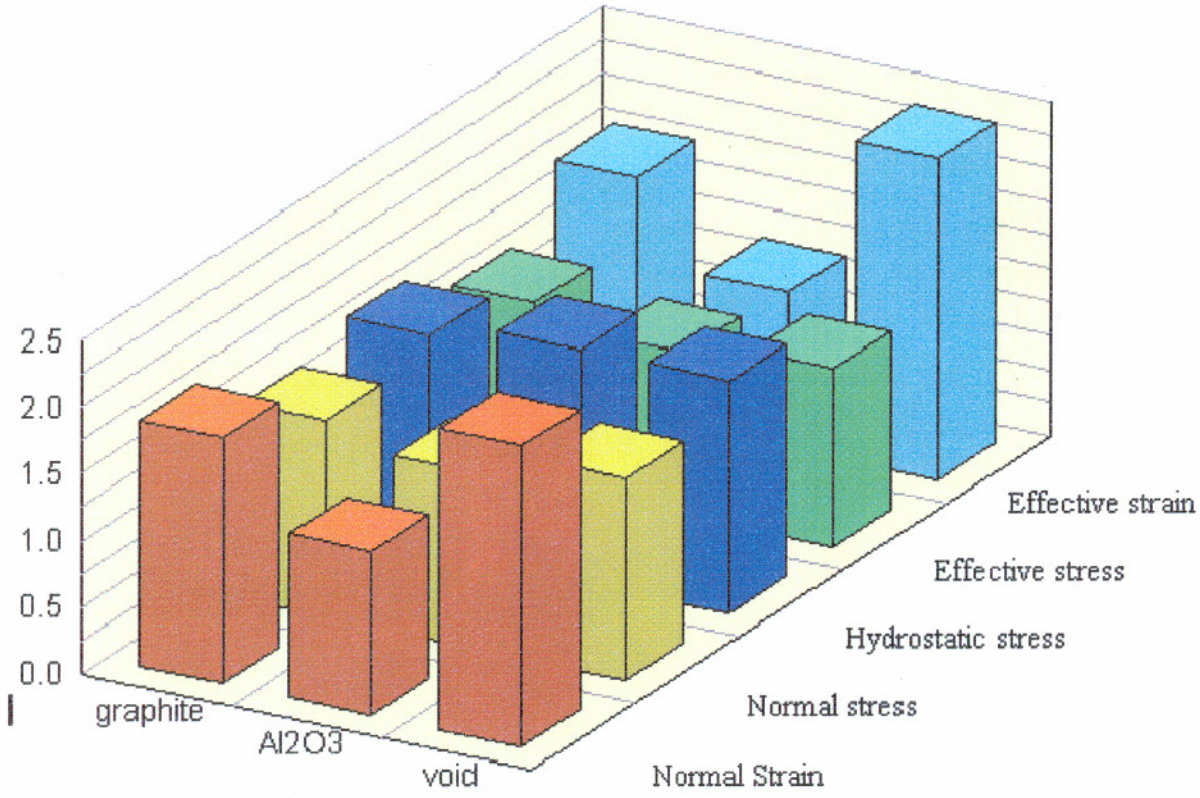

Figure 5-21 Stress and strain concentration factors in the steel matrix with graphite, or Al_2O_3, void (Applied stress = 300 MPa).

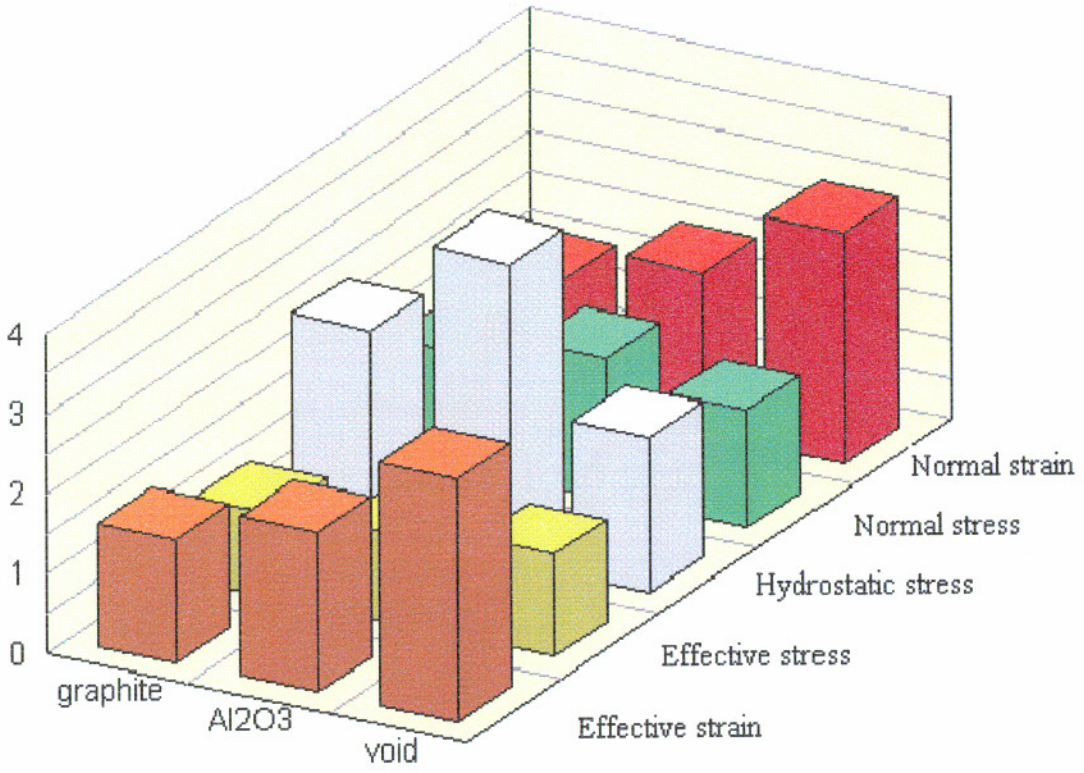

Figure 5-22 Stress and strain concentration factors in the steel matrix with graphite, or Al_2O_3, void (Applied stress = 450 MPa).

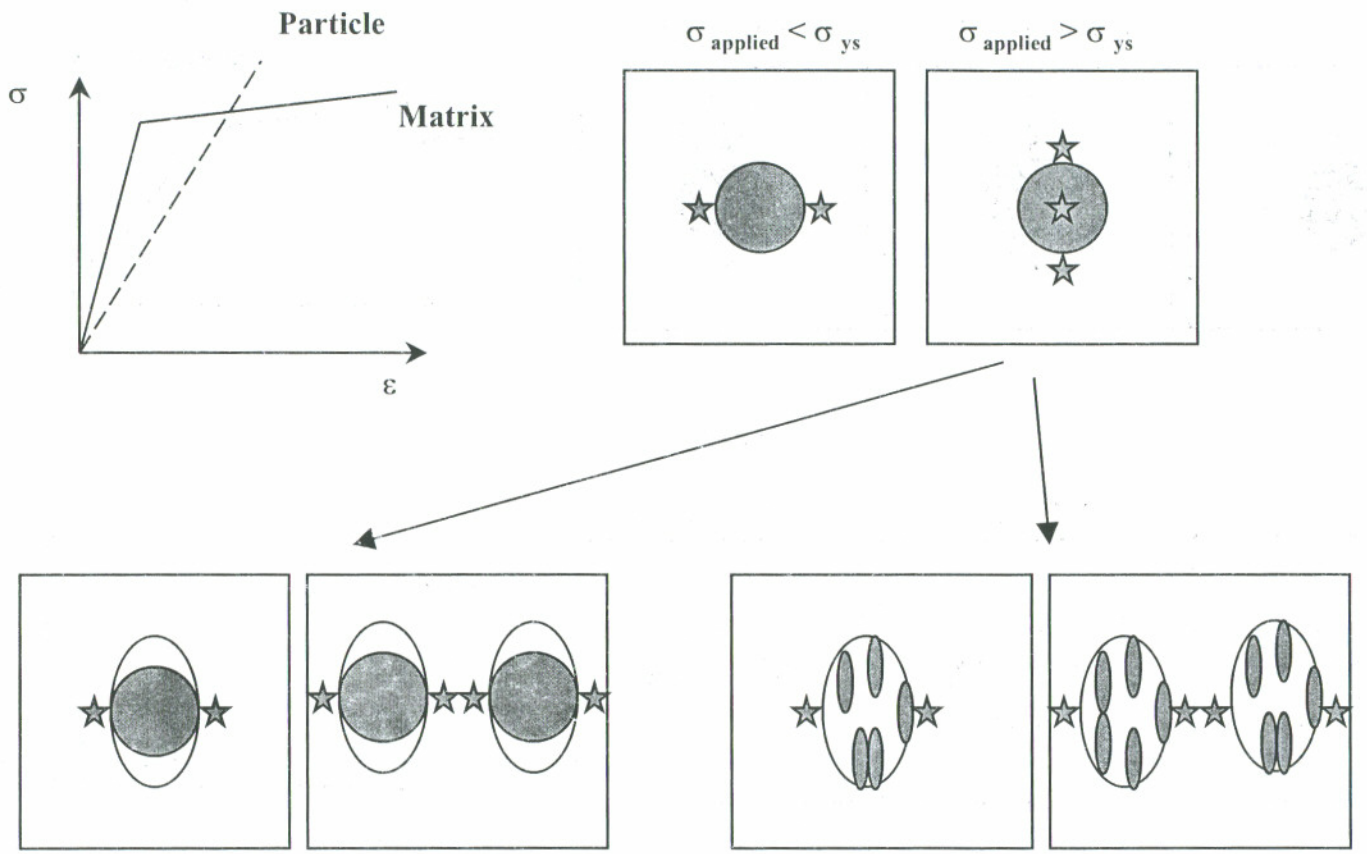

(a) Graphite

Figure 5-23 Relationship between failure modes and materials properties.

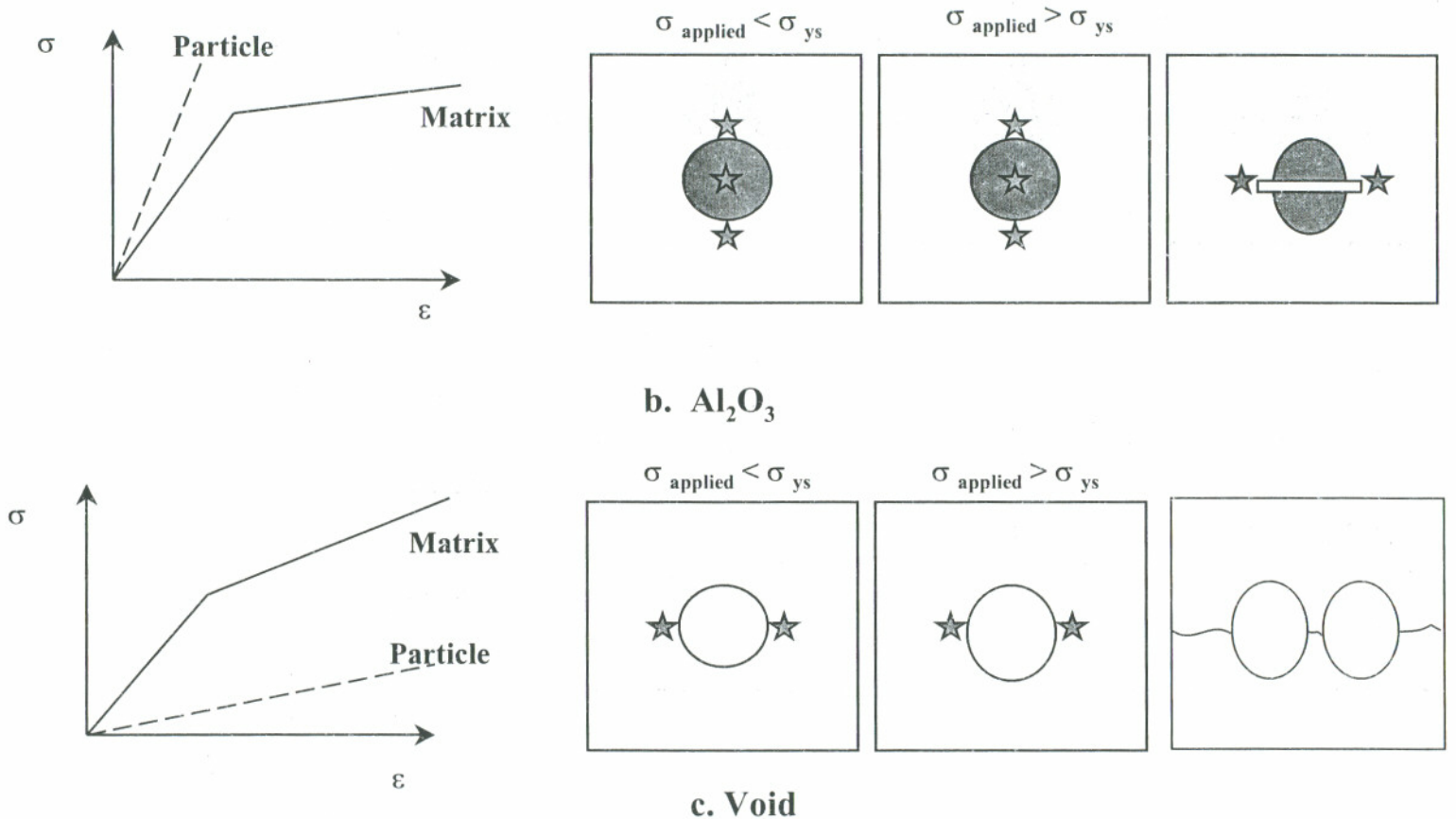

Figure 5-23 Relationship between failure modes and materials properties.

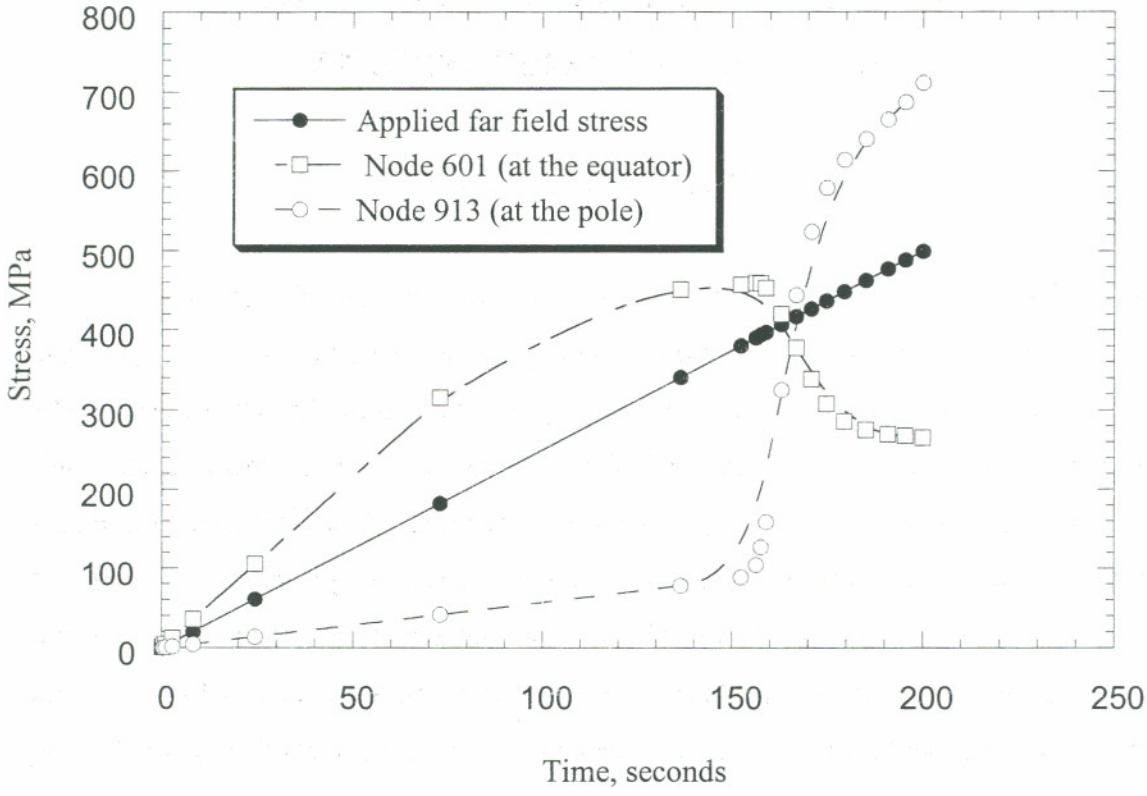

Figure 5-24 Stresses at the graphite pole and equator as a function of the applied far field stress (A transient analysis on unit cell model of the steel matrix with a graphite particle).

CHAPTER 6
THE INTERACTION BETWEEN CRACKS AND SECOND PHASE PARTICLES

6.1 INTRODUCTION

In the past 20 years, numerical modeling has become an important tool in fracture analysis, since relatively few practical problems have closed-form analytical solution. For a body is subject to either plane stress or plane strain loading, and composed of an isotropic linear elastic material, it may be possible to find a stress function that leads to the desired solution. Westergard[134] and Williams[135] used such an approach to derive solutions for stresses and strains near the tip of a sharp crack in an elastic material. Linear elastic fracture mechanics are invalid for blunt cracks because LEFM theory assumes sharp cracks. For the problems with complex material properties (such as elastic-plastic properties and multiple phases), complex boundary conditions and geometry, closed-form solutions are not possible, the stresses and strains must be estimated numerically. Hu[136] et al used superposition to solve the crack and inclusion interaction problems. However, his method only works for elastic bodies.

The fracture toughness of normally homogeneous materials has been the subject of countless experimental investigation and theoretical studies based on continuum mechanics. It is well known, fracture toughness for a given material is a function of constraint (or triaxiality of stress state) which in turn is affected by geometrical variables such as relative crack size, sample geometry. In reality, materials are heterogeneous. For a deeper

understanding and qualification of the underlying process, microscopic heterogeneity has to be taken into account. Currently, the crack growth mechanisms for both ductile fracture and cleavage fracture involve the effects of the second phase particles near the front of a crack[137]. As a cracked structure is loaded, local strains and stresses at the crack tip become sufficient to nucleate voids or microcracks. For ductile fracture, these voids grow as the crack blunts, and they eventually link with the main crack. As this process continues, the crack grows. For cleavage fracture, microcracks in second phase particles propagate into matrix, causing failure by cleavage. The nucleation of microcracks or voids is dependent of the stress and strain field around second phase particles. Most researchers only considered the effect of a crack on the stress and stain distribution and ignored the interaction between crack and second phase particles. Localized stresses around the particles which can be generated from the elastic and/or thermal mismatch between the particle and the matrix were neglected. The crack tip stress intensity factors would be influenced by the localized stresses. Depending on the localized stresses, a crack path would be changed either attracted or repelled by the particles. When the particles have a higher thermal expansion and higher elastic modulus, a crack has a tendency to be repelled and propagate around the particles[138]. Also, large inclusions break first and create larger dimples. Therefore, the relationship between cracks and particle material properties, size and distribution are very important for understanding the crack growth mechanisms. Kim el al [139] using boundary element method studied the interaction of crack/SiC particles in Al_2O_3 matrix and the interaction of crack/Al_2O_3 particles in SiC matrix. To avoid complicated problems, they neglected the difference of elastic properties between the matrix and the particle, and only considered thermally induced residual stresses. Their simulation was only suited for cases for which the particles and matrix have similar elastic properties and no plastic deformation involved.

To date, the role of graphite and its damage effect on the fracture toughness of cast iron and steel remain unclear. The mechanical properties of steel matrix and graphite are quite different as shown in Table 5-1. Dong et al[119] found that the initiation of voids at the graphite/matrix interface begins at an early stage of plastic deformation. Their main conclusion was that graphite nodules can be regarded as voids in numerical or analytical

modeling of constitutive behavior of cast iron. In the present study, a 2D plane stress model with a single particle near the tip of an edge crack in elastic-plastic steel matrix was used to study the interactions between a graphite particle, Al_2O_3, void and a microcrack. Only mode I fracture toughness is involved in this model by using an edge crack and remote loading perpendicular to crack face. Two cases were studied: the initial crack is a sharp crack or a blunt crack. All calculations were conducted on a HP workstation using ANSYS finite element software (version 5.3). These calculations were not intended to model an actual component in service or a real experimental test for a given material with a certain geometry. The results of this study are rather designed to provide insight into basic mechanisms. The fracture toughness of the steel matrix with a sharp crack and a graphite particle was evaluated by J integral.

6.2 MESH DESIGN

A critical step in modeling the 2-D crack tip is the selection of the type of element used to represent the region surrounding the crack. If regular (i.e., nonsingular) elements are used in which the displacement-based approximations within each element are in a polynomial form, it is well known that the convergence rate is greatly retarded. In Ansys, triangular element (Plane 2) will lead to the square-root singularity of LEFM by moving mid-side nodes. The collapsed eight-noded isoparametric quadrilateral element (Plane 82) can be used to represent the 1/r singularity associated with elastic-perfectly plastic material behavior. For the case of work-hardening material response, it has been suggested that the use of singular elements will tend to over predict stresses and under predict strains near the crack tip. For that reason, regular elements in dense mesh are sometimes preferred for problems where high plastic strains are expected[140].

The regular Plane 2 element was chosen in this study which is a six-noded, quadratic triangular element. Figure 6-1 and 6-2 shows the finite element mesh of one half of a rectangular plate with sharp and blunt edge cracks loaded under uniaxial tension, respectively. A circular graphite particle was located in front of the crack tip. The Plane 2

elements were non-uniformly distributed. A smaller element size was chosen in the areas near the crack tip and around the graphite particle, because elastic-plastic problems require more mesh refinement in the regions of the body where yielding occurs. The calculations were carried out under the assumption of plane stress. For comparison, the same mesh was used for analysis of three other cases: (i) without a second phase particle, simply replacing the particle material properties with the matrix material properties, (ii) replacing graphite with Al_2O_3; and (iii) replacing graphite with voids.

A state of uniform axial tension was applied on the top lines in Figure 6-1 and 6-2. The lower lines were made a mirror symmetry line by fixing the y direction, but allowing it to stretch in the x direction. The crack tip is fixed in x direction to prevent rigid body motion. The crack tip was defined as a semicircle with the radius of 1 micron. The circular particle was located in front of the crack tip. The stress concentrations depend on crack length, crack sharpness, particle size, particle material properties, particle size, the spacing between the particle and crack. This study focused on the interaction between the particle and the crack and kept the crack length a fixed parameter.

6.3 J INTEGRAL EXTRACTION PROCEDURES

The procedures to extract fracture toughness parameters, such as stress intensity factor K and linear elastic energy release rate G, have been well established. J integral extraction is not as straightforward as these procedures and thus has rarely been used in finite element analysis. Also, the J integral result is more difficult to interpret. However, J integral has a great advantage that J integral can be used to evaluate the fracture toughness of materials no matter a material has a linear elastic or nonlinear elastic-plastic behavior and can be easily converted to the generally used parameter, stress intensity factor K in the linear elastic regime. In this study, J values were used to evaluate the potential for crack growth.

J integral in a two-dimensional form was simply defined by Rice[141]:

$$J = \int_{\Gamma} W dy - \int_{\Gamma} t_i \frac{\partial u_i}{\partial x} ds \tag{6-1}$$

$$t_i = \sigma_{ij} n_j \tag{6-2}$$

where Γ is any path surrounding the crack tip; t_i is the traction vector; u_i is the displacement vector; s is the distance along the path; n_i is the unit outer normal; σ_{ij} is the stress tensor.

For elastic materials:

$$W = \frac{1}{2}\sigma_{ij}\varepsilon_{ij} \tag{6-3}$$

For plastic materials:

$$\begin{aligned} W &= W^e + W^p \\ W^e &= \frac{1}{2}\sigma_{ij}\varepsilon_{ij}^e \\ W^p &= \int_0^{\varepsilon^p} \sigma d\varepsilon^p \end{aligned} \tag{6-4}$$

where W^e, and W^p are elastic strain energy density and plastic strain energy density, respectively, ε^p is the effective strain and σ is the effective stress.

In this study, J integral was extracted by using a modified APDL program recommended by Ansys (Ansys on-line help). APDL stands for Ansys Parametric Design Language which allows you to build your model in terms of parameters (variables). And thus, you can make design changes easily and conveniently. To extract J integral, two steps were taken in this program:

(1) Calculate the first term in the J definition Eq. (6-1):

$$\int_{\Gamma} W dy$$

(a) Store the volume and strain energy per element and then calculate strain energy density by:

W=element strain energy/element area(volume) (include nonlinear effects)

(b) Define a path for the line integral

(c) Map the strain energy density calculated by sub-step (a) onto the path.

(d) Integrate energy with respect to the global Y and obtain the first term in Eq. (6-1).

(2) Calculate the first term in the J definition equation:

$$\int_{\Gamma} t_i \frac{\partial u_i}{\partial x} ds$$

(a) Map the component stresses σ_x, σ_y, σ_{xy} onto the path;

(b) Define the path unit normal vector;

(c) Calculate the tractor t_x and t_y using the following equations:

$$t_i \frac{\partial u_i}{\partial x} = t_x \frac{\partial u_x}{\partial x} + t_y \frac{\partial u_y}{\partial x} \quad (6\text{-}5)$$

$$t_x = \sigma_x n_x + \sigma_{xy} n_y \quad (6\text{-}6)$$

$$t_y = \sigma_{xy} n_x + \sigma_y n_y \quad (6\text{-}7)$$

where t_x and t_y are the traction vectors along x axis and y axis, respectively;

(d) Shift the path a small distance in positive and negative X directions to calculate the derivatives of the displacement vector:

$$\frac{\partial u_x}{\partial x} = \frac{u_x^{(2)} - u_x^{(1)}}{\Delta x} \quad (6\text{-}8)$$

$$\frac{\partial u_y}{\partial x} = \frac{u_y^{(2)} - u_y^{(1)}}{\Delta x} \quad (6\text{-}9)$$

$$u_i^{(1)} = u_i \big|_{\Gamma - \Delta X/2} \quad (6\text{-}10)$$

$$u_i^{(2)} = u_i \big|_{\Gamma + \Delta X/2} \quad (6\text{-}11)$$

(e) Use the result from sub-step (c) and (d) to calculate the integrand in the term of J and integrate it with respected to the path distances. This gives the second term of Eq.

(6-4)

To maintain the validity, the following requirements were met during J calculation:

(1) The material properties of matrix are isotropic;

(2) No unloading should occur in our elastic-plastic analysis;

(3) All loading should be static;

(4) The deformation is independent of time:

(5) The plastic deformation is in the same magnitude as the elastic deformation.

6.4 RESULTS AND DISCUSSION

6.4.1 STRESS AND STRAIN DISTRIBUTION AT A SHARP CRACK TIP

6.4.1.1 Stress and Strain Distribution Without a Particle

First, to provide a comparison for the particle/crack interaction study, the stress and strain distributions at a sharp crack tip along the path (θ=0) without a particle were investigated. Figure 6-3 and 6-4 presents the normal stress and strain results respectively when the applied stress was 1/4 of the steel yield strength. Under this loading level, the steel should mainly exhibit its linear elastic characteristics. Curve fitting results shows that the stress and strain can be described by

$$\sigma_y = 267.12\, r^{-0.5190} \qquad R = 99.9\% \qquad (6\text{-}12)$$

$$\varepsilon_y = 1.041 \times 10^{-3}\, r^{-0.4999} \qquad R = 99.1\% \qquad (6\text{-}13)$$

where σ_y is in a unit of MPa, r is in a unit of micron. Eq. (6-12) and (6-13) perfectly demonstrated the $r^{-1/2}$ strain and stress singularity and ensured the numerical accuracy of the mesh design. At this applied stress level, almost all the area at the crack tip is in the singularity dominated zone. Therefore, stress intensity factors can be used for defining the amplitude of singularity and for evaluating the fracture toughness. For mode I fracture, the

relationship between the normal stress and stress intensity factor is[142]

$$\sigma_{yy} = \frac{K_I}{\sqrt{2\pi r}} \cos\left(\frac{\theta}{2}\right)\left[1 + \sin\left(\frac{\theta}{2}\right)\sin\left(\frac{3\theta}{2}\right)\right] \tag{6-14}$$

when $\theta = 0$, Eq. (6-14) can be simplified to

$$\sigma_{yy} = \frac{K_I}{\sqrt{2\pi r}} \tag{6-15}$$

Comparing Eq. (6-15) with Eq. (6-12), K is obtained as 669 MPa-$\mu m^{1/2}$ (or, 0.669 MPa-$m^{1/2}$ = 609 psi-$inch^{1/2}$). By *Kcal* Command in Ansys, K is 692 Mpa-$\mu m^{1/2}$. Using J-K conversion,

$$K_I = \frac{2}{\pi}\sigma\sqrt{\pi a} = \sqrt{\frac{J_I E}{1-\nu^2}} \tag{6-16}$$

K is exactly 669 MPa-$\mu m^{1/2}$. Therefore, the J integral extraction procedures used in this study is quite accurate.

To further study the elastic-plastic response, the stress distribution at a higher applied stress, 200 MPa, was evaluated. Figure 6-5 and 6-6 shows the normal stress, equivalent stress and hydrostatic stress distribution under the applied stress of 100 MPa and 200 MPa, respectively. The stress distribution patterns are the same for both loading level. Due to the elastic-plastic material property, the stresses did not go to infinity at the crack tip and the peak stress is at a small distance from the crack tip. The stress concentration factors for the normal stress are 4.78 and 3.42 for the applied stress of 100 MPa and 200 MPa, respectively.

6.4.1.2 Stress Distribution with a particle or void

Figure 6-7 and 6-8 presents the interaction between a sharp crack with a graphite particle at two load levels: 100 MPa and 200 MPa. It is obvious that the matrix volume affected by graphite is much larger at the higher stress level. The graphite always carried a

lower load than the surrounding matrix. Under the lower applied stress, the peak stress location is the same as the case without a particle, but the peak stress was increased by 20%. Under the higher applied stress, the peak stress was at the graphite/matrix interface on the side of the crack tip. Although the peak stress was even lower when the graphite is exists, a plastic zone was formed with a size of 1.87 μm across at the right side of graphite, as shown in Figure 6-8. Also, the graphite carried much higher percentage load comparing with at the lower applied stress level.

It has been reported that graphite particles are often formed in the steels with alumina inclusions. To determine which particle is more harmful when an edge crack exists, the graphite particle was replaced by an Al_2O_3 particle. Figure 6-9 and 6-10 present the stress distribution as replacing a graphite particle with a harder Al_2O_3 particle at two stress levels. At the lower stress level (100 MPa applied stress), the peak stresses in matrix are at the same location comparing the case without a particle. Unlike graphite, there was not a sharp stress drop inside the Al_2O_3 particle instead of a rise at the left interface. At 200 MPa applied stress, the highest stress is inside the Al_2O_3 particle and there is no plastic zone at the right side of the particle. The stress level in the matrix adjacent to the right interface was certainly lower than those for the case without a particle and the case with a graphite particle. The Al_2O_3 particle carries higher normal stresses and equivalent stresses than does the surrounding matrix. Therefore, the chance to break the particle is much higher. At the crack tip, the normal stress is lower than that in the graphite case. Therefore, Al_2O_3 reduced the stress concentration at the crack tip and the potential for the main crack growth was lowered. But there is a stronger possibility to initiate a microcrack at the matrix close to Al_2O_3 interface or inside the Al_2O_3 particle. Subsequently the main crack may grow by connecting with the new microcracks.

Figure 6-11 and 6-12 considers a void in front of the crack tip. Comparing Figure 6-11 with 6-7, it can be seen that the stress distribution was similar to the case with graphite. The only difference was that the stress at the right edge of void is much higher than the stress at the right interface of the graphite particle. This result suggested that a graphite particle in front of a sharp crack behaves like a void but less detrimental than a void. Both graphite and

void increase the stress concentration at the crack tip. Therefore, the crack growth mode may be directly extend the main crack.

6.4.2 STRESS AND STRAIN DISTRIBUTION AT A BLUNT CRACK TIP

6.4.2.1 Stress and Strain Distribution Without a Particle

Figure 6-13 shows the normal stress contours when the applied stress is 100 MPa for the case without a particle. It is clear that the plastic zone was confined in a small area at a crack tip. A circular hole in an isotropic linear elastic plate has a stress concentration factor (SCF) of 3.0. The SCF can be much higher for a blunt crack. It depends on the radius of the crack front. In our case, the crack tip is a semicircle. The peak stress is located a small distance from the crack tip and is 4.65 times of the applied stress. For a sharp crack in linear elastic material, the stress distribution exhibits a $r^{-0.5}$ singularity at a crack tip. For a fully plastic, nonhardening materials, the stress distribution should exhibit a r^{-1} singularity. Figure 6-14 and 6-15 present the normal stress and strain distribution along the path $\theta = 0$, respectively. A stress singularity of $r^{-0.59}$ and a strain singularity of $r^{-0.65}$ were observed which are close to those for the sharp crack.

Figure 6-16 presents a normal stress contour for the case that the applied load is 200 MPa. There is a larger yielding area comparing to Figure 6-13 when the applied load is 100 MPa. Outside the plastic zone the normal stress varies as $r^{-1.25}$ shown in Figure 6-17.

6.4.2.2 Interactions Between a Graphite Particle and a Blunt Crack

When a graphite particle exists in front of a blunt crack, the discontinuity of material properties will disturb the stress distribution. Figure 6-18 presents the normal stress contour when the graphite radius is 1 micron, and the distance between the crack tip and the graphite particle is 1 micron, and at 100 MPa remote loading. Although the peak stress is almost the same with the case without a graphite particle, the stress concentration effects act over a

wider distance when a graphite particle exists. The volume over which the stresses act is important for ductile failure.

Along the path $\theta = 0$, the $r^{-0.59}$ singularity does not exit anymore. The graphite particle carries almost the same load as the far field which is much lower than the stress carried by the immediate surrounding matrix. Thus there is a sharp stress gradient from the crack tip to the graphite/matrix interface, as shown in Figure 6-19. From the right interface of graphite/matrix, the normal stress gradient follows $r^{-1.19}$. The equivalent stress and hydrostatic stress also follow the same trends as the normal stress.

Figure 6-20 presents the normal stress contour when the applied load is 200 Mpa. The peak normal stress is also only sightly higher than the case without a graphite particle. And the peak normal stress is confined in a small area between the crack tip and the left inclusion/matrix interface. Figure 6-21 illustrates the normal stress, equivalent stress and hydrostatic stress distribution along the path $\theta = 0$. The graphite particle carries higher normal and equivalent stresses than the far field. At the right particle/matrix interface, the matrix is also yielding. Beyond the yielding area, the stresses decreased more gradually compared with the case at 100 MPa remote load.

Figure 6-22 shows the hydrostatic stress field around a graphite particle at a crack tip, which is different with the hydrostatic stress field around a particle in a matrix without a crack. The particle located in the center of hydrostatic stress field caused by a crack could debond the whole surface at the same time. But the particle in the homogenous matrix may only start debonding from one or two points which have the maximum stress, and form interface cracks, and then debond the whole surface by crack propagation.

6.4.3 J INTEGRAL FOR A SHARP CRACK

For small scale yielding, the path-independence of J integral has been proved by analytical method. However, for large scale yielding and complex situations, the path-independence is hard to be proved by analytical approaches. For large scale yielding, Hayes[143], using finite element analysis, proved that the difference of J values of five paths

is in the range of 2 to 2.5%. Therefore, the J integral is also path-independent when the cracked body under large scale yielding. In this study, J path-independence is also investigated by the finite element method.

The J integral was computed for a wide variety of contours, shown in Figure 6-23. The larger the subscript on J in these plots the more remote is the contour from the crack tip; for example, J_1 is for the contour closest to the crack tip. J_1, J_2 and J_3 are the J integrals for the paths in between the crack tip and the particle. J_4 is the integral for the path through the particle. J_5, J_6 and J_7 are the J integrals for the paths in the far field, shown in Figure 6-23. The calculated results are listed in Table 6-1 for the cases: no particles and voids, a graphite particle, an Al_2O_3 particle, and a void. The path independence of J reflected by the model without a particle. For the model with a particle, J is no longer path-independent in the area between the crack tip and the particle. However, in the far field the J integrals are path-independent. Comparing the J integrals in the far field, it has been found that for both load levels (100 MPa and 200 MPa)

$$J(\text{Void} + \text{Crack}) > J(\text{Graphite} + \text{Crack}) > J(\text{Crack}) > J(Al_2O_3 + \text{Crack}).$$

At the higher load level, the effect of a particle or void on J integral was more significant. The graphite or a void in front of a crack is equivalent to a longer crack because the longer crack, the higher J integral, shown in Figure 6-24.

6.5 SUMMARY AND CONCLUSIONS

For any numerical calculation, the accuracy obtained, the type of elements chosen and the physical model used are very important. Basic verification of the calculation is necessary. Prediction of crack growth in this work was associated with stress and strain distribution between an edge crack and a second phase particle. Thus, the spacing between the crack tip and particle and the size of the particle is a length scale of physical significance in this model. Hence, the results obtained in this work were expected to be reasonably insensitive to the element size use in the mesh. This was confirmed by repeating some of computations with a more refined mesh (i.e., with more elements between the crack tip and

the particle, inside and around the particle. The singularities of stress at a crack tip without a particle obtained from this analysis obeys the $1/r^{0.5}$, $1/r$ at elastic and elastic-plastic state, respectively. This confirms that the mesh near the crack tip is well refined to capture the stress field in this region. Basing on the calculation results, the following conclusions can be drawn:

1. The peak stresses were always at the equatorial direction for a graphite particle in front of an edge crack, regardless of whether the stress level in surrounding matrix was higher than the yielding stress. In the unit cell model, the peak stress location could be at either poles or equators.

2. For a small scale yielding, the matrix without particles shows a $r^{-0.5}$ stress singularity in this model. Increasing the applied remote stress level and the presence of a particle in front of the crack, increases the yielding area. Outside the plastic zone, the stress gradient drops slower than $r^{-0.5}$.

3. A graphite particle in front of an edge crack carried lower stress than the surrounding matrix. An Al_2O_3 particle could lower the crack tip stress concentration by carrying more stress itself. Therefore, the crack growth mode could be different:

(1) When graphite is in front of a crack, the crack growth could take place by crack extension due to the high stress concentration between graphite and crack.

(2) For Al_2O_3, the crack growth could result from a new crack inside the particle that links with the main crack.

4. J integral is path-independent for the far field. J integral is path-dependent for the field between the particle and crack tip.

5. Confirmed that J is path independent for a sharp crack in a homogenous matrix However, when a particle or void is in front of a sharp crack , J integral in the far field followed the order:

$$J(\text{Void} + \text{Crack}) > J(\text{Graphite} + \text{Crack}) > J(\text{Crack}) > J(Al_2O_3 + \text{Crack}).$$

Table 6-1 J integral (N /μm) for the steel matrix with a sharp crack and a second phase particle or void

Applied Stress	Particle	Path I J_1	Path II J_2	Path III J_3	Path VI J_4	Path V J_5	Path VI J_6	Path VII J_7
100 MPa	None	2.0	1.9	2.2	2.2	2.2	2.2	2.2
	Graphite	2.6	2.5	3.1	2.2	2.1	2.5	2.5
	Al_2O_3	1.9	1.7	2.1	2.2	2.2	2.2	2.2
	Void	3.3	3.6	3.4	3.4	2.7	2.7	2.7
200 MPa	None	6.9	6.7	8.0	9.6	8.8	10.1	10.1
	Graphite	17.8	18.3	19.4	12.9	17.2	17.2	17.4
	Al_2O_3	6.5	6.1	7.1	9.3	8.6	9.6	9.6
	Void	196.3	255.1	65.0	-	45.8	45.4	45.4

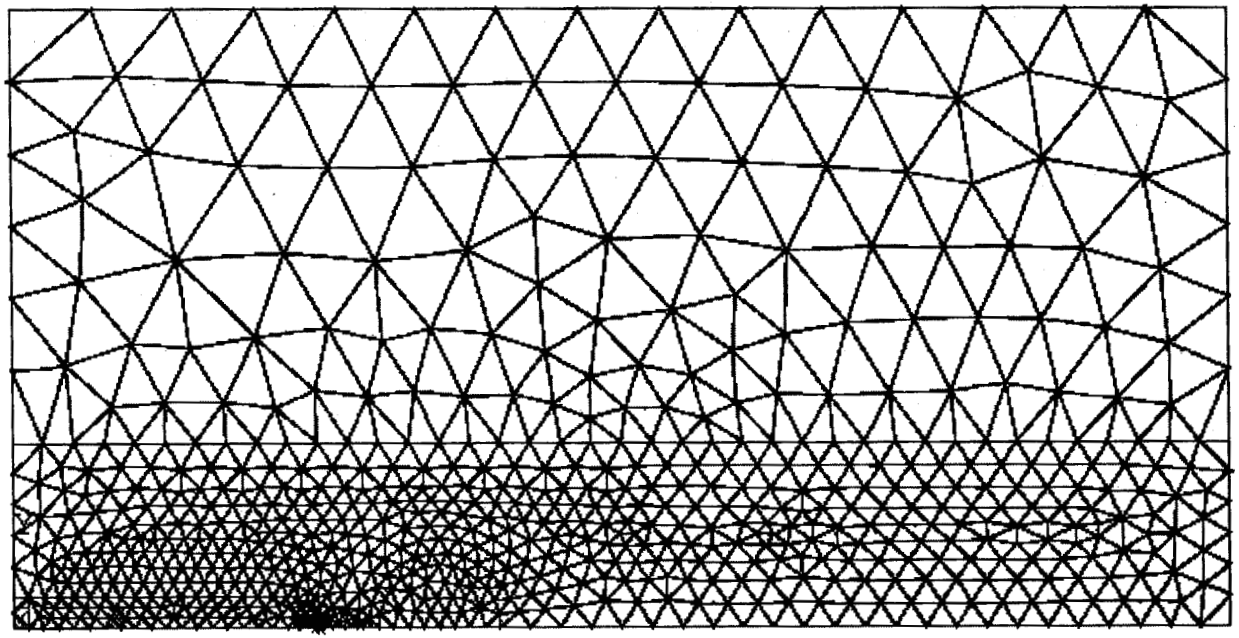

(a) Whole model

Figure 6-1 Mesh for a sharp crack/particle interaction model.

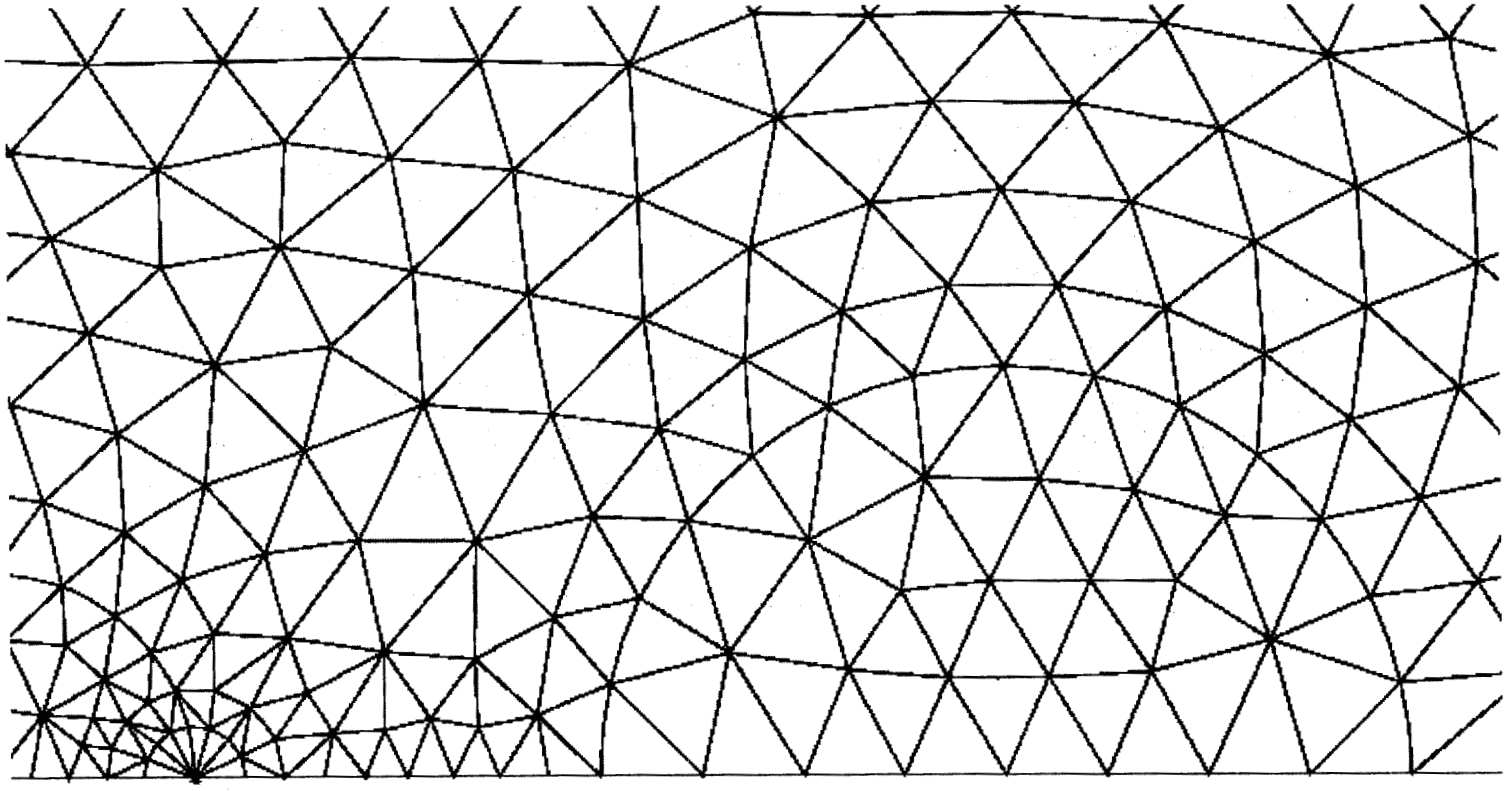

(b) Closer view of the crack tip and the particle

Figure 6-1 Mesh for a sharp crack/particle interaction model.

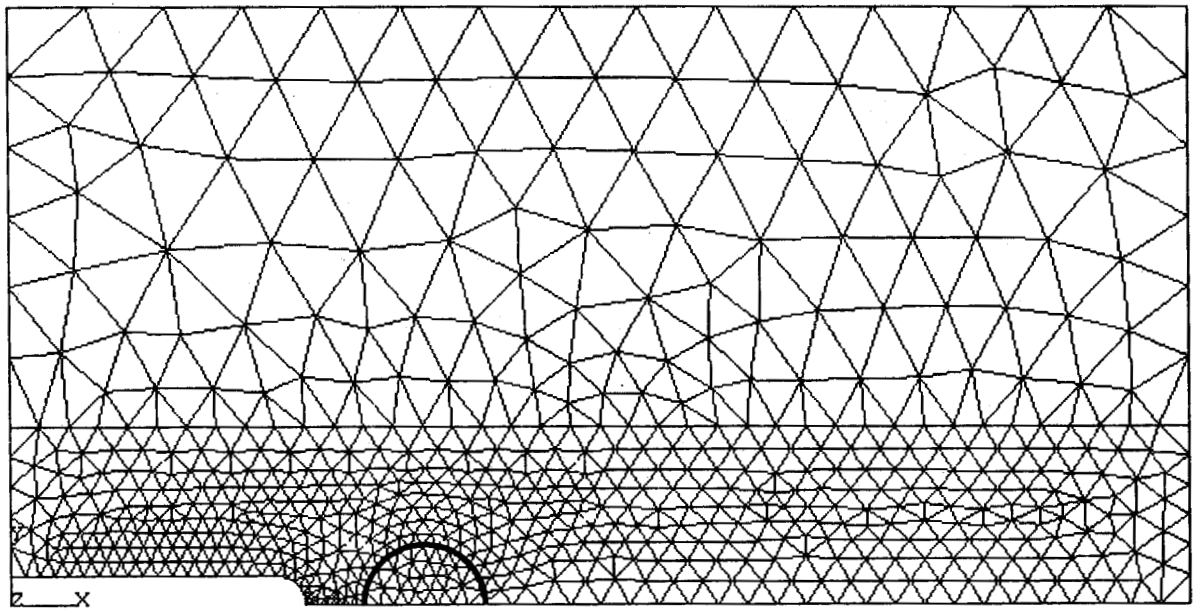

Figure 6-2 Mesh for the blunt crack / particle interaction model.

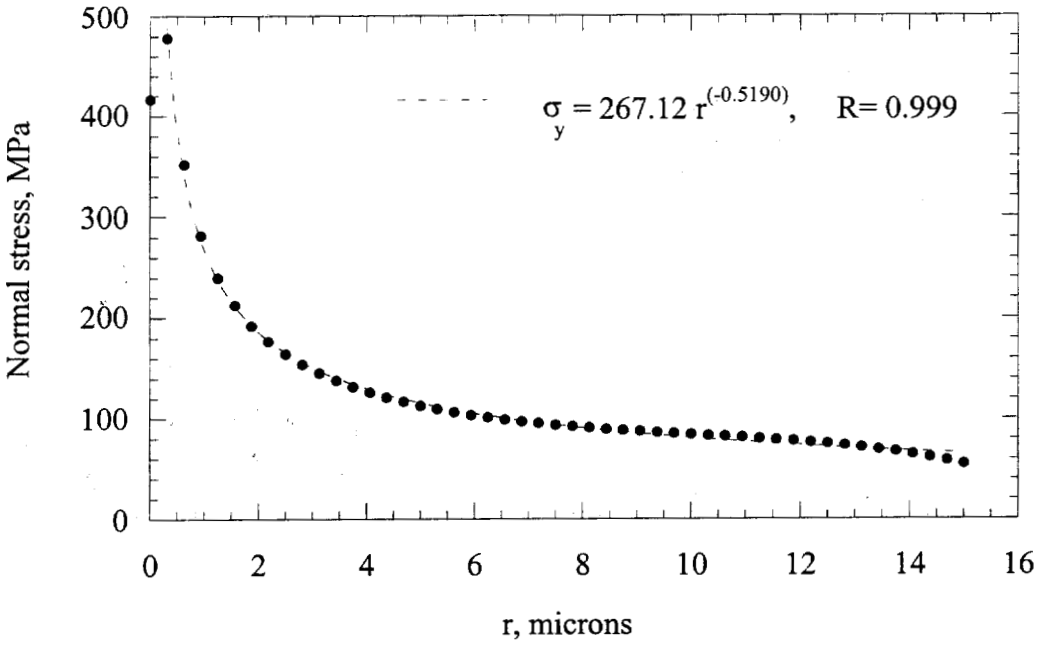

Figure 6-3 Stress distribution at a sharp crack tip without a particle (Applied stress = 100 MPa).

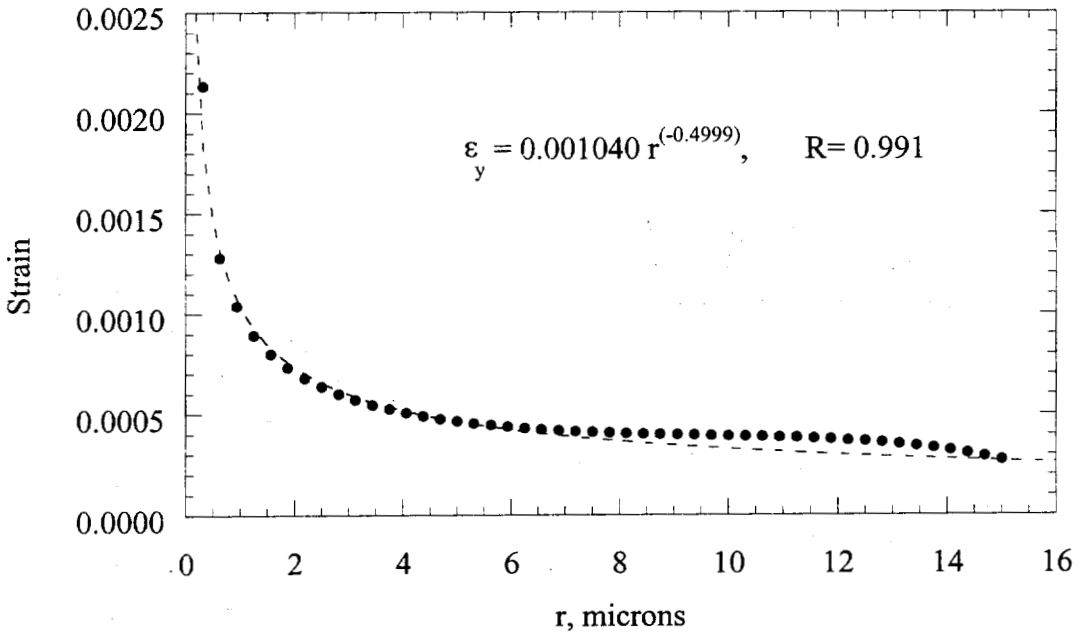

Figure 6-4 Strain distribution at a sharp crack tip without a particle (Applied stress = 100 MPa).

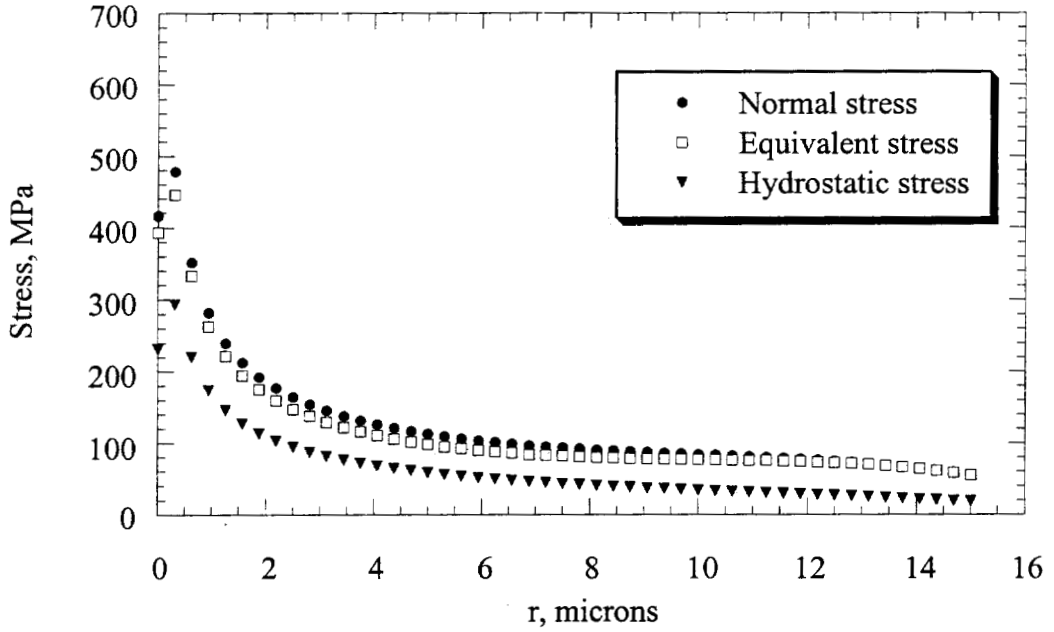

Figure 6-5 Distributions of normal stress, equivalent stress and hydrostatic stress at a sharp crack tip (Applied stress = 100 MPa).

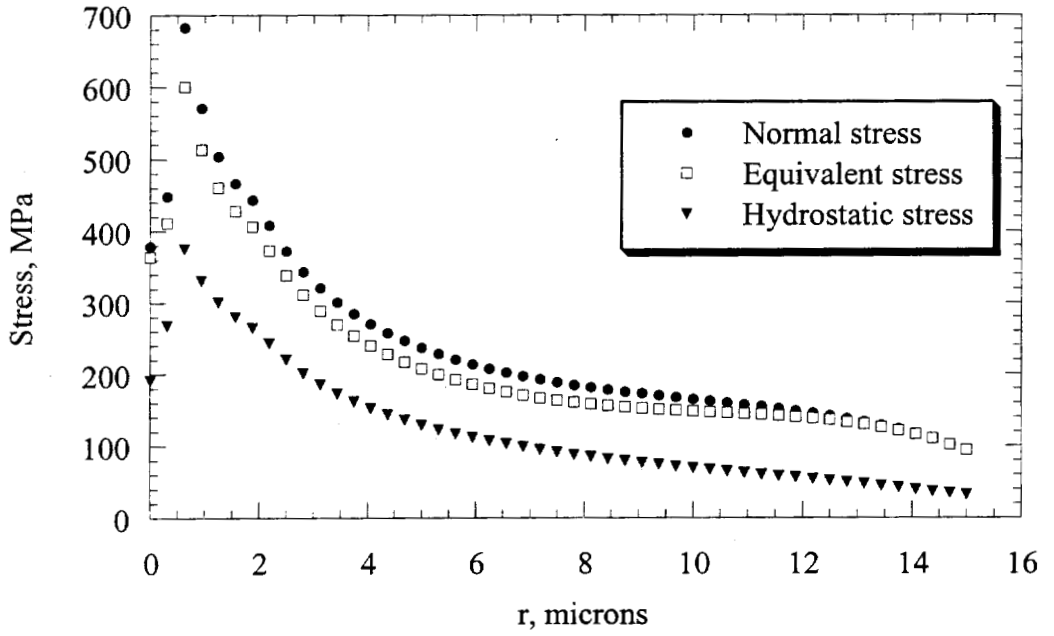

Figure 6-6 Stress distribution at a sharp crack tip without a particle (Applied stress = 200 MPa).

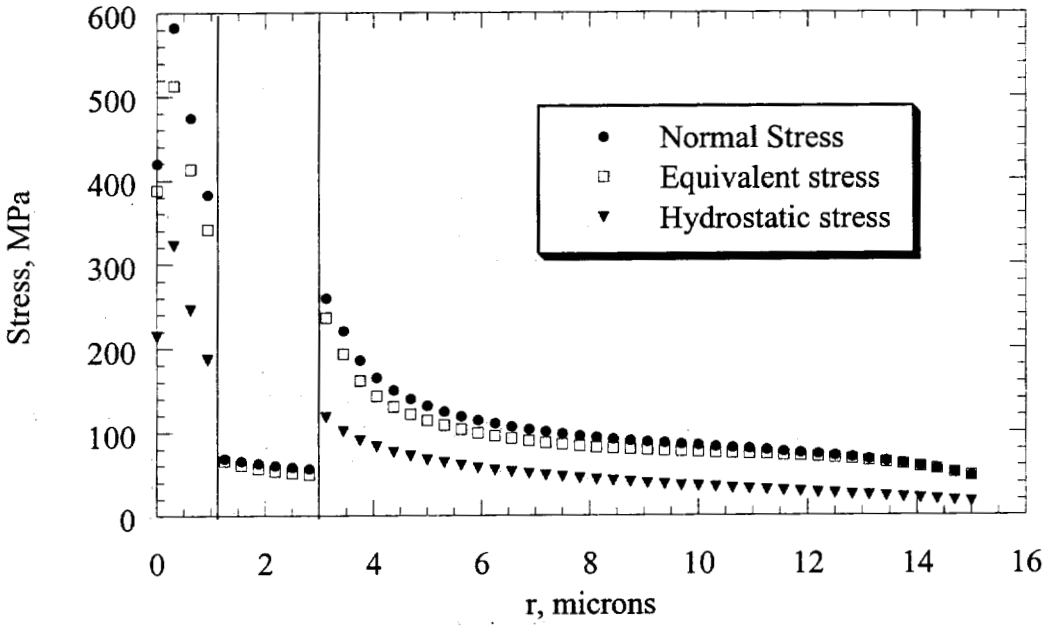

Figure 6-7 Stress distribution in front of a sharp crack tip with a graphite particle (Applied stress = 100 MPa).

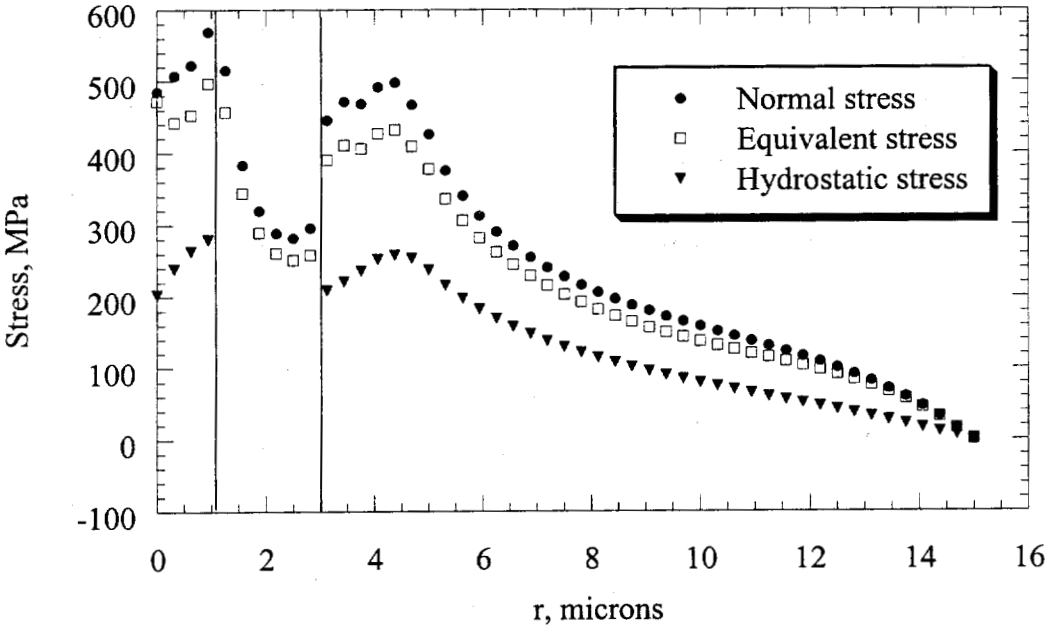

Figure 6-8 Stress distribution in front of a sharp crack tip with a graphite particle (Applied stress = 200 MPa).

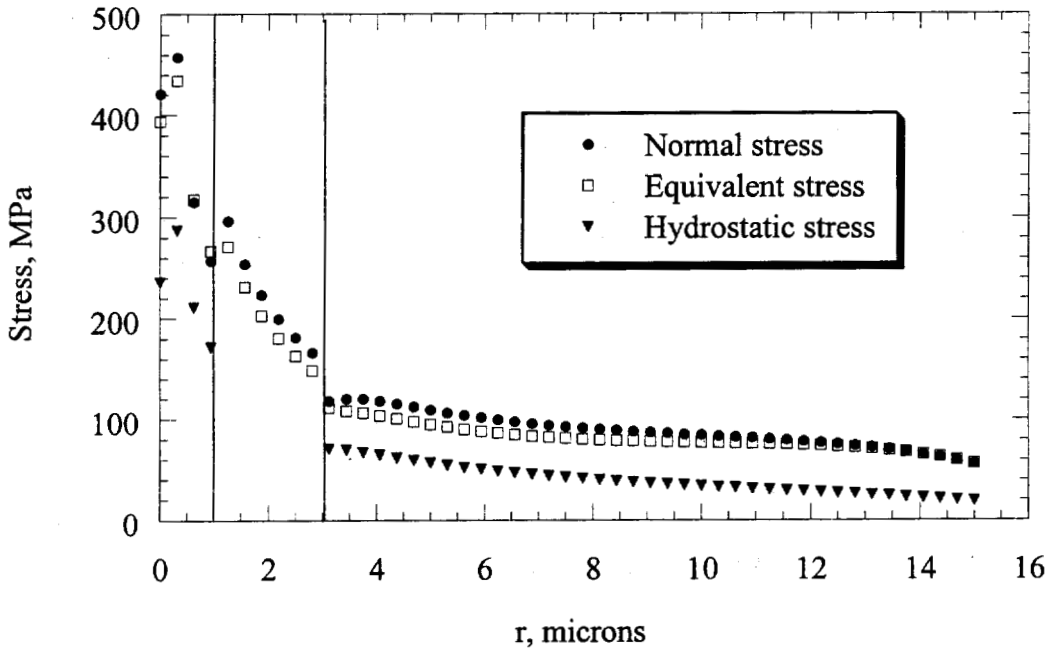

Figure 6-9 Stress distribution in front of a sharp crack tip with a Al_2O_3 particle (Applied stress = 100 MPa).

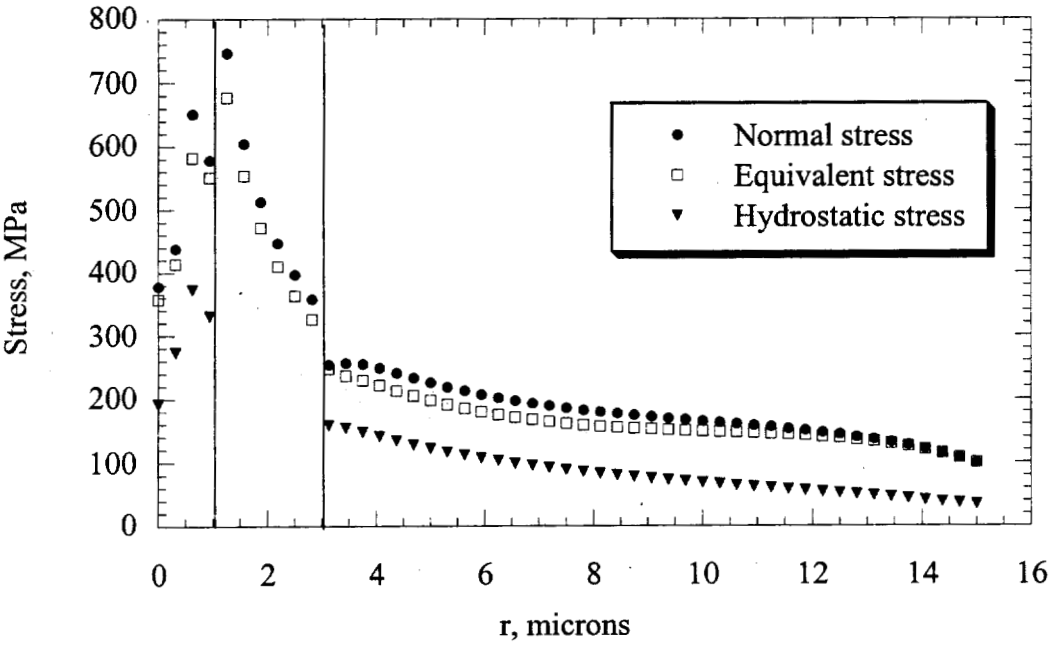

Figure 6-10 Stress distribution in front of a sharp crack tip with a Al_2O_3 particle (Applied stress = 200 MPa).

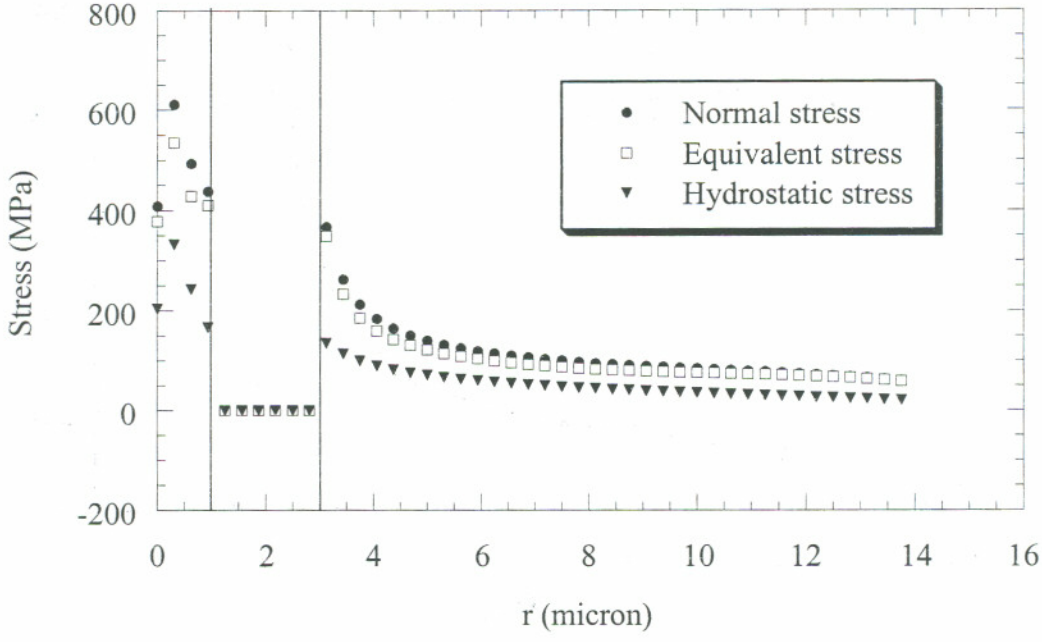

Figure 6-11 Stress distribution in front of a sharp crack tip with a void (Applied stress = 100 MPa).

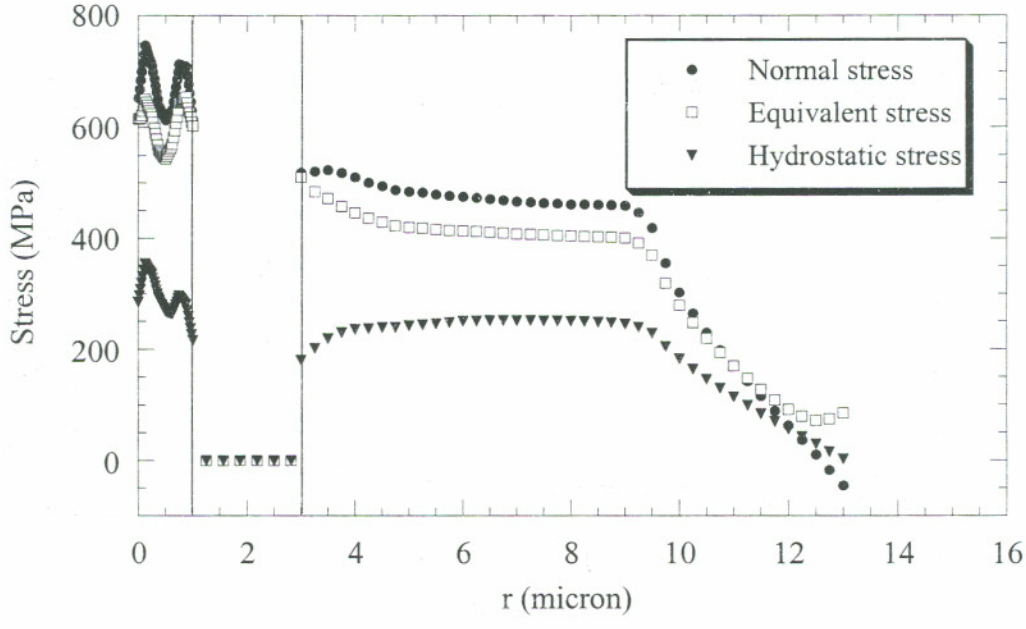

Figure 6-12 Stress distribution in front of a sharp crack tip with a void (Applied stress = 200 MPa).

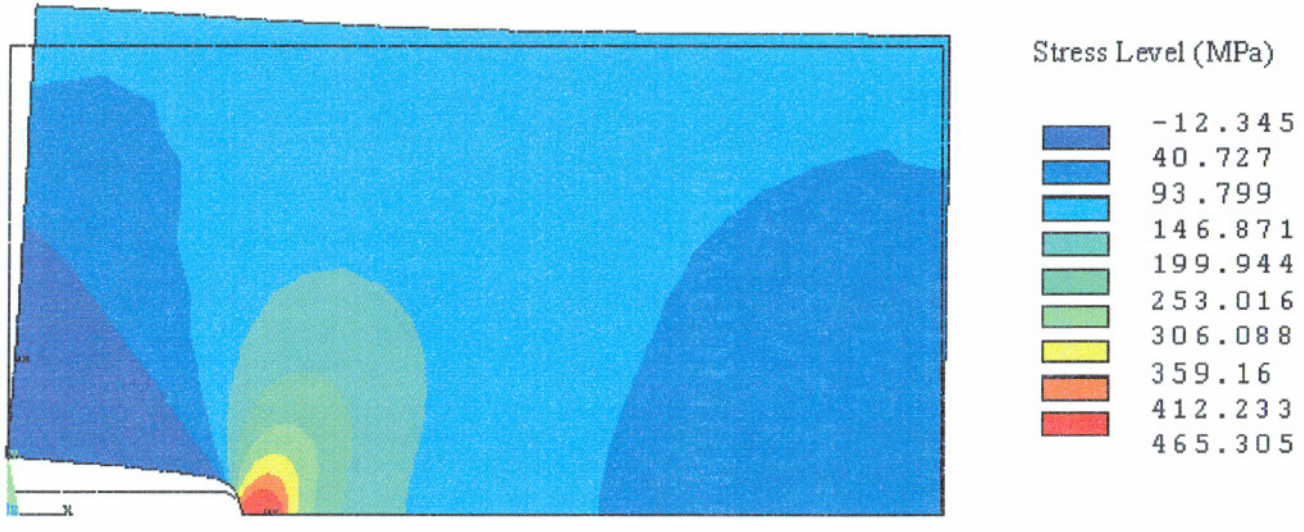

Figure 6-13 Normal stress contours in front of a blunt crack (Applied Stress = 100 MPa).

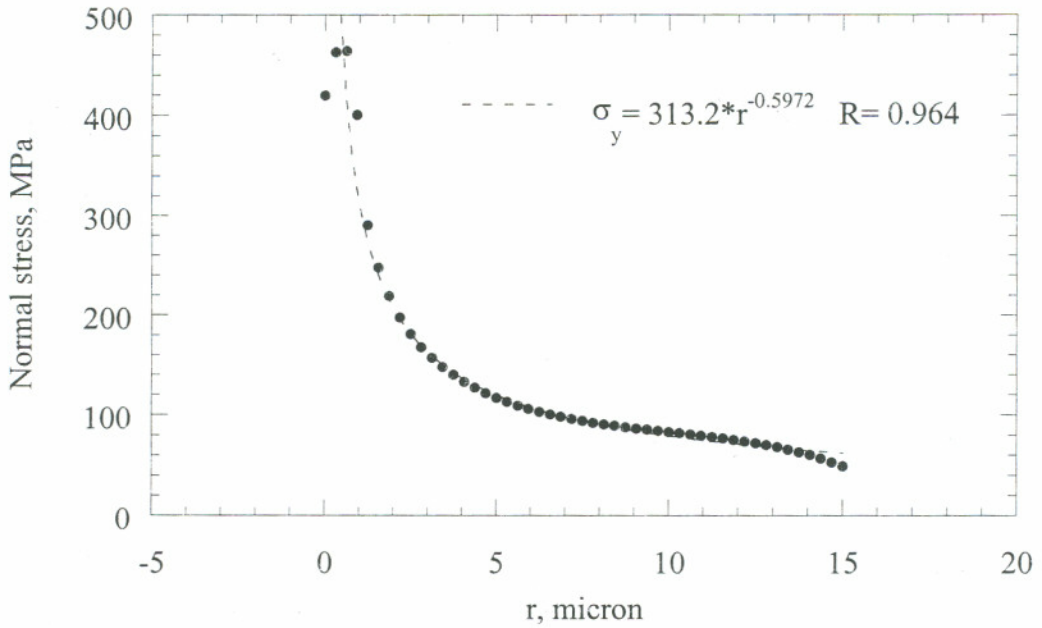

Figure 6-14 Normal stress distribution at a blunt crack tip (Applied stress = 100 MPa).

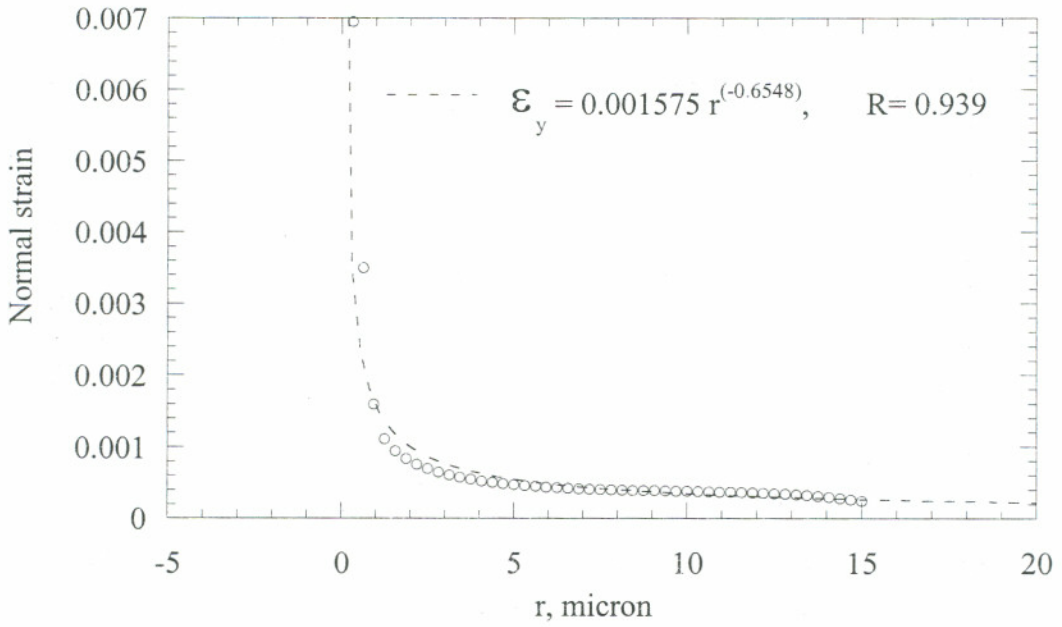

Figure 6-15 Normal strain distribution at a blunt crack tip (Applied stress = 100 MPa).

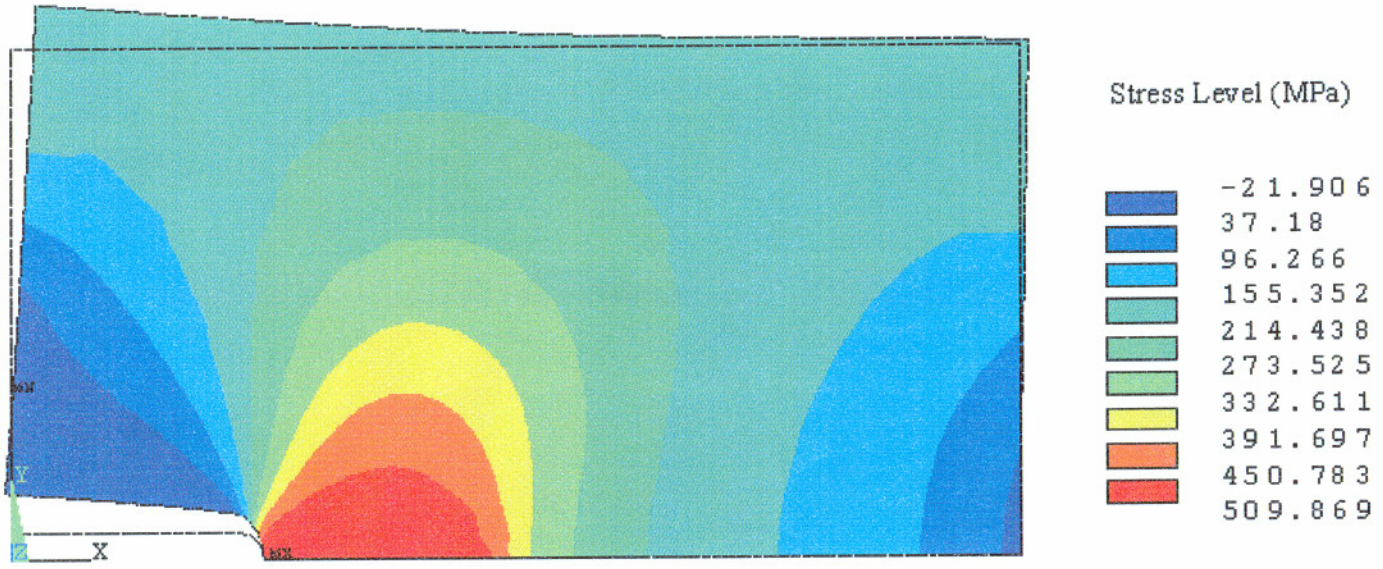

Figure 6-16 Normal stress contours in front of a blunt crack (Applied stress = 200 MPa).

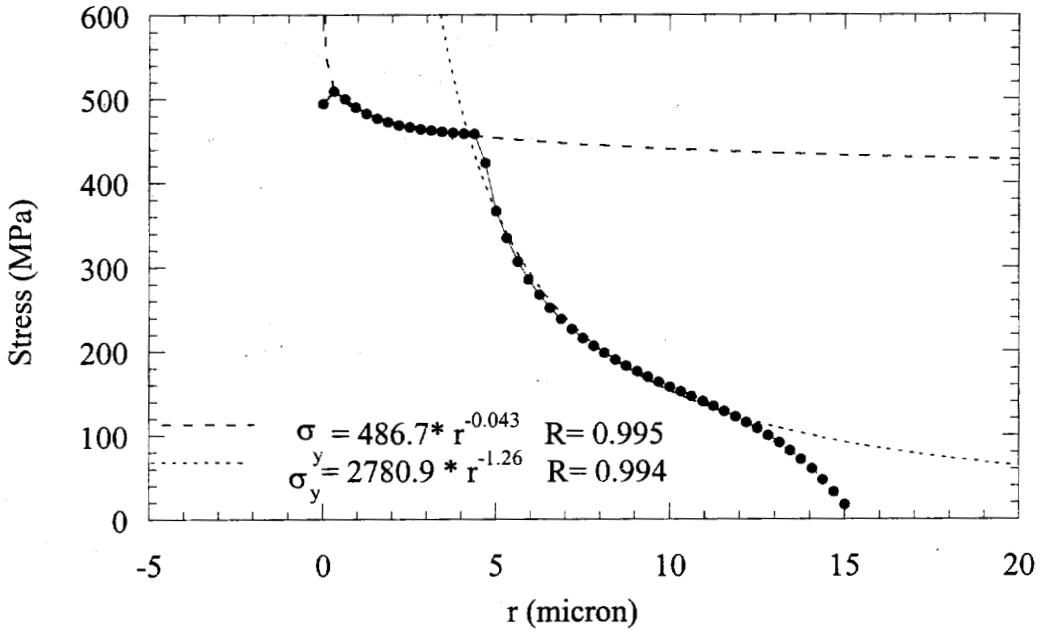

Figure 6-17 Normal stress distribution in front of a blunk crack (Applied stress = 200 MPa).

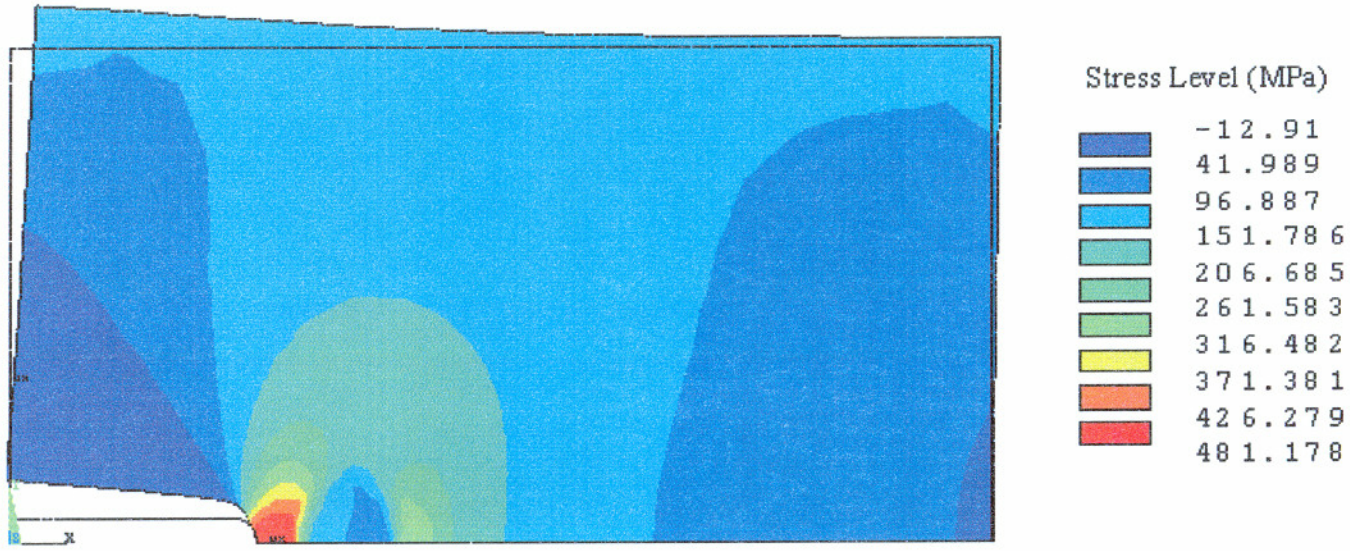

Figure 6-18 Normal stress contours in front of a blunt crack with a graphite particle (Applied stress = 100 MPa).

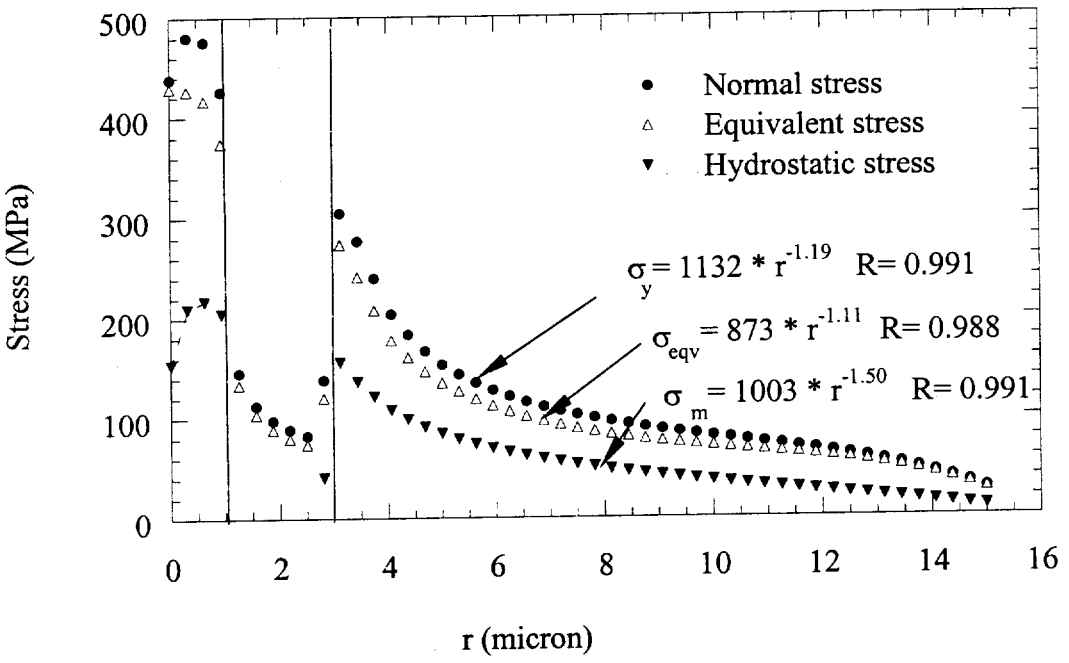

Figure 6-19 Stress distribution in front of a blunt crack with a graphite particle (Applied stress = 100 MPa).

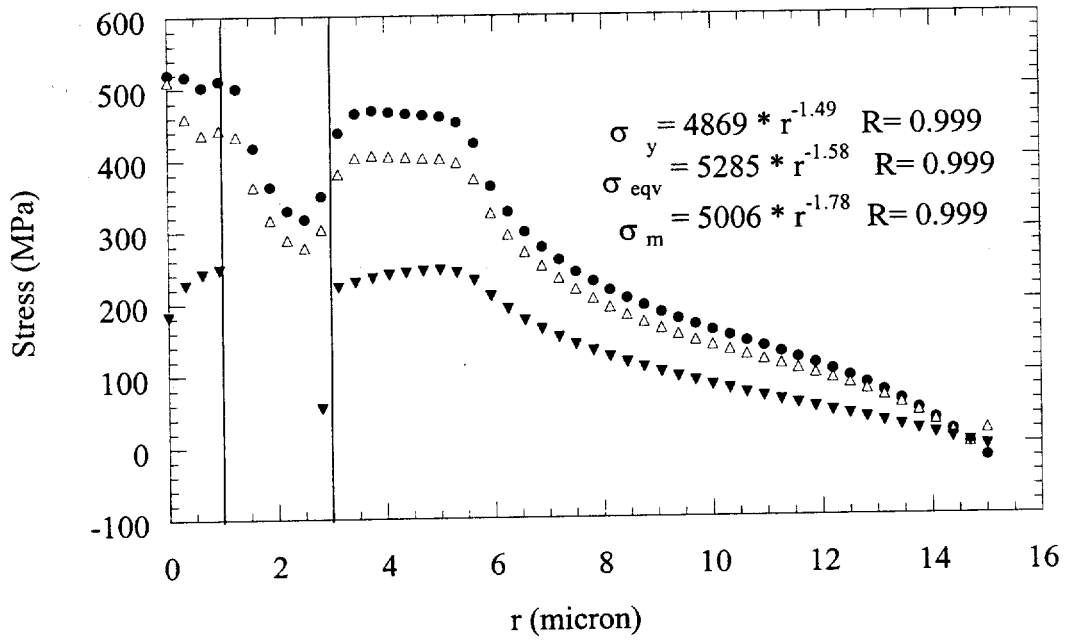

Figure 6-22 Stress distribution in front of a blunt crack with a graphite particle (Applied stress = 200 MPa).

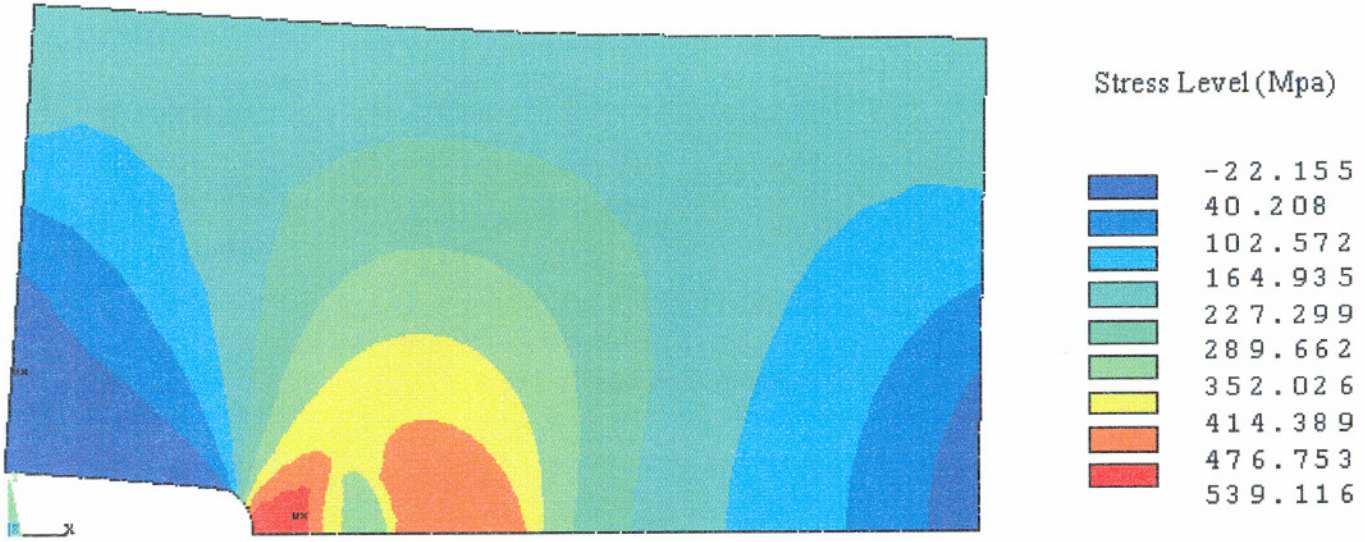

Figure 6-20 Normal stress contours in front of a blunt crack with a graphite particle (Applied stress = 200 MPa).

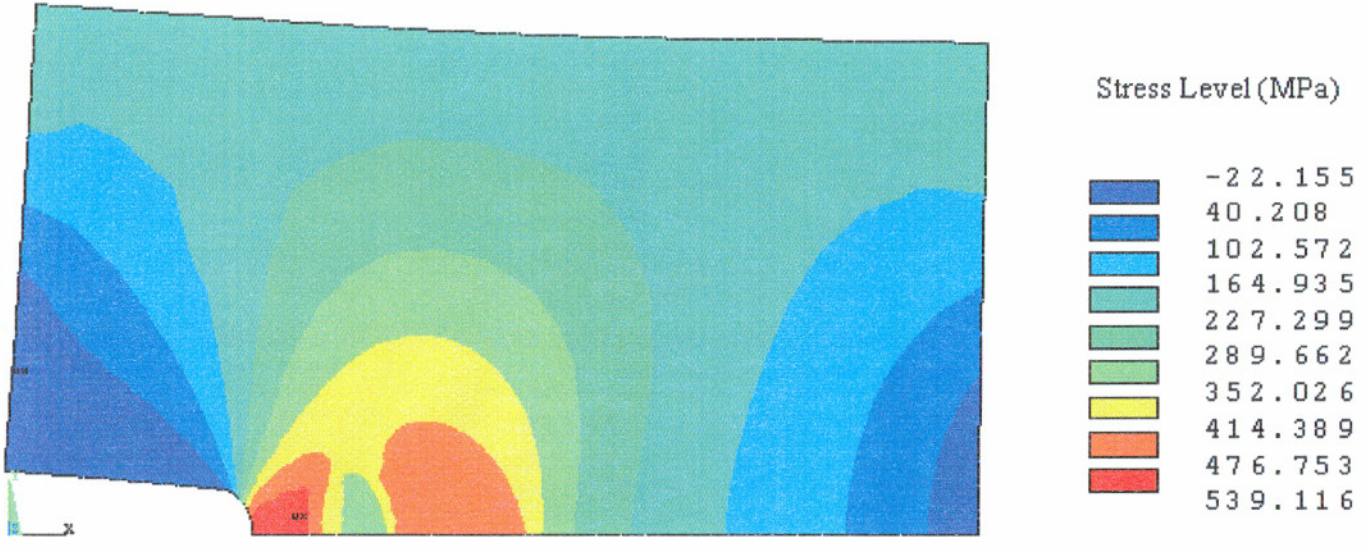

Figure 6-21 Normal stress contours in front of a blunt crack with a graphite particle (Applied stress = 200 MPa).

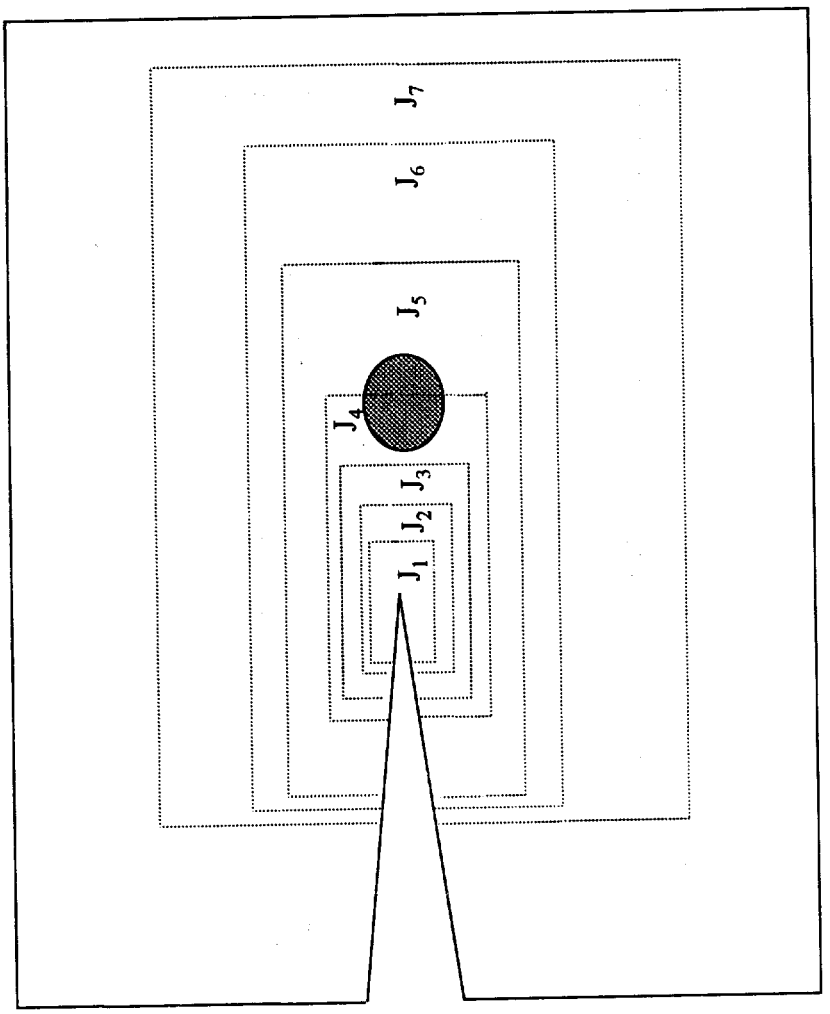

Figure 6-23 Paths for J integral calculation.

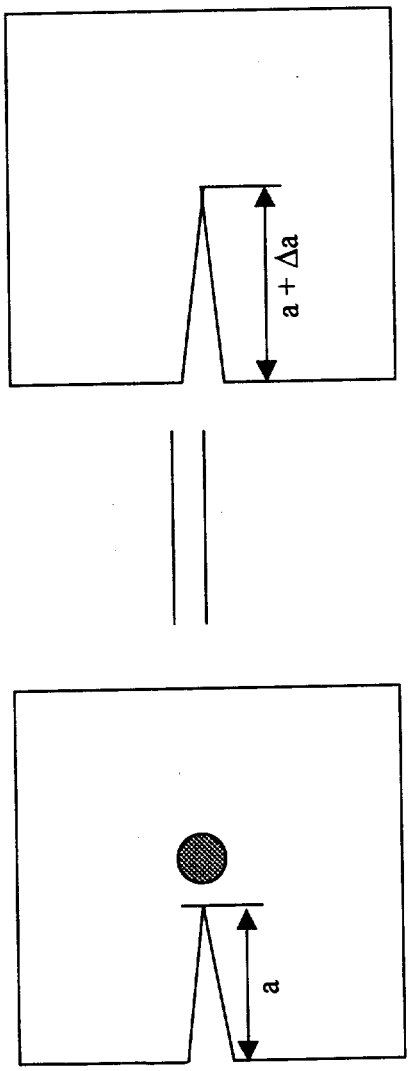

Figure 6-24 J integral results indicated that the influence of a graphite particle in front of a crack was equivalent to an effective crack growth.

CHAPTER 7
CONCLUSIONS

Graphite in cold worked and annealed low alloy steels were characterized using optical microscopy, scanning electron microscopy and transmission electron microscopy. Graphite dissolution kinetics, the influence of graphite content on martensite and Bainite transformation were studied using Gleeble thermal-mechanical testing system. The effect of graphite on mechanical properties of Bainitic and martensitic low alloy steels was investigated using hardness testing and fracture toughness testing. The graphite/matrix and graphite/crack interactions were studied using finite element analysis. The following conclusions can be drawn from the results presented in this study:

1. Focused ion beam cross section and fractography study showed that graphite in cold worked and annealed steels has a perfect interface with iron matrix.
2. Carbides in graphitized Steel 1 were identified as cementite rich with Mn and Cr. There were two kinds of carbides in Steel 2: the spheroidized cementite and the angular Nb(C,N). The absence of cementite in the vicinity of graphite reveals that free carbon came from cementite dissolution not Nb (C, N).
3. Graphite preferentially formed at the regions segregated with Al, Si in Steel 1. In Steel 2, a lot of graphite formed at broken Nb(C, N).
4. Transmission electron microscopy study supported the cementite spheroidizing mechanism that carbon atoms diffuse from sub-grain boundary to the cementite lamellar surface with smaller curvature.
5. TEM study on deeply cold worked steels showed that cold work could accelerate

cementite dissolution.

6. A carbon diffusion driving force model was proposed which gave good explanations for the nose location in published graphitization "C" curves, for the observation that fine pearlite favors graphitization, for Si effect on graphitization.
7. A dislocation transport model was proposed to illustrate the function of inclusions on graphitization during cold work.
8. Graphite can be dissolved by controlling the austenite conditions. As the austenitizing temperature and time increase, the volume fraction of graphite decreases. Graphite can be completely dissolved by austenitizing at 1000 °C for more than 30 minutes
9. Martensite transformation temperatures decrease as the graphite volume fractions decreased.
10. Martensite hardness increases as graphite content decreases.
11. Bainite TTT curves for steels with and without graphite were established in this work. Analysis in terms of the AR and JMA yields values of the time exponent n in the range of 2 to 3 and 1 to 2, respectively. Graphite content didn't significantly influence Bainite transformation kinetics, but affected the fraction of transformed Bainite. It has been observed that the transformation fraction decreases as the transformation temperature increases. In the lower Bainite regime, more Bainite was formed in the low graphite content steel. However, in the upper Bainite regime, more Bainite was formed in the high graphite content steel.
12. Bainite hardness depends on both transformation temperatures, graphite content, alloy composition. The less graphite, the higher Bainite hardness. The relationship between transformation temperature and Bainite hardness of high strength steels can be perfectly described by a second order polynomial equation.
13. The location of maximum stress or strain concentration depended on the particle and matrix properties. A graphite particle is hard to break or debond without involving matrix plastic deformation, because graphite carries much lower stress than does the matrix during elastic loading. When the matrix was yielding massively, the stress

concentrations inside a graphite particle and at the two poles were greatly increased. This is consistent with the experimental results. Modeling a graphite particle as a void could overestimate the stress and strain concentration around this particle and couldn't explain the interface debonding phenomena.

14. Stress induced diffusion could be one of the reasons graphite nucleated in the interface or near an inclusion like Al_2O_3. The carbon concentration at the Al_2O_3/matrix interface could be $e^{3.7}$ times of far field carbon concentration.

15. The stress concentration at a crack tip would be influenced by the localized stresses around second phase particles.

16. The numerical model used in this study agrees with the concept that J is path independent for a crack in a homogenous matrix. However, it has been found that J integral is path-dependent for the field between the particle and crack tip. The particle disturbs the crack tip stress and strain field, but J integral is path-independent for the far field. Furthermore, in far field, the J integral followed the order:

$$J(\text{Void + crack}) > J(\text{Graphite + Crack}) > J(\text{Crack only}) > J(Al_2O_3\text{+Crack}).$$

REFERENCES

1. Bidash, V.I., Prikhod'ko, A.I. "Graphitization of Low-Carbon Steel During a Spheroidizing Anneal", *Metal Science and Heat Treatment*, vol. 29, no. 1-2, pp. 116-119, 1987.

2. Sueyoshi, H., Tanaka, R. "Heat-Treatment and Machinability of the Tri-Phase Steel Composed of Ferrite, Martensite, and Graphite", *Journal of the Japan Institute of Metals*, vol. 54, no. 2, pp. 231-236,1990.

3. Azevedo, A.L.T. "Graphite Formation Over Steel Sheets During Annealing". *35th Annual Congress of Assoc. Brasileira de Metais*, vol. 1, Sao Paulo, Brazil, 6-11 July 1980, Assoc. Brasileira de Metais, Av. Paulista, 2073, Sao Paulo, Brazil, pp. 559-571, 1980.

4. Yano, I., Arase, K., Saijio, K. "Carbon Diffusion on the Surface of Low-C Mild Steel During Its Annealing", *Journal of Metal Finishing Society of Japan*, vol. 25, pp. 131-38, 1974.

5. Bukalil, R.H., Santos, M.P.D., Pereira, L.C. "Graphite Formation on the Surface of Cold Rolled Low Carbon Steel Sheets During Annealing", *Metalurgia ABM*, vol. 41, no. 337, pp. 699-703, 1985.

6. Okamoto, A. "Graphite Formation in High-Purity Cold-Rolled Carbon Steels", *Metallurgical and Materials Transactions A*, vol. 20A, no. 10, pp. 1917-1925, 1989.

7. Moss, C.J., Davidson, J.L. "Graphitisation in Type A201 Carbon Steel in Petro-Chemical Plant After Long Term Service", *Materials Forum*, vol. 17, no. 4, pp. 351-359, 1993.

8. Baranov, A.A., Bunin, K.P. "The Function of Inclusions in the Graphitization of Iron and Steel", *Russian Castings Production*, no. 7, pp. 317-319, 1964.

9. Gavrilyuk, V.G. "A Nuclear-Gamma-Resonance Study of the State of Cementite in Cold-Worked Steel", *Fizika Metallov i Metallovedenie*, vol. 45, no. 5, pp. 968-980, 1978.

10. Gulyaev, A.P. "On the Iron-carbon Diagram", *Metal Science and Heat Treatment (English Translation of Metallovedenie i Termicheskaya Obrabotka Metallov)*, vol. 32, no. 7-8, pp. 493-494, 1991.

11. Hasebe, M., Ohtani, H., Nishizawa, T. " Effect of Magnetic Transition on Solubility of Carbon in B.C.C. Iron and F.C.C. Co--Ni Alloys", *Metallurgical and Materials Transactions A*, vol. 16A, no. 5, pp. 913-921, 1985.

12. Ohtani, H., Hasebe, M., Nishizawa, T. "Calculation of Fe--C, Co--C and Ni--C Phase Diagrams", *Transactions of the Iron and Steel Institute of Japan* , vol. 24, no. 10, pp. 857-864, 1984.

13. Kosowski, A. "Free Enthalpy of the Reaction of Cementite Formation From Austenite", *Archives of Metallurgy*, vol. 32, no. 4, pp. 625-629, 1987.

15. Liang, Y. *Physical Chemistry*, Metallurgy Publisher, Beijing, p. 361, 1983.

16. Darken, L.S., Gurry, R.W. "Free Energy of Formation Cementite and Solubility of Cementite in Austenite", *Journal of Metals*, no. 11, 1951.

16. Liang, Y. *Physical Chemistry*, Metallurgy Publisher, Beijing, p. 369, 1983.

17. Darken, L.S., Gurry, R.W. *Physical Chemistry of Metals*, McGraw-Hill, New York, pp. 397-401, 1953.

18. Deich, I.S., Apayev, B.A. "Carbide Transformations in the Post-Strain Aging and Tempering of Carbon and Cobalt Steel", *Fizikai Khimiya Obrabotki Materialov*, no. 3, pp. 126-133, 1978.

19. Okada, M. "Graphitization of the Weld Heat-Affected Zone in Carbon Steel", *Transaction of the Japan Institute of Metals*, vol. 23, no. 7, pp. 353-359, 1982.

20. Deich, I.S. "Carbide Formation and Graphitisation in Carbon Steels Alloyed With Cobalt", *Fiz. Elektron. Tverd. Tela.(Izhevsk)*, no. 4, pp. 81-87, 1981.

21. Niedzwiedz, Z., Taub, A., Weiss, B.Z. "Behavior of Carbide and Graphite in Steel During Graphitization", *Israel Journal of Technology*, vol. 4, no. 4, pp. 233-242, 1966.

22. Gofman, Y.M., Vinokurova, G.G. "Graphitisation of Carbon Steel Streamlines", *Thermal Engineering*, vol. 35, no.7, pp. 392-394, 1988.

23. Sueyoshi, H., Suenaga, K. "Effects of Pre-Treatment on the Graphitization Behaviour in Hypoeutectoid Low Alloy Steels", *Journal of the Japan Institute of Metals*, vol. 42, no. 7, pp. 676-682, 1978.

24. Benedicks, C.A.F. *Non-metallic Inclusions in Iron and Steel*, Chapman and Hall, Ltd., London, 1930.

25. Foulds, J.R. "Graphitization of Steels in Elevated-Temperature Service", *First International Conference on Microstructures and Mechanical Properties of Aging Materials*, Chicago, Illinois, USA, 2-5 Nov.,1992, The Minerals, Metals & Materials Society (TMS), pp. 61-69, 1993.

26. Jena, A.K., Chaturvedi, M.C. *Phase Transformation in Materials*, Prentice Hall, Englewood, New Jersey, p. 191, 1992.

27. L'nyanoy, V.N. "Carbon Migration on the Ferrite Surface", *Izvestiya Akademii Nauk SSSR, Metally*, no. 4, pp. 101-105, 1980.

28. Inokuti, Y. "Formation of Graphite on the Surface of Cold Rolled Low-C Steel Sheet During Annealing", *Transactions of the Iron and Steel Institute of Japan*, vol. 15, no. 6, pp. 314-23, 1975.

29. Port, R.D., Mack, W.C., Hainsworth J. "The Mechanism of Chain Graphitization of Carbon and Carbon/Molybdenum Steels", *Proceedings, First International Conference on Heat-resistant Materials*, 1991, ASM International, Materials Park, OH, pp. 587-594, 1991.

30. Port, R.D. "Non-Weld-Related Graphitization Failures", *Proceedings, Corrosion 89*, April 1989, Paper No.248, NACE, Houston, TX, 1989.

31. Smith, G.V. *Properties of Metals at Elevated Temperature*, McGraw-Hill, New York, p. 330, 1950.

32. Tkachenko, F.K. "Effects of Cold Plastic Deformation on Transformations in Heated Steel", *Izvestiya Akademii Nauk SSSR, Metally*, no. 5, pp. 120-123, 1978.

33. Gridnev, V.N., Gavrilyuk, V.G., Polushkin, Y. A. "Carbon Distribution in Plastically Worked Steel", *Dopovidi Akademii Nauk Ukrains'koi RSR*, no. 2, pp. 88-92, 1980.

34. Kou, BC; Lui, TS; Chen, LH. "Study on the Graphitization of Malleable Cast Iron", *Chukung (Journal of Chinese Foundrymen's Association) (Taiwan)*, vol. 20, no. 3, pp. 1-5, 1995.

35. "Properties and Selection: Iron, Steel and High Performance Alloys", *Metals Handbook*, 10th ed., vol. 1, ASM International, Materials Park, OH, p.6, 1990.

36. Fukui, K., Saito, Y., Shinagawa, I., Yagi, H., Igarami, H. "Graphitized High Carbon Sheet Steel With Excellent Formability for Heat Treatment Use", *Sumitomo Metals* (Japan), vol. 45, no. 45, pp. 140-144, 1993.

37. Solv'ev, V.P., Kuragin, O.V. "Evaluating the Influence of Different Elements on Iron Graphitization [Previously Titled: Evaluation of Effect of Chemical Elements on Graphitization of Cast Iron.]", *Soviet Casting Technology* (USA), no. 7, pp. 10-11, 1991.

38. Borruto, A., Felli, F. "Process of Graphitization by Heat Treatment", *Metallurgia Italiana*, vol. 76, no. 5, pp. 218-225, 1984.

39. Jena, A.K., Chaturvedi, M.C. *Phase Transformation in Materials*, Prentice Hall, Englewood, New Jersey, p. 456, 1992.

40. Sobotka, J., Vodarek, V., Tomasova, M., Sobotkova, M. "The Problem of the Formation of Graphite in Creep of Low-Alloy Steel 15020", *Hutnik (Prague)*, vol. 36, no. 7, pp. 267-274, 1986.

41. Bunin, K.P., Malinochka, Y.N. *Introduction to Metallography*, Moscow, Metallurgizdat, pp. 24-25, 177-183, 1964.

42. Yamamoto, S., Kobayashi, H., Kawano, Y., Kirihata, A. "Extended Huckel Molecular Orbital Calculation of the Cementite Stability and Graphitization of Fe-C-Si Alloys", *Proceedings, Physical Metallurgy of Cast Iron IV*, Tokyo, Japan, 4-6 Sept. 1989, Materials Research Society, pp. 103-110, 1990.

43. Zhukov, A.A. "What Is New in the Theory of Graphitizing. The Electron Structure of Components in Graphitizing Systems", *Metallovedenie i Termicheskaya Obrabotka Metallov*, no. 1, pp. 7-14, 1987.

44. Zhukov, A.A. "On the Problem of Complete Insolubility of Components in Binary and Ternary Systems", *Izvestiya Vysshikh Uchebnykh Zavedenii, Mashinostroenie*, no. 1, p. 146, 1966.

45. Zhukov, A.A. "Variations of Composition, Structure and Hardness of Cementite on Hardening", *Metal Science and Heat Treatment*, vol. 11, no. 1, p. 18, 1970.

46. Okamoto, T., Kagawa, A. "Lattice Parameters of Cementite in Fe-C-Si Alloy", *Metal Science*, no. 10, pp. 471, 1970.

47. Zhoukov, A.A., Schulte,G.Yu., Yanchenko, A.B. "On the Effect of Cementite-insoluble Elements on the Activity of Carbon in Cementite and Liability of Iron to Graphitization", *Russian Metallurgy*, no. 1, pp. 70-75, 1994

48. Smith, M.A., Sinharoy, S., Levenson, L.L. "Thermal Decomposition of Nickel Carbide: an Auger Line shape Study", *Journal of Vacuum Science Technology*, vol. 16, no. 2, pp. 462-465, 1979.

49. Rawlings, K.J., Foulias, S.D., Hopkins, B.J. "The Diffusion of Carbon to and from W(100)", *Surface Science*, vol. 109, no. 3, pp. 513-521, 1981.

50. Labohm, F., Engelen, C.W.R., Gijzeman, O.L.J, Geus, J.W., Bootsma, G.A. "The Effect of the Structure of the Carbide Layer on Ni(100) on Its Reactivity With Oxygen", *Surface Science*, vol. 126, no. 1-3, pp. 429-436, 1983.

51. Arabczyk, W., Storbeck, F., Mussig, H.J. "Electron Spectroscopy Studies on Carbon Segregation From a Mono-Crystalline alpha -Fe(111) Specimen", *Applied Surface Science* (The Netherlands), vol. 65-66, pp. 94-98, 1993.

52. Arabczyk, W., Rausche, E., Storbeck, F. "On the Underlayer and Overlayer Adsorption of Oxygen, Nitrogen and Carbon on the Iron (111) Surface", *Surface Science*, vol. 247, no. 2-3, pp. 264-268, 1991.

53. Yoshihara, K., Nii, K. "The Precipitation of Carbon and the Segregation of Sulfur on the Surface of Cold-Rolled Low Carbon Steels", *Journal of the Japan Institute of Metals,* vol. 44, pp. 549-54, 1980.

54. Nii, K., Yoshihara, K. "Segregation of Sulfur and Precipitation of Two-Dimensional Compound on Fe (100) Surfaces", *Journal of the Japan Institute of Metals,* vol. 19, pp. 857-65, 1980.

55. Wang, S.J., Grabke, H.J. "Diffusion of Sulphur in Metals by Reaction with Hydrogen Sulphide-hydrogen Mixtures", *Z. Metallkunde*, vol. 61, no. 8, pp. 597-603, 1970.

56. Christian, JW. *The Theory of Transformations in Metals and Alloys*, Pergamon Press, Oxford, 1965.

57. Kawasaki, M., Inoyama, N., Kawano, Y. "Kinetic Analysis of the First Stage Graphitization in Fe--C--Si White Cast Irons", *Journal of the Japan Institute of Metals*, vol. 48, no. 7, pp. 669-674, 1984.

58. Rundman, K.B., Rouns, T.N. "On the Effects of Molybdenum on Kinetics of Secondary Graphitization in Quenched and Tempered Ductile Irons", *Transactions of the American Foundrymen's Society, Proceedings of the 86th Annual Meeting*, vol. 90, Chicago, pp. 82-117, 487-497, 1982.

59. Sueyoshi, H., Suenaga, K. "Effect of Austenitizing Treatment Followed by Slow Cooling on Graphitization in Hypo-Eutectoid Alloy Steels", *Journal of the Japan Institute of Metals*, vol. 51, no. 6, pp. 518-524, 1987.

60. Fujihira, A. "The Kinetics and the Rate Controlling Process of Graphite Nodule Growth", *Journal of the Japan Institute of Metals*, vol. 44, no. 1, pp. 6-15, 1980.

61. Tanaka, R., Fujihira, A. "Effect of Pre-Quenching Temperature on the Graphitization of Structural Low Alloy Steel", *Journal of the Japan Institute of Metals*, vol. 30, no. 3, pp. 279-284, 1966.

62. Pacyna, J., Jedrzjewska-Strach, A. "The Effect of Carbon on Structure and Properties of Steels with Silicon in the Annealed State", *Archives of Metallurgy*, vol. 39, no. 1, pp. 53-69, 1994.

63. Port, R.D., Mack, W.C., Hainsworth, J. "The Mechanism of Chain Graphitization of Carbon and Carbon Molydenum Steels", *Heat-Resistence Materials,* Fontana, Wisconsin, USA, 23-26 Sept. 1991, ASM International (USA), pp. 587-594, 1991.

64. Semenova, I.O., Movchan, V.I. "Mechanism of Structure Formation During Graphitization of Nickel Steels", *Izvestiya Vysshikh Uchebnykh Zavedenii, Chernaya Metallurgiya*, vol. 28, no. 1, pp. 97-101, 1985.

65. "Properties and Selection: Iron, Steel and High Performance Alloys", *Metals Handbook*, Tenth Edition, vol. 1, Materials Park, OH: ASM International, p. 664, 1990.

66. Creamer, E.L. "Metallurgical Condition of Several Carbon Steels after Long-term, Elevated Temperature Exposure", *Evaluation of Materials in Process Equipment after Long Term Service in Petroleum Industry*, (MPC-12), ed. Ciuffreda, A. R., New York, NY:ASME, pp. 13-21, 1980.

67. Gofman, Y.U.M. "Concerning Safety of Steel 20 Articles Operating at High Temperatures", *Teploenergetika,* no. 8, pp. 21-22, 1992.

68. Zhukov, A.A. "In Defense of the Graphitization Theory (Previously Titled: for the Theory of Graphitization.)". *Russian Castings Technology*, no. 12, p. 44, 1993.

69. Argon, A.S., Im, J., Safoglu, R. "Cavity Formation From Inclusions in Ductile Fracture", *Metallurgical and Materials Transactions A*, vol. 6A, no. 4, pp. 825-839, 1975.

70. Beremin, F.M. "Cavity Formation From Inclusions in Ductile Fracture of A508 Steel", *Metallurgical and Materials Transactions A*, vol. 12A, no. 5, pp. 723-731, 1981.

71. Tanaka, K., Mori, T., Nakamura, T. "Cavity Formation at the Interface of a Spherical Inclusion in a Plastically Deformed Matrix", *Philosophical Magazine*, vol. 21, no. 170, pp. 267-79, 1970.

72. Goods, S.H., Brown, L.M. "The Nucleation of Cavities by Plastic Deformation", *Acta Materialia (USA)*, vol. 27, no. 1, p. 27, 1979.

73. Eshelby, J.D. "The Determination of the Elastic Field of an Ellipsoidal Inclusion, and Related Problem", *Proceedings of the Royal Society*, vol. A241, pp. 376-396, 1957.

74. Thomson, R.D., Hancock, J.W. "Ductile Failure by Void Nucleation, Growth and Coalescence", *International Journal of Fracture*, vol. 26, no. 2, pp. 99-112, 1984.

75. Birkle, A.J., Wei, R.P., Pellissier, G.E. "Analysis of Plane-Strain Fracture in a Series of 0.45C-Ni-Cr-Mo Steels with Different Sulfur Contents", *ASM Transactions of Quart.*, vol. 59, no. 4, pp. 981-990, 1966.

76. Osborne, D.E., Embury, J.D. "Influence of Warm Rolling on the Fracture Toughness of Bainitic Steels", *Metallurgical and Materials Transactions A*, vol.4, no. 9, pp. 2051-2061, 1973.

77. Schwalbe, K.H. "Crack Propagation in AlZnMgCu 0.5 During Static Loading", *Engineering Fracture Mechanics*, vol. 6, no. 3, pp. 415-434, 1974.

78. Rice, J.R., Tracey, D.M. "On the Ductile Enlargement of Voids in Triaxial Stress Fields", *Journal of the Mechanics and Physics of Solids*, vol. 17, no. 3, p. 201, 1969.

79. Li, J.Y., Zhang, W.Y. "Effect of Titanium Nitride Inclusions on Fracture Toughness in Ultrahigh Strength Steel", *Journal of the Iron and Steel Institute*, vol. 29, no. 2, pp. 158-164, 1989.

80. Xiao, J.M. *Toughness and Toughening of Metallic Materials*, Shanghai Science and Technology, Shanghai, p. 304, 1980.

81. Brooksbank, D., Andrews, K.W. "Stress Fields Around Inclusions and Their Relation to Mechanical Properties", *Journal of The Iron and Steel Institute*, vol. 21, no. 4, p. 291, 1972.

82. Kiessling, R., Nordberg, H. "Influence of Inclusions on Mechanical Properties of Steel--Critical Inclusion Size", *Proceedings, Soviet-Swedish Symposium on Clean Steel,* Sandviken, Sweden, vol.1, pp. 159-169, 1971.

83. Van Vlack, L.H. *Materials Science for Engineers*, Addison-Wesley, Reading, p. 512, 1970.

84. "Metallography, Structures and Phase Diagrams", *Metals Handbook*, 8th ed., vol. 8, Taylor Lyman ed., ASM International, Materials Park, OH, p. 276, 1973.

85. Chattopadhyay, S., Sellars, C.M. "Quantitative Measurements of Pearlite Spheroidization", *Metallography*, vol. 10, no. 1, pp. 89-105, 1977.

86. Sevillano, J.G. "Room Temperature Plastic Deformation of Pearlitic Cementite", *Materials Science and Engineering*, vol. 21, no. 3, p. 221, 1975.

87. Inoue, A., Ogura, T., Masumoto, T. "Burgers Vectors of Dislocations in Cementite Crystal", *Scripta Metallurgica,* vol. 11, no. 1, pp.1-5, 1977.

88. Inoue, A., Ogura, T., Masumoto, T. "Transmission Electron Microscope Study on Deformation and Fracture of Cementite in Cold-Rolled Steels", *Transactions of Japan Institute of Metals*, vol. 17, no. 3, pp. 149-157, 1976.

89. Maurer, K., Warrington, D.H. "Deformation of Cementite", *Philosophical Magazine*, vol. 15, no. 134, p. 321, 1967.

90. Gridnev, V.N., Nemosshkalenko, V.V., Meshkov, Y.Y. Gavrilyuk, V.G., Prokopenko V.G.; Razumov, O.N. "Mossbauer Effect in Deformed Fe-C Alloys" *Physica Status Solidi (A),* vol. 31, no. 1, p. 201, 1975.

91. Abe, H., Suzuki, T., Lavigne, J.J. "Dissociation and Dissolution of Cementite in Low-Carbon Steel by Cold Rolling and Annealing", *Transactions of the Iron and Steel Institute of Japan*, vol. 21, no. 5, pp. 332-337, 1981.

92. Languillaume, J., Kapelski, G., Baudelet, B. "Cementite Dissolution in Heavily Cold Drawn Pearlitic Steel Wires", *Acta Materialia (USA)*, vol. 45, no. 3, pp. 1201-1212, 1997.

93. Kalish, D., Cohen, M. "Structural Changes And Strengthening in the Strain Tempering of Martensite", *Materials Science and Eng*ineering, vol. 6, no. 3, p. 156, 1970.

94. Gridnev, V.N., Gavrilyuk, V.G. "Cementite Decomposition in Steel During Plastic Deformation(Review)", *Physics of Metals (USSR)*, vol. 3, no. 5, pp. 889-902, 1982.

95. Buono, V.T.L., Gonzalez, B.M., Andrade, M.S., "Kinetics of Strain Aging in Drawn Pearlitic Steels", *Metallurgical and Materials Transactions A*, vol. 29A, no. 5, pp. 1415-1423A, 1998.

96. Araujo, F.G.S., Gonzalez, B.M., Cetlin, P.R., Coelho, A.R.Z., Mansur, R.A. "Cementite Decomposition and the Second Stage Static Strain Aging of Pearlitic Steel Wires", *Wire Journal International (USA),* vol. 26, no. 2, pp. 191-194, 1993.

97. Belous, M.V., Novozhilov, V.B. "Effect of Repeated Plastic Deformation on the State of the Carbide Phase in Steels", *Physics of Metals (USSR),* vol. 4, no. 3, pp. 552-556, 1982.

98. Languillaume, J., Kapelski, G., Baudelet, B. "Evolution of the Tensile Strength in Heavily Cold Drawn and Annealed Pearlitic Steel Wires", *Materials Letters (Netherlands)*, vol. 33, no. 3-4, pp. 241-245, 1997.

99. Bernstein I.M., Thompson, A.W. "Hydrogen Embrittlement of Steels", *Encyclopedia of Materials Science and Engineering*, Pergamon Press Ltd., Oxford, vol. 3, pp. 2241-2245, 1986.

100. Flemings, M.C. *Solidification Processing*, McGRaw-Hill, New York, p. 336, 1974.

101. Neri, M.A., Colas, R., Valtierra, S. "Graphitization in High Carbon Commercial Steels", *Journal of Materials Engineering and Performance,* vol. 7, no. 4, pp. 467-473, 1998.

102. Kung, C.Y., Raymond, J.J. "An Examination of Validity of Existing Empirical Formulae for the Calculation of Ms Temperature", *Metallurgical and Materials Transactions A*, vol. 113 A, no. 2, pp. 323 - 331, 1982.

103. Andrews, K.W. "Empirical Formulae for the Calculation of Some Transformation Temperatures". *Journal of the Iron and Steel Institute*, vol. 203, pp. 721-727, 1969.

104. Winchell, P.G; Cohen, M. *Electron Microscopy and the Strength of Crystals*, (ed. G. Thomas and J. Washburn), Interscience, pp. 995, 1963.

105. Inman, C.H. *Physical Properties of Martensite and Bainite*, The Iron and Steel Institute, Special report 93, pp. 180-181, 1965.

106. Kelly, P.M., Nutting, J. "Strengthening Mechanisms in Martensite", *Physical Properties of Martensite and Bainite*, The Iron and Steel Institute, p. 167, 1965.

107. Kirkaldy, J.S., Venugopalan, D. *Phase Transformation in Ferrous Alloys*, AIME, pp. 125-148, 1984.

108. Austin J.B., Rickett, R.L. "Kinetics of Decomposition of Austenite", *Transactions of the America Institute of Mine Engineers*, vol. 135, pp. 396-415, 1939.

109. Lee, E.-S., Kim, Y. G. "A Transformation Kinetic Model and Its Application to Cu-Zn-Al Shape Memory Alloys— I. Isothermal Conditions". *Acta Materialia (USA)*, vol. 38, p. 1669, 1990.

110. Starink, M.J. "Kinetic Equations for Diffusion-Controlled Precipitation Reactions", *Journal of Materials Science (UK)*, vol. 32, no. 15, pp. 4061-4070, 1997.

111. Takahashi, T., Abe, T., Tada, S. "Effect of Bainite Transformation and Retained Austenite on Mechanical Properties of Austempered Spheroidal Graphite Cast Steel", *Metallurgical and Materials Transactions A*, vol. 27A, no. 6, pp. 1585-1594, 1996.

112. Bhadeshia, H.K.D.H. *Bainite in Steels*, The Institute of Materials, London, p. 295, 1992.

113. Terasaki, T. "Study of Predictive Equations of Thermal Factor and Hardness Related to Weld Cold Cracking", *Tetsu-to-Hagane (Journal of the Iron and Steel Institute*), vol. 67, no. 16, pp. 2715-2723, 1981.

114. Yurioka, N., Suzuki, H., Okumura, M., Ohshita, S., Saito, S. "Carbon Equivalents to Assess Cold Cracking Sensitivity and Hardness of Steel Welds", *Nippon Steel Technical Report*, no. 20, pp. 61-73, 1982.

115. Brown, W.F., Srawley, J.E. "Plane Strain Crack Toughness Testing of High Strength Metallic Materials", *ASTM STP 410*, ASTM, Philadelphia, 1966.

116. Gross, B. "Stress Intensity Factors for a Single-Edge-Notch Tension Specimen by Boundary Collocation of a Stress Function", *NASA TN D-2395*; Washington, National Aeronautics and Space Administration, 1965.

117. Dawes, M.G., Pisarski, H.G., Squirrell, S.J. *Fracture Mechanics Tests on Welded Joints*, ASTM, pp. 191-213, 1988.

118. Steglich, D., Brocks, W. "Micromechanical Modeling of the Behavior of Ductile Materials Including Particles", *Computational Materials Science*, vol. 9, no. 1&2, pp. 7-17, 1997.

119. Dong, M.J., Prioul, C., Francois, D. "Damage Effect on Fracture Toughness of Nodular Cast Iron: Part I. Damage Characterization and Plastic Flow Stress Modeling", *Metallurgical and Materials Transactions A*, vol. 28A, no. 11, p. 2245, 1997

120. Levy, A.J. "The Debonding of Elastic Inclusions and Inhomogeneities", *Journal of the Mechanics and Physics of Solids*, vol. 39, no. 4, pp. 477-505, 1991.

121. Kelly, A., Nicholson, R.B. *Strengthening Methods in Crystals*, Elsevier Publishing Co., Essex, pp.1-8, 1971.

122. Al-Ostaz, A., Jasiuk, I. "Influence of Interface and Arrangement of Inclusions on Local Stresses in Composite Materials", *Acta Materialia (USA)*, vol. 45, no. 10, pp. 4131-4143, 1996.

123. Xu, X.Q., Watt, D.F. "Basic Role of a Hard Particle in a Metal Matrix Subjected to Tensile Loading", *Acta Materialia (USA)*, vol. 42, no. 11, pp. 3717-3729, 1994.

124. Double, D.D., Hellawell, A. "Growth Structure of Various Forms of Graphite", *Proceedings, 2nd International Symposium On the Metallurgy of Cast Iron*, Geneva, pp. 509-25, 1975.

125. Era, H., Kishitake, K., Nagai, K., Zhang, Z.Z. "Elastic Modulus and Continuous Yielding Behaviour of Ferritic Spheroidal Graphite Cast Iron", *Materials Science and Technology (UK)*, vol. 8, no. 3, pp. 257-261, 1992.

126. Dierickx, P., Verdu, C., Rouais, J.C., Reynaud, A., and Fougeres, R. "Study of Physico-Chemical Mechanisms Responsible for Damage of Heat Treated and As-cast Ferritic Spheroidal Graphite Cast Irons", *5th International Symposium On the Physical Metallurgy of Cast Iron*, Nancy, France, 1994.

127. Miao, B., Fang, K., Bian, W., Liu, G. "On the Microstructure of Graphite Spherulites in Cast Irons by TEM and HREM", *Acta Materialia (USA)*, vol. 38, no. 11, pp. 2167-2174, 1990.

128. Marini, B., Mudry, F., Pineau, A. "Experimental Study of Cavity Growth in Ductile Rupture", *Engineering Fracture Mechanics*, vol. 22, no. 6, pp. 989-996, 1985.

129. Dryden, J.R., Deakin, A.S., Purdy, G.S. "Elastic Analysis of Deformation Near a Spherical Carbon Particle Embedded in Iron", *Acta Materialia (USA)*, vol. 35, no. 3, pp. 681-689, 1987.

130. Huang, J.T., Zhang, B.Z., Zhu, J.G. "Improvement of Whisker Tensile Tests", *The First Pacific Rim International Conference on Advanced Materials and Processing (PRICM-1)*, Hangzhou, China, 23-27 June, 1993, The Minerals, Metals & Materials Society (USA), pp. 707-710, 1993.

131. Li, C.M., Oriani, R.A., and Darken, L.W. "Hydrogen", *Z. Phys. Chem.*, vol. 49, p. 271, 1966.

132. Beltran, R., Maldonado, J.G., Murr, L.E., and Fisher, W.W. "Effects of Strain And Grain Size on Carbide Precipitation And Corrosion Sensitization Behavior in 304 Stainless Steel", *Acta Materialia (USA)*, vol. 45, no. 10, pp. 4351-4360, 1997.

133. Melander, A. "Finite Element Study of Short Cracks With Different Inclusion Types Under Rolling Contact Fatigue Load", *International Journal of Fatigue*, vol. 19, no. 1, p.13, 1997.

134. Westergard, H.M. "Bearing Pressures and Cracks", *Journal of Applied Mechanics*, vol. 6, pp. 49-53, 1939.

135. Williams, M.L. " On the Stress Distribution at the Base of a Stationary Crack", *Journal of Applied Mechanics*, vol. 24, pp. 109-114, 1957.

136. Hu, K.X., Chandra, A., and Huang, Y. "Fundamental Solutions for Dilute Distributions of Inclusions Embedded in Microcracked Solids", *Mechanics of Materials*, vol. 16, no. 3, pp. 281-294, 1993.

137. Anderson, T.L. *Fracture Mechanics, Fundamentals and Applications*, CRC Press, Boca Raton, Florida, p. 318, 1991.

138. Swearengen, J.C., Beauchamp, E.K., and Eagan, R.J. "Fracture Toughness of Reinforced Glasses", *Fracture of Mechanics of Ceramics*, vol. 4, Plenum Press, New York, pp. 973-987, 1978.

139. Kim, B.N., Watanabe, M., Enoki, M., and Kishi, T. "Simulation of Fracture Behavior in Particle-dispersed Ceramic Composites", *Engineering Fracture Mechanics*, vol. 29, no. 3, pp. 289-303, 1998.

140. Solecki, JS. *Fracture Mechanics*, Swanson Analysis Systems, Canonsburg, PA, pp. 1-30, 1989.

141. Rice, J.R. "A Path Independent Integral and the Approximate Analysis of Strain Concentration by Notches and Cracks", *Journal of Applied Mechanics*, vol. 35, pp. 379-386, 1968.

142. Anderson, T.L. *Fracture Mechanics, Fundamentals and Applications*, CRC Press, Boca Raton, Florida, p. 22, 1991.

143. Hayes, D.J., Turner, C.E. "Application of Finite Element Techniques to Post-yield Analysis of Proposed Standard Three-point Bend Fracture Test Pieces", *International Journal of Fracture*, vol. 10, no. 1, pp. 17-32, 1974.

VITA

The author was born in Taiyuan, China on October 26, 1966. She enrolled Metallic Materials Department, Sichuan Union University (former Chengdu University of Science and Technology), China, in the fall of 1983 and received her Bachelor and Master of Engineering in Metallic Materials and Heat Treatment in 1987 and 1990, respectively. She was waived all of the China National Graduate School Entrance Examinations as a prestigious honor for the students who demonstrated the top 2% academic performance during the undergraduate study.

After graduation, she worked as an instructor and failure analysis laboratory manager in Chengdu University of Science and Technology. During this time, she won the Outstanding Teacher Award twice, published two papers.

The author came to the Oregon Graduate Institute of Science and Technology in the fall of 1995 to pursue her Ph.D. During this time, she kept a G.P.A of 4.0 and finished several research projects sponsored by U.S. Navy, Oregon Department of Transportation and industrial companies. She coauthored three papers and numbers of technical reports. For her exemplary performance on sponsored research projects, she was selected as the recipient of 1996-1997 Wilson W. Clark Fellowship and her name entered the plaque located the main administration building of Oregon Graduate Institute of Science and Technology, Portland, Oregon.

She married Jiaqing Pang in 1991.